Polyelectrolytes and Their Counterions Studied by EPR Spectroscopy

Dissertation

zur Erlangung des Grades

„Doktor der Naturwissenschaften"

am Fachbereich Chemie und Pharmazie
der Johannes-Gutenberg-Universität
in Mainz

von

Dariush Hinderberger

geboren in Heidelberg

Mainz 2004

Dekan: Prof. Dr. R. Zentel

Tag der mündlichen Prüfung: 02. März 2004

Der Gründliche.

Ein Forscher ich? O spart dies Wort! -
Ich bin nur schwer - so manche Pfund!
Ich falle, falle immerfort
Und endlich auf den Grund!

Friedrich Nietzsche

In memoriam Friedrich Hinderberger

Contents

.   Introduction

Polyelectrolytes are macromolecular substances that are soluble in water or other ionizing solvents and dissociate into macromolecular ions that carry multiple charges (polyions) together with an equivalent amount of ions of small charge and opposite sign (Figure i). They play an important role in fields of scientific research as diverse as molecular biology and nanotechnology.[1-6] Many biological macromolecules such as DNA or proteins are polyelectrolytes and use electrostatic interactions to trigger and control structural changes or binding of small molecules.[5] Synthetic polyelectrolytes are also applied commercially in cosmetics, fuel cells, and food and oil industry.[7,8]
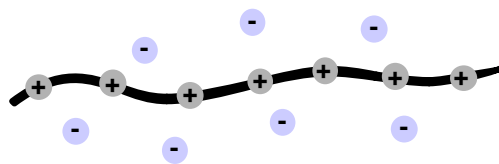
Fig. i. Scheme of the "physicist's view"[15] of a polyelectrolyte that is dissociated into a polyion and small counterions in polar solvents;

Highly charged biological as well as synthetic polymeric materials have been under extensive experimental and theoretical investigation for several decades and it is commonly acknowledged that their interesting structural properties stem from the delicate balance of two opposing interactions.

First, gain in entropy upon release of counterions leads to highly charged polymers, and electrostatic repulsion between the like charges on each repeat unit leads to a preference for extended conformations of the polyelectrolyte chain. Second, polyelectrolytes are usually dissolved in water or other solvents with high dielectric permittivity, which are poor solvents with respect to the polymer backbone (hydrocarbons). Poor solubility is equivalent to an attractive hydrophobic interaction between repeat units on the polyelectrolyte, which favors more collapsed structures.[1]

Polyelectrolytes are probably the least understood class of macromolecules, which is remarkable when considering their importance in molecular biology and materials science. Despite numerous studies on polyelectrolytes, the combined effects of polyelectrolyte-counterion and polyelectrolyte-solvent interactions on polyelectrolyte structure are not fully comprehended. This is mainly due to the importance of a multitude of intertwined length scales in polyelectrolytes as compared with uncharged polymers, which makes theoretical and experimental investigations of the latter ones much simpler.[9] It is known that the screening of intramolecular electrostatic repulsion by

oppositely charged, in particular multivalent, counterions can lead to a dominance of hydrophobic attraction and thus to more collapsed, globular chain conformations.[10,11,12] Within the last decade theoretical investigations of the aforementioned interactions, driven by increasing computing power and sophisticated algorithms, have been carried out and led to predictions of *pearl-necklace*-like conformations in solution that could not yet be convincingly verified by experiments.[13]

As in many fields of polymer science, abstractions are made from the actual chemical structure of the polyelectrolyte (see Fig. i) in order to be able to physically describe these complex materials. Such a simplified "physicist's view"[15] of the materials may, however, not be sufficient to account for all of the observed polyelectrolyte features. To develop chemically more realistic models, it is necessary to gain insight into specific interactions in the polyion-counterion-solvent system. The interactions between the polyion and the small counterions are of particular interest, as they predominantly determine chain conformation.

Characterization methods that probe macroscopic properties (such as conductivity) or can characterize long-range order (light-, x-ray-, and neutron-scattering) have been applied extensively in the past.[1,3,14] Scattering experiments are usually carried out under addition of large amounts of inert salt (e.g. 1M NaCl), which effectively screens Coulomb interactions not only along one polyelectrolyte chain but also between different chains. This is necessary to damp intermolecular components of the scattering function. Information about chain conformations, such as the radius of gyration, $<R_G^2>^{0.5}$, or the mean square end-to-end distance $<R^2>^{0.5}$ of chains can be gained by scattering methods, whereas a detailed, *local* picture of electrostatic interactions between polyelectrolyte and counterions cannot be obtained.

Magnetic resonance methods, such as electron paramagnetic resonance (EPR) spectroscopy[16] on spin-carrying counterions, being local, sufficiently sensitive and highly selective, have the potential to provide complementary information on microscopic structure and dynamics of polyelectrolyte materials.[17,18] Ionic spin probes, which substitute for low molecular weight counterions, have been used previously to gain detailed information on structure and dynamics of polymer systems containing charges.[17-22]

In this work, a variety of EPR methods are applied to elucidate interactions between several paramagnetic spin probes with multiple charges and oppositely charged polyelectrolytes in solution. These spin probes can be considered as tracers for multivalent counterions. It is the aim of this work to contribute to a better understanding of the nature of polyelectrolyte-counterion interaction, and it is particularly hoped that the experimental findings can help to bridge the gap that still persists between theoretical description and experimental investigation of complex polyelectrolyte materials.

This thesis is divided into five chapters. The first two chapters provide the foundation for the understanding of the experimental results. In Chapter 1, the standard theoretical description of polyelectrolytes is introduced, with particular focus on polyelectrolyte-counterion interactions. The fundamentals of electron paramagnetic resonance (EPR) spectroscopy, as far as they are necessary to

comprehend the experimental findings, are introduced in Chapter 2. The main results on characterizing interactions between polyelectrolyte chains and oppositely charged ions in liquid and frozen solution are discussed in Chapters 3 and 4. These investigations first focus on a very well defined model system of a rigid-rod polyelectrolyte built from coordination of Ru^{2+} centers and organic spacers. Having presented the basic phenomena in this model system, experimental findings from studies on commercially available flexible, highly charged polyelectrolytes PDADMAC and PSS are scrutinized and discussed. Both these polyelectrolytes are already extensively used in industrial applications.[1]

Chapter 3 presents experimental results from EPR spectroscopy and gives a qualitative, in large parts *model-free* analysis of the spectroscopic findings. In Chapter 4 those data are analyzed according to recent *theoretical models of polyelectrolyte systems*. It is shown that in particular the analysis with polyelectrolyte models can provide information on the *axial* distribution of counterions along the polyelectrolyte chain and the *radial* distribution perpendicular to the chains, while changes in rotational *dynamics* of the counterions induced by interaction with the polyelectrolyte can be derived from the original data without treatment with such a model.

The final chapter summarizes the conclusions drawn from the experimental results and discusses the general applicability of EPR spectroscopy to gain further insight into structure and dynamics of systems that are dominated by electrostatic interactions.

1   Fundamentals of Electrostatic Interactions and Polyelectrolytes in Solution

Polyelectrolytes are polymers that bear charges. However, they cannot be fully described by a mere superposition of electrolyte and neutral polymer behavior.[1,2,15] Their interesting macroscopic features are a direct consequence of their intricate microscopic structure in solution, which is determined in particular by electrostatic interactions between large polyions and numerous small counterions.

To provide a basis for discussing these interactions, this chapter will commence (Section 1.1) with a general introduction to the theory of simple strong electrolytes in solution. Starting from Poisson-Boltzmann theory the Debye-Hückel approximation is derived. In the second section (1.2), basic concepts used to describe polymer systems are presented. Then, some specific approaches to incorporate electrostatic interactions into the theoretical description of polymers are presented that are of interest in the analysis of the experimental results of Chapters 3 and 4.

1.1   Theoretical description of electrolyte solutions

1.1.1   Primitive model and Poisson-Boltzmann theory

Most theoretical and experimental investigations of ions in solution are based on the Poisson-Boltzmann (PB-) theory,[23] although considerable efforts were dedicated to development of theoretical approaches to charged systems beyond PB-theory.[24] The foundation of the Poisson-Boltzmann approach is the *primitive model* of electrolytes. Within this model, ions are described as small hard spheres of diameter $a=2r_{ion}$ and charge $q_i=z_i{}^*e$ that are distributed in a dielectric continuum of constant permittivity ε with volume V at a constant temperature T.[23]

The starting point of the description of solutions of electrolytes is Poisson's equation

$$\nabla^2\phi(r) = -\frac{\rho(r)}{\varepsilon_0\varepsilon(r)}, \tag{1.1}$$

which relates the local electrostatic potential $\phi(r)$ to the local charge density $\rho(r)$ and is merely a restatement of Coulomb's law. In the primitive model, $\varepsilon(r)$ is replaced by the constant ε. This differential function can be solved for diverse actual charge distributions and delivers the respective electrostatic potential.

For an infinite ensemble of charges the charge density is $\rho(r) = \sum\limits_{i=1}^{N} q_i \delta(r - r_i)$ and eq. 1.1 provides the Coulomb potential due to all ions as

$$\phi(r) = -\frac{1}{4\pi\varepsilon_0\varepsilon} \sum_{i=1}^{N} \frac{q_i}{|r - r_i|} . \tag{1.2}$$

In equation 1.2, $|r\text{-}r_i|$ is the 3-dimensional geometric distance $[(x\text{-}x_i)^2 + (y\text{-}y_i)^2 + (z\text{-}z_i)^2]^{\frac{1}{2}}$ between the charged particles. It is convenient to define $\phi_i(r)$, which is the electrostatic potential at any r due to all but the i-th charge:

$$\phi_i(r) = \phi(r) - \frac{q_i}{4\pi\varepsilon_0\varepsilon |r - r_i|} . \tag{1.3}$$

One can carry out the canonical (NVT) ensemble average while keeping ion i fixed at the position r_i, thus giving:

$$\left\langle \phi_i^{r_i}(r) \right\rangle = \left\langle \phi^{r_i}(r) \right\rangle - \frac{q_i}{4\pi\varepsilon_0\varepsilon |r - r_i|} , \tag{1.4}$$

in which the first term on the right-hand side is the electrostatic potential at position r in a system in which the i-th charge is fixed at r_i and the others are averaged over the whole volume. After carrying out the averaging and restating the overall charge density of the system in terms of its radial distribution function one can deduce the following version of equation 1.1:

$$\nabla^2 \left\langle \phi^{r_i}(r) \right\rangle = -\frac{1}{\varepsilon_0\varepsilon} \sum_k c_k q_k \exp\left[-\frac{w_{ik}(r)}{kT} \right] \tag{1.5}$$

in which still the i-th particle is fixed and c_k and q_k are the concentration and the charge of the k-th species, respectively, and $w_{ik}(r)$ denotes the potential of mean force acting on the i-th ion. Note that equation 1.5 is exact within the primitive model and that the main difficulty is posed by the proper choice of $w_{ik}(r)$.

Under the condition that $r > 2r_{ion}$ and if one approximates the potential of mean force by $w_{ik}(r) = q_k \left\langle \phi^{r_i}(r) \right\rangle \equiv q_k \psi(r)$ one can derive the *non-linear Poisson Boltzmann* equation:

$$\nabla^2 \psi(r) = -\frac{1}{\varepsilon_0\varepsilon} \sum_k q_k c_k \exp\left[\frac{q_k \psi(r)}{kT} \right] . \tag{1.6}$$

Starting from this non-linear differential equation, in the next section the further approximations made in the Debye-Hückel approach for description of strong electrolytes are explained.

1.1.2   Debye-Hückel approximation

In the seminal work by Debye and Hückel,[25] a linearization of the exponential term on the right-hand side of equation 1.6 is performed by expanding the exponential as a power series and neglecting all terms beyond the linear term:

$$\sum_{i=1}^{N} q_k c_k \exp\left[\frac{q_k \psi(r)}{kT}\right] \approx \sum_k q_k c_k - \frac{1}{kT}\sum_k c_k q_k^2 \psi(r) \quad . \tag{1.7}$$

Note that this approximation is only valid in the case of weak potentials, i.e. for $\psi(r) << kT/q_k$. The first term on the right-hand side of equation 1.7 vanishes for a system that is electroneutral as a whole. Substituting this approximation into equation 1.6 gives the *linearized Poisson-Boltzmann* equation

$$\nabla^2 \psi(r) = \frac{1}{\varepsilon_0 \varepsilon kT}\sum_k c_k q_k^2 \psi(r) \quad . \tag{1.8}$$

One can relate the constant terms in equation 1.8 to the ionic strength $I = 1/2\sum_k z_k^2 c_k$ and define the *Debye length* λ_D

$$\frac{\sum_k c_k q_k^2}{\varepsilon_0 \varepsilon kT} = \frac{e^2 \sum_k c_k z_k^2}{\varepsilon_0 \varepsilon kT} = \frac{2e^2 I}{\varepsilon_0 \varepsilon kT} = \frac{1}{\lambda_D^2} \quad , \tag{1.9}$$

so that the equation at the heart of Debye-Hückel theory is now written as:

$$\nabla^2 \psi(r) = \frac{1}{\lambda_D^2}\psi(r) \quad . \tag{1.10}$$

The Debye length is a screening length that quantifies the range of an electrostatic potential of an ion in an ensemble of small ions. Equation 1.10 is exact in the limit of infinite dilution.

To solve this equation, boundary conditions have to be established for the potential that describes the system of interest. For an ensemble of small ions an appropriate potential is given by a spherically symmetric *screened Coulomb potential*, which takes into account screening of one charge by all the other surrounding ions. The potential is then given as:

$$\psi(r) = \frac{q_k}{4\pi\varepsilon_0 \varepsilon} \cdot \frac{1}{r}\exp\left[-\frac{r}{\lambda_D}\right], \tag{1.11}$$

in which the effect of the Debye screening length becomes obvious.

For simple electrolyte systems, many experimental findings could be reproduced by the simple Debye-Hückel approach of equations 1.10 and 1.11, but for systems as complex as polyelectrolytes, in which many small ions are permanently connected to form a polyion and are surrounded by counterions, this approach breaks down. The prerequisite of weak potentials around the ions is not very likely to be fulfilled for systems with such a of high charge density as polyelectrolytes. This is

one of the main complications that arise when describing the electrostatic interactions in polyelectrolyte-counterion systems.

The next sections introduce concepts to rationalize and describe the conformations of polyions and the distribution of small counterions around them.

1.2   Polyelectrolytes in solution

It is the aim of this section to shortly review the basic concepts of polymers in solution that are of relevance to the description of polyelectrolytes, too. This description concentrates on static properties and excludes chain dynamics. In addition, the striking phenomena that originate from polyion-counterion interaction in solution are pointed out.

1.2.1   Static chain properties: concepts

Description of polymer chains in solution usually starts from ideal single chains. In such ideal chains there is no interaction among polymer repeat units and between repeat units and solvent. The main parameters to describe a linear, ideal polymer chain consisting of N monomers in a melt or in solution are the

i)   mean-square end-to-end distance, $\langle R^2 \rangle$

ii)   mean-square radius of gyration, $\langle \vec{R}_G^2 \rangle = \dfrac{1}{N} \sum_{n=1}^{N} \langle \vec{r}_n^2 \rangle$

iii)   contour length l_c,

which are calculated from quantities schematically shown in Figure 1.1.
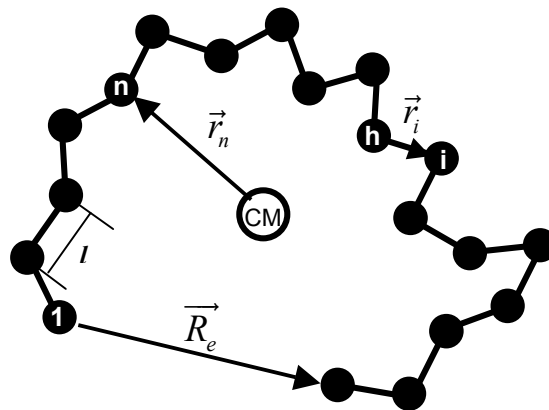
Figure 1.1. Schematic drawing of a linear ideal polymer chain; **CM**: Center of mass of the system; *l*: spacing between two repeat units; R_e: end-to-end vector; r_n: vector connecting CM and *n*-th repeat unit; r_i: vector connecting *h*-th and *i*-th repeat unit;

Note that all these factors are averaged over the full ensemble of repeat units and all possible position for these repeat units. The mean-square end-to-end distance gives an average distance between the two ends of the chain. Its final form is highly dependent on the model of repeat unit distribution. The mean-square radius of gyration is defined as the averaged quadratic distance of all segments r_n from the center of mass of the macromolecule and is experimentally most easily

accessible, e.g., by scattering techniques. Finally, the contour length is the largest possible end-to-end distance and is simply the product of the number of bonds between monomeric units and the length that is projected onto the contour of the macromolecule.

The next step is to rationalize the chain conformation. For polyelectrolytes, this poses a much more severe problem than for neutral polymer, for which chain structure can often be described by one of the following models. In addition to "trivial" conformations such as infinite extended chains, several models of different degree of sophistication have been developed[9,26], such as the

i)   *freely jointed chain* (FJC) model,

ii)   *freely rotating chain* (FRC) model,

iii)   *worm-like chain* (WLC) model,

which are just three of the more prominent models.
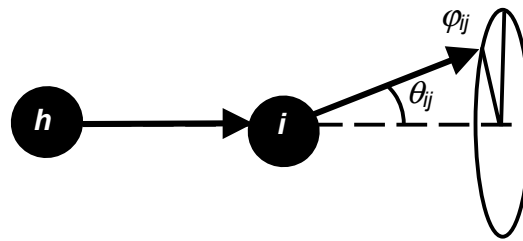
Figure 1.2. Definition of the bond angles and torsion angles between polymer repeat units. θ_{ij} are the angles between bond vectors, while the torsion angles φ_{ij} determine how strongly tilted a bond is at constant bond angle;

Chain flexibility in polymers usually stems from the torsion angles φ_{ij} between the repeated polymer segments, while the bond angles θ_{ij} are usually rather fixed (both of which are defined in Figure 1.2). The FJC model assumes a constant segment length $l = |\vec{r_i}|$ and no correlation between the directions of the bond vectors, i.e., $\langle cos\,\theta_{ij}\rangle = 0$ with the angle between two adjacent monomers θ_{ij}. The most popular version of the model divides a macromolecule into M segments (repeat units), which are usually *not* coincident with the N chemical monomers but built of several monomers (also called *Kuhn segments*) of length b. The mean-square end-to-end distance in the FJC model is simply

$$\left\langle \vec{R}^2 \right\rangle = Ml^2 , \tag{1.12}$$

where l is the length of one segment, regardless whether it is coincident with a bond length or meant as a Kuhn-segment length. In the FRC model, bond angles θ_{ij}, are fixed for all i, j. The torsion angles, though, are all equally probable and the rotation around the bond direction is still allowed so that the difference in bond potential is neglected. The mean-square end-to-end distance now becomes

$$\left\langle \vec{R}^2 \right\rangle = Ml^2 \frac{1+cos\,\theta}{1-cos\,\theta} . \tag{1.13}$$

Refinement of this description is achieved by adding a constraint on the rotation of the segments, which in a real system might stem from steric hindrance due to side groups. An important quantity to describe the decay of correlation of bond vectors along the chain is the persistence segment s_p:

$$s_p = -\frac{1}{ln(cos\,\theta)} \quad . \tag{1.14}$$

The WLC model (also sometimes called Kratky-Porod[27] model) is a special case of the FRC model assuming small bond angles, i.e., $\theta \ll 1$. This model has proven to be in excellent agreement with experimental findings for very stiff macromolecules, such as DNA. Worm-like chains will be of utmost importance for the description of polyelectrolytes, since those highly charged polymers can often be assumed to be stiffer than their (hypothetical) neutral chain analogue. This is due to electrostatic repulsion of charges along the backbone that increases the rigidity. The WLC model lays the foundation for the Odijk-Skolnick-Fixman (OSF)[1,28,29] approach for description of polyelectrolytes, which is explained in more detail in section 1.2.4.

Persistence length l_p

The so-called persistence length l_p is the central parameter for the evaluation of chain rigidity in the WLC model. It is derived from the persistence segment defined in equation 1.14 when assuming small bond angles, as done in the WLC model. For $\theta \ll 1$, the cosine in equation 1.14 can be expanded in a power series and the expression for the persistence segment becomes:

$$s_p = -\frac{1}{ln(cos\,\theta)} \approx \frac{2}{\theta^2} \quad . \tag{1.15}$$

The persistence length is finally defined as the length of such a persistence segment:

$$l_p \equiv s_p l = l\frac{2}{\theta^2} \quad , \tag{1.16}$$

and can also be evaluated as the length scale, at which the mean scalar product of the tangent vectors of the bond angles has decayed to $1/e$.

The WLC model is capable of describing different chain conformations. With $l_p \to \infty$, the worm-like chain becomes a rod-like chain.

From ideal to real chains

The next level of sophistication is achieved by accounting for the intrinsic volume that each real monomer needs in space and by allowing ideal chains to have - attractive or repulsive - interactions among repeat units along their backbone. These effects can be included into polymer models by introduction of the so-called *excluded volume*.[9] The excluded space can be illustrated by hard-core repulsion potential that prevents the centers of two (spherical) monomers from approaching each other closer than twice their radius.

The concept of *solvent quality*[9] rationalizes excluded volume effects and monomer-solvent interaction. Usually, one uses a categorization with respect to the temperature of the system. A so-called θ-temperature is defined, at which real chains have ideal chain conformations, i.e., the excluded volume vanishes. The three most important categories of solvent quality are:

    i)   poor solvents ($T<\theta$)

    ii)   "θ"-solvents ($T=\theta$)

    iii)   good solvents ($T>\theta$).

In poor solvents ($T<\theta$), monomer-monomer attraction is significantly stronger than monomer-solvent attraction, which leads to a negative excluded volume and more collapsed chain structures compared to the ideal chain. In θ-solvents (i.e., at the θ-temperature), monomer attraction and hard-core repulsion cancel each other and with exception of small corrections, the chain conformation is that of an ideal chain. Finally, in good solvents ($T>\theta$), monomer-monomer and monomer-solvent attraction are energetically almost equally favorable and the excluded volume is positive but slightly reduced compared to the hard-core potential. This state is also referred to as a *swollen chain*, it has a larger radius of gyration than the ideal chain due to swelling by solvent molecules.

A rather simple scaling law dependence for chain size R on the number of monomers or segments N is found for the excluded volume interaction:[1,8]

$$R \propto N^{\nu} \ . \tag{1.17}$$

For the poor solvent case ($T<\theta$), the scaling exponent ν equals 1/3, at the θ-temperature one finds $\nu=1/2$, and in the good solvent case $\nu=0.588$.

Concentration regimes

One generally classifies solutions of polymer chains in three distinct regimes: dilute solutions, semi-dilute solutions, and concentrated solutions.[1,8] The concentrations that mark the transition from one regime to another are called *overlap concentrations* and marked as c^*(dilute→semi-dilute) and c^{**}(semi-dilute→concentrated).

Usually, one speaks of the dilute regime if the single polymer chains are well isolated in solution, i.e., there is no significant entanglement of polymer chains. Alternatively, following de Gennes,[30] one could divide individual chains into small "*blobs*" (globular domains) that are dilute in solution. In semi-dilute solutions, there is overlap between individual chains or alternatively one has a dense-packing of blobs. In a concentrated solution, finally, there is immense overlap between chains and there is a dense network of polymer chains.

This classification is very powerful for neutral polymers, but bears some problems when applied to polyelectrolytes. In polyelectrolyte systems, highly charged macromolecules interact with each other even at very low concentrations,[1] which is due to long-range correlations between the

charged polymers. Therefore, polyelectrolyte solutions are usually classified as semi-dilute even when there are no significant mechanical entanglements of the chains.

1.2.2 Counterion condensation

Having introduced basic concepts of Debye-Hückel theory in Chapter 1.1 and of polymers in solution in Section 1.2.1, it is now the target to combine both these models to describe polyelectrolytes and their counterions in solution.

The concept of *counterion condensation* was introduced by Manning in 1969[31,32] and specified in 1979[33] and is still the central model used to describe the interaction of the *ensemble* of counterions with polyelectrolytes in solution. Within this model, the polyion is always assumed to be an infinitely long rigid-rod with equally spaced charges (spacing *b*), and a fraction of counterions is electrostatically bound or *condensed* to the polyion, reducing the effective charge density on the rod-like chain, while the other fraction is unbound or *free*. It is an effect that is determined by the interplay of opposing electrostatic (energetic) and entropic effects. Coulomb energy decreases when the counterions are very close to the polyion chain, while entropy maximization counteracts the corresponding reduction of effective volume of the system and thus counterion condensation.

In a refined view of the condensed state, one may also differentiate between those counterions that form specific ion-pairs with charges on the chain - so-called *site-bound* counterions - and such counterions that are trapped in the electrostatic potential around the polyion - so-called *territorially bound* counterions.[33] This is schematically depicted in Figure 1.3.

In equation 1.9, the Debye length λ_D was defined as a measure for the screening of an ion by all
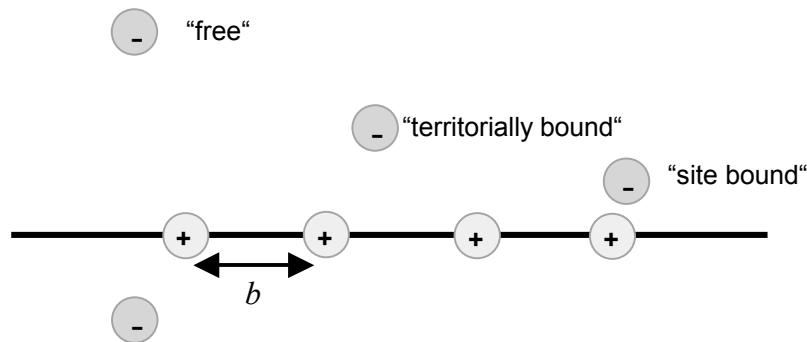
Figure 1.3. Schematic illustration of the concept of counterion condensation; Excerpt of an infinite rigid-rod-like polyelectrolyte chain and the three different counterion regimes following Manning; *b* is the charge spacing along the chain;

surrounding ions within the Debye-Hückel approach. For a quantification of counterion condensation one needs to introduce another electrostatic screening length, the *Bjerrum length λ_B*:[1]

$$\lambda_B = \frac{e^2}{4\pi\varepsilon_0\varepsilon kT} \, .$$

(1.18)

The Bjerrum length is a specific function of the solvent permittivity and is the distance between two unscreened charges, at which the electrostatic interaction equals thermal energy *kT*. In water, at 298 K, λ_B attains a value of 0.71 nm.

The crucial parameter for counterion condensation is the ratio of Bjerrum length and charge spacing, called *Manning parameter*:[1]

$$\xi_M = \frac{\lambda_B}{b} .$$ (1.19)

The linear charge density along the chain in the case without counterion condensation, d_0=e/*b*, is reduced to d_c=βd_0 if counterions are condensed to the chain, with $0 \leq \beta \leq 1$ being the fraction of free counterions.

Evaluation of the populations of condensed and free counterions leads to simple findings that correlate the Manning parameter to the onset of counterion condensation:[1,2]

$$\xi_M < \frac{1}{z_i} \implies \beta \to 1,\ d_c = d_0$$

$$\xi_M \geq \frac{1}{z_i} \implies \beta \to \frac{1}{\xi_M},\ d_c = \beta d_0 = \frac{e}{\lambda_B}$$ (1.20.a, b)

In relations 1.20, z_i is the charge valence of the ions, and one should observe counterion condensation for $\xi_M \geq 1/z_i$. From 1.20, another feature of counterion condensation becomes apparent: the condensation threshold decreases with the charge valence of the ions, so that multivalent counterions are always preferred to monovalent ions and may even expel the latter from the condensed state. This is also plausible when considering the entropy of the overall system. If one *z*-valent ion is condensed, *z* monovalent ions can be expelled thus increasing entropy (number of individual particles) of the system. This effect has been utilized in this study (see Chapter 3) to probe polyelectrolytes by adding multivalent, EPR-active tracers for counterions.

Counterion condensation has been successfully used to interpret experimental data for DNA[34] but often fails to describe highly flexible polyelectrolytes. This is a consequence of the fact that the approximation of a polyelectrolyte chain as an infinite rigid-rod is poor for very short or highly flexible chains. Since the interplay between chain conformation and electrostatic potential is highly non-linear, it can only be introduced into a Debye-Hückel-like description artificially by modifying the linear charge density for each stage of condensation. Analytical and numerical solutions to the non-linear Poisson-Boltzmann equation (eq. 1.6) for infinite rod-like polyions suggest that they intrinsically possess the effect of counterion condensation.[1,15] This is depicted in the next section.

By adding large excess of inert salt (e.g. NaCl) one can screen the electrostatic potential, e.g. of equation 1.11, to such an extent that the polyion behaves like a neutral polymer and counterion condensation effectively ceases. A weak point of this treatment is that it is hardly possible to estimate the "cutoff distance" for the condensed state, i.e., the distance that marks the transition from a condensed to a free counterion state.

Despite all shortcomings of this simple approach, it is still the most widely used concept to estimate and characterize counterion-polyion interaction. Together with the distinction of site-, and territorially bound states on the one hand and free states on the other hand it will be consistently used in the explanation of experimental findings of this work.

1.2.3   The cell model

The cell model or more specifically the *cylindrical cell model* is one of the most thoroughly investigated models for the theoretical description of polyelectrolytes in solution.

This model is applied in many studies as it can be derived analytically from the non-linear PB equation and alternatively also numerical simulations using sophisticated algorithms are possible. In addition, many of the observed and suggested effects of polyion-counterion interaction can be illustrated that go beyond the simple Manning picture.

As shown in Figure 1.4, the model for the polyelectrolyte system consists of a linear, rigid polyion that is surrounded by a cylindrical volume of the same length, which marks the region where counterions are considered condensed to the chains. The following assumptions are made:[15]

i)   high dilution of polyelectrolyte (i.e. only single chains)

ii)   the cylindrical volume (i.e. the radius must be selected) equals the overall volume that the polyelectrolyte has in solution

iii)   counter- and co-ions are distributed such that each cylinder is electroneutral

The last point is true for most of the studies but recently a modified version of the model has been developed[36] that does not require electroneutrality and thus allows a fraction of counterions that do not interact with the polyion. Although – as in the case of Manning condensation – this is a rather simple
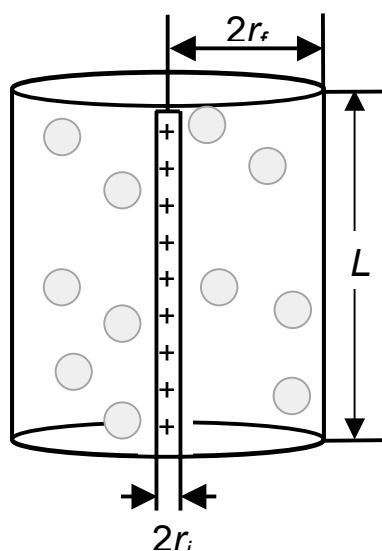

Figure 1.4. Sketch of the cylindrical cell volume description of dilute solutions of rigid polyelectrolytes; L is the chain length, r_i marks the initial and r_f the final radial coordinate of the cylindrical volume; Note that cylinders must be overall electroneutral;

view of the polyelectrolyte system, there is a variety of typical polyelectrolyte characteristics that can be explained in such a model. Much of the data interpretation of Chapter 4 will be performed with respect to the illustration shown in Figure 1.4, since one may assume counterions outside of the cylindrical volume (in the charged cylindrical cell model explained in Section 4.1) as unbound and those inside the volume either site- or territorially bound. To assess the quality of agreement of the predictions with experimental results, one has to always keep in mind that this model also starts off from Poisson-Boltzmann theory, thus assuming weak electrostatic potentials and that it effectively assumes a pure superposition of polymer and electrolyte behavior, which is inadequate. Despite these deficiencies, this is so far the most promising approach to describe polyelectrolyte-counterion interaction. A very detailed and thorough inspection of the cylindrical cell model can be found in Reference 15.

1.2.4   Odijk-Skolnick-Fixman (OSF) theory

The last two sections focused on the description of counterions in solutions of rigid polyelectrolyte chains. In this section, I present an approach based on the worm-like chain (WLC) model that was introduced by Odijk, Skolnick, and Fixman (hence OSF) in 1977.[28,29]

The core idea of this model is to introduce a cutoff-distance for the electrostatic interaction and include the polyion behavior of the chains by assuming an additional contribution to the overall persistence length l_p of a polyelectrolyte chain due to electrostatic repulsion of the backbone charges:[1]

$$l_p = l_{p,0} + l_{p,e} \; . \tag{1.21}$$

In equation 1.21, $l_{p,0}$ is the persistence length of the (hypothetical) neutral polymer analogue and $l_{p,e}$ is the electrostatic contribution, as depicted in Figure 1.5.
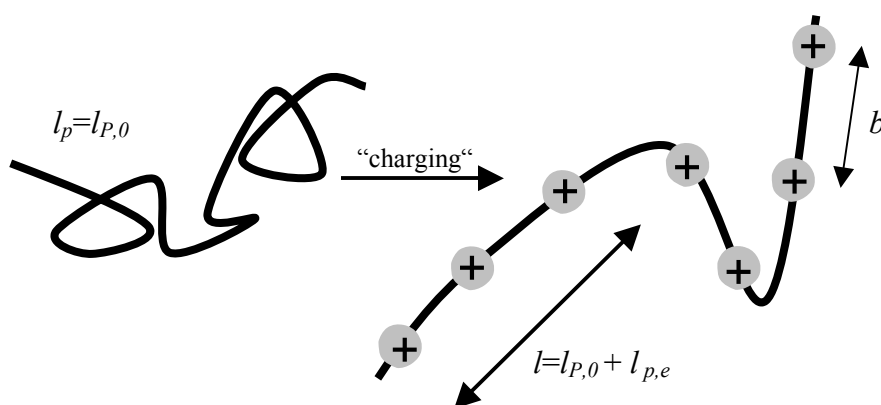
Figure 1.5. Schematic depiction of the fundamental assumption underlying the OSF approach; The "charging" describes the transition from an hypothetical neutral polymer to the same polymer chain with equally spaced (spacing *b*) charges

Hence, the polyelectrolyte chain can in this picture be described as a worm-like chain near the rigid-rod limit with significant bending only taking place at long lengthscales. Note that this treatment is based on the linearized PB equation, eq. 1.10, and assumes a simple screened exponential Coulomb

potential as shown in equation 1.11 to describe the polyion potential. From the expression for the free energy of an infinite OSF-like chain one can calculate the electrostatic persistence length for a system above and below the counterion concentration threshold:

$$l_{p,e} = \frac{\lambda_D^2}{4\lambda_B} \propto \frac{1}{I}; \quad \xi_M \geq 1/z_i \ (\lambda_B \geq b)$$

$$l_{p,e} = \frac{\lambda_B \lambda_D^2}{4b^2} \propto \frac{1}{I}; \ \xi_M < 1/z_i \ (\lambda_B < b)$$

(1.22.a, b)

The ionic strength dependence of electrostatic persistence length in a solution gives experimental access to verify the OSF assumption. The inverse linear dependence found in equations 1.22 could only be verified for polyelectrolytes that already have intrinsic stiffness in their polymer backbone. For flexible polyelectrolytes, often a dependence on the inverse square root of the ionic strength is found, which opposes predictions of OSF theory.[1]

In initial OSF theory, the expression for the electrostatic persistence length was derived from the linearized PB equation (eq. 1.8), which may be the reason for the apparent inability to quantitatively describe the persistence length behavior of flexible polyelectrolyte. In recent years, many studies have focused on calculating $l_{p,e}$ from the non-linear PB equation, foremost with numerical methods,[36,37] for which better agreement (i.e. agreement over a larger I-range) with experimental data on DNA could be achieved. Expansion of the concept of electrostatic persistence length to flexible polyelectrolytes, though, was only achieved by a more elaborate mean-field approach.[38]

The description of polyelectrolyte systems with many different chemical structures over a broad concentration and ionic strength range is probably impossible to achieve within one theory. These systems are far more complex than neutral polymers, since they are mainly governed by long-range electrostatic interactions, while all complications of describing chain conformations apply in the same way as for neutral polymers. From an experimentalist's point of view, one has to carefully inspect the investigated system and the length- and timescales that are accessible with the applied technique. Based on this information, it might then be possible to select one of the existing simple models to describe the experimentally accessible parameters.

Throughout this work, even flexible polyelectrolytes will often be treated within either the simple Manning- or a modification of the cell model. This is mainly based on the fact that the applied technique of Electron Paramagnetic Resonance (EPR) on spin-carrying counterions is a method that delivers information on the dynamics and immediate surroundings of the tracer molecules, which ranges from ~0.1nm to ~5nm. Hence, long-range effects do not directly influence accessible parameters and the assumptions made with respect to polyelectrolyte conformation need only hold for the EPR lengthscale.

2 Fundamentals of EPR Spectroscopy on Polyelectrolytes

"Electron paramagnetic resonance (EPR) is a spectroscopic method for determining the structure and dynamics and the spatial distribution of paramagnetic species".[39] This description summarizes all advantages and disadvantages of EPR spectroscopy. Due to lack of naturally occurring paramagnetic systems, in many cases one has to artificially introduce stable free radicals. These are called spin labels if they are covalently linked to the investigated system and spin probes if their interaction is of non-covalent nature.[40,92] This apparent disadvantage, though, can often be of great value, as these spin probes can be detected very specifically and with higher sensitivity as compared to the related method of nuclear magnetic resonance (NMR) on, e.g., ^{1}H-nuclei.[41]

This chapter will give a concise introduction into the theoretical foundations of EPR and its different experimental techniques. It is outside the scope of this chapter, though, to discuss the techniques in detail, the reader is referred to References 16 and 39 for this purpose.

2.1 Introduction: resonance condition

When Stern and Gerlach experimentally proved the existence of a magnetic moment of a beam of silver atoms in their famous experiment in 1920,[42] they were not aware that this magnetic moment originated from the electron spin of the unpaired s-electron of silver. Uhlenbeck and Goudsmit assigned the found half-integral angular momentum (the silver beam was split in two components) to the intrinsic property of the electron, the spin, which had to be introduced artificially to the "old" quantum mechanics.[43,44] In the framework of relativistic quantum mechanics derived by Dirac the spin emerges as an intrinsic degree of freedom of the electron (or respective nuclei).[45] After the description of the resonance phenomenon in terms of classical physics, the quantum mechanical description will be used to discuss spin interactions and specifics of experiments.

Each electron with its spin angular momentum $\boldsymbol{S}$ gives rise to a magnetic moment $\boldsymbol{\mu}$:

$$\boldsymbol{\mu} = -g\beta_e \boldsymbol{S} ,\qquad (2.1)$$

where g is the electron g-value (for the free electron g_e=2.0023193043737), β_e is the Bohr magneton, β_e=e$\hbar$/2m_e. If an electron is subjected to an external magnetic field $\boldsymbol{B}$,[46] the z-axis of the system can be defined as the direction of vector $\boldsymbol{B}$ and the strength of the field can be quantified by the magnitude B_0. The spin magnetic states are not degenerate any more and the energy of the electron in the B-field becomes dependent on the magnetic quantum number m_S, which can attain the value ±1/2, depending on the direction of the electron spin with respect to the outer B-field:

$$E = g\beta_e B_0 m_S , \tag{2.2}$$

The two spin states differ by an energy that can be matched by electromagnetic radiation at the *Larmor frequency* ω_S according to the resonance condition:

$$\Delta E = \hbar\omega_S = g\beta_e B_0 . \tag{2.3}$$

In EPR spectroscopy, this condition is fulfilled by microwave (mw) radiation and usually available resonance frequencies range from 1 GHz to 95 GHz. Historically, these frequencies are divided into *bands*, and in this work measurements were performed in the range 9.3 GHz-9.8 GHz (B_0~0.340 T = 3400 G), called X-band, and at the tenfold frequency of ~94 GHz, called W-band. The magnetic field will always be given in Gauss (G).

Note that in EPR always an *ensemble* of magnetic moments of electron spins is detected and that the measured quantity is the *macroscopic magnetization*, the net magnetic moment per volume:

$$\boldsymbol{M}_0 = \frac{1}{V}\sum_{i=1}^{N} \boldsymbol{\mu}_i , \tag{2.4}$$

The resonance condition is altered by magnetic interaction of the electron spin with, e.g., magnetic nuclei in its vicinity. The spin Hamiltonian for the system can best describe the different energetic contributions.

2.2   Spin Hamiltonian and types of interactions

The static, i.e., the time-independent Hamiltonian of an effective electron spin S that is coupled to m nuclei of spin I is given by:[39,47]

$$H_0 = H_{EZ} + H_{ZFS} + H_{HF} + H_{NZ} + H_{NQ} + H_{e-e} . \tag{2.5}$$

In this *spin Hamiltonian* all contributions to energy are neglected except for those involving the spin. This is possible as all other contributions to the overall Hamiltonian are energetically well separated from the magnetic interactions. The Hamilton operator in equation 2.5 contains all relevant terms for this study: the electron Zeeman interaction (H_{EZ}), the zero-field splitting (H_{ZFS}), the hyperfine interaction (H_{HF}), the nuclear Zeeman interaction (H_{NZ}), and the nuclear quadrupole interaction (H_{NQ}),

and weak electron-electron interaction (H_{e-e}). These terms will be explained in detail in the following paragraphs.

Electron Zeeman interaction

This interaction contributes by far the dominating term in the Hamiltonian, at least for a system with $S=1/2$ at practically used static magnetic fields. Hence, the quantization axis is the z-axis, which is often called the *high-field approximation*. The electron Zeeman term describes the splitting of the two degenerate electron spin states ($\pm 1/2$) upon interaction with an external magnetic field, as it has been introduced classically in equation 2.3:

$$H_{EZ} = \beta_e \boldsymbol{B}^T \boldsymbol{g} \boldsymbol{S} \ , \tag{2.6}$$

$\boldsymbol{S}$ is the spin-vector operator and the g-factor from eq. 2.3 now has the general form of a 3×3 matrix. It can be formulated as a symmetric tensor with three principal values g_{xx}, g_{yy}, g_{zz} and three Euler angles describing their orientation relative to the molecular coordinate system. Where necessary in this work, the *g*-molecular frame is chosen as the reference frame. In solution, when molecular rotation about all axes is fast, the $\boldsymbol{g}$-matrix is averaged to an isotropic *g*-factor, which determines the center of the CW EPR spectrum:

$$g_{iso} = \frac{1}{3} \left(g_{xx} + g_{yy} + g_{zz} \right). \tag{2.7}$$

Zero-field splitting

The zero-field splitting describes the dipole-dipole interaction between individual spins that form a group spin with $S>1/2$, e.g. in a transition metal ion such as Mn^{2+} (S=5/2).[48] The (2S+1)-fold degeneracy of the ground state even in the absence of an external *B*-field is removed, which leads to a transition even at zero field. This interaction adds the so-called fine structure term to the Hamiltonian with the symmetric and traceless zero-field interaction tensor $\boldsymbol{D}$:

$$H_{ZFS} = \boldsymbol{S}^T \boldsymbol{D} \boldsymbol{S} \ . \tag{2.8}$$

Note that the fine structure term vanishes completely if the spin system has a cubic symmetry and S$\leq$2 and is reduced to only the (small) hexadecapolar distortion to the magnetization density if the system has an overall spin of $S>2$.

Hyperfine interaction

The interaction of an electron spin with surrounding nuclear spins is called hyperfine interaction. It is extremely useful in EPR spectroscopy, as information on the direct magnetic environment of the electron spin can be gained. The contribution to the Hamiltonian is given by:

$$H_{HF} = \sum_{i=1}^{N} \boldsymbol{S}^T \boldsymbol{A_i} \boldsymbol{I_i} = H_F + H_{DD} \ , \tag{2.9}$$

where I is the nuclear spin operator and A the hyperfine interaction tensor. The sum runs over all pairwise interactions of the electron with respective nuclear spins. The hyperfine interaction Hamiltonian consists of two parts: the isotropic Fermi contact and the electron-nuclear dipole-dipole coupling, called H_F and H_{DD} in equation 2.9, respectively.

In liquid solution and fast tumbling of the spin probe, the Fermi contact interaction is the only contribution to the hyperfine interaction:

$$H_F = \sum_{i=1}^{N} a_{iso,i} S_i^T I_i \; , \tag{2.10}$$

where $a_{iso,i}$ is the isotropic hyperfine coupling constant for the respective nucleus i:

$$a_{iso} = \frac{2\mu_0}{3\hbar} g_e \beta_e g_N \beta_N |\psi_0(0)|^2 \; , \tag{2.11}$$

and μ_0 is the vacuum permeability, g_N and β_N are the nuclear g-factor and the nuclear magneton, respectively, and $|\psi_0(0)|^2$ is the electron spin density at the nucleus. The isotropic hyperfine coupling originates from non-vanishing electron spin density at the *s*-orbitals (indeed, also from higher orbitals[16] but only in an indirect manner) of the atom. Hence, this mechanism works through direct contact between the unpaired electron and the nucleus, which explains its name, *contact interaction*.

In contrast, the dipole-dipole interaction:

$$H_{DD} = \sum_{i=1}^{N} S_i^T T_i I_i \; , \tag{2.12}$$

with the dipolar coupling tensor T acts through space. For isotropic rotation in liquid solution this term averages to zero.

Nuclear Zeeman interaction

Not only the electron spin but also the nuclear spins interact with the external magnetic field B through the nuclear Zeeman interaction:

$$H_{NZ} = -g_N \beta_N B^T I \; , \tag{2.13}$$

where I is the nuclear spin quantum number. In equation 2.13 the nuclear Zeeman interaction is considered isotropic, which is a very good approximation for most EPR experiments, also in this work.

Nuclear quadrupole interaction

If a nucleus has a spin $I \geq 1$, the charge distribution is non-spherical and it has a quadrupole moment. The term that contributes to the overall Hamiltonian can then be written as a traceless nuclear quadrupole tensor P coupling the nuclear spin I with itself:

$$H_{NQ} = I^T P I \; . \tag{2.14}$$

As a measure of the magnitude of the quadrupolar coupling, usually the asymmetry parameter of the **P**-tensor elements $\eta=(P_{xx}-P_{yy})/P_{zz}$ and the quantity $e^2qQ/\hbar$ are reported, latter of which containing the product of electric field gradient eq and quadrupole moment Q. In cubic symmetry, the quadrupole moment becomes zero and thus the quadrupole interaction vanishes.[49]

In CW EPR spectra, quadrupole couplings only appear as second order effects but in experiments that probe the nuclear environment of an electron spin, such as ESEEM (see sections 2.6/2.7) and ENDOR, they can be observed as first order splittings or they may broaden observed nuclear peaks.

Electron-electron interactions weaker than zero-field splitting

Two or more electron spins that are very strongly coupled, e.g. because they are located on the same atom or are spatially close, can usually be described as one system with an overall spin $S > \frac{1}{2}$. If the coupling is relatively weak, the spins are rather treated as individual spins interacting with each other and the interactions may be introduced as perturbations of the two isolated electron spin states. There are two types of interactions between the electron spins: *Heisenberg spin exchange coupling* and *dipolar coupling*, so that a Hamiltonian describing a coupled system of two electron spins becomes:

$$
\begin{aligned}
H(S_1, S_2) &= H(S_1) + H(S_2) + H_{e-e} \\
&= H(S_1) + H(S_2) + H_{exch} + H_{DD,e}
\end{aligned}
\tag{2.15}
$$

where $H(S_1)$ and $H(S_2)$ stand for the Hamiltonians of the respective electron spins without electron-electron interaction, H_{exch} is the exchange-interaction Hamiltonian and $H_{DD,e}$ is the Hamiltonian that accounts for the electron-electron dipolar interaction.

Exchange interaction

The Heisenberg spin exchange interaction,[50] shortly called exchange interaction, is described by a coupling term

$$
H_{exch} = \boldsymbol{S_1}^T \boldsymbol{J} \boldsymbol{S_2},
\tag{2.16}
$$

where **J** is the exchange-coupling tensor. In most cases, the spin exchange interaction actually exchanges the states of two spatially close spins. In liquid solution, exchange coupling stems from direct overlap of the electron-bearing orbitals and is therefore correlated to the frequency of intermolecular collisions, which in turn is a measure of the local concentration of radicals.[50] Hence, the exchange process can be empirically described similar to kinetics of a bimolecular chemical reaction.

During the orbital overlap, the electrons of the two species can be exchanged, which can influence CW EPR spectra by broadening, narrowing, or shifting of lines. This effect is displayed in Figure 2.1, where simulations of CW EPR spectra are shown that only differ in the assumed exchange

rate. [51] From top to bottom the exchange interaction increases and one can observe the main regimes of exchange interaction on the CW EPR spectra:

   i)   no exchange,

   ii) slight broadening of spectra,

   iii) strong exchange broadening shortly before all three lines merge into one broad line ("exchange collapse"), and finally,

   iv) exchange narrowing.

Note also the shifts in the centers of the outer two lines. The shown effects are valid for systems that are determined by only one exchange frequency. If there is a distribution of exchange frequencies dominating the spectra, the broadening may look different than that shown in Figure 2.1. In frozen solution (solid), spin exchange can take place through bond or even through solvent and is significant up to an electron-electron distance of ~1.5 nm. [52]

Figure 2.1. Effect of increased spin exchange interaction on simulated CW EPR spectra at room temperature; All parameters are equal except for the spin exchange frequency that is varied from top to bottom: zero, 10^7, 10^8, 10^9; simulations were performed with the spectral simulation program by Schneider and Freed (see Ref. 51);

   In biradicals in liquid solution, exchange coupling may also arise from delocalization and overlap of electron spin density through the molecular σ- or π-bonding system.

   Exchange coupling can be differentiated into an isotropic and anisotropic contribution. For a system consisting of $S_1=S_2=1/2$, it is custom to describe the isotropic part of the exchange coupling as a chemical bond between the two electrons that can be in a singlet state (overall $S=0$) or a triplet state (overall $S=1$). In this framework, the exchange coupling can either be *ferromagnetic* or *antiferromagnetic*. In a ferromagnetically-coupled system, the exchange coupling is negative, i.e., the spin-triplet state is energetically favored over the spin-singlet state, which corresponds to a weak antibonding of the two electrons. In an antiferromagnetically-coupled system, the exchange coupling is positive, i.e., the spin-singlet state is energetically favored over the spin-triplet state, which corresponds to a weak bonding of the two electrons.

   Following Anderson, [53,54] there are three physical effects contributing to the isotropic exchange coupling. First, if two electron-bearing orbitals overlap there are two unpaired electrons that are distributed over the transiently formed overall orbital. Owing to the Pauli exclusion principle, the Coulomb repulsion is stronger if the two electron spins are aligned in an antiparallel fashion (in a crude picture: they can cover the same space) and form a singlet state than for the case of parallel spins in a triplet state. Thus, this effect causes a ferromagnetic contribution. Second, delocalization of electron spins in overlapping orbitals has an effect on the average kinetic energy of the electrons, which gives an antiferromagnetic contribution. Finally, the presence of unpaired electrons can also
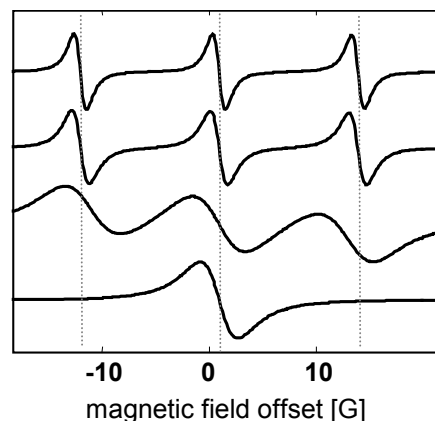
lead to polarization effects on electron densities in neighboring atoms or molecules. The sign of this contribution is not easily predictable and may be either positive or negative.

For organic radicals, the anisotropic part of the exchange coupling tensor, which arises from spin-orbit coupling, is often negligible (unlike in some transition-metal systems) and equation 2.16 simplifies to:

$$H_{exch} = J_{12}\mathbf{S_1}^T\mathbf{S_2},$$ (2.17)

where J_{12} is the exchange coupling constant.

Electron dipole-dipole interaction

In analogy to the magnetic dipolar coupling term of the hyperfine interaction between an $\mathbf{S}$ and an $\mathbf{I}$ spin, the dipole-dipole interaction between electrons also acts through space and the dipolar interaction Hamiltonian $H_{DD,e}$ and is given by:[39]

$$H_{DD,e} = \mathbf{S_1}^T\mathbf{D}\mathbf{S_2},$$ (2.18)

where $\mathbf{D}$ is the dipolar coupling tensor between the two spins $\mathbf{S_1}$ and $\mathbf{S_2}$. In the framework of the high-field approximation and neglecting anisotropies of the $\mathbf{g}$-tensors, the dipolar coupling tensor in its principal axes frame becomes:

$$\mathbf{D} = \frac{\mu_0 g_1 g_2 \beta_e^2}{4\pi\hbar}\frac{1}{r_{12}^3}\begin{pmatrix} -1 & & \\ & -1 & \\ & & 2 \end{pmatrix} = \begin{pmatrix} -\omega_{DD} & & \\ & -\omega_{DD} & \\ & & 2\omega_{DD} \end{pmatrix},$$ (2.19)

where r_{12} is the vector connecting spin $\mathbf{S_1}$ and $\mathbf{S_2}$ and ω_{DD} is the dipolar interaction frequency.

As described for the dipolar contribution to the hyperfine interaction, the dipolar coupling between electron spins in the fast motion limit is averaged to zero and exchange interaction through direct collisional exchange is the dominant electron-electron interaction mechanism. Note that in liquid solution of high viscosity, though, the dipolar interaction between electrons might not be negligible any more, as it was discussed in detail by Salikhov et al. (see Ref. 55).

In recent years, the measurement of dipolar couplings between electrons has become a powerful tool to extract information on distance distributions of nitroxide spin probes in frozen solution or in solids (see eq. 2.19).[56] This is discussed in Section 2.6.3, when one of these techniques is introduced.

2.3   Spectral analysis of continuous wave (CW) EPR

Despite the development of sophisticated pulse EPR methods, the standard EPR method to detect paramagnetic species is still continuous wave (CW) EPR. For technical reasons, CW EPR is performed by irradiation of a linearly polarized microwave field of constant frequency ω and variation

of the B_0-field. During the field sweep, microwave radiation is absorbed whenever the resonance condition of equation 2.3 is fulfilled. The *B*-field sweep is very slow as compared to all interactions that determine the Hamiltonian of equation 2.5 (Section 2.2).[16] Therefore, the Hamiltonian can be treated as time-independent. Note that usually, to enhance signal sensitivity, one measures the CW EPR absorption spectra with field modulation and phase-sensitive detection, so that the first-derivative of the spectrum is observed.

CW EPR spectra of nitroxide radicals

In this section, I shall present the factors influencing CW EPR spectra of nitroxide free radicals (general structure shown in Figure 2.3), the by far most important class of free radical spin probes, in room temperature solution and frozen solution. A large part of the experimental results of Chapters 3 and 4 rely on analysis of CW EPR spectra of the nitroxide radical *Fremy's salt* (FS, potassium nitrosodisulfonate, see Figure 2.3 and Scheme 3.3).

For nitroxides in dilute liquid solution, many of the terms in the Hamiltonian of eq. 2.5 are irrelevant (such as zero-field splitting) and only the electron-Zeeman interaction and the hyperfine coupling to the magnetic ^{14}N nucleus (I=1) remain. As described by equations 2.7 and 2.10, the *g*-and hyperfine (*A*-) tensors, though, are averaged to isotropic values due to fast motion of the spin probe and the Hamiltonian describing a nitroxide becomes:

$$H_{nit} = g\beta_e \boldsymbol{B}^T \boldsymbol{S} + a_{iso}\boldsymbol{S}^T \boldsymbol{I} \,. \tag{2.20}$$

Solving this Hamiltonian yields the energy eigenvalues and assuming that a constant magnetic field B_0 is applied in *z*-direction, the spin vectors $\boldsymbol{S}$ and $\boldsymbol{I}$ are replaced by the magnetic quantum numbers m_S (m_S =±1/2) and m_I (m_I =0, ±1):

$$E_{nit} = g\beta_e B_0 m_S + a_{iso}m_S m_I \,. \tag{2.21}$$

The spectroscopic selection rules for EPR on this system are Δm_S =±1 and Δm_I =0, so that the resonance condition for the irradiated microwave becomes:

$$\Delta E_{nit} = \hbar\omega_S = g\beta_e B_0 + a_{iso}m_I \,, \tag{2.22}$$

which explains the three-line pattern of the nitroxide CW EPR spectra. Figure 2.2 depicts the energy states of equation 2.21 as a function of the magnetic field (e.g. during a field sweep) and also shows the three allowed transitions that lead to the three-line nitroxide spectrum (equation 2.22). In CW EPR, in general $2I$+1 lines can be observed due to the hyperfine interaction.

Equation 2.22 also nicely shows that the major advantage of performing high-field/high-frequency CW
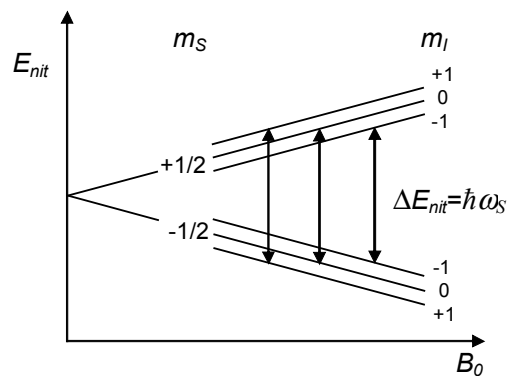

Figure 2.2. B_0-field dependence of the energy states of a nitroxide free radical (eq. 2.21); also shown are the allowed EPR transitions fulfilling the selection rules Δm_S =±1 and Δm_I =0 (eq. 2.22);

EPR, e.g., going to W-band frequencies, is the improved *g*-resolution, while the hyperfine resolution remains unaltered. It thus becomes possible to separate contributions to the spectra from electron-Zeeman and hyperfine anisotropies.

Figure 2.3 presents the molecular coordinate system that is usually chosen for the description of the interactions of the nitroxide radical. The $2p_z$ orbital of the nitrogen atom defines the *z*-axis, while the *x*-axis is along the N-O bond and the *y*-axis perpendicular to both. In most nitroxides, the coordinate frames (i.e., the directions of the main tensor elements) of the electron-Zeeman and hyperfine interaction are almost collinear. Symmetry considerations suggest that this is also the case for an isolated Fremy's salt dianion. If it were possible to measure the three components of the spectra along their respective direction individually, one would detect three spectra as also shown in Figure 2.2, in which the center line position marks *g*-tensor elements g_{xx}, g_{yy}, and g_{zz}, and the spacing is determined by the main hyperfine tensor elements: A_{xx}, A_{yy}, and A_{zz} (see eq. 2.9 and values in Fig. 2.3).
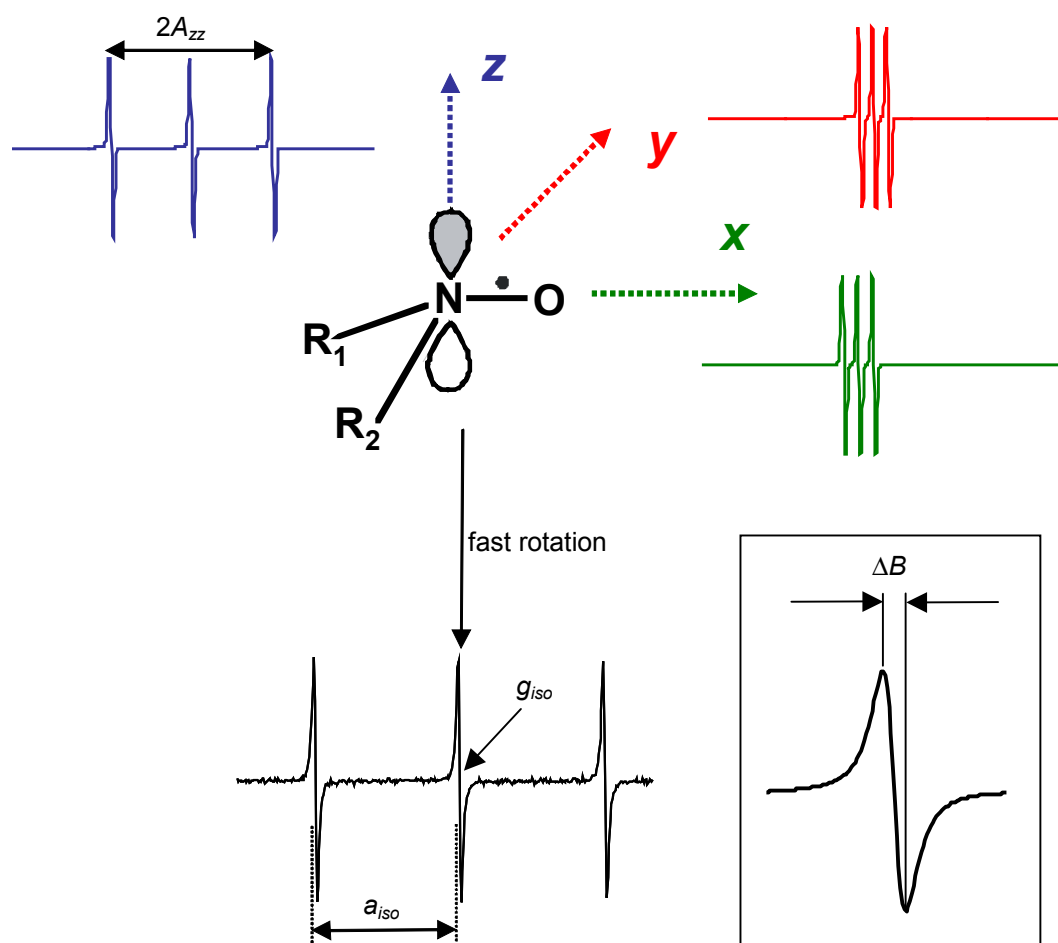
Figure 2.3. Chemical structure of nitroxide radicals (Fremy' salt dianion: $R_1=R_2=SO_3^-$) and principal axis system of electron-Zeeman and hyperfine tensors. Typical values for the main elements of the *g*- and hyperfine tensors of Fremy's salt are given (see Section 3.2.2): g_{xx}=2.0086, g_{yy}=2.0064, g_{zz}=2.0029 and $A_{xx}=A_{yy}$=5.2 G, A_{zz}=28.5 G; These values were determined from simulations of Fremy's salt powder spectra in DMF/glycerol/water at 80 K performed with the program by Schneider and Freed.[51]
Fast rotation (i.e., faster than a typical rotational correlation time of τ_c~10 ps) leads to the averaged spectrum shown in the lower part with an isotropic *g*-value $\boldsymbol{g_{iso}}$ (typically ~2.0060) that determines the center of the central line and a spacing between the lines that is dominated by a_{iso} (typically ~13G).
The inset in the lower right corner defines the peak-to-peak linewidth ΔB.

Note that the microwave (mw) irradiation (either in the CW or pulsed mode) and detection of magnetization are usually described in the laboratory axis frame, in which the *z*-axis is defined by the direction of the static B_0-field. One usually relates the molecular axis frame to a coordinate system that rotates at the frequency of the irradiated microwave, *the rotating frame*.[39,58,64] As the mutual relation of the Hamiltonian in the different frames is described by transformation with *Wigner rotation matrices* in a straightforward fashion, in the following the axis frame can be used that allows the simplest description of the respective parameter. Detailed presentations of these transformations can be found in References 39, 58, and 64.

The inset in Figure 2.3 defines the peak-to-peak linewdith of one line. In the case of purely Lorentzian lineshapes, the peak-to-peak linewidth of the first-derivative spectrum is related to the full width at half maximum (FWHM) of the Lorentzian absorption line by ΔB=FWHM/($3^{-\frac{1}{2}}$).[39] In this case, the linewidth is inversely proportional to the so called *spin-spin relaxation (or phase-memory) time T_m,* which is a measure of the amplitude of stochastic variations of local magnetic fields for individual spins. Hence, interactions with further electron or nuclear spins may well change the overall lineshape and linewidth. In addition to T_m, one characterizes the return of the magetization to its equilibrium state by a *spin-lattice relaxation time T_1*. In the solid state, one usually has T_1>>T_m, while in liquids $T_1 \approx T_m$.

Rotational diffusion of spin probe/spin label molecules in CW EPR can roughly be characterized by the rotational correlation time τ_c, as belonging to one of the following regimes: i) liquid isotropic ($\tau_c \leq$1ps), ii) slow motion ($\tau_c \approx$1ns), and finally iii) rigid limit ($\tau_c \geq$1μs). Note that translational motion – as long as the spins remain in the observed sample volume and the static field is homogeneous – does not influence the spectral shape since only the angular motion relative to the applied B_0-field changes magnetic interactions.

Information on dynamics

Before introducing the model of rotational diffusion that is used in this work to characterize rotational dynamics from CW EPR spectra of nitroxide free radicals, the formalism to rationalize rotational motion is presented.[57]

In general, a rotational diffusion process for a distribution of spins, $P(\Omega,t)$, can be described by the time-dependent Smoluchowski equation:

$$\frac{d}{dt}P(\Omega,t) = -\boldsymbol{\Gamma}_\Omega P(\Omega,t),$$
(2.23)

where Ω stands for the parameters (angles) describing the orientation and Γ_Ω denotes the time-independent rotational motion operator. The general solution to eq. 2.23 is given in equation 2.24:

$$P(\Omega,t) = \exp\left[-t\boldsymbol{\Gamma}_\Omega\right]P(\Omega,t=0).$$
(2.24)

where the exponential function is an *evolution operator* transforming a distribution at time $t=0$ into the distribution at any time t. Note that for the system at equilibrium, the distribution of spins does not change under evolution, so that $\Gamma_\Omega P(\Omega,t=0)=0$.

An important quantity that characterizes the rotation is the conditional probability $W(\Omega,t|\Omega_0,t=0)$ of the distribution of spins to be at a certain orientation Ω at a time t if the diffusion started at time $t=0$ at the orientation Ω_0:

$$W\left(\Omega,t\,|\,\Omega_0,t=0\right)=\exp\left[-t\boldsymbol{\Gamma_\Omega}\right]\delta\left(\Omega-\Omega_0\right). \tag{2.25}$$

In equation 2.25, δ denotes the Dirac delta function.

The evolution of rotational diffusion is best described by either spherical harmonic functions,[16,58] $Y_{l,m}(\Omega)$ of given order l, or more generally the Wigner rotation matrix elements,[57,58] $D_{l,m,n}(\Omega)$. Using the Wigner matrix elements, the autocorrelation function $\rho(t)$ of the Wigner function characterizing rotational reorientation is defined as the average overlap of that function with its form at initial time $t=0$:

$$\rho\left(t\right)=\left\langle D_{l,m,n}\left(\Omega(t)\right)\middle|D_{l,m,n}\left(\Omega(t=0)\right)\right\rangle. \tag{2.26}$$

After several conversions, one obtains an expression for the autocorrelation function that describes the reorientation starting from the initial distribution of spins $P(\Omega,t=0)$:

$$\rho\left(t\right)=\int_\Omega P\left(\Omega(t=0)\right)D^*_{l,m,n}\left(\Omega(t)\right)\exp\left[-t\boldsymbol{\Gamma_\Omega}\right]D_{l,m,n}\left(\Omega(t)\right), \tag{2.27}$$

where the asterisk marks the complex conjugate of the Wigner rotation matrix element.[57]

Now the rotational correlation time, which had been mentioned before, can be calculated from the expression for the autocorrelation function if the properties $\rho(t=0)=1$ and $\rho(\infty)=0$ are fulfilled, which is intrinsically true for both, spherical harmonic and Wigner rotation functions of order $l>0$. The correlation time τ_c in the most general approach is then given by the integral of the autocorrelation function over time:

$$\tau_c=\int_{t=0}^\infty\rho\left(t\right)dt, \tag{2.28}$$

Isotropic Brownian motion

The simplest model for interpretation of CW EPR spectra with respect to rotational motion is assuming *isotropic Brownian motion*.[16] This means that the tip of an orientation vector of the radical makes a random walk over the surface of a sphere. In this case, the motional operator Γ_Ω is given by following expression:

$$\boldsymbol{\Gamma_\Omega}=-D_r\nabla^2_\Omega. \tag{2.29}$$

In equation 2.29, D_r is the Stokes-Einstein coefficient of rotational diffusion of a sphere and ∇_Ω^2 is the angular Laplacian operator. The autocorrelation function now becomes:

$$\rho(t) = \exp\left[-tD_r l(l+1)\right],\tag{2.30}$$

where l is the order of the Wigner matrix. As spin interactions are second-rank tensors, one is generally interested in the second order ($l=2$) of these functions. Hence, inserting equation 2.30 into equation 2.28 and performing the integration yields the general form of the rotational correlation time of isotropic Brownian motion as:

$$\tau_c = \frac{1}{6D_r},\tag{2.31}$$

which shows that the rotational correlation time is a meaningful single parameter that is directly related to rotational diffusion.

Using the Stokes-Einstein relationship,[16] one can relate τ_c to the temperature T, the solvent viscosity η, and the molecular dimensions (spherical radius r) of the rotating molecule:

$$\tau_c = \frac{4\pi\eta r^3}{3kT}.\tag{2.32}$$

Note, though, that this is valid only for spherical molecules and that the effective radius r may depend on specific interactions with the solvent.[116] Nonetheless, it is a good approximation also for most small nitroxide radicals in isotropic solvents.

Anisotropic Brownian motion

Departing from the simple model of isotropic rotation of a spherical molecule, the next level of sophistication for interpretation of CW EPR spectra with respect to rotational motion is introduction of *anisotropy* to the Brownian motion.[51,57] Schneider and Freed (Ref. 51) have developed a uniaxial
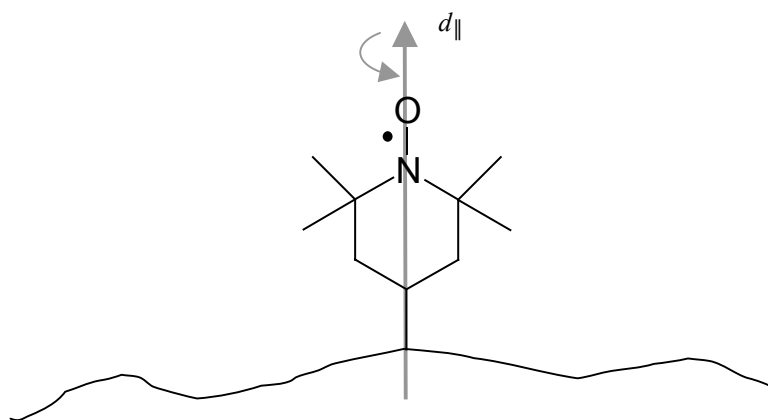

Figure 2.4. Model of anisotropic Brownian rotational diffusion assuming one axis of fast rotation (rotational rate $d_\parallel$, shown in gray) and two perpendicular axes of slow reorientation (rotational rate $d_\perp$, not shown). The nitroxide spin label is assumed to be linked to a macromolecule (e.g., a protein), which induces the anisotropy of Brownian diffusion.

model of *fast rotation* about one axis and slower rotation about the axes perpendicular to that of fast rotation. This model has been worked out explicitly to account for reorientation of nitroxide spin labels chemically linked to proteins or other macromolecules. As shown in Figure 2.4, the model assumes that the fast rotation (rotational rate $d_\parallel$) is not (or only moderately) linked to the motion of the macromolecule, while the reorientation perpendicular to the axis of fast rotation (rotational rate $d\perp$) is slower and strongly influenced by the macromolecule dynamics.

For this case, the motional operator Γ_Ω is now given by the following expression:

$$\boldsymbol{\Gamma_\Omega} = \nabla_\Omega \bullet D_r \bullet \nabla_\Omega .$$

(2.33)

In equation 2.33, D_r now is the rotational gradient operator (explained in Reference 51) and the Wigner rotation matrices are eigenfunctions of D_r in the diagonalized form of equation 2.34:[57]

$$D_r = \begin{vmatrix} D_\perp & 0 & 0 \\ 0 & D_\perp & 0 \\ 0 & 0 & D_\parallel \end{vmatrix} .$$

(2.34)

In equation 2.34, $D\perp$, is the rotational operator component perpendicular to the axis of fast rotation and $D_\parallel$ is the rotational operator component parallel to the axis of fast rotation. Note that rotational operator components denoted by $D\perp,_\parallel$ are not identical with rotational rates $d\perp,_\parallel$. Deduction of the rotational rates from the operator components is concisely shown in References 51 and 57 and is not presented in any more detail in this work.

Extraction of dynamic parameters from measured CW EPR spectra

In Chapters 3 and 4 of this work, numerous CW EPR spectra of nitroxide radicals are presented and analyzed. Extraction of dynamic information from these spectra is achieved in either of two ways: the framework of simple isotropic Brownian motion or anisotropic uniaxial rotation.

In the former case, characterization of rotational motion yields only one parameter, the rotational correlation time τ_c, while the latter involves rotational rates parallel ($d_\parallel$) and perpendicular ($d\perp$) to the axis of fast rotation.

Rotational correlation times τ_c are gained from linewidth analysis as described by Robinson and coworkers.[59] These authors implemented the seminal theoretical work on analysis of nitroxide dynamics by Freed and coworkers[60,61] in a MATLAB program. The central point of analysis is the apparent linewidth R_2 as a function of the nuclear quantum number m:

$$R_2(m) = A' + A(m) + B(m) \cdot m + C(m) \cdot m^2 + X(m) ,$$

(2.35)

where A, B, C are only weakly m-dependent quantities that are calculated from g and A values and the rotational correlation time. The quantity A' accounts for the spin rotation mechanism[16,59] and $X(m)$ summarizes contributions from all other broadening processes. In Reference 59 it is found that the "B-parameter" for nitroxides with ^{14}N nucleus is numerically equal to half the difference of linewidths of

the m=-1 and m=1 manifold, $B = (\Delta B(m$=-1$) - \Delta B(m$=1$)) / 2$. In this publication also $R_2(m)$ and $B(m)$ are plotted as a function of the rotational correlation time and it is found that the linewidths and the B-parameter linearly increase with the rotational correlation time for 10^{-11} s $< \tau_c < 10^{-8}$ s. Extraction of the rotational correlation time is achieved by calculating R_2 from the experimentally gained B-parameter (i.e., half the difference of high- and low-field linewidths) interpolating the known τ_c-dependence of $R_2(m)$ and B for nitroxides. Essentially, one thus uses previously established dependencies of linewidths and rotational correlation times for nitroxides to find the rotational correlation times that belong to a certain linewidth.

The advantage of this treatment within the framework of isotropic Brownian rotation over any other model is that one can characterize rotational motion with only one parameter, the rotational correlation time τ_c. This comes at the cost of loosing detailed knowledge of the motional process.

To obtain such a more detailed picture of rotational motion, simulations of some of the CW EPR spectra of Chapter 3 are performed with the simulation program by Schneider and Freed[51] that is based on their aforementioned theoretical treatment of anisotropic Brownian rotational motion (see Figure 2.4). Through these simulations one obtains the directions of fast (and slow) rotational diffusion within the molecular coordinate frame and the respective rotational rates parallel and perpendicular to the axis of fast rotation, $d_\parallel$ and $d\perp$. The anisotropy of rotation is quantitatively summarized in the ratio α of these rotational rates: $\alpha = d_\parallel / d\perp$.

Extracting information on the spin probe environment

In addition to spin probe dynamics, CW EPR spectra also contain information on the chemical environment of the spin probe.[16] This information is present in the spectra mainly in the ^{14}N hyperfine splitting: all interactions of the nitroxide molecule with its surroundings that lead to a change in the electronic structure of the spin probe also change the hyperfine interaction. Therefore, the same kind of spin probe in solvents of different polarity, proticity (pH) or hydrophobicity will show deviations in the hyperfine splitting a_{iso} (i.e., the line spacing) in liquid state CW EPR spectra, and different values for A_{zz} in powder-like CW EPR spectra.

The reason for this can be understood when inspecting the (coincident) molecular g- and A-coordinate frame shown Figure 2.3. It becomes clear that hydrogen bonding of the NO-oxygen atom to, e.g., solvent protons affects the A_{xx}-value and, to a much stronger degree, also the g_{xx}-value, while due to molecular geometry the changes in polarity mainly influence the A_{zz}-value (and to a lesser degree also g_{xx}). A very good example of the application of spectral analysis with respect to magnetic tensor components can be found in work by Wegener, Steinhoff and coworkers (see Ref. 63). These authors found evidence for a light-induced opening of the proton entrance channel of the single mutant of bacteriorhodopsin by comparison of magnetic tensor elements, g_{xx} and A_{zz}, from high-field/high frequency EPR (W-band frequencies, ~95 GHz) spectra before and after illumination.

Note that in this work, only shifts in a_{iso} of liquid state CW EPR spectra are used to probe the microenvironment of the spin probes. Therefore, a more detailed description of this form of spectral analysis is not given at this point.

2.4   Time evolution of spin ensembles

In Section 2.2 the spin Hamilton operator for individual electron spin S is explained in detail. In EPR spectroscopy, one always detects an *ensemble* of spins, not just single spins. In addition, in pulse EPR experiments one has to follow the *time evolution* of these ensembles of spins. The static Hamiltonian alone is not sufficient for describing such experiments.

Following Dirac, the state vectors describing an ensemble can be represented in the so-called "bra-ket" notation, in which $<i|$ denotes the i-th bra and $|j>$ j-th ket of the respective eigenfunction.[64] One has to distinguish between a *pure ensemble*, in which all members of the ensemble are described by the same state vector, say $|\psi>$, and a *mixed ensemble*, which can be viewed to consist of n different fractions of pure ensembles that can each be described by an individual ket states, say $|\psi_1>$ and $|\psi_2>$.[64]

For n pure subensembles, the expectation value of an observable A is given by:[39]

$$\langle A \rangle = \sum_{i=1}^{n} w_i \langle \psi_i | A | \psi_i \rangle , \qquad (2.36)$$

and each state bra and ket is defined using the respective coefficients c such that:[39,64]

$$|\psi_i\rangle = \sum_{k=1}^{n_H} c_k^{(i)} |k\rangle , \qquad \langle \psi_i | = \sum_{l=1}^{n_H} c_l^{(i)*} \langle l | , \qquad (2.37.\text{a, b})$$

where n_H denotes the Hilbert space dimension of the state. Inserting equations 2.37 into equation 2.36 yields a new expression for the expectation value of the observable:

$$\langle A \rangle = \sum_{i=1}^{n} \sum_{k=1}^{n_H} \sum_{l=1}^{n_H} w_i c_l^{(i)*} \langle l | A | k \rangle c_k^{(i)} = \sum_{k=1}^{n_H} \sum_{l=1}^{n_H} \overline{c_l^* c_k} \langle l | A | k \rangle , \qquad (2.38)$$

Note that in equation 2.38 the average is only taken over the i-dependent coefficients, as the basis bra and ket states as well as the operator A are independent of i. One can now define the density matrix (operator) σ.[39,64]

$$\sigma = \sum_{i=1}^{n} w_i |\psi_i\rangle \langle \psi_i | = \sum_{k=1}^{n_H} \sum_{l=1}^{n_H} \overline{c_l^* c_k} |k\rangle \langle l | , \qquad (2.39)$$

Finally, the expectation value of A is found to be the sum of the diagonal elements of the multiplied operators:

$$\langle A \rangle = tr\{A\sigma\} , \qquad (2.40)$$

which makes the evaluation independent of the initial basis sets.

It is convenient for the description of EPR experiments, though, to use basis sets, in which the states are eigenstates of the static Hamiltonian H_0 of the system. These are then called the eigenbasis.

Note that each pure state of an ensemble of isolated spins S can be expressed as a coherent superposition of its $2S+1$ mutually orthogonal eigenfunctions, which span a Hilbert space of $2S+1$ dimensions. In a mixed ensemble, the mixed state is described by the average of the coefficients c_l and c_k, i.e. by the density matrix of equation 2.39. To be more precise, the magnetization on single transitions can be described by one matrix element of σ, say σ_{kl}. In the density matrix of a multiple spin system, differences of diagonal elements σ_{ll} and σ_{kk} are called *polarization* of transition kl, while the off-diagonal element σ_{kl} quantifies *coherences* on this transition. It is evident from equation 2.39 that the density matrix is a Hermitian operator ($\sigma_{kl}=\sigma_{lk}^{*}$). The Hilbert space dimension n_H is calculated as the product of the dimensionalities of the m spins:

$$n_H = \prod_{i=1}^{m} n_i = \prod_{i=1}^{m} (2J_i + 1), \tag{2.41}$$

where J_i is any kind of nuclear or electron spin of the coupled system.

One can now combine the density operator, which describes the state of the spin ensemble, with the Hamiltonian, which depicts the forces and interactions that are prevalent in the ensemble. This is achieved in the *Liouville-von Neumann equation*, which can be viewed as a quantum-mechanical analogue of the Bloch equations:[39]

$$\frac{d\sigma(t)}{dt} = -i\left(H\sigma - \sigma H\right) = -i\left[H(t), \sigma(t)\right], \tag{2.42}$$

where on the right hand side, the equation is simply restated as a commutator of the spin Hamiltonian and the density operator. This equation can be derived from the time-dependent Schrödinger equation. Note that the Liouville-von Neumann equation neglects relaxation, i.e. irreversible loss of magnetization, which can be introduced as shown in equation 2.43:

$$\frac{d\sigma(t)}{dt} = -i\left[H(t), \sigma(t)\right] - \Xi\left[\sigma(t) - \sigma_{eq}\right], \tag{2.43}$$

where Ξ represents the relaxation super-operator and σ_{eq} is the density operator for the system at thermal (Boltzmann) equilibrium. Ξ describes the interaction of the spin system with its environment (the "lattice") and if only microwave (mw) and radiofrequency (rf) radiation is used (as in magnetic resonance spectroscopy). It can often be safely assumed that the environment is not perturbed by the irradiation and Ξ is time-independent. Therefore, relaxation and the time evolution of the spin ensemble can be discussed separately and for the remainder of this section, only the Liouville-von Neumann equation (2.42) will be discussed to lay the foundation for the understanding of the pulse EPR experiments that are introduced in the remaining part of this chapter.

Integration of equation 2.42 with a *time-independent* Hamiltonian H yields:

$$\sigma(t) = \exp[-iHt]\sigma(0)\exp[iHt] = U(t)\sigma(0)U^{\dagger}(t),$$ (2.44)

where the exponential factors $U(t)$ and its Hermitian adjoint $U^{\dagger}(t)$ are the *propagator operators*, which propagate the spin density operator in time (this is a unitary transformation). This equation allows calculating the state of the spin density after a certain time interval. If the Hamiltonian is time-dependent, the expression for the propagator becomes more complicated.[39]

2.4.1   Density operator formalism

The external perturbations that are used in pulse EPR experiments, such as microwave or radiofrequency pulses, are usually time dependent and thus are described by time-dependent Hamiltonians. In many cases it is possible, though, to divide such an experiment in short time intervals in which the Hamiltonian is constant. The density operator after each of these consecutive time intervals is then modified as shown in equation 2.44, which means that one can consecutively apply the propagators for each time interval. At the time of detection the spin density operator then becomes:

$$\sigma(t_n) = U_n...U_2 U_1 \sigma(0) U_1^{\dagger} U_2^{\dagger}...U_n^{\dagger},$$ (2.45)

after n time intervals. Analogously, the expectation value of any observable A shown in equation 2.40 can then be evaluated at any point in time:

$$\langle A \rangle = tr\left\{ U_n...U_2 U_1 \sigma(0) U_1^{\dagger} U_2^{\dagger}...U_n^{\dagger} A \right\},$$ (2.46)

The approach to divide an experiment in time intervals during which the spin Hamiltonians are constant is called *density operator formalism*.[39,49] Note that propagators of free evolutions of the spin system (no pulses) only change the phase of the density matrix element that describes the state of the system (unless they are diagonal elements), while propagators of external perturbations cause transfers between matrix elements.

2.4.2   Product operator formalism

If the spin system of interest is too large, it becomes more convenient to decompose the density operator σ into a linear combination of orthogonal basis operators. This approach is called *product operator formalism*.[65] Each set of basis operators consists of as many operators as there are matrix elements in the density matrix operator, i.e. they span a space $n_L = n_H^2$ called Liouville space:

$$\sigma(t) = \sum_{i=1}^{n_L} b_i(t) B_i,$$ (2.47)

where B_i are the basis operators and only the coefficients b_i are time-dependent. The choice of basis operators is crucial in this approach. Depending on the experiment that is carried out, different sets of basis operators may be most suitable. A single electron spin $S=1/2$ ($n_L=4$) can, e.g., be described by the

Cartesian basis operators S_x, S_y, S_z, and the identity operator **1**, a single nuclear spin with I=1/2 (n_L=4) can accordingly be described by the Cartesian basis operators I_x, I_y, I_z, and again the identity operator **1**. All sixteen products of these operators then form the product basis.

In Sections 2.5 – 2.7 all pulse experiments that have been used to characterize polyelectrolyte-spin probe systems in Chapters 3 and 4 are presented. The remainder of this section is therefore concerned with the product operator description of pulse EPR experiments. For this, a model system of one electron spin S=1/2 and one nuclear spin I=1/2 is used. Such a model system at thermal equilibrium is depicted in Figure 2.5 in a four-level scheme. The overall state of the spins is
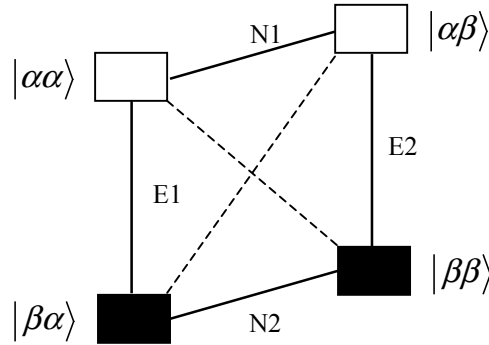

Figure 2.5. Four-level scheme describing a system of an electron spin S=1/2 and a nuclear spin I=1/2 at thermal equilibrium (the lower two states are populated in excess).
The allowed electron Zeeman transition are marked "E" (vertical), while the allowed nuclear Zeeman transitions are marked "N" (horizontal). The diagonal transitions are the forbidden transitions that violate the spectroscopic selection rules.

conveniently expressed by defining for m_S,m_I=1/2≡α and m_S,m_I=-1/2≡β, so that the four possible states are: |$\alpha\alpha$>, |$\beta\alpha$>, |$\beta\alpha$>, |$\beta\beta$>, where the first letter denotes the electron spin state and the second letter the nuclear spin state.

The allowed transitions as described in equation 2.21 are the two electron Zeeman transitions marked "E1" and "E2" in Figure 2.5 and the two nuclear Zeeman transitions marked "N1" and "N2". The forbidden transitions are those transitions drawn as diagonal dashed lines.

There must be 16 (n_L*n_L=4*4) Cartesian basis operators for this system from which any arbitrary density operator can be constructed as a linear combination. The basis operators are calculated as the Kronecker product of the two basis sets:

$$\{B_1, B_2, ...B_{16}\} = \{S_x, S_y, S_z, 1\} \otimes \{I_x, I_y, I_z, 1\}, \tag{2.48}$$

and are summarized (after normalization) in Table 2.1.[39,65] This table also gives the physical interpretation of the individual operators and nicely shows the great advantage of the product operator formalism over other descriptions: at any stage of a complicated experiment it is still in principle possible to follow the propagation of any operator term and also to correlate it with a physical meaning.

Not only the density operators, but also the Hamiltonians can be constructed within the product operator formalism from basis operators.

Table 2.1. Cartesian basis operators of the four-level scheme in Figure 2.5. These product operators have been calculated as shown in eq. 2.48 and their physical interpretation is also given.

product operator	interpretation
½ **1**	unity operator
S_x, S_y, I_x, I_y,	electron/nuclear coherences
S_z, I_z	electron/nuclear polarization
$2 S_z I_z$	longitudinal electron-nuclear two-spin order
$2 S_x I_z$, $2 S_y I_z$	electron coherence in anti-phase
$2 S_z I_x$, $2 S_z I_y$	nuclear coherence in anti-phase
$2 S_x I_x$, $2 S_y I_y$ $2 S_x I_y$, $2 S_y I_x$	electron coherences and electron-nuclear double/zero quantum coherences

This allows describing the evolution of a spin system as a whole during a pulse EPR measurement in the framework of this formalism.

For any product operator *A* that evolves under another product operator *B* to the final product operator *C* one can write in analogy to equation 2.44:

$$\exp\left[-i\phi B\right] A \exp\left[i\phi B\right] = C$$
$$\equiv A \xrightarrow{\phi B} C$$

(2.49)

In equation 2.49, the shorthand notation in the lower part is introduced for convenience. The general solutions for spin systems only containing ½-spins (i.e., only Cartesian product operators) are:[39]

$$A \xrightarrow{\phi B} A \cos\phi - i\left[B, A\right]\sin\phi \quad \text{for } \left[B, A\right] \neq 0$$
$$A \xrightarrow{\phi B} A \qquad\qquad\qquad \text{for } \left[B, A\right] = 0$$

(2.50.a, b)

Commutators as shown in equations 2.50.a, b can rather easily be assessed for multiple spin systems since operators of different spins always commute.[39]

Application of the product operator formalism to pulse EPR

If the effective spin Hamiltonian of a system ($H_0^{\text{eff}} = H_1 + H_2$) is diagonal, all its basis operators commute so that equations 2.49 and 2.50 are valid. Furthermore, equations 2.50 can then be applied sequentially for all terms in the Hamiltonian. The evolution of an initial spin state (described by its spin density operator σ_1 at time t_1) under this Hamiltonian up to detection at time t_2 can then be expressed as:

$$\sigma_1 \xrightarrow{H_0^{\text{eff}}(t_2-t_1)} \sigma_2$$
$$\Leftrightarrow \sigma_1 \xrightarrow{H_1(t_2-t_1)} \sigma_i \xrightarrow{H_2(t_2-t_1)} \sigma_2$$

(2.51)

where σ_i denotes some intermediate spin state. All transformations that are relevant for the four-level scheme of Figure 2.5, i.e., which transform the initial spin states of Table 2.1, can be found in

References 39 and 66 and are not presented in detail here. Instead, some of the basics that are necessary for the description of pulse EPR measurements are introduced at this point.

2.4.3   Basics of pulse EPR measurements

Equilibrium state of magnetization

The initial state of a spin system in an external magnetic field B_0 has to be known before it is manipulated by the irradiation of mw pulses. It is then possible to follow the fate of the spin system by describing the applied experiment in the product operator formalism. In most cases, the initial spin state is in thermal equilibrium due to interactions among the spins and interaction between the spins and the environment. One can then assume the equilibrium state is characterized by a Boltzmann distribution, which can be represented in terms of a density operator σ_{eq}:

$$\sigma_{eq} = \frac{\exp\left[\dfrac{-H_0\hbar}{k_B T}\right]}{tr\left\{\exp\left[\dfrac{-H_0\hbar}{k_B T}\right]\right\}}, \qquad (2.52)$$

where the denominator is the partition function of the system. Assuming the validity of the *high-field approximation*, i.e., the electron Zeeman interaction dominates the Hamiltonian (see Section 2.2) one can replace H_0 by the electron Zeeman term H_{EZ}. In analogy to the combined equations 2.3 and 2.6, one finds that $H_{EZ} = \omega_S S_z$. If the *high-temperature approximation*, i.e., $\omega_S S_z \ll k_B T$ is also valid (which is true at X-band frequencies for $T > 4.5$ K) one can perform a series expansion and drop all terms and constants that do not alter the spin state (shown in detail in Ref. 39):

$$\sigma_{eq} \approx -S_z. \qquad (2.53)$$

This means that the initial equilibrium spin state is simply the spin component aligned antiparallel to the direction of the quantization axis given by the external magnetic field (as explained in Section 2.3 for CW EPR). As indicated by equation 2.4, this also means that the macroscopically detectable magnetization is aligned in the same manner.

Microwave pulses

It was mentioned before that in pulse EPR the microwave irradiation is usually "switched on" only for a short time t_P and then "switched off" again. The switching process ideally takes place instantaneously (so called *rectangular pulses*) but is practically limited by the switching time. During the time t_P the magnetization of the spin system (in a vectorial picture) is rotated by a *flip angle* β if the microwave radiation fulfills the resonance condition of eq. 2.3:

$$\beta = \omega_1 t_P. \qquad (2.54)$$

The flip angle can thus be controlled either by changing the time t_P (when the incident mw power is held constant) or by changing the mw field power ω_1 at constant pulse duration. Typical pulse durations at X-band (at maximum available mw power) are 16 ns for a $\pi/2$ (90°) pulse.

Not only the flip angle but also the *excitation bandwidth*, i.e., the fraction of the spins in the EPR spectrum that is excited by the mw field is determined by the pulse duration. The excitation profile can be approximately characterized in frequency domain (i.e. after Fourier transformation (FT) of the pulse), which delivers a FWHM of the excitation of:[39]

$$FWHM \approx \frac{1.207}{t_P} . \tag{2.55}$$

Hence, the shorter t_P is the larger the excitation bandwidth becomes. Pulses can either be *selective*, i.e., they only excite one transition of a spin S (or I) or *non-selective* and excite all allowed or partially allowed transitions of that spin.

In the framework of the product operator formalism, an ideal non-selective pulse that acts on, say, a spin in the S_z state from the x-direction of the rotating frame equals the following transformation:

$$S_z \xrightarrow{\ \beta S_x\ } \cos\beta S_z - \sin\beta S_y . \tag{2.56}$$

Equation 2.56 is valid if the excitation bandwidth is nuch larger than the width of the spectrum of the transformed spin, since only then the static Hamiltonian can be neglected for the time of the irradiation. The product operators for the explanation of the individual experiments are introduced whenever they are needed later in this chapter.

The detection of magnetization after a pulse EPR experiment is performed in the x-y-plane of the rotating frame, usually in the phase-sensitive *quadrature mode*, which means that the detected signal consists of a real and imaginary component and is a measure of the quantum-mechanical expectation value $<g\beta_e(S_x+iS_y)>$.

2.5   Fourier Transform (FT) EPR

The simplest pulse EPR (or NMR) experiment consists of one $\pi/2$ pulse that transforms the equilibrium magnetization from S_z to the x-y plane (initially to the –y direction), where it is detected as a transient signal, the *free induction decay* (FID). The pulse sequence of this experiment is depicted in Figure 2.6, where also the technical (instrument dependent) dead time after the mw pulse is shown. If one wants to detect the complete spectrum (or spectral line), the excitation bandwidth of the non-selective pulse should be broader than the spectrum of interest, i.e., $\Delta\nu = 2/T_m \leq 1.207/t_p$, where T_m is the phase memory time (see Section 2.3) of the spin packet. This experiment is called Fourier transform (FT) EPR as the detected FID is processed by FT.

One obtains a spectrum that is in principle equal to an absorption signal from CW EPR (note that for comparison to spectra detected in the CW mode one has to pseudomodulate the absorption spectrum).[67]
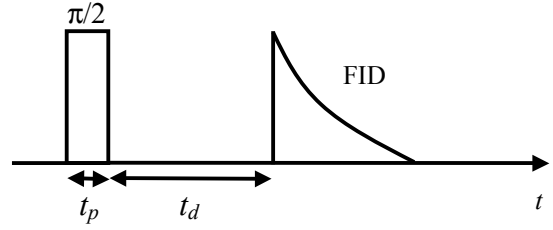

Figure 2.6. Pulse scheme for the FT EPR method. t_p is the duration of the $\pi/2$ pulse, t_d is the detection dead time. The FID is shown for the on-resonant case, $\Omega_s=0$.

Starting from the equilibrium spin state σ_{eq}, the experiment can be described in the product operator formalism:[39]

$$S_z = \sigma_{eq} \xrightarrow{(\pi/2)S_x} \sigma(t) = \cos(\Omega_s t) S_y - \sin(\Omega_s t) S_x, \tag{2.57}$$

where Ω_s is the difference of the irradiated mw from the systems Larmor (i.e., resonance) frequency: $\Omega_s=\omega-\omega_L$. From eq. 2.57, one can distinguish two cases for the free evolution period of $\sigma(t)$. If the mw pulse is *on-resonant*, i.e., its frequency ω exactly matches the Larmor frequency of the system ($\Omega_s=\omega-\omega_L=0$), the signal remains in the S_y state (i.e., along the –y-axis) until the signal has decayed to the equilibrium state with relaxation time T_m. If the mw pulse is *off-resonant*, ($\Omega_s=\omega-\omega_L\neq0$), the magnetization precesses with the frequency Ω_s in the x-y-plane of the rotating frame (this is equal to describing a spiral in this plane) and also decays with T_m. After quadrature detection (especially for the off-resonant case) and FT in both cases yields the spectral line centered at zero ($\Omega_s=0$) or at Ω_s ($\Omega_s\neq0$).

In this study, FT EPR has only been used to detect radicals with very narrow spectral lines, so that the above description is sufficient for the understanding of the experiment.

2.6   Pulse EPR methods based on the primary echo

The *primary echo* is the simplest of all *electron spin echoes* (ESE) and is the EPR-analogue of the *nuclear spin echo* found by E. L. Hahn in 1950.[68] An echo was first measured in EPR by Blume[69] in 1958 and has since also been found in other spectroscopic methods.[70] The term primary echo describes the reappearance of magnetization as an "echo" of the initial magnetization after a pulse sequence $(\pi/2)$-τ-(π)-τ-echo, as shown in Figure 2.7, and is a phenomenon based on the non-linear behavior of a spin ensemble with a distribution of Larmor frequencies.[39,68] In the product operator framework using the Cartesian operators, neglecting relaxation of the spin system, the experiment can be described by eq. 2.58:

$$S_z = \sigma_{eq} \xrightarrow{(\pi/2)S_x} \sigma_1 = S_y \xrightarrow{free\ evolution} \sigma_2 = \cos(\Omega_s\tau) S_y - \sin(\Omega_s\tau) S_x$$

$$\sigma_2 \xrightarrow{(\pi)S_x} \sigma_3 \xrightarrow{free\ evolution} \sigma_4 = -\cos(\Omega_s\tau) S_y - \sin(\Omega_s\tau) S_x \tag{2.58}$$

where Ω_s is again the precession frequency of individual spin packets about the z-axis in the rotating frame. As in FT EPR, this pulse sequence also starts with a $\pi/2$-pulse (duration t_{p1}) along the x-axis that transforms the initial magnetization along the z-axis into magnetization along –y. After the pulse,

the system is allowed to freely evolve for a time τ, in which the different spin packets defined by their precession frequency accumulate a phase difference ($\Omega_s\tau$), i.e., the spin density vectors "fan out" in the x-y-plane. Then again a π-pulse
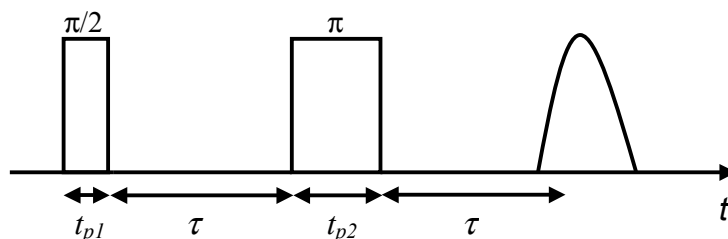

Figure 2.7. Pulse sequence for the primary echo (ESE) measurement. t_{p1} and t_{p1} are the durations of the $\pi/2$ and π pulses, respectively, and τ denotes the free evolution periods.

(duration t_{p2}, at equal mw strength $t_{p2}=2t_{p1}$) is irradiated from the x-axis, which inverts only the phases of the y-components of the overall magnetization vector (only the first term in the definition of σ_3 is sign inverted). After another free evolution period τ, the spins are "refocused" and an echo of the originally inverted spin packets is observable along the y-axis. The echo can then be detected at the time $2\tau+\tau_{p1}+\tau_{p2}$, often shortly noted as 2τ, in the quadrature mode.[39]

This method cannot refocus magnetization from spins that have relaxed during the experiment. Therefore, the echo intensity is strongly dependent on the phase memory time T_m and the echo sequence can only refocus the *inhomogeneously broadened* signals (i.e., such signals that consist of many overlapping spin packets with different Larmor frequency).

The primary echo is the basis of many pulse EPR experiments. Three of the most important experimental techniques, all of which are used in this work in Chapters 3 and 4, are presented in brief in the remainder of section 2.6. For a detailed discussion of theoretical and technical aspects the reader is referred to Reference 39. To distinguish phenomena and experiments derived from the primary echo from similar effects and techniques based on other forms of echoes, one often adds the prefix "2-pulse" or "2p" in front of the respective phrase (see 2.6.2)

2.6.1 Field-swept, ESE-detected spectra

A simple modification of the primary echo experiment is to repeatedly irradiate the mw pulses of Figure 2.7 during a sweep of the magnetic field. This experiment is in principle analogous to CW EPR (except for the fact that in CW EPR one detects the absorption signal in the first derivative mode) but the detected lineshape may be strongly dependent on relaxation. If the phase memory time of spin packets is very short (i.e., shorter than the timescale of the echo experiment), they cannot contribute to the echo signal as their signal component has already relaxed by the time of detection.

Therefore, echo signals from solutions of paramagnetic substances at ambient temperature are usually not detectable and in the solid state all spin components with $T_m\ll\tau$ cannot contribute to the signal. Such short phase memory times for nitroxide- and other organic radicals in solid state or frozen solution may arise from very strong dipolar or exchange interactions among the electron spins.

2.6.2   2-pulse electron spin echo decay (ESED) and envelope modulation (2-p ESEEM)

Due to the dependence of the echo signal intensity on the phase memory time T_m, a modified primary echo experiment can be used to measure T_m.

2-pulse ESE decay (2-p ESED)

Since the primary echo sequence leads to a refocusing of inhomogeneous broadenings, the decay of the echo signal on incrementing the second free evolution period τ in steps of $\Delta\tau$ is a direct measure of the phase memory time T_m. The modified pulse sequence to achieve this is presented in Figure 2.8.

In principle, the product operator description of eq. 2.58 is also valid for this experiment. One simply has to view the ESED experiment as a consecutive execution of as many echo experiments as there are different values for τ, and each of these "experiments" can be described by eq. 2.58. Ideally, the normalized echo intensity
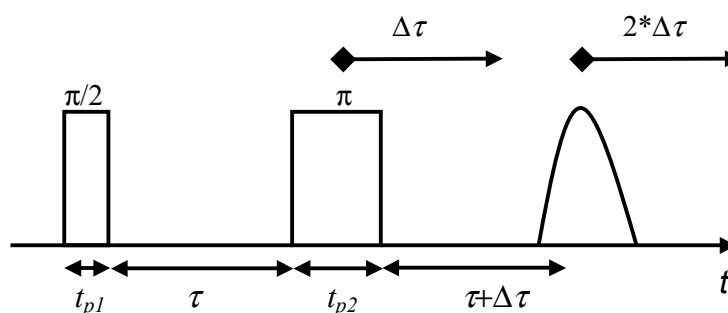

Figure 2.8. Pulse sequence for the ESE decay (ESED). The difference to the ESE measurement is that the position of the refocusing π pulse is increased in steps of $\Delta\tau$, and accordingly the position of the echo is increased by twice the increment.

$V(2\tau)/V(0)$ can then be analyzed as a function of $\tau+\Delta\tau$ by an exponential decay with the characteristic time T_m:

$$\frac{V(2\tau)}{V(0)} = \exp\left[\frac{-2\tau}{T_m}\right], \tag{2.59}$$

If the spin system is not determined by only a *single* phase memory time, one can try to analyze the decay as a biexponential or stretched exponential decay.[71] Interpretation is then not as straightforward as with equation 2.59 but still valuable insight into the environment of the radicals can be gained, as the environment strongly affects the ESE decay.

There are several physical processes that lead to spin-spin relaxation, e.g., methyl group rotation or instantaneous diffusion.[72] Depending on temperature and chemical environment of the EPR-active substance under investigation one of these processes might dominate the decay of magnetization. Often, though, T_m is not only determined by a single process, which can then lead to a non-single exponential behavior as described above.

2-pulse ESE Envelope Modulation (ESEEM)

When a primary echo decay is recorded, one can often detect a repeated oscillation (or modulation) with a certain frequency that is superimposed on the regular decay.

This modulation of the echo decay is called (two-pulse) *Electron Spin Echo Envelope Modulation* (2-p ESEEM) and arises from redistribution of electron coherence during the experiment. The resulting modulation for the two-pulse echo decay stems from weak hyperfine coupling of the detected electron spin to magnetic nuclei. In the following paragraphs, the origin of these modulations is briefly explained using the model system, $S=1/2$, $I=1/2$ of Section 2.4.2 (see Figure 2.5). The pulse sequence in this experiment is that of the ESED experiment in Figure 2.8.

After the $\pi/2$ pulse irradiated from the x-axis, coherences are generated on the two allowed electron transitions (marked "E1/2" in Figure 2.5) and the two forbidden transitions (when also the nuclear spin is flipped, dashed diagonals in Figure 2.5). It is informative to only follow one of the transitions, say "E1", since the other cases are analogous. In a vectorial picture, the magnetization vector of this transitions starts to precess in the x-y-plane during the first free evolution period after the $\pi/2$ pulse.[39] The frequency of the precession is: $\Omega_{E1}=\omega_{E1}+(\omega_{N1}-\omega_{N2})/2=\omega_{E1}+\omega/2$, where ω_{E1} is the Larmor frequency of the spins and ω_{N1} and ω_{N2} are the frequencies of the two nuclear transitions of Figure 2.5. During the evolution period τ the magnetization vector acquires a phase of $\phi_{E1}=\Omega_{E1}\tau$.

The π pulse after the interval τ then inverts the phase (as shown in the beginning of section 2.6) of the coherence, but it also redistributes this coherence within *all* electron transitions according to their transition amplitudes, since there is also a probability that the weakly hyperfine-coupled nuclear spin might be flipped by this pulse, as the high-field approximation is not strictly valid for the nuclear spin. The selection rule thus does not strictly apply. Hence, all four coherences are populated after the inversion pulse and starting from their initial equal phase their respective magnetization vectors now start to precess with different frequencies. After the time τ, only the magnetization stemming from the initially inverted E1 coherence forms the primary echo that is detected in y-direction. The magnetization that has been redistributed to the other three coherences has acquired a phase difference $\phi_x=(\omega_x-\omega_{E1})\tau$, where x stands for the respective coherence (e.g., E2), and forms so-called *coherence transfer echoes*. These echoes oscillate with $\cos(\omega_x-\omega_{E1})\tau$. This means that a fraction of the total echo amplitude oscillates with this factor. When recording the ESE decay, one scans through these oscillations by successively varying τ.

Taking into account all possible coherence-transfer pathways and their weighting factors, the modulation depth in 2-p ESEEM can be characterized by the parameter k:

$$k = \sin^2\left(\eta_\alpha - \eta_\beta\right) = \sin^2\eta , \tag{2.60}$$

where η_α and η_β are the angles between the magnetic field direction and the nuclear spin (manifolds α and β) quantization axes and η is the difference between them. If one assumes weak hyperfine couplings and isotropy of the *g*-tensor, the modulation depth becomes:

$$k = \frac{9}{4}\left(\frac{\mu_0}{4\pi}\right)^2\left(\frac{g\beta_e}{B_0}\right)^2\frac{\sin^2 2\theta}{r_{e-n}^6} , \tag{2.61}$$

where r_{e-n} is the electron-nuclear spin and θ is the angle between their connecting vector and the B_0-direction.distance. In Section 2.7.2 it is explained how the r_{e-n}^{-6} dependence of the modulation depth is used to extract average electron-nuclear distances from ESEEM time domain data.

The spin density operator of the magnetization at the time of echo formation can be calculated in the framework of the product operator formalism using the Cartesian product basis. The only difference to the transformation described by equation 2.58 is that during the periods labeled "free evolution" now the Hamiltonian H_0 acts on the spin system. This Hamiltonian is given by:

$$H_0 = \Omega_s S_z + \frac{\omega_+}{2} I_z + \omega_- S_z I_z,\tag{2.62}$$

where $\omega_+=(\omega_{N1}+\omega_{N2})$ and $\omega_-=(\omega_{N1}-\omega_{N2})$. After a series expansion of spin density operator at the time of the echo and some trigonometric transformations one obtains a formula that describes the modulation of the ESE decay (not taking into account relaxation):[39]

$$V_{2-pESEEM}(2\tau) = 1 - \frac{k}{4}\left[2 - 2\cos(\omega_\alpha \tau) - 2\cos(\omega_\beta \tau) + \cos(\omega_- \tau) + \cos(\omega_+ \tau)\right],\tag{2.63}$$

where $\omega_\alpha=|\omega_{E1}|$ and $\omega_\beta=|\omega_{E2}|$. Note that the signal contains modulations from both nuclear spin manifolds (ω_α and ω_β) and from their sum and difference frequencies (ω_+ and ω_-). Combining equations 2.59 and 2.63 one obtains a description of the time domain signal that includes electron spin relaxation and nuclear modulation:

$$\frac{V'(2\tau)}{V'(0)} = \exp\left[\frac{-2\tau}{T_m}\right] \cdot V_{2-pESEEM}(2\tau),\tag{2.64}$$

It is important to note that the modulations due to p different nuclei are multiplicative, which is called the *product rule* and also gives rise to some complications: $V_{2-p}(2\tau)=\prod V_{2-pESEEM}(2\tau,p)$. The simplest way of analyzing such time-domain data is to divide out the electron spin relaxation (e.g., dividing by the single exponential or a stretched exponential decay) and subsequently perform an FT of the signal to the frequency domain. Such 2-p ESEEM frequency domain spectra are often hard to interpret because of the existence of the sum and difference peaks at ω_+ and ω_-. This problem is avoided in the 3-p ESEEM experiment, which is described in Section 2.7.

The analysis of 2-p ESEEM (and also 3-p ESEEM) data in the time- and frequency domain gives the experimental possibility to probe the direct magnetic environment (up to ~0.7 nm) of the detected electron spin. In principle it contains information similar to that gained from electron-nuclear double resonance (ENDOR) methods but has the advantage that no hardware for radiofrequency irradiation is required.[39] These experiments are particularly interesting for obtaining distances between the electron spin and the coupled nuclear spins. One specific method (for 2-p and 3-p ESEEM) is described in Section 2.7.2.

2.6.3   Double electron-electron resonance (DEER)

The EPR spin Hamiltonian that has been introduced in Section 2.2 contains a term $H_{DD,e}$ that describes weak dipolar couplings between electron spins (equations 2.18/2.19). From eq. 2.19 it is obvious that this magnetic interaction between two dipoles can be used to gain information on the distance distribution between electron spins in a system, as there is a distinct r_{12}^{-3} dependence of the dipolar coupling. Often (e.g., for nitroxides), it is not possible to analyze the splittings stemming from the dipolar interaction in CW or ESE-detected EPR spectra directly, since the lines are too broad and hide the dipolar splitting. Therefore, pulse methods were developed to separate dipolar couplings from other effects in the spin system.[39,56,73,74]

In the following, one pulse EPR method (at X-band frequencies, ~9.4GHz) is described that allows extraction of interradical distance information, which is of particular interest for disordered system, in which, e.g., X-ray crystallography cannot be applied.[52,75] This method is called *double electron-electron resonance* (DEER) spectroscopy and especially the 4-pulse variant of this technique is in the focus.[39,76]

The pulse scheme of the 4-p DEER method is presented in Figure 2.9.a. On a spin packet "1" in the powder spectrum of Figure 2.9.b with resonance frequency (i.e., mw frequency) ω_1, a *refocused echo* ("observe") experiment[39] is performed, while on spins "2" with resonance frequency ω_2 only a π pulse ("pump") is irradiated. Using the refocused echo has the advantage that the dipolar evolution can be detected without any dead time. The time at which the π pump pulse (time t) is irradiated is varied between the position of the primary echo (that is not detected but allowed to dephase again) and the last π pulse in the observer experiment. The π pulse at ω_2 inverts the "2" spins and thus changes the local magnetic field at the position of the "1" spins. Hence the precession frequency of the "1" spins changes and the magnetization gains a phase difference of $\Delta\phi_{DD}=\omega_{DD}t$. One records the echo intensity of the refocused echo as a function of the pump pulse position t and can gain information on the
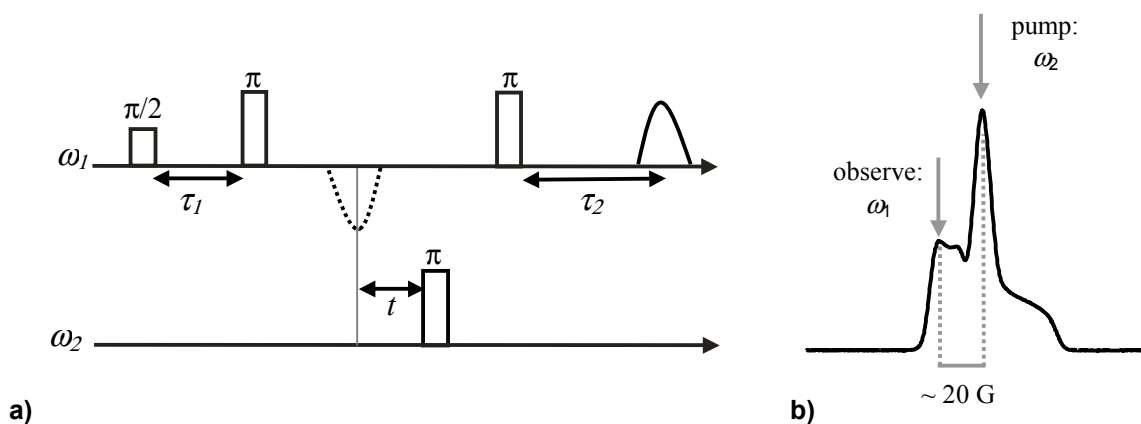
Figure 2.9. Pulse scheme (a) and excitation/observation positions (b) of the 4-pulse DEER experiment; the time t of irradiation of the mw with frequency ω_2 is incremented in the experiment. Since neither τ_1 nor τ_2 are varied, all decays and modulations of the signal stem from dipolar coupling of spins "1" to spins "2"; The observer and pump positions shown in b) are those used for the nitroxide radicals in all DEER experiments that are presented in Chapters 3 and 4.

dipolar coupling between the two spins. In addition, since the time intervals in the refocused echo subsequence are not changed, this is a constant time experiment, which eliminates additional complications due to transverse (spin-spin) relaxation. Figure 2.9.b also shows one disadvantage of this experiment: to avoid overlap of the observer and pump pulses one needs a spectral distance of at least 15 G, which is no problem to achieve with nitroxide radicals (shown in Figure 2.9.b) but makes use of this method impossible for spectra with a width of less than ~15 G (see the excitation profiles in Refs. 39 and 76).

Extraction of the distance information may be difficult depending on the respective system, but the effect of inverting spins "2" that are dipolar coupled to spins "1" is rather straightforward. The dipolar interaction frequency ω_{DD} has already been defined implicitly in equation 2.19:

$$\omega_{DD} = \frac{\mu_0 g_1 g_2 \beta_e^2}{4\pi\hbar} \frac{1}{r_{12}^3}, \tag{2.65}$$

Applying the product operator formalism, one finds that the normalized echo intensity $V_{\text{4-pDEER}}(t)$ becomes:[39,74]

$$V_{4-pDEER}(t) = \cos\left[\left(\omega_{DD}(3\cos^2\theta_{12} - 1)\right)t\right], \tag{2.66}$$

where the dipolar interaction frequency is multiplied by the weighting factor that accounts for the angle θ_{12} between the vector connecting a certain spin pair (1-2) and the outer B_0-field direction. Equation 2.66 shows that the echo amplitude is modulated by the dipolar interaction between spin pairs. One can either analyze the time-domain data (i.e., the modulation of the ESE decay with T_m) or the frequency domain spectra after FT of the modulation. Note that for multiple spins, the modulation of the echo intensity is multiplicative.[39]

There are also finite couplings to further electron spins that are remote from the observed spin packet. If these remote spins are homogeneously distributed such couplings contribute only a background signal that can be described by an exponential decay:

$$V_{4-pDEER}^{\text{hom}}(t) = \exp\left[-kCF_2|t|\right], \tag{2.67}$$

where C is the volume concentration of the electron spin, F_2 is the fraction of "2"-spins that is inverted by the pump pulse and k is a constant factor:

$$k = \frac{2\pi\mu_0 g_1 g_2 \beta_e^2}{9\sqrt{3}\hbar}. \tag{2.68}$$

Distance range

The range of interspin distances that is accessible by the DEER method is limited by two factors. The lower limit is approximately 1.5nm as for systems with closer distances, the dipolar coupling is so

strong (ω_{DD}~35MHz=12.5G) that it exceeds the technical excitation bandwidth of the mw pulse generators at X-band frequencies. Hence, spin pairs that are closer than this value are not excited.

The upper limit of accessible distances strongly depends on the maximum dipolar evolution time t and thus finally on the time τ_2 used for the observer pulse scheme. Spin pairs that are relatively far apart have a low dipolar coupling frequency and the period of the dipolar oscillation in the time-domain signal is very long. One usually needs at least one full period of a modulation in order to unambiguously extract a frequency, especially if several modulations contribute to the signal. One can extend the accessible time range, e.g., by using deuterated solvents[52] or solvents without methyl groups (this increases T_m) but the distance range can probably not be extended much farther than ~8nm. All spins that are farther apart than this upper distance limit (up to ~40nm) only contribute to the homogeneous background signal of eq. 2.67.

Data analysis

The simplest type of analysis for the 4-p DEER experiment is to divide out the homogeneous part of the signal (eq. 2.67) and FT the modulation. This gives a *Pake pattern*, i.e., a dipolar spectrum, and from the singularities in these spectra one can directly read off the dipolar coupling frequency ω_{DD} and calculate the spin-spin distance from the following equation:[52,75]

$$r_{12} = \sqrt[3]{\frac{52.16\text{MHz}}{\omega_{DD}}}\text{nm} \ . \tag{2.69}$$

Analysis is mathematically more demanding when performed in the time domain. However, the great advantage is that not only samples that show distinct distances with a narrow distribution width (such as biradicals with a rigid chemical backbone)[76] can be characterized but also samples with broad spin distance distributions, as is the case in many macromolecular systems. It is also advantageous, as singularities in Pake patterns might not always be easily detectable.

One way of analyzing time domain data is to simulate modulations based on some physical model of a distance distribution and then fit this simulated signal to the experimental time traces by variation of the respective fit parameters. In this case, one uses the analytical expression of 2.66 or the more intricate mathematics of *shell factorization analysis*, in which the spherical volume around the observer spin is viewed to be built of thin spherical shells.[39,52,77] Without going into the details, one can see from eq. 2.70 that within this analysis, one can use any arbitrary radial distribution function $G(r)$, with usually only a few fit parameters, as a fit model:

$$\ln\left(\frac{V_{4-pDEER}(t)}{V(0)}\right) = -\int_{r_{\min}}^{r_{\max}} 4\pi r^2 G(r)\left(1 - V_r(r,t)\right)dr \ , \tag{2.70}$$

where $V_r(r)$ denotes the signal within a certain thin shell.

Recently, also a model-free *direct integral transformation* of time domain data to distance distributions has been reported.[52,77] This method has the great advantage that no prior knowledge of

the electron spin distribution is needed. A similar approach has been successfully applied in NMR spectroscopy (see citations in References 52 and 77) and is based on elimination of the signal contributions stemming from spins at larger distances and mapping of dipolar frequencies to distances after an approximate integral transformation of a linearized version of eq. 2.70.

Finally, one can conclude that the 4-p DEER experiment is a powerful tool for determining distance distributions or local concentrations of radicals. 4-p DEER is only one of the pulse EPR methods for distance determinations[56] that have been developed and already widely applied in the last decade. Other methods are, e.g., based on 3-p DEER,[73,74] the "2+1" pulse sequence,[78] or double-quantum EPR.[79]

2.7   Pulse EPR methods based on the stimulated echo

The *stimulated echo* is based on the pulse sequence shown in Figure 2.10. In a vector picture of magnetization, the initial $\pi/2$-τ-$\pi/2$ sequence creates a *polarization grating* along the z-direction, which is stored there for the time T.[39] The polarization grating is spaced at $1/\tau$ and magnetization in this grating (neglecting spectral diffusion effects) decays with the spin-lattice relaxation time T_1, which in solids usually is much longer than the phase memory time T_m. This is the main advantage of stimulated echo-based pulse EPR experiments: during the evolution time additional pulses can be irradiated. After the third $\pi/2$ pulse, the polarization pattern is transferred to the x-y plane, where it now can be detected.

In the framework of the product operator formalism, the spin density operator σ at a time t after the third pulse is given by:

$$
\begin{aligned}
\sigma(\tau+T+t) = &-\frac{1}{2}\Big[\cos\big(\Omega_s(t-\tau)\big)+\cos\big(\Omega_s(t+\tau)\big)\Big]S_y \\
&+\frac{1}{2}\Big[\sin\big(\Omega_s(t-\tau)\big)+\sin\big(\Omega_s(t+\tau)\big)\Big]S_x
\end{aligned}
\tag{2.71}
$$

where Ω_s is again the resonance offset of a spin packet. From closer inspection of eq. 2.71 one finds that the terms containing $(t-\tau)$ lead to an echo at $t=\tau$ and the terms containing $(t+\tau)$ form a so-called *virtual echo* at time $t=-\tau$, which can actually be detected when a fourth pulse to convert the virtual
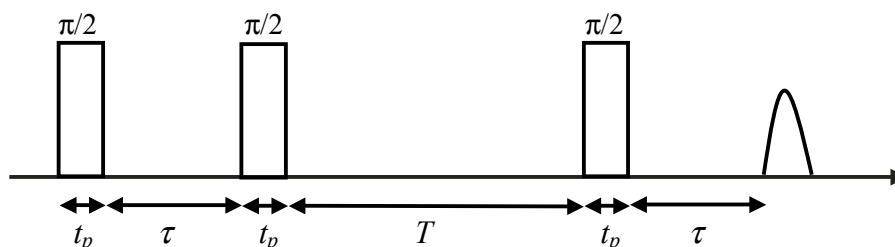

Figure 2.10. Pulse sequence for the stimulated echo measurement. t_p is the durations of the $\pi/2$ pulses, τ denotes the free evolution period in which magnetization relaxes with T_m, while T is the time period in which magnetization - stored as a polarization grating - decays with the much longer spin-lattice relaxation time T_1.

echo to a real echo is applied (this is not investigated further here, see Ref. 39).

The terms with the argument $\Omega_s(t-\tau)$ lead to defocusing of half of the magnetization at the time of echo formation. The overall echo intensity is therefore only half that of the primary echo.

If there is weak hyperfine coupling of the detected electron spin to magnetic nuclei, this might lead to modulations of the stimulated echo decay, analogous to the modulations of the primary echo decay described in Section 2.6.2. The last two sections of this chapter now briefly discuss the foundations of this variant of the ESEEM experiment and how information on electron-nuclear distance can be gained.

2.7.1   3-pulse electron spin echo envelope modulation (3-p ESEEM)

The pulse sequence for the stimulated echo decay experiment is shown in Figure 2.11. Unlike in the ESE decay, where the echo signal intensity decays with the phase memory time T_m, in the stimulated echo decay experiment the decay of the echo signal is determined by the electron spin lattice relaxation time and spectral diffusion of magnetization. These relaxation mechanisms lead to a much slower decay but it is often difficult to assign a physical meaning to the characteristic decay time. The simplest method to analyze the decay is to fit an arbitrary, phenomenological decaying function to the time-domain data. In this study, a stretched exponential function is chosen for this purpose:

$$\frac{V_{3-p}(\tau,T)}{V(0)} = \exp\left[\frac{-T}{T'}\right]^x ,\qquad(2.72)$$

where T' simply is the characteristic decay time that combines relaxation due to all mechanisms and x is the stretch factor. The stimulated echo decay itself is not of interest in this study, eq. 2.72 is merely used to eliminate the echo decay from time-domain data that also show modulations due to hyperfine coupling to magnetic nuclei (3-p ESEEM).

3-pulse ESEEM

When the decay of a stimulated echo is observed (Figure 2.11), often a modulation of the echo
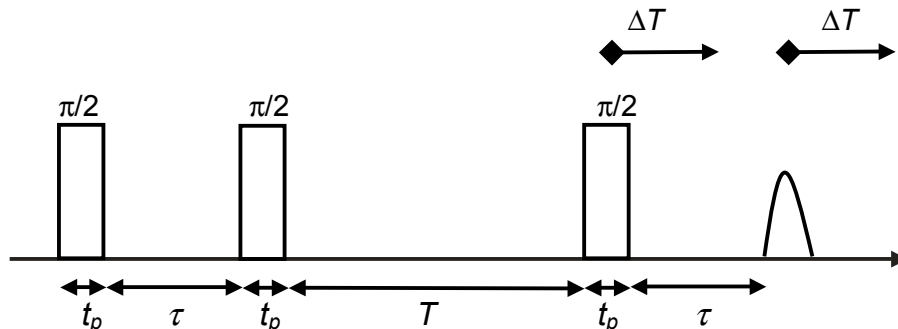

Figure 2.11. Pulse sequence for the stimulated echo decay measurement. t_p is the durations of the $\pi/2$ pulses, the time τ is kept constant, while T is successively incremented by ΔT and the decay of the echo amplitude is recorded as a function T.

envelope, similar to that in the primary echo decay ensues. In the following, this 3-pulse ESEEM effect is explained in brief, again using the model system $S=1/2$, $I=1/2$ of Section 2.4.2 (see Figure 2.5).[39] The explanation also relies on Section 2.6.2, where the 2-p ESEEM effect has been introduced.

Up to the end of the first free evolution period (after time τ), the system in 3-p ESEEM is exactly in the same state (described by spin density matrix) as in 2-p ESEEM. In contrast to the π pulse applied at this time in 2-p ESEEM, the $\pi/2$ pulse in the 3-p ESEEM experiment now additionally creates nuclear coherence. This nuclear coherence is then redistributed, e.g., from the allowed E1 transition to E2 or the two forbidden transitions (dashed lines in Figure 2.5), which populates off-diagonal density matrix elements. During time T these off-diagonal elements (nuclear coherences) can evolve with the *nuclear frequencies* ω_{N1} and ω_{N2} and, e.g., gain the phase $\phi_{N1}= \omega_{N1}T$.

The last $\pi/2$ pulse transfers the nuclear coherence back to electron coherence, and an echo is formed after another period of $\sim\tau$. The transfer of magnetization during the second and third $\pi/2$ pulses is symmetric, so that like in 2-p ESEEM also the electron coherence is redistributed among the electron transitions. Concerning the transfer of electron coherence the 3-p ESEEM experiment contains all pathways of the 2-p ESEEM, the latter can even be seen as a limiting case of the former with $T=0$. The modulation depth in the 3-p variant is also proportional to the depth parameter k, defined in equation 2.60.

Quantitative description of the 3-p ESEEM effect is much more difficult, since it crucially depends on the resonance offset and the evolution periods τ and T. For the model system of Figure 2.5, the modulation formula is found within the product operator formalism:[39]

$$V_{3-pESEEM}(\tau;T) = 1 - \frac{k}{4}\Big\{ \big[1-\cos(\omega_\beta\tau)\big]\big[1-\cos(\omega_\alpha(\tau+T))\big] \\ + \big[1-\cos(\omega_\alpha\tau)\big]\big[1-\cos(\omega_\beta(\tau+T))\big]\Big\},$$
(2.73)

where k is the modulation depth and again $\omega_\alpha=|\omega_{E1}|$ and $\omega_\beta=|\omega_{E2}|$. Note that unlike in 2-p ESEEM, no modulation arises from sum or difference frequencies, which is one reason why the ESEEM spectra gained after FT of the time domain signal may be significantly easier to understand than 2-p ESEEM spectra. A slightly modified product rule applies for 3-p ESEEM on systems with several nuclei.[39]

Those factors in eq. 2.73 containing $1-\cos(\omega_{\alpha,\beta}\tau)$ vanish for certain values of $\omega_{\alpha,\beta}$:

$$\omega_{\alpha,\beta} = \frac{2\pi n}{\tau},$$
(2.74)

where $n=(0, 1, 2\dots)$. This simply means that the modulation for a given nuclear frequency may vanish for τ values that fulfill equation 2.74. This leads to *blind spots* in the ESEEM spectrum, i.e., values of τ for which modulation of the echo decay due to certain nuclear spins vanishes. In practice, the modulation never vanishes completely but the modulation depth is reduced significantly. To assure that all modulations have been detected, this makes it usually necessary to perform the 3-p ESEEM

experiments at several values of τ (e.g. in a 2-dimensional experiment, in which τ and T are incremented). However, in certain cases appearance of blind spots might even be of considerable advantage. By suppressing a strong modulation due to a certain nuclear spin (most often ^{1}H), modulations by other nuclear spins that have a shallow modulation depth might become detectable more easily. One example, where a blind spot for the ^{1}H nuclear modulation is used to detect modulation from ^{14}N nuclear spins, is presented later in Chapter 3.

The overall 3-p ESEEM signal consists of three contributions: the electron spin-spin relaxation (T_m) during the interval τ, nuclear spin-spin relaxation ($T_m^{(n)}$) during the interval T and the ESEEM signal of eq. 2.73:

$$V_{3-p}^{'}(\tau;T) = \exp\left[\frac{-T}{T_m^{(n)}}\right]\exp\left[\frac{-\tau}{T_m}\right]V_{3-p}(\tau;T).$$ (2.75)

As mentioned before, analysis of 3-p ESEEM spectra after FT of the time domain signal might be substantially simpler since only the original nuclear resonance frequencies appear. On the other hand, time-domain analysis might be complicated by the fact that modulation depths in this experiment are not as reliable as in its 2-p analogue.[39] In Section 2.7.2 one semi-quantitative method to characterize systems of electrons and nuclei is described, which is based on the model of spherical coordination of electron spins by the respective nuclear spins.[39,80]

Other methods that are based on the 3-p ESEEM scheme by inserting an inversion π pulse during the evolution time T have been developed in the last two decades (e.g., the two-dimensional HYSCORE) and are powerful tools in the investigation of many systems.[39] In this study, though, they are not presented since they could not deliver insight into the investigated systems that goes beyond the findings with the simpler analysis of 3-p ESEEM data.

2.7.2   Ratio analysis of 3-p ESEEM

One method to quantitatively extract information on the distance and the number of nuclear spins that are in the vicinity of a detected electron spin has been developed by Ichikawa, Kevan and coworkers.[80] This characterization method is called *ratio analysis* of ESEEM data. It is applicable to echo decays gathered by 2-p or 3-p ESEEM, but is only used for 3-p ESEEM data in this study. Ratio analysis has the advantage that it is by far not as complicated as simulation of 3-p ESEEM data for systems containing several nuclei and disordered systems. In such systems, the product rule of ESEEM signals has to be applied before the overall signal is *powder-averaged* (i.e., integrated over the whole angular range).

Ratio analysis uses the simplification of describing the system as follows: one electron spin is seen as being surrounded by coordination spheres of certain types of nuclei. If such spherical symmetry is assumed and the orientations of electron-nuclear spin vectors are thus uncorrelated, the product rule can be applied *after* the powder average has been calculated, which tremendously

simplifies the mathematical description of the system.[39] It is then possible to find relatively simple equations that describe the decay $V_{max,th}(\tau, r_{e-n}, a_{iso})$ and $V_{min,th}(\tau, r_{e-n}, a_{iso})$ of the *extrema*, i.e., the maxima and minima in the *theoretical* ESEEM signal imposed by the hyperfine coupling of electron and nuclear spin, with time T. These expressions only depend on the values for τ, the electron-nuclear distance r_{e-n} and the isotropic hyperfine coupling a_{iso}. Corresponding equations for a system of $S=1/2$ and $I=1$ are shown in Appendix A7 and in the original publication.[80] From the experimental data, it is also possible to obtain decay curves for the maxima and minima of the modulation, $V_{max,exp}$ and $V_{min,exp}$ by interpolating data points between the respective extrema (in this study, this interpolation was achieved by using polynomials up to 5th order).

The main parameter for description of the system is the function that describes the decay of the *ratio* of the maxima and minima, both for the calculated and the experimental signal:[39,80]

$$R_{exp}(\tau) = \frac{V_{max,exp}(\tau)}{V_{min,exp}(\tau)}; \quad \left[R_{th}(\tau, r_{e-n}, a_{iso})\right]^n = \left[\frac{V_{max,th}(\tau, r_{e-n}, a_{iso})}{V_{min,th}(\tau, r_{e-n}, a_{iso})}\right]^n, \quad (2.76.a, b)$$

where n is the number of equivalent nuclei in the closest coordination sphere. For the analysis, one can then fit the theoretically calculated ratio R_{th} to the experimentally extracted ratio R_{exp} by variation of only the parameters r_{e-n}, a_{iso} and n. Numerically, one uses the linearized form of equations 2.76.a, b for this fitting procedure:

$$\log\left(\log(R_{exp}(\tau))\right) \simeq \log(n) + \log\left(\log(R_{th}(\tau, r_{e-n}, a_{iso}))\right), \quad (2.77)$$

In practice, the number of nuclei n can even be removed as an optimization parameter by calculation from the following equation:[80]

$$n = \frac{\sum_l V^2_{max,exp,l} \ln(R_{exp,l}) \ln(R_{th,l})}{\sum_l V^2_{max,exp,l} \left[\ln(R_{th,l})\right]^2}, \quad (2.78)$$

which leaves this analysis method only dependent on two variables, r_{e-n} and a_{iso}. Hence, it is possible to obtain quantitative information on the direct environment of an electron spin, namely the closest distance of a certain type of magnetic nuclei and the number of nuclei at such a distance.

The assumption that only nuclei in the closest coordination shell contribute to the modulation can be justified if the hyperfine coupling is very weak ($a_{iso}<0.1$MHz), which is true for nuclei sufficiently far away from the electron. The spherically averaged modulation depth $<k_i>$ due to a certain nucleus i is then given by (see equation 2.61): [39,80]

$$\langle k_i \rangle = \frac{8}{5} I(I+1) \left(\frac{\mu_0}{4\pi}\right)^2 \left(\frac{g\beta_e}{B_0}\right)^2 \frac{1}{r^6_{e-n,i}}, \quad (2.79)$$

In a spherical model, the number of nuclei increases only proportional to r_i^2. Together with the r^{-6} dependence from equation 2.79 it is therefore a reasonable assumption that only nuclear spins in the first coordination sphere significantly contribute to the signal. The estimated uppermost electron-nuclear distance that can be characterized by this method is (depending on the type of nucleus) ~0.7nm.

One should be aware that not all effects that lead to a damping of either the initial modulation depth or the experimentally observable ratio R_{exp} are accounted for in the theoretical considerations. Such effects could be due to, e.g., additional nuclear quadrupole coupling (see Section 2.2) of nuclei with $I \geq 1$. Thus, one has to assure that quadrupole coupling can actually be neglected.

Based on the work by Ichikawa and coworkers,[80] a fitting program was written in MATLAB and used for analysis of 3-p ESEEM data in Chapter 3. In this program, the original time-domain data can be processed (elimination of the stimulated echo decay, finding of extrema and interpolation to obtain $V_{max,exp}$, $V_{min,exp}$, and R_{exp}) and the simulations according to the formulae in Appendix A6 are carried out.

Not all of the assumptions made in the ratio analysis are strictly valid. In particular the systems under investigation in this study - polyelectrolytes and charged, EPR-active counterions - show local order due to electrostatic assembly, which makes the model of spherical coordination seem somewhat crude. Nonetheless, given the complexity of the system, this method of 3-p ESEEM data analysis can give an approximate picture of the local environment of an unpaired electron spin, which is not accessible otherwise.

3　Spin Probing and EPR Spectroscopy of Polyelectrolyte-Counterion Interactions

In Chapters 3 and 4 of this thesis the experimental work is summarized and interpretation of the experimental results are given. In this chapter, with a few exceptions, the EPR data are analyzed in an essentially *model-free* approach. This analysis is then used to gain information on the structure and dynamics of the investigated polyelectrolyte systems. In Chapter 4, interpretations of experimental results are given that are based on models from polyelectrolyte theory.

This chapter starts with the introduction to the approach to use charged spin probes as tracers for counterions and presents the investigated materials. The next section, 3.2, describes experiments that were performed on a model rigid-rod polyelectrolyte to prove the applicability of the spin probing approach – evidence for electrostatic attachment of charged spin probes to polyelectrolyte charges is presented. In the last section of this chapter the investigations are expanded to systems containing highly charged, flexible polyelectrolytes.

3.1　Investigated systems

In this section all the investigated polyelectrolytes and spin probes are introduced. Then, the effect of changing the solvent from water to mixtures of water and organic solvents is discussed shortly. All data on the materials used, sample preparation and the experimental set-up for EPR spectroscopy are summarized in Appendices A1-A2.

3.1.1　Studied polyelectrolytes and spin probes

There is a vast variety of synthetic polyelectrolyte materials on the one hand and of spin probes on the other hand. In order to find systems in which effects of polyelectrolyte-spin probe interaction are observable, various commercially available polyelectrolytes, spin probes, and solvents were considered or had to be screened for use. Technical details of all materials and sample preparation procedures are documented in Appendix A1.

The choice of polyelectrolytes was finally restricted to two totally distinct types of polymers. Scheme 3.1 displays the structure of a rod-like, self-assembling coordination polymer with Ru^{2+} as the charge-bearing group along the chain

$$2(n+1)*PF_6^-$$
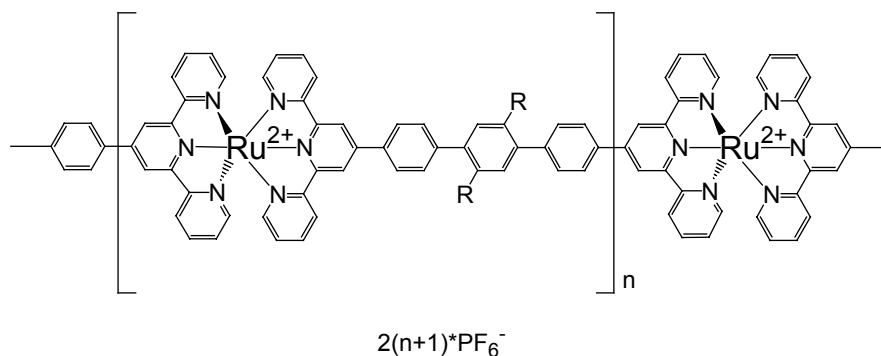
Scheme 3.1. Molecular structure of rodlike coordination polyelectrolyte containing divalent Ruthenium ions as charged groups (*RuCP*). The number of repeat units n is 20-25.
**R**=(O-(CH$_2$)$_2$)$_2$-O- CH$_2$CH$_3$
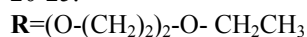
(*RuCP*).[81,82] This material has been supplied by Oliver Schmelz and Prof. Matthias Rehahn from the *Deutsches Kunststoff-Institut* (*DKI*) in Darmstadt. The complex formation of Ru^{2+} ions and two terpyridine based spacer molecules leads to octahedrally coordinated Ru-centers with kinetically stable coordination bonds (for details on synthesis see References 81, 82). Several polymers of this kind with different organic spacer molecules and metal ions (especially of the Fe-group in the periodic table of elements) have recently been developed for two reasons. First, they are excellent model systems to probe solution behavior of polyelectrolytes as they retain their rigid extended conformation regardless of factors like ionic strength. Second, because of their regularly spaced transition-metal ions and fully conjugated π-electron spacers there is potential interest in their electronic and optical properties and for catalysis.

Unlike conventional polyelectrolytes, RuCP are not soluble in water but only in solvents such as dimethyl formamide (DMF), dimethyl sulfoxide (DMSO), and dimethylacetamide (DMAc). This constituted a problem because of the poor solubility of the used anionic spin probe in these solvents. The solution of this problem will be explained in detail in Section 3.2.

In addition to the unusual rod-like RuCP, two commercially available flexible, unbranched polymers were investigated, which are displayed in Scheme 3.2. Their charged groups, namely sulfonates (-SO$_3^-$) and quaternary ammonium groups (-NR$_4^+$), show a high degree of dissociation. Scheme 3.2 displays molecular structures of these cationic and anionic *strong polyelectrolytes*.
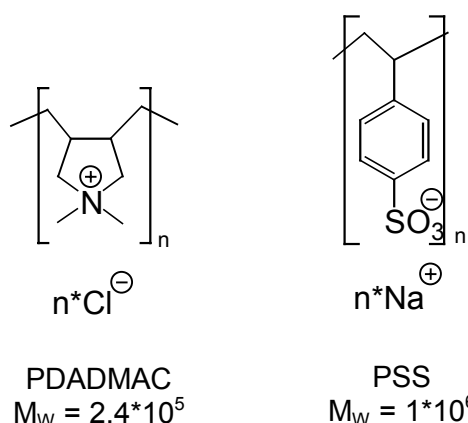
Scheme 3.2. Molecular structure and mass-average molecular weight (M$_W$) of the two flexible polyelectrolytes used in this work.
Left: PDADMAC=poly(diallyldimethylammonium chloride);
Right: PSS=poly(4-styrene sulfonate)
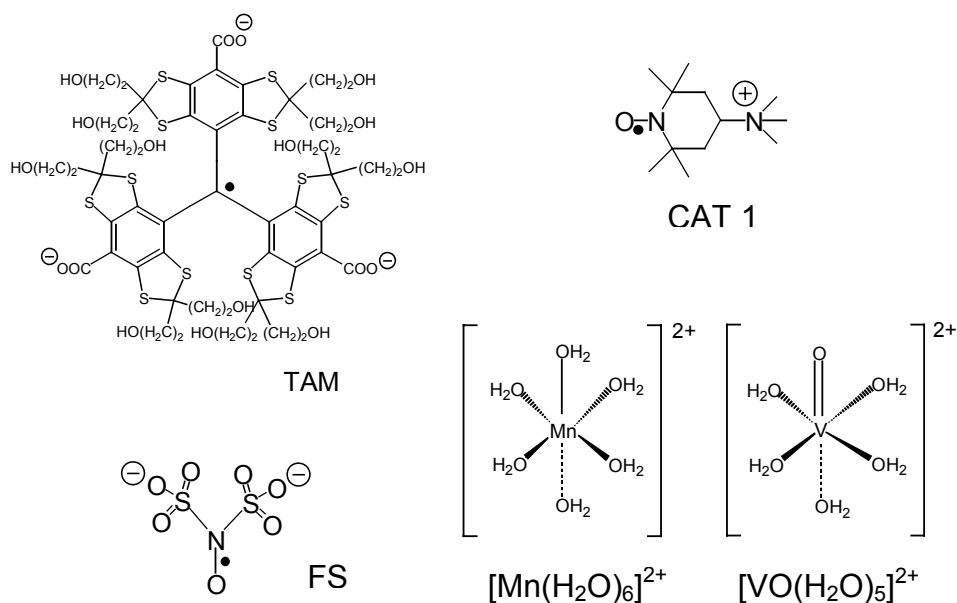
Scheme 3.3. Molecular structure of the charged spin probes used in this work.
Left: anionic spin probes: TAM=triarylmethyl trianion, sodium salt;
FS =Fremy's salt dianion (potassium nitrosodisulfonate);
Right: cationic spin probes: CAT 1=trimethyl ammonium TEMPO (iodide salt);
$Mn(H_2O)_6^{2+}$= octahedrally coordinated manganese (V) ion (chloride salt; S=5/2, I=5/2);
$VO(H_2O)_5^{2+}$=distorted octahedrally coordinated oxovanadyl (IV) ion (sulfate; S=1/2, I=7/2)

The cationic polyelectrolyte PDADMAC (poly(diallyldimethylammonium chloride)) is extensively used not only in scientific research[1,683,84] but also in industrial applications, e.g., to recover crude oil from oil/water emulsions. The anionic polyelectrolyte PSS (poly(4-styrene sulfonate), sodium salt) is also well known and often used in science and industry.[1,4,84,85] Both polyelectrolytes have high molecular masses corresponding to a high degree of polymerization (PDADMAC: $M_W/M_{monomer}$~1500; PSS: $M_W/M_{monomer}$~5500). The results for these polyelectrolytes can thus be compared to theoretical predictions for the long-chain limit.

The selection of charged spin probes used for EPR spectroscopy is presented in scheme 3.3. One can see that the spin probes belong to either of three different classes of paramagnetic species: i) nitroxide radicals (organic: CAT 1, inorganic: Fremy's salt, FS); ii) carbon-centered radical (TAM); iii) transition metal ions (Mn^{2+} and VO^{2+}). The procedure for sample preparation of PDADMAC and PSS was as follows: the concentration of the used spin probe is held fixed in all samples, usually at a value for which spin probe-spin probe interaction without the addition of oppositely charged polyelectrolyte is insignificant. This is necessary to exclude all effects that could stem from simply altering the initial bulk concentration of the ion of spectroscopic interest. Then a series of samples with variable concentrations of polyelectrolyte is prepared and thereby the ratio R of spin probe to repeat units of polyelectrolyte is varied:

$$R = \frac{c(spin\ probe)}{c(polyelectrolyte)}$$

It is important to note that by simply counting charged monomeric units of the polyelectrolyte any ambiguity arising from the broad molecular weight distribution (polydispersity index $M_W/M_N \gg 1$) is avoided. The high molecular weights of both PDADMAC and PSS ensure that all effects that are observable stem from long-chain polyelectrolyte behavior.

In the most extensively studied system that consists of the spin probe FS and the polyelectrolyte PDADMAC, FS concentration typically is 0.5 mM and PDADMAC concentration is varied between 2 mM and 140 mM in monomers, i.e. $0.0035 < R \leq 0.25$.

The charged spin probes simply constitute added salt since no original counterions of the polyelectrolytes are replaced by methods of ion exchange or dialysis. As explained in Section 1.2.2, for entropic reasons multivalent ions expel monovalent ions from the state "condensed" to the polyelectrolyte chains, so that with the exception of CAT 1 all spin probe ions are expected to come into interaction distance with the oppositely charged polyelectrolytes by *electrostatic self-assembly*. In a simple picture this can be anticipated by noting that multivalent ions reach the critical Manning parameter ξ for counterion condensation already at lower values than monovalent ions: $\xi = l_B / b > 1/|z_i|$, where $z_i = 1, 2, 3\ldots$ is the number of charges on the respective counterions.

A closer look at the polyelectrolytes

Obviously the RuCP and the conventional PDADMAC/PSS polyelectrolytes represent two different classes of polymers. Synthesis of coordination polymers like RuCP in itself is a very demanding task, whereas synthesis of PDADMAC and PSS is established for production of very large quantities. From a force-field calculation (Universal Force Field 1.02 as implemented in Cerius2, v.3.8, Molecular Simulations, Inc.) for the optimization of geometry of three repeat units a Ru-Ru-distance of $r=2.35$ nm is obtain, which is in good agreement with the previously reported value of 2.32 nm.[81] From solution NMR endgroup analysis one finds a condensation of 20-25 repeat units per macromolecule,[82] so that one can assume that each individual macromolecule at full extension has an end-to-end distance of at least 46 nm – not taking into account possible bending of the molecule at long distances.

Both conventional polyelectrolytes used here have a rather flexible (only single carbon-carbon bonds) and hydrophobic polymer backbone. The chain flexibility may nevertheless be reduced significantly as their charged groups are strongly dissociated in solution, which adds electrostatic rigidity to the chain as described by OSF theory (see Section 1.2.4).

In order to obtain an approximation for the monomer-spacing parameter b, again force field calculations for the optimization of geometry of small chains of 32 monomeric units are performed using the MMFF94 force field (SPARTAN 5.1.2, Wavefunction, Inc.). Depending on the chain conformation, for PDADMAC this yields an upper limit value of $b = 0.85$ nm, for PSS of $b = 0.78$ nm. The Bjerrum length in water at 291 K is 0.72 nm, so that one obtains as lower limits: ξ(PDADMAC) $= 0.85$ and ξ(PSS) $= 0.92$. In water, the Manning parameter for fully extended chains of PDADMAC and PSS is thus above the critical value of condensation for multivalent probe ions ($|Z_i|^{-1} = \frac{1}{2}$ and $\frac{1}{3}$, respectively), whereas it is close to, but below the critical value for monovalent counterions. In

practice, the chains may not be fully extended and effective ξ values may be larger. Numerical calculations of the distribution equilibrium of bound and free monovalent counterions around a cylindrical macroion were carried out following a simple two-state model (eq. 1.20.a, b in Section 1.2.2). Again assuming fully extended chains, such calculations suggest that for PDADMAC in the whole concentration range studied the fraction of apparently unbound monovalent counterions is between 20 % and 30 %, for PSS ca. 35 %.

An important parameter in most theoretical considerations and simulations of polyelectrolyte systems is the charge density on the polymer as well as on the small counterions.[1,2] Due to the high degree of dissociation, the chosen polyelectrolytes can be considered as having a high (positive or negative) charge density along their chain backbone.

A closer look at the spin probes

All materials used as spin probes are soluble in water up to relatively large concentrations but in small amounts they also dissolve in polar organic solvents. Except for this, the spin probes are very different in size, molecular structure, and foremost in their charge and magnetic (EPR) properties.

The two transition metal cations - manganese and oxovanadyl radicals - are octahedrally coordinated by six water (Mn^{2+}) or distorted octahedrally coordinated by additional five water molecules (VO^{2+}). They best resemble those theoretical point-like, multivalent ions with a high charge density that are assumed in computer simulations. Furthermore, many studies that probe conformational changes of polyelectrolytes induced by multivalent ions in solution use Mg^{2+} or other alkaline earth metals. The used manganese and oxovanadyl ions are good representatives for these spherical species with high charge density, too. Note that, due to its similar radius, Mn^{2+} can replace Mg^{2+} in many biological systems without changes in the functionality of the system.[86] CW EPR spectra of the oxovanadyl ion (electron configuration d^1, $S=\frac{1}{2}$) are made up of eight lines stemming from the hyperfine interaction of the single electron spin with the I=7/2 nuclear spin of vanadium.[87,88] As the oxovanadyl ion in the oxidation state IV is only stable in a narrow pH-regime (1< pH <3), HCl was added to attain this pH in the final solution. This complication is not significant, though, as it simply adds monovalent ions to the ionic strength of all solutions containing this spin probe. The full CW EPR spectrum of the manganese ion (electron configuration *high spin d^5*) consists of 36 lines due to hyperfine coupling of the S=5/2 electron spin to the I=5/2 manganese nuclear spin. However, only six lines are sufficiently narrow for detection.[89] These lines are still very broad ($\Delta B_{pp} \approx 25$ G) at conventional X-band frequencies (~9.4 GHz), which may hide possible spectral effects arising from polyelectrolyte-Mn^{2+} interaction. This is due to relaxation induced by zero field splitting as described in Section 2.1 and can be overcome by high-field/high-frequency EPR measurements at W-band (~94 GHz).

In this work, all Mn(II) spectra are measured at W-band, which reduces peak-to peak linewidths to $\Delta B_{pp} \approx 9G$.

The TAM spin probe is trivalent, much larger than the transition metal ions, and tristar-shaped with a large separation of the ionic groups (~1.1 nm from geometry optimized structure in MMFF94 force field). Hence, the charge density distribution on this molecule should rather be similar to that of three rigidly connected monoions (carboxylates). In this radical, which was originally designed and synthesized as an *in vivo* agent for EPR imaging, the electron is centered on the sp^2-hybridized central carbon atom and - with the exception of ^{13}C and ^{33}S satellite peaks and very weak coupling to remote ^1H nuclei on the side chains - does not show resolved hyperfine coupling to nuclear spins.[90,91] Therefore, the FT (or CW) EPR spectrum in solution only consists of one narrow, nearly Lorentzian line, which is quite sensitive to the solvent and parameters such as oxygen content. Due to lack of significant anisotropy of the *g*- and hyperfine tensors in low-viscosity solvents, there is no systematic dynamic information available from the CW or FT EPR spectra of TAM probe ions.

CAT 1 is the only monovalent spin probe employed in this work. It belongs to the well-known class of TEMPO (2,2,6,6-tetramethylpiperidine-1-oxyl) radicals that are often used for spin probing (as in this work) or spin labeling studies.[92] The CW EPR spectrum in solution of such nitroxide-based radicals comprises three lines from the hyperfine interaction of the unpaired electron ($S=1/2$) with the ^{14}N nuclear spin ($I=1$). Mainly due to unresolved or only partially resolved hyperfine interaction with the twelve hydrogen atoms ($I=1/2$) on the four methyl groups, the lines have widths much larger than the actual intrinsic linewidth, which is only dependent on the electron transverse relaxation time. As explained in Section 2.3, the lineshape is also changed to non-Lorentzian because of these unresolved hyperfine lines.

Most of the results reported here have been achieved by using the radical Fremy's salt dianion (FS) with cationic PDADMAC polyelectrolyte. Like all nitroxide radicals it exhibits a three-line CW EPR spectrum but it is well suited for the use as spin-carrying counterion as it is divalent, small and has very narrow lines, since there is no hyperfine coupling to intramolecular protons (see Section 2.3). In addition, the three FS lines are almost purely Lorentzian-like in shape except for a small deviation due to electrostatic repulsion between the like-charged FS ions.[50,93] The narrow and Lorentzian lines have made FS a spin probe that has been used extensively in studies of rotational motion in CW EPR spectra.[94] The spectroscopic advantages of FS come at the cost of reduced stability in solution. FS is stable in aqueous solution at ambient temperatures and basic pH for several days, whereas TEMPO radicals may well be stable for several years and over a broader pH-range. Because of the fast reduction of FS at neutral and acidic pH values, in all experiments with FS as spin probe the pH has been adjusted to a final value of ~10-12 by addition of KOH, which - as described for the oxovanadyl ion before - only increases the ionic strength in *all* solutions of a series of measurements.

3.1.2   Variation of solvents

As mentioned before, the use of solvents for FS/RuCP mixtures will be explained in detail in the following Section 3.2. EPR measurements of FS/PDADMAC were carried out in four different solvent

systems: deionized Milli-Q-water, ethanol/water (1:1 in volume), N-methylpropionamide/water (NMPA, 2.3:1 in volume), and glycerol/water (2:1 in weight). All solvent systems and their properties are summarized in Table 3.1 and the technical specifications are described in the Appendix A1.

Table 3.1. Investigated solvent systems and their properties. All data are given for T=293K. Viscosities were measured relative to water. The given densities and relative permittivities are mean-field approximations that are calculated from the static relative permittivities of the individual components as explained in the text.

solvent system	composition	density ρ [g/cm^3]	rel. viscosity	rel. permittivity ε_r
water	1	1.000	1.000	80
ethanol/water	1:1	0.895	2.627	~50
NMPA/water	2.3:1	0.951		~140
glycerol/water	2:1	1.170	13.630	~57

The density ρ as well as the relative permittivity ε_r are calculated from the respective values of the individual components. When estimating averaged values for permittivity one should keep in mind that this dielectric property is a function of the solvent-solvent interaction. Assuming that the liquid mixtures are fully homogeneous one may approximate the effective relative permittivity by a simple linear superposition of the values of each component weighted by their weight proportion.[95] Such approximate values are reported in Table 3.1.

Besides pure water two other low viscosity solvent mixtures, ethanol/water with lower and NMPA/water with higher permittivity are used. Use of glycerol/water with a dielectric permittivity lower than that of water allows for experiments in a high-viscosity solvent mixture.

In these solvent mixtures all materials fully dissolve. The solvent variation is performed to study the effect that changing the dielectric properties has on i) polyelectrolyte backbone-solvent interaction with consequences on chain conformation as explained in Chapter 1.2, ii) polyelectrolyte charge dissociation, and iii) spin probe-solvent interaction.

By using glycerol/water mixtures one increases macroscopic viscosity by a factor of five (as compared to ethanol/water or NMPA/water) to thirteen (as compared to water), so that molecular rotational and translational motion is also slowed down. For charged spin probes whose CW EPR spectra are sensitive to rotational reorientation, such as FS, this allows for yet another variation in the investigated systems and delivers additional information on the *whole* system including polyelectrolyte. Glycerol/water mixtures are also advantageous for the study of shock-frozen solution at *T*=80 K by pulse EPR methods. In frozen purely aqueous solution effects like local crystallization complicate data interpretation, a problem that is largely avoided in the glass-forming solvent system that includes glycerol.

Polyelectrolyte systems containing the spin probe TAM were investigated in water and glycerol/water, whereas those systems containing transition metal ions were only studied in water.

3.2   Electrostatic attachment of spin probes to a model rigid-rod polyelectrolyte

Before presenting the systematic study of conventional polyelectrolytes, investigations of electrostatic effects in the system containing the coordination polymer RuCP and FS spin probes are presented. Two experiments were applied to investigate this system. First, double electron-electron resonance (DEER, see Section 2.6.3) measurements of the respective frozen solutions (T=80 K or 20 K) were carried out to probe local FS concentrations and distance distributions. Second, conventional CW EPR (see Section 2.3) was applied to probe the room temperature rotational dynamics of FS in the mixture with oppositely charged RuCP polymer.

3.2.1   Localized electrostatic attachment of FS to cationic Ru-centers

The main difficulty that was encountered in the preparation of samples of this system was the poor solubility of RuCP in aqueous solutions on the one hand and the poor solubility of FS in RuCP-solutions in DMF on the other hand. Several solutions containing DMF and glycerol/water in different compositions were tested for their ability to dissolve both RuCP and FS. All these mixtures contained polymer and spin probe of equal nominal (monomer) concentration, c=0.5 mM, and for reasons mentioned above the pH was adjusted to ~9.5. In compositions of more than 70% DMF in volume, apparently homogeneous solutions of RuCP and FS were achieved, but DEER measurements showed no deviation of DEER time traces from an exponential decay, which is what is expected for a homogeneous three-dimensional distribution of FS spin probes. The DEER time trace for solutions containing 50 vol.% DMF and 50 vol.% glycerol/water (1:1 in vol.) is presented in Figure 3.1.a, c. For this combination of solvents, shortly (i.e., a few minutes) after addition of glycerol/water to the DMF solution one could observe precipitation of solid from the dark red solution. Separation of the precipitate (apparently RuCP) by use of a centrifuge gave a clear light red solution, which was subsequently used for the EPR measurements. The time trace in Figure 3.1.a was recorded in frozen solution at a temperature of T=80K, whereas the time-domain data in 3.1.c were acquired at T=20K. The latter measurement at lower temperature was necessary in order to obtain data with dipolar evolution times up to t=2.5μs, i.e. to probe the long-time behavior of the DEER signal, which reflects the possible longer distances in the spin probe distance distribution. With decreasing temperature the transverse relaxation time is increased, which allows for a refocused echo at longer evolution times and also the Boltzmann population difference of initial and excited electron spin states become more favorable.[16,39]

Both time traces clearly *cannot* be simulated by a single exponential decay function, as would be expected if the FS dianions were distributed homogeneously throughout the sample. The simulation shown in red in Figure 3.1.a is an exponential decay that is modulated by oscillations at two frequencies, which correspond to a bimodal distance distribution that is on display in Figure 3.1.b. The distance distribution has maxima of the Gaussian distance peaks of ~2.4 nm and ~4.4 nm.
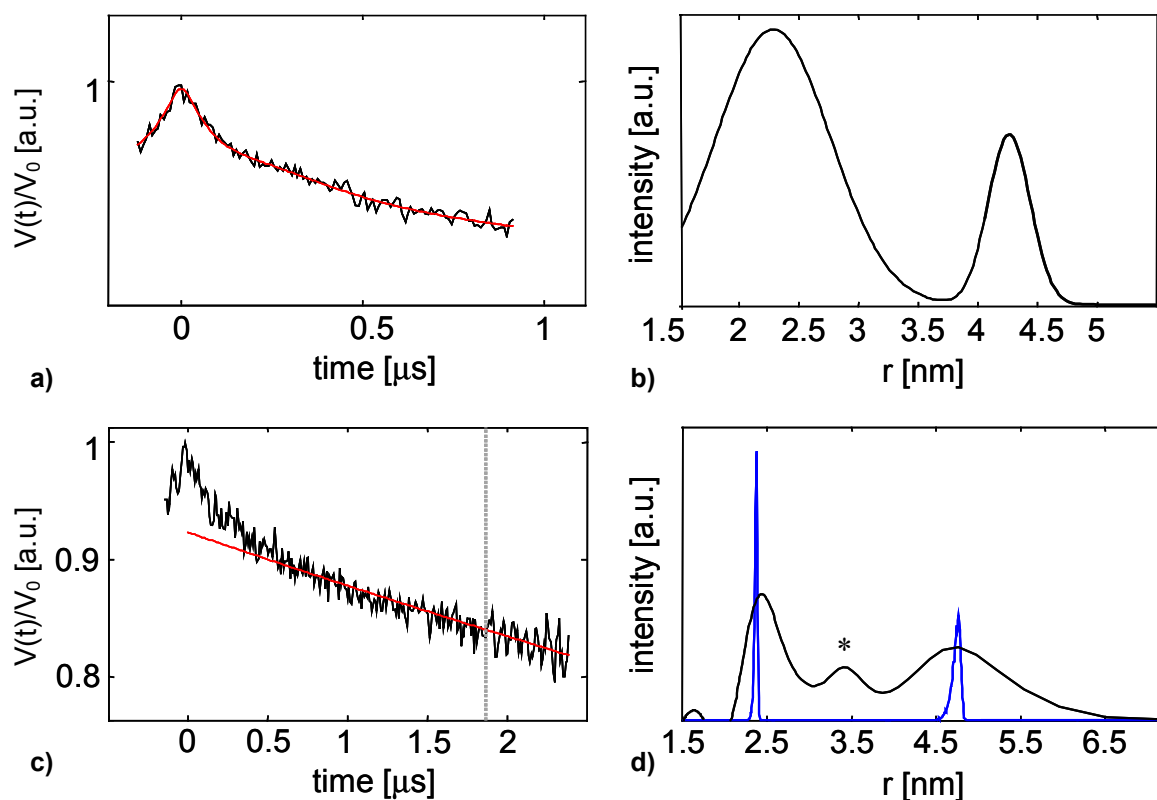
Figure 3.1. DEER time-domain data (a,c) and extracted distance distributions (b,d) of FS in solutions of RuCP in 50 vol.% DMF/50 vol.% glycerol/water. The time trace in a) was recorded at *T*=80K and the distance distribution shown in b) corresponds to the simulation overlaid in red in a). Time domain data of c) were taken at *T*=20K and the red line is an exponential fit to the data between 1.9 and 2.4 μs (marked by the gray dotted line). The broad distance distribution (solid black line) shown in d) is obtained by integral transformation as explained in the text (see section 2.4.3), the overlaid blue line is a Ru-Ru distance distribution obtained from an MD simulation as explained in the text (the amplitude is scaled by a factor of 0.1 for comparability with the experimental distribution). The asterisk in d) marks a noise artefact.

Figure 3.1.c and d show time domain data for longer dipolar evolution times and their analysis by a direct integral transformation according to Reference 77 that has also been described in brief in Section 2.6.3. This method of data analysis of the modulations is inherently *model-free*, yet it largely reproduces the bimodal distance distribution and yields approximate Gaussian distance peaks at 2.4 nm and 4.7 nm. The latter value is more reliable than the fitted value of 4.4 nm from the experiment with a maximum evolution time of 1μs. This is due to the fact that, according to eq. 2.66 (Section 2.6.3), FS electron spins that are irradiated with the second microwave frequency at this distance modulate the refocused echo decay of the observed spin probes with a frequency of ~0.5 MHz, so that the first full period of this oscillation is completed after ~2μs. I consider the peak that appears at ~3.5 nm in Figure 3.1.d (asterisk) to be an artifact due to incomplete averaging of experimental noise - in the short time domain data of Figure 3.1.a,c with better signal-to-noise ratio, no such distance is observed. The reason for the rather large remaining noise and shallow modulation depth might be that a fraction of RuCP polymer is lost from the solution (precipitation!), so that the nominal ratio of FS/Ru is larger than unity, effectively reducing the modulation depth by a larger contribution from the exponential background decay.
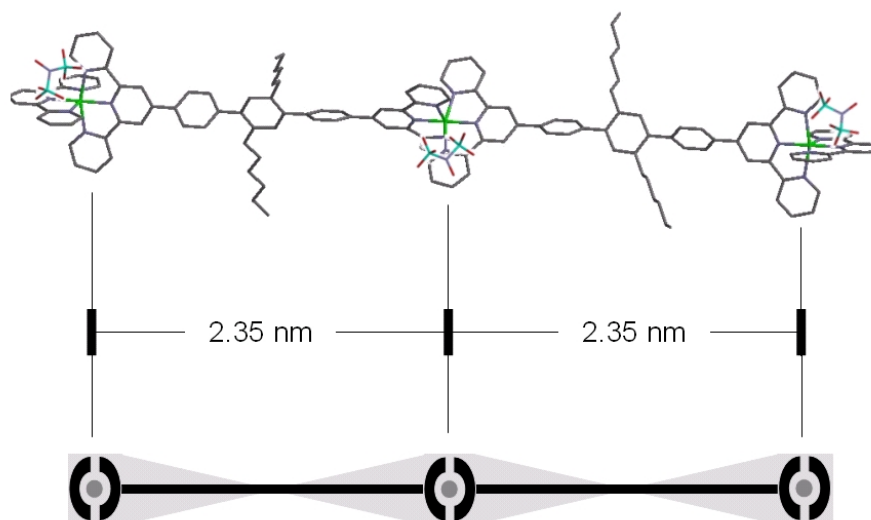
Figure 3.2. Sketch of possible localized binding of FS ions to Ru-centers in RuCP. **Upper part:** An excerpt from the RuCP chain that has been geometry-optimized by force-field calculations (UFF 1.02) as explained in the text. The distinct distances between FS found from DEER data analysis (~2.4 nm and ~4.7 nm) agree very well with the distances between Ru-centers separated by one or two organic spacers, respectively.
Lower part: Schematic plot of most probable attachment sites for FS ions (gray area). The relatively broad distribution of spin probe distances can be explained if one accounts for the degrees of freedom of the electrostatic attachment.

Nonetheless, both methods of data analysis prove that for the major fraction of FS ions in frozen solution of this specific composition there are two distinct distances. Remarkably, these two distances correspond rather nicely to the distances between Ru-centers of RuCP that are separated by one (~2.4 nm) or two (~4.7 nm) spacers. The geometry-optimized excerpt from a RuCP chain that is shown in the upper part of Figure 3.2 was also used for Molecular Dynamics (MD) simulations that were also carried out in the program package Cerius2 (v.3.8, Molecular Simulations, Inc.). The system was first pre-equilibrated (canonical ensemble in a Berendsen temperature bath, 20 000 steps, time step $0.5*10^{-15}$s) and then sampled by a 2 ns run with the same time step (Nosé-Hoover thermostat, $4*10^6$ steps, time step $0.5*10^{-15}$s). The respective distance distribution is also shown in Figure 3.1.d (blue solid line). This Ru-Ru-distance distribution is much narrower than the extracted FS-FS distribution, but the maxima in the distribution (2.35 nm and 4.7 nm) are almost identical to those obtained from direct DEER transformation. This is clear evidence that the FS dianions and the regularly spaced dication Ru-centers of RuCP form pairs, i.e. that the divalent FS counterions are electrostatically attached to the charges on the coordination polyelectrolyte. In the simple picture of (spherically symmetric) Coulomb interaction this pairing is favored as it leads to a twofold increase in electrostatic interaction energy as compared to the interaction with original counterions PF_6^- and K^+, respectively. Additionally, in the simple picture of Manning theory the replacement of monovalent counterions by divalent counterions is favored by the gain in entropy for the system as a whole. Assuming a fully stretched conformation, one would expect distances of 2.35 (the average of 2.32 and 2.38) nm, 4.7 nm and – if experimentally detectable – 7.05 nm between FS ions that are localized at

the RuCP charge centers. Due to too short relaxation times of the refocused echo even at temperatures of 20 K, it was not possible to obtain time traces long enough to observe those very slow oscillations (frequency ~0.15 MHz) that are caused by FS ions of a distance of ~ 7 nm. One would have to optimize experimental conditions by e.g. using fully deuterated solvents[75] such that time traces until at least t=6μs can be obtained. Detection of such a slow oscillation could then reveal the existence of FS spin probes attached to Ru-centers that are separated by two intermediate repeat units of RuCP.

The relatively large width of the distance distribution peaks (full width at half maximum, FWHM, for the 2.4 nm peak ≈ 0.5 nm, for the 4.7 nm peak ≈ 1 nm) can be attributed to the electrostatic nature of the localized counterion attachment. The upper part of Figure 3.2 shows that if one assumes octahedral symmetry around a Ru-center there are at least four equal positions of closest contact for FS counterions. The lower part of Figure 3.2 gives a schematic plot of the volume around RuCP polymer, in which FS ions are most likely to reside. Approximations taken from force-field calculations suggest side lengths for the (hypothetical) square "box" that stands for the attachment volume around the Ru^{2+}-site of ~0.6 nm. This value approximates the dimensions of the volume, in which FS ions can access the oppositely charged Ru-ions. The existence of such an attachment volume effectively adds a degree of freedom to the electrostatic attachment of FS to Ru^{2+}, which results in a broader distribution of distances between attached spin probes. This additional degree of freedom has a square root dependence on the number of spacers in between the Ru-centers, so that the distance distribution between next-neighbors is affected stronger than that of direct neighbors, which may explain the observed increase in width of the FS distance peak when going from 2.4 to 4.7 nm. The electrostatic origin of the FS distance distribution also accounts for the fact that FS distance peaks are Gaussian-like and not asymmetric (only distances shorter than the expected ones, see 3.1.d). The asymmetry observed in the MD results reflects that upon bending of an ideal rigid-rod, the maximum distance must be that of full linear extension, which is at the same time the most likely distance. This geometric constraint of course does not apply to electrostatic attachment.
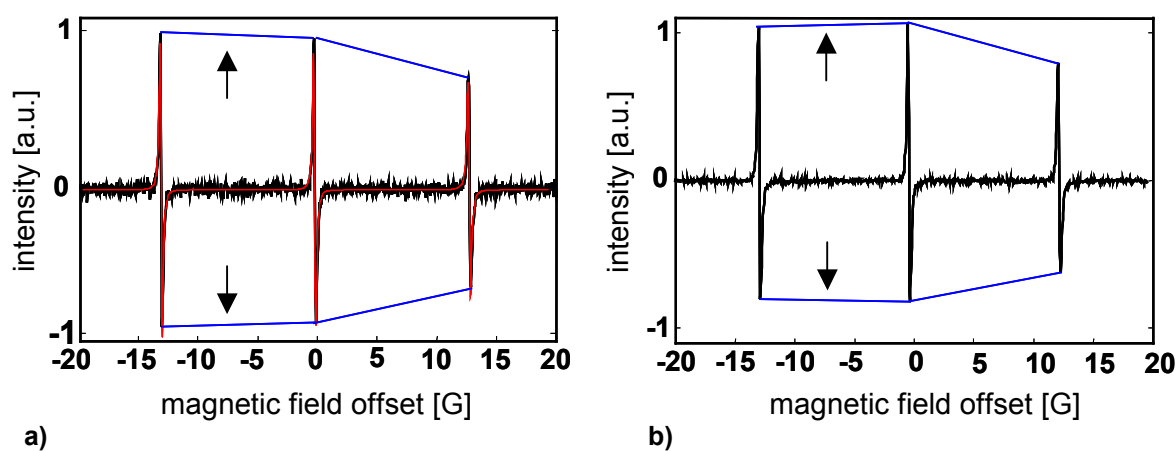
Figure 3.3. CW EPR spectra (X-band, ~9.8 GHz) at room temperature of **a)** 0.5 mM FS + 0.5 mM RuCP (monomeric units) in 50 vol.% DMF/50 vol.% glycerol/water (1:1); **b)** 0.5 mM FS in 50 vol.% DMF/50 vol.% glycerol/water (1:1); A spectral simulation of FS/RuCP according to the rotational diffusion tensor explained in the text is shown in red. The blue lines connect the peaks of the measured spectra and are meant as guides to the eye. Arrows point to the difference in relative line intensities between the two cases.

3.2.2   Local attachment geometry and *dynamic electrostatic attachment (DEA)*

In order to probe the dynamics of the observed attachment process (see Section 2.3), CW EPR was performed on liquid solutions of the same samples and the spectrum is put on display in Figure 3.3.a (black solid line). Figure 3.3.b shows the CW EPR spectrum of FS in the same solvent system without RuCP (black solid line). Comparison of the two spectra shows that the main difference lies in a change in the relative amplitudes of the three hyperfine lines upon addition of RuCP. In Figure 3.3, blue guiding lines connect the maxima and minima of the lines to make this change better recognizable. In Section 2.2 it has been explained that linewidths and relative amplitudes of the different hyperfine manifolds reflect the rotational diffusion of the spin probe molecule. In spectra of pure FS, the center-field line is the narrowest and has the highest relative amplitude, followed by the low-field manifold and the high-field manifold. This pattern is also observed for pure FS in all other solvents (see next section). In the spectrum with RuCP added (1:1 Ru^{2+}:FS^{2-}), the low-field line is the narrowest and most intense, the center-field line is slightly *less* intense and the high field line is significantly further decreased in intensity. This indicates that rotational diffusion is significantly altered by the presence of the coordination polyelectrolyte. In order to qualitatively and quantitatively understand the change in rotational dynamics upon addition of RuCP, the simulation program by Schneider and Freed (see Section 2.3 and Ref. 51) is used, which can take into account the effect of anisotropies in the rotational diffusion tensor for simulations of CW EPR spectra. For simplicity, axial symmetry of the diffusion tensor was assumed.

The best simulation for free FS ions in pure solvent can reproduce the lineshape pattern very well - except for the slight phase distortion of the experimental spectrum - (simulation not shown in Figure 3.3.b) and the unique axis of the tensor of rotational diffusion that has been used in the simulation is visualized in Figure 3.4. The simulation of FS/RuCP is shown in Figure 3.3.a (red line). Again, except for the slight error due to imperfect
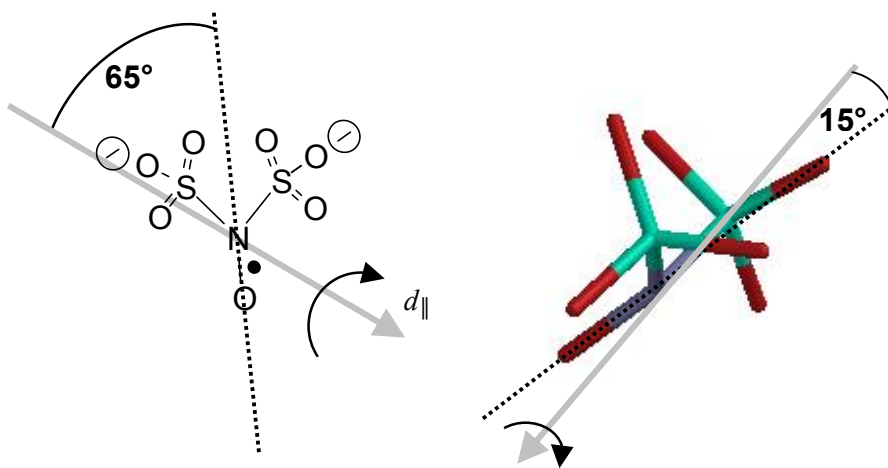

Figure 3.4. Visualization of the rotational diffusion tensor for FS in the solvent system 50 vol.% DMF/50 vol.% glycerol/water (1:1); the gray arrow illustrates the principal axis of fast rotation of FS (65° from the NO-bond axis, see projection on the right and 15° out of plane of the plane ONS(2)). The respective tensor elements of rotational diffusion are: $d_\parallel$=30*10^9 s^{-1} (parallel to unique axis in gray), $d_\perp$=5 *10^9 s^{-1} (perpendicular to gray axis).
In this case, the axis of fast rotation points towards one of the charged sulfonate groups, probably because the whole FS molecule rotates around an electrostatic bond with one counterion (K^+).

phasing, the simulation nicely reproduces the CW EPR spectrum. The only difference as compared to the simulation of pure FS is the direction of the unique axis of the rotational diffusion tensor, which is sketched in Figure 3.5. All other simulation parameters for both simulations were identical. Values for the *g*- and hyperfine tensors were taken from simulations of CW EPR spectra of FS in the rigid limit in that solvent system (not shown) and are as follows:

> *g*-tensor: g_{xx}=2.0086, g_{yy}=2.0064, g_{zz}=2.0029;
>
> hyperfine-tensor: A_{xx}=A_{yy}=5.2 G, A_{zz}=28.45 G;
>
> additional linewidth=0.046 G;
>
> rotational diffusion rates: $d_{\parallel}$=30*10^9 s^{-1}, $d_{\perp}$=5*10^9 s^{-1}

Remarkably, rotational diffusion of the FS dianion in the pure solvent is already slightly, but signifcantly anisotropic, although the molecule is rather small. The fact that rotation about the axis pointing to one sulfonate group is six times faster than rotation perpendicular to this axis (sketches in Figure 3.4) could be explained by assuming that a dynamic contact ion pair between one of the sulfonate groups and one of their counterions (K$^+$) is formed. On the timescale of the rotational correlation time, the interaction of - on average - one sulfonate group with small, monovalent cations is non-negligible. This interaction causes a dynamic electrostatic attachment-detachment process between sulfonate groups and potassium ions and could impose a geometric constraint on the system such that rotation perpendicular to the ion pair axis is slowed down – the whole system of FS and potassium counterion would have to rotate. At the same time, rotation parallel to the nitrogen-sulfur bond in FS is less affected by such ion pairing. These conclusions can also be reconciled with the simple statistical picture supplied by the Debye-Hückel approximation. Assuming full (macroscopic)

dissociation of K$_2$FS into 2K$^+$ + FS^{2-}, there will - in the time-average - be at least two potassium ions close to the two sulfonate groups. On the timescale observable by CW EPR this of course does not mean that one of the sulfonate groups is permanently neutralized by a counterion, while the other is not compensated. Because of the symmetry of the FS molecule, both sulfonate groups should be equivalent. Thus it seems more likely that there is also a detachment of one close ion pair and reattachment (not necessarily
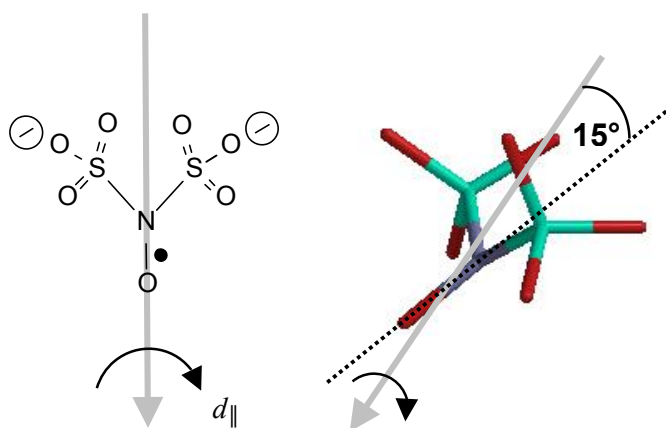
Figure 3.5. Visualization of the rotational diffusion tensor for FS with oppositely charged RuCP in the solvent system 50 vol.% DMF/50 vol.% glycerol/water (1:1); the gray arrow illustrates the principal axis of fast rotation of FS (15° tilted away from the NO-bond axis, in the plane spanned by S(1)NS(2)). The respective tensor elements of rotational diffusion are: $d_{\parallel}$=30*10^9 s^{-1} (parallel to unique axis in gray), $d_{\perp}$=5 *10^9 s^{-1} (perpendicular to gray axis). In this case, the axis of fast rotation points along a bisecting line of the two charged sulfonate groups, which is suggestive of attachment to an ion along this direction.

of the same potassium ion) at the other sulfonate group. The maximum lifetime of such individual ion pairs can also be deduced to be less than 10^{-9} s, as otherwise significant contributions of slowed down FS ions would yield bimodal CW EPR spectra. On the timescale of one rotation (τ_c) one sulfonate group could hence be closer to a cation, while on sufficiently long timescales (as in the Debye-Hückel approximation) the time-averaged cation distance is the same for both sulfonate groups.

In solution of the rigid-rodlike coordination polymer RuCP, rotational diffusion preferably takes place about an axis bisecting the angle between both sulfonate groups (see Figure 3.5). This is clear evidence of the Ru^{2+}-centers influencing rotation of FS - and in combination with the proof of direct electrostatic attachment of FS to Ru^{2+} one can safely assume that the local geometry of attached state of FS looks as suggested in Figure 3.5. Unlike monovalent potassium ions, the divalent Ru-ion seems to interact with both FS sulfonate groups simultaneously: as described before this is favorable energetically and entropically. The lifetime of each individual "three-center ionic assembly", though, must be in the same order of magnitude as the ion pairs formed with monovalent ions, as otherwise one would observe contributions of much slower FS ions in a bimodal (attached and detached) CW EPR spectrum, which is clearly not the case. In addition, the experimental EPR spectra with and without RuCP can be simulated very well with identical parameters except for the direction of the unique axis of the rotational diffusion tensor. Even the magnitudes of the rotational diffusion tensor elements are the same, which suggests that there is no significant impact on the local viscosity for the FS molecules and that only the local geometry of electrostatic interaction is changed.

Hence, the distance distribution that has been obtained from DEER measurements gives an actual "snapshot" of the attached states of FS ions. One can then construct the full picture of the electrostatic interaction between regularly spaced, divalent Ru-centers and divalent spin carrying counterions:

i.   Although the charge density along the RuCP chains is not very high, on average FS ions are close to charges of RuCP.

ii. FS-ions are attached to RuCP by forming "three-center ionic assemblies" with Ru^{2+}-ions with lifetimes $33*10^{-12}$ s $< t < 1000*10^{-12}$ s. FS spin probe overall motion alternates between attachment and detachment periods. This process will henceforth be called *dynamic electrostatic attachment* in order to emphasize the transient nature of this attachment in liquid solution.

iii. In the solvent mixture used in the experiments a large fraction of FS spin probes seems to be attached at any time.

iv. In these attached states one Ru^{2+}-ion interact with both sulfonate groups of FS simultaneously.

Applying two experimental techniques, CW EPR and DEER, to a system of divalent spin carrying counterions and oppositely charged, rod-like coordination polymer the electrostatic self-assembly of this polyelectrolyte-counterion system could successfully be characterized. Electrostatic self-assembly is a transient process and leads to specifically site-bound spin probe counterions.

With these concepts gained from analysis of the model system, it is now the aim to elucidate electrostatic interactions in systems containing long, flexible, highly charged polyelectrolytes and spin probes as tracers for counterions.

3.3   Electrostatic attachment of spin probes to flexible polyelectrolytes in solution

According to the basic theory of polyelectrolyte-counterion interaction introduced by Manning,[31,32] (see Section 1.2.2) attachment of multivalent counterions to the polyelectrolyte backbone should be preferred to attachment of monovalent counterions for reasons of maximizing the entropy of the complete system. This is also in agreement with the findings from the preceding section. It has been pointed out that a given counterion is not permanently attached (*"condensed"*) to a specific backbone charge in fluid solution, at least for divalent centers. The somewhat misleading term *electrostatic* or *counterion condensation* is established for this kind of attachment, but in the last section the term *dynamic electrostatic attachment* (DEA) has been used to emphasize the transient nature of the attachment. This section expands the conception of DEA from the model rod-like coordination polyelectrolyte to conventional, highly charged polyelectrolytes. For these systems, two major polymer properties change in comparison to RuCP: very high charge densities along the chain and the possibility of chain conformational changes. This means that on the one hand there is much more information available on the self-assembly of such polyelectrolytes and small ions, which is responsible for many of the intriguing polyelectrolyte properties. On the other hand, these additional factors are likely to complicate the analysis of EPR data immensely. In the remainder of this chapter, results from EPR methods as diverse as CW EPR, Fourier transform (FT) EPR, Electron-spin-echo (ESE)-detected EPR, DEER and electron-spin-echo-envelope-modulation (ESEEM) are presented. Much emphasis is put on methods for analyzing the obtained data. Analysis of these systems is carried beyond that of the model system RuCP and includes characterization of spin-carrying counterions in terms of local concentration and radial distribution function, and interaction of counterion electron spin and magnetic nuclei on the polyelectrolyte. Moreover, the effect that electrostatic attachment of counterions has on polymer conformation will also be considered.

Unlike in the case of RuCP, addition of oppositely charged PDADMAC polyelectrolyte to solutions of multivalent spin probes in pure solvent causes a marked increase in the peak-to-peak linewidths, broadening in the wings of the spectral lines and changes in the spectral lineshape, but the principal pattern of relative amplitudes remains the same as in the systems without PDADMAC. The first of these observations indicates a stronger polyelectrolyte-counterion interaction for PDADMAC, as might have been expected due to the higher charge densities of the repeat units and the polyelectrolyte chain. The series of CW EPR (X-band, ~9.4 GHz) measurements of spin probe FS in water/PDADMAC is shown in Figure 3.6, whereas in Figure 3.7 details of FS spectra *without* PDADMAC, with 139 mM (*R*=0.0036) PDADMAC, and with 11 mM (*R*=0.0455) added PDADMAC

are shown. In addition, the spectra of the complete series of measurements in the glycerol/water mixture can be found in Appendix A3. To exclude effects other than electrostatic ones as the reason for the observed changes in the spectra, reference samples were measured of the *neutral* spin probe 4-oxo-2,2,6,6-tetramethylpiperidine-1-oxyl with cationic and anionic polyelectrolyte, the cationic spin probe 4-trimethylammonium-2,2,6,6-tetramethylpiperidine-1-oxyl with the cationic polyelectrolyte PDADMAC, and FS with the anionic polyelectrolyte PSS for such concentration ratios where maximum line broadening was observable for the systems under investigation. No line broadening could be detected in any of the reference systems (spectra not shown). Hence, the change in macroscopic viscosity on adding the polyelectrolyte cannot be held responsible for the observed drastic spectral changes. In fact, no impact of viscosity in the low viscosity solvents was found even for those samples containing the highest amounts of polyelectrolyte. This is conclusive evidence that dynamic electrostatic attachment is the main cause of the observed spectral changes.
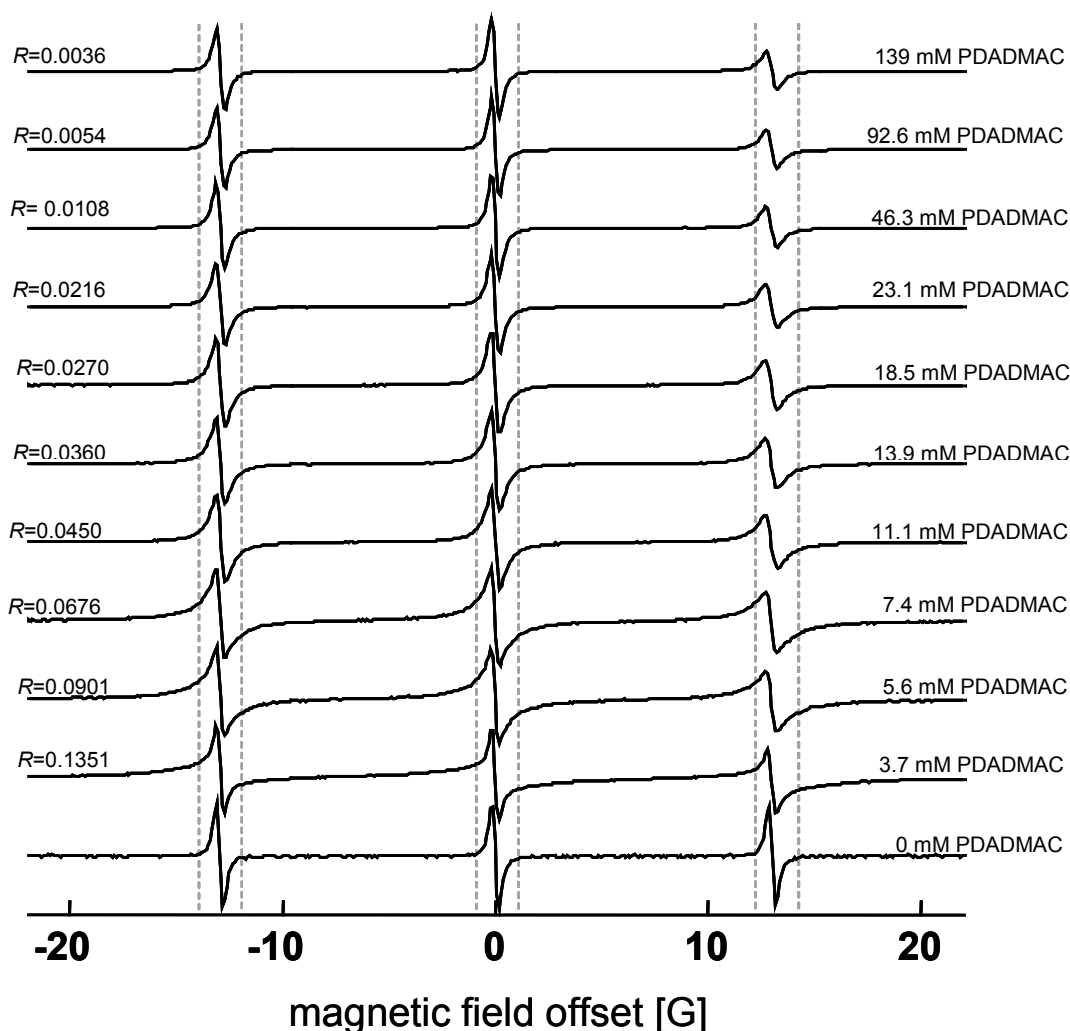

Figure 3.6. Complete set of CW EPR spectra at X-band of FS + PDADMAC in water. The concentration of PDADMAC (in monomeric charged units) is varied and given on the left hand side above each spectrum. The respective ratios of c(FS)/c(PDADMAC) are given on the left hand side.
The three pairs of gray dashed lines mark the magnetic field position at which the lines in the FS spectrum without PDADMAC have already reached baseline level. It is apparent that most prominently at high *R*-values (low PDADMAC concentration) the three EPR lines have significantly broader flanks. At low *R*-values (high PDADMAC concentration) this broadening is diminished again.

3.3.1   Dynamic electrostatic attachment – from site binding to territorial binding of counterions

From the FS spectra in Figures 3.6, 3.7 and in Appendix A3 it is apparent that there is no change in the principle spectral composition upon addition of PDADMAC polyelectrolyte. All spectra still show the three-line pattern expected for spin probes in the fast motion limit (see Section 2.3). It is well known that for a spin probe rotational correlation (reorientation) time longer than approximately 10^{-9} s, CW EPR spectra become much more complex in shape,[16] and for rotational correlation times longer than $\sim 10^{-6}$ s one expects a powder-pattern-like spectrum. This allows for the safe conclusion that, like in systems containing model polyelectrolyte RuCP, the attached FS state has a lifetime on the *sub-nanosecond timescale*, as otherwise bimodal spectra (having a fast and a slowly rotating component) would be expected, which are not observed. Spin probes in the attached state must be in some equilibrium with detached spin probes and exchange between the two states must proceed at a rate significantly faster than 10^9 s^{-1}. A detailed characterization of the local geometry of the attached state for FS probe molecules and the equilibrium with the detached state is presented in the following paragraphs.
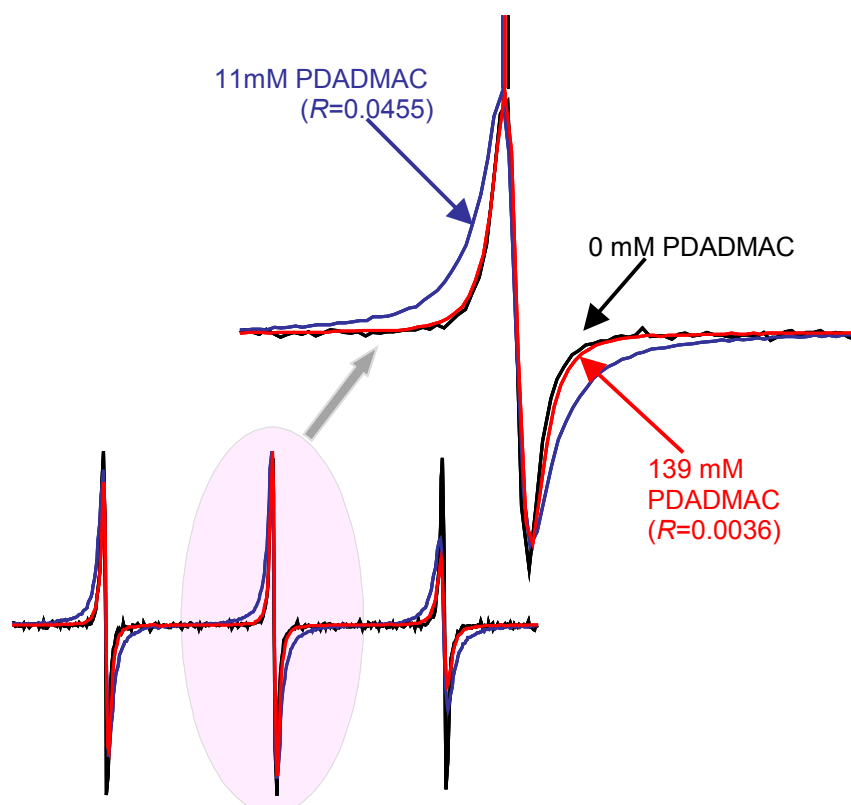
Figure 3.7. Plots of CW EPR spectra (X-band) of FS in water.
Black line: FS without PDADMAC; red line: FS +139 mM PDADMAC (R=0.0036); blue line: FS +11 mM PDADMAC (R=0.0455);
The magnified plot of the central EPR line shows increase of the peak-to-peak linewidths with increasing R-value (marked with the three vertical lines above the detail plot of the central line) and the drastic increase of broadening in the wings of the spectra with increasing R. Also note the change in relative amplitudes of the three lines.

As for FS in solutions of RuCP, the spectral simulation program by Schneider and Freed[51] was used to provide initial approximate fits for the relative intensities of the three lines of the nitroxide spectrum assuming an intrinsic linewidth as observed in the absence of polyelectrolyte in the four solvents described before. In all solvents, the basic pattern of line amplitudes of FS without polyelectrolyte is retained, although the differences in amplitudes increase drastically: the center line is the most intense, followed by low-field line and the high-field line (see Figure 3.7). Evidently, the high-field line is affected most strongly by addition of PDADMAC, which is well-known to be indicative of a slowdown in rotational dynamics.[16] In contrast to the spectra of FS and RuCP, there is immense additional broadening, in particular in the flanks of the spectra. Therefore, the simulated spectra could not reproduce the broadening in the spectra, so that these rough preliminary fits (absorption spectra) were then Fourier transformed to give the time-domain data $V_{sim}(t)$, and multiplied with an empirical broadening function (stretched exponential function) to account for broadening:

$$V(t) = V_{Sim}(t) \cdot \exp\left[-j \cdot t\right]^x, \tag{3.1}$$

where j is a characteristic decay time constant and x is the stretch factor characterizing the width of the distribution of decay times. After inverse Fourier transformation and pseudomodulation[67] a derivative-mode spectrum was obtained. This additional broadening affects the narrower low-field and center-field lines more strongly than the high-field line that is already significantly broadened by slowed down rotational diffusion. The stretched exponential broadening function accounts for the distribution of relaxation time constants and use of this empirical broadening function is justified in the next section, when the broadening is quantified.

From Figure 3.8 it can be understood that multiplication of the initial spectral simulations (accounting for the dynamics) with the stretched exponential function in eq. 3.1 reproduces lineshapes to satisfactory precision, so that the information of dynamics derived from this analysis is reliable. CW EPR spectra in the full *R*-range and in fluid solutions of all four solvents have been examined by this method, but only one spectrum and simulation are shown as an example: the sample of *R*=0.011 (46 mM PDADMAC) in NMPA/water as solvent. While the
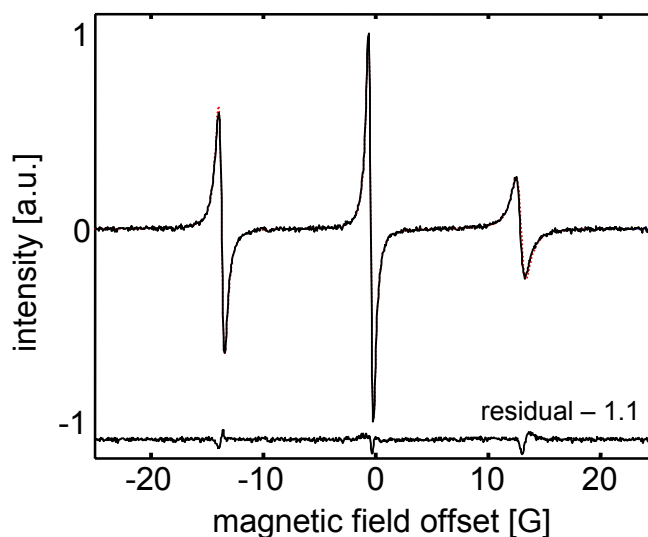
Figure 3.8. X-band (9.77 GHz) EPR spectrum (solid line) of FS + PDADMAC (*R*=0.011, 46 mM PDADMAC) in 70% NMPA/30% water at 293 K. A simulation as described by eq. (3.1) in the text, assuming preferred rotation about the axis indicated in Figure 3.4, is superimposed (dotted red line) and the residual of the experimental and the simulated spectrum is shown. The rotational diffusion tensor used for the simulation was $d_\parallel = 3.7 \cdot 10^9$ s^{-1}, $d_\perp = 5.5 \cdot 10^7$ s^{-1} and broadening parameters for this case were: $j=1.8 \cdot 10^{13}$ s^{-1}, $x=0.1$;

parameters j and x of eq. 3.1 that comprise the information of the line broadening will not be discussed in detail here (they merely empirically provide the broadening), the rotational diffusion tensor underlying the simulations is of utmost interest at this stage of analysis.

Again the assumption was used that rotational diffusion of FS is uniaxial, and even the same unique axis as shown in Figure 3.4 for FS in DMF/glycerol/water gave simulations that rather nicely reproduced spectra of FS+PDADMAC in all four solvents. The anisotropy of rotation, though, upon addition of PDADMAC was much larger than in the pure solvents. Over the whole range of concentrations studied in the three low-viscosity samples, the rotational diffusion rates decreased only by approximately 10% with increasing polyelectrolyte concentration. In glycerol/water as solvent, there is a distinct dependence of rotational diffusion on polyelectrolyte concentration, which is the focus of discussion in Section 3.3.5. The magnitudes of the diffusion tensor elements parallel and perpendicular to the unique axis of the rotational diffusion tensor in Figure 3.4 are summarized in Table 3.2.

Table 3.2. Rotational diffusion rates from simulations of CW EPR spectra in all four solvents as explained in the text. The two rates, $d_\parallel$ and $d_\perp$ represent the components parallel and perpendicular to the unique axis shown in Figure 3.4. For glycerol/water, rates of samples with the highest (first) and the lowest amount of PDADMAC (second) are given, as they change immensely upon increase of PDADMAC concentration.

	in water	in ethanol/water	in NMPA/water	in glycerol/water
$d_\parallel$	$4.5 \cdot 10^9$ s^{-1}	$3.7 \cdot 10^9$ s^{-1}	$3.7 \cdot 10^9$ s^{-1}	$1.3 \cdot 10^9$ s^{-1}/$5.4 \cdot 10^9$ s^{-1}
$d_\perp$	$3.0 \cdot 10^8$ s^{-1}	$5.5 \cdot 10^7$ s^{-1}	$5.5 \cdot 10^7$ s^{-1}	$2.0 \cdot 10^7$ s^{-1}/$5.5 \cdot 10^7$ s^{-1}
$\alpha = d_\parallel / d_\perp$	15	67	67	65 / 98

The first remarkable result is that dynamic electrostatic attachment of FS to the charges on the PDADMAC backbone seems to take place along the same preferred direction as in the case of small cations like potassium. This proves that attachment to such highly charged polyelectrolyte bearing monovalent charged centers is fundamentally different from that of FS to RuCP. Qualitatively, this may well be deduced from the differences of these two polyelectrolytes. Assuming simple Coulomb interaction and applicability of Manning theory, it has already been described in Section 3.2 that a large fraction of divalent FS ions should replace monovalent chloride counterions in the "condensed" state. PDADMAC has many more charges than RuCP and a high charge density along the backbone, so that one can expect the interaction that the FS ions are subjected to is stronger close to PDADMAC chains. Overall, rotational dynamics will reflect that there are larger contributions from the attached state, which should lead to a slowdown of rotational dynamics. The larger anisotropy α of rotational diffusion is also indicative of lifetimes of the attached state that on average are longer than with single counterions or RuCP. Attachment to a charge on a long chain must affect rotation perpendicular to the direction of one sulfur-nitrogen bond of FS more strongly than parallel to it as such rotation involves motion of either the whole chain, or the local chain segment or at least substantial backbone fluctuations.

Surprisingly, in water, rotation about the unique axis is ~15 times faster, in all three other solvent mixtures even more than sixty times faster than perpendicular to it. Moreover, in water rotation perpendicular to the major axis is one order of magnitude faster than in the organic solvent/water mixtures. In ethanol/water and NMPA/water FS rotational diffusion seems to be identical within the limits of precision of this simulation procedure. The simplest manner to explain these findings would be to correlate rotational dynamics to macroscopic viscosity of the solvent mixtures or even of the whole system including polyelectrolyte. This explanation can be ruled out, since from the three organic solvent/water mixtures only high polymer content in glycerol/water induces a polyelectrolyte-dependent slowdown of FS rotational dynamics, whereas the nominal viscosity already at low polymer content is much larger than that of the other solvents (see Table 3.1). This fact is used in Section 3.3.5 to indirectly derive information on the PDADMAC chain dynamics. Note that pure viscosity effects should also influence $d_\parallel$, i.e., changes in the ratio α can hardly be explained in this way.

With the exception of $d_\perp$ in water, all rotational rates are in the same order of magnitude, which shows that the microviscosity experienced by FS ions is similar in all the systems and dominated by the dynamic electrostatic attachment. Faster rotation perpendicular to the main axis of FS in water in this case also means a reduced anisotropy α of rotation as compared to the other solvent systems ($\alpha \sim 15$ in water vs. $\alpha > 60$ in mixtures). Assuming that α is determined mainly by the lifetime of the electrostatically attached state, one could interpret the reduction of α as stemming from lower contributions from attached states to overall dynamics. Consequently, either the lifetime of the attached state in water or the fraction of FS ions attached to PDADMAC at any time is lower than in the other solvents. Which of the two possibilities is realized cannot be concluded from the dynamic parameters alone. However, these parameters strongly indicate that in water polyelectrolyte-FS counterion interaction is different from the interaction in mixtures of water with organic solvents.

One should finally bear in mind that the used analysis of the complex rotational dynamics imposed by dynamic electrostatic attachment in terms of Brownian diffusion with an axially symmetric rotational diffusion tensor amounts to a considerable simplification that comes at the expense of loosing some information on microscopic details of the process. It would be intriguing to characterize such details by resorting to more sophisticated models of rotational diffusion such as the model of slowly relaxing local structure introduced by Polimeno and Freed.[96] However, for the present data sets such an approach does not seem to be warranted, as the fits with the more simple model of Brownian diffusion are excellent. Future investigations should include concurrent analysis of data obtained at X-band (9.4 GHz) and W-band (94 GHz) frequencies with glycerol/water mixtures as a solvent, as this may provide the stronger constraints that are required for such a more detailed model.

Characterization of site binding

So far it was shown that from simulation of CW EPR spectra a preferred direction of dynamic electrostatic attachment could be obtained. In the following, results from pulse EPR measurements of

FS/PDADMAC in glycerol/water are presented that will help to elucidate the local attachment environment.

There is a plentitude of EPR methods to characterize the immediate and more distant environment of electron spins.[39] This is most importantly achieved by analyzing intra- and intermolecular interactions of the spin probe electron spin with magnetic nuclei in the surroundings. The method arsenal includes CW EPR spectral analysis (Section 2.3), 2-pulse ESEEM (Section 2.6.2), 3-pulse ESEEM (Section 2.7) and related techniques such as its four-pulse variant[39] and DEFENCE, and finally CW and pulse ENDOR (electron-nuclear double resonance).[39] Here, data are presented from 3-pulse ESEEM and subsequent ratio analysis as explained in Section 2.7.2. Qualitatively the results were also verified with DEFENCE and 4-pulse ESEEM, but since no new information in addition to 3-pulse ESEEM results was gathered from these experiments, solely findings and conclusions are explained from 3-pulse ESEEM and ratio analysis.

Typical 3-pulse ESEEM data for a frozen solution (T=80 K) of FS in the presence of PDADMAC (R=0.011) in glycerol/water are shown in Figure 3.9. Ratio analysis (see Section 2.7.2) is performed as follows: after division of the time-domain signal by the stimulated echo decay (approximated by a stretched exponential function), maxima and minima of the modulation curve are extracted by polynomial fitting of the experimental trace, and upper and lower envelopes are then determined by polynomial fitting of the maxima and minima, respectively (Figure 3.9.a). In the Fourier transform of the time domain signal (Figure 3.9.b) sharp and narrow peaks were observed at a frequency of 1.1 MHz, which is the nuclear Zeeman frequency of a ^{14}N nuclear spin at the static field
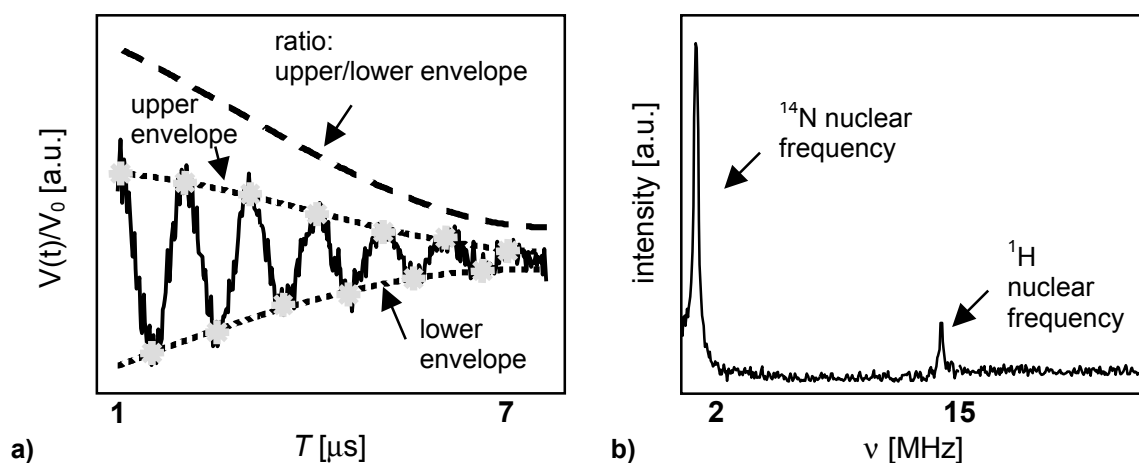

Figure 3.9. Time-domain and frequency-domain data from 3-pulse ESEEM (X-band, 9.77 GHz) measurement of FS + PDADMAC (R=0.011, 46 mM PDADMAC) in glycerol/water (T=80K).
a) Time-domain data after division by a stretched exponential decay (solid line); filled gray circles: maxima and minima of ^{14}N modulation; dotted lines: upper and lower envelopes of ^{14}N modulation; dashed line: ratio of upper/lower envelope; See section 2.7.2 for a full description of the procedure of ratio analysis;
b) frequency-domain data (Fourier transform of time-domain data); the peaks at the nuclear Zeeman frequencies of ^{14}N (~1.1 MHz) and ^{1}H (~14.7 MHz) are marked;

B_0≈3460 G used in the experiments. In the absence of polyelectrolyte, no modulation was observed at this frequency. Therefore the measured modulation is assigned to the quaternary nitrogen in the

PDADMAC repeat unit (Scheme 3.2). The unusually narrow ^{14}N ESEEM line is due to the nearly tetrahedral symmetry of the quaternary nitrogen, which leads to a small nuclear quadrupole coupling. Indeed, DFT (ADF 2002.01 package,[62] BLYP density functional, TZ2P basis set) calculations of quadrupole couplings of quaternary ^{14}N nuclei provide values of approximately e^2qQ/h=200 kHz. Note that all data were recorded with τ=200 ns, corresponding to a blind spot for the modulation due to ^{1}H nuclei,[39] so that modulation due to ^{14}N nuclei dominates, which significantly simplifies data analysis.

No general trend for the fit parameters $r_{e\text{-}N}$, a, and n was found when varying polyelectrolyte concentration, hence only the typical data of Figure 3.9 are shown. For samples in the whole R-range, an electron-nuclear distance of closest approach of $r_{e\text{-}N}\approx0.43$ nm is found, a virtually negligible isotropic hyperfine coupling of $a\approx0.07$ MHz, and an average number of $n\approx0.20$ ^{14}N nuclei in the shell of closest approach. The value of 0.2 nitrogen nuclei means that statistically only 20% of all spin probes are in close contact to a PDADMAC ammonium group.

Although this kind of data analysis is strictly valid only for spherical coordination shells and neglect of angular correlation,[39,80] one may assume that it is a good approximation in the present case where the number of nuclei at closest approach for a given electron spin is usually zero or one. Neglect of nuclear quadrupole coupling probably introduces an error mainly in a, but may also lead to a slight underestimate in $r_{e\text{-}N}$. For comparison, force-field (MMFF94 force field in SPARTAN, Wavefunction, Inc.) calculations of two FS molecules and a short section of a PDADMAC chain with twelve monomeric units were performed to get an estimate of an electrostatic closest approach. It is found that in such a model system in vacuum the closest distance between the nitrogen atom of the FS nitroxide group and the charge-bearing ammonium ion on the PDADMAC chain is approximately 0.4 nm, and thus rather close to the values found from ratio analysis of ESEEM data.

Equilibrium of site bound, territorially bound and unbound counterions

In order to evaluate the significance of results from EPR measurements in frozen solution for the polyelectrolyte/counterion systems at ambient temperatures one has to check whether the system forms a glassy state upon freezing. The only solvent system in these studies that gave *quantitatively* reproducible results from EPR spectroscopy upon shock freezing was glycerol/water, so that only these data are presented in depth. For the other solvents, including pure water, the ESEEM time domain data and frequency domain analysis also indicate close contact of FS spin probe and ^{14}N nuclei, as modulations corresponding to the 1.1 MHz frequency domain signal were also found. These samples lack quantitative reproducibility, though, so that they will not be considered in more detail.

During shock freezing of a glass-forming system, one may assume that thermodynamic equilibrium can be reached at each temperature as long as typical rates for conformational changes, redistribution of counterions, etc. are faster than the cooling rate. With approach to the glass transition temperature, viscosity increases dramatically and the rates of all dynamic processes decrease by orders of magnitude. It is therefore assumed that the state of the system after shock freezing is an ensemble of static structures (a "snapshot", as it was called for the experiments on RuCP) roughly corresponding to

the distribution of structures at the glass transition temperature of approximately 180 K. Although this is a significantly lower temperature than the one at which liquid solutions were studied by CW EPR spectroscopy, it is supposed that the same general phenomena occur and that the same general structural model for the polyelectrolyte-counterion system can be used in the discussion. Note however that *quantitative* findings for the glassy state cannot simply be assumed to pertain also to liquid solution.

The results from ratio analysis of 3-pulse ESEEM data are direct evidence for electrostatic attachment (site-binding) of FS counterions to PDADMAC monomeric units. Together with the performed force field

distance r_{e-N}
~0.43 nm

Figure 3.10. Sketch of geometry and dynamics of FS counterions condensed to a PDADMAC chain. This is a snapshot of the local geometry of an FS spin probe that is site-bound to a PDADMAC ammonium group. The gray arrow depicts the direction parallel to the axis of fast rotation of FS (see Figure 3.4). The distance $r_{e-N} \approx$ 0.43 nm was obtained from ratio analysis of three-pulse ESEEM data (see Figure 3.9).

calculations, the estimate of approximately 0.43 nm for the electron-^{14}N distance is a clear indication that contact ion pairs are formed. In other words, for some counterions no solvent molecules are located between the two oppositely charged moieties (ammonium and sulfonate groups). Figure 3.10 is a representation of the combination of this finding with the results for the rotational diffusion tensor of FS in PDADMAC (Figure 3.4). For all polyelectrolyte concentrations studied ($R \ll 1$), the coordination number of ^{14}N nuclei is approximately 0.2. Hence at a given time only 20% of FS spin probes form such contact ion pairs with PDADMAC chain monomer units, regardless of the ratio of spin probes to polyelectrolyte repeat units. Figure 3.10 thus only gives a *snapshot* of the attached state in what is called *dynamic electrostatic attachment* in this work. Counterion attachment corresponds to the site-bound state in a dynamical equilibrium:

(free $\rightleftarrows$) territorial binding $\rightleftarrows$ site binding.

Dynamic information from CW EPR spectra in liquid solution indicates that the rate constant for the exchange between territorially bound and site-bound spin-carrying counterions is significantly larger than 10^9 s^{-1}. It was already described in detail that if the lifetime of the site-bound (attached) state were of the order of a nanosecond or longer, one should observe bimodal spectra, i.e., a superposition of two dynamic components corresponding to territorially bound and site-bound FS probes. Furthermore, in the presence of polyelectrolyte there is no spectral component with linewidths and relative intensities as they are observed in the absence of polyelectrolyte. This excludes the existence of a significant fraction of free divalent spin-carrying counterions. Such a picture, where at any given time
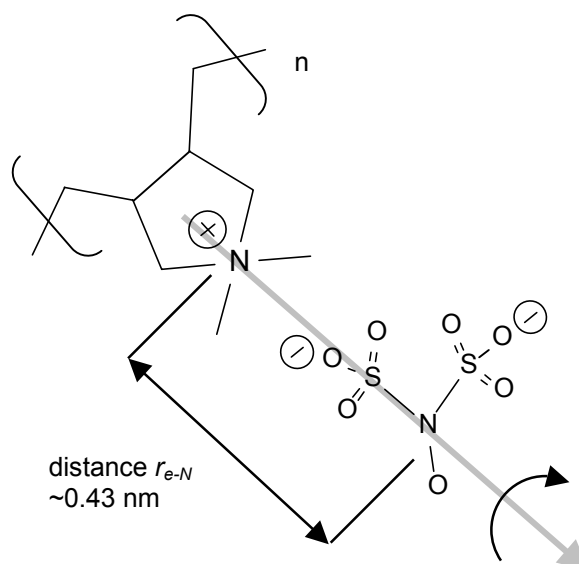
all the FS counterions are either territorially bound or site-bound is also consistent with the fact that the exchange between these two states is very fast, which requires that diffusion lengths are short. The picture is also in agreement with simple polyelectrolyte theory, which - as outlined in Section 3.1.1 - predicts our systems to be in the regime of saturated counterion condensation of divalent FS spin probes.

Strictly speaking, the proposed direct contact ion pair formation has only been proven for the system of FS/PDADMAC in glycerol/water. Nonetheless, it is a sound assumption that the site-bound state of FS in the three other solvents is very similar to that in glycerol/water. As described earlier, ESEEM signals could be found in stimulated echo decays even for purely aqueous systems. In addition, the rotational diffusion tensor has been shown to be very similar in all systems (Figures 3.4 and 3.10) – it is only doubtful that the parameters r_{e-N}, a, and n are identical to those found in glycerol/water.

Dynamic electrostatic attachment of transition-metal cations

Before the complete series of FS (and also TAM) probe ions are analyzed in a systematic, quantitative manner, spectra of transition metal cations $[Mn(H_2O)_6]^{2+}$ and $[VO(H_2O)_5]^2$ are inspected briefly. Figure 3.11 shows representative spectra of both species in water with and without PSS polyelectrolyte added.

The line broadening in the manganese high-field/high-frequency and oxovanadyl X-band EPR spectra upon addition of PSS points to a similar electrostatic attachment as observed for the anionic spin probes. The full spectra, and in particular the detail plots (Figure 3.11.c) and d)) clearly show that addition of the polyelectrolyte does not only induce an increase in peak-to-peak linewidth, but also a change in the lineshape similar to the one observed for FS and as will be shown later also for TAM probes. The main difference to those spin probes is, though, that upon variation of concentration of the oppositely-charged polyelectrolyte there is no further alteration in the spectra (hence only one spectrum with PSS added is shown for each spin probe).

In the case of Mn^{2+}, the observed broadening upon addition of PSS is assigned to deformation of the octahedral coordination of the Mn^{2+} ion with water molecules due to dynamic electrostatic attachment. This dynamic deformation of the coordination polyhedron modulates the zero-field splitting, which is averaged in perfect octahedral symmetry except for a small contribution due to the hexadecapolar moment of the charge distribution (see Section 2.2).[39] The modulation of the zero-field splitting in turn shortens the transverse relaxation time and thus broadens the line in an analogous manner as described by Strandberg and Westlund for Gd^{3+}.[97] Contributions to linewidths by other mechanisms, as they are explained for FS and TAM in the next paragraph are negligible for lines as broad as for manganese ($\Delta B_{pp} \approx 9$ G at W-band). However, the detail plot in Figure 3.11.c illustrates that with PSS there is also a lineshape change with broadening especially at the wings of the lines, which might be an indication that one observes peaks made up of distributions of linewidths.
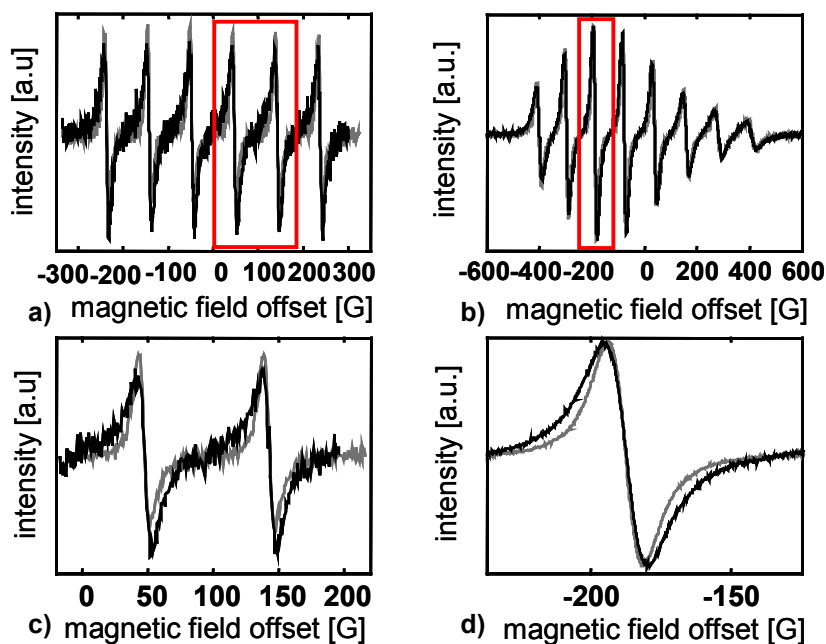
Figure 3.11.a) and **c)**: High-field/high-frequency (94 GHz) EPR spectra of Mn^{2+} of two different Mn/PSS ratios *R* in aqueous solution. Black line: *R*=0.05; gray line: Mn in pure water; **a)** full spectra; **c)** detail plot of lines 4 and 5 of the spectra.
b) and **d)**: X-band (~9.4 GHz) EPR spectra of VO^{2+} of two different VO/PSS ratios *R* in aqueous solution. Black line: R=0.01; gray line: VO in pure water; **b)** full spectra; **d)** detail plot of the third line of the respective spectra.

    Changes in linewidth and lineshape of VO^{2+} spectra can be explained in an analogous manner as those in Mn^{2+} spectra. Through dynamic attachment to PSS sulfonate groups one can expect the oxovanadyl coordination polyhedron to be deformed, too. In this case, the dynamic deformation changes the ^{51}V nuclear quadrupole interaction, which has been shown to be very sensitive to distortions of the central vanadium ion coordination.[88] Reduction of symmetry from perfect C_{4v} symmetry can effectively increase the nuclear quadrupole coupling and thus lead to strong broadening effects, as observed in the spectra presented here. Other effects, like slowdown of rotational dynamics due to addition of polyelectrolyte are probably too small as compared to the modulation of quadrupole interaction to further affect the spectra. Although the use of both transition metal cations has not been fully exploited in this work – both ions bear potential for use of more advanced techniques such as ENDOR and ESEEM – these results obviously show that dynamic electrostatic attachment is a general phenomenon in organic and inorganic spin-carrying counterions. Especially the oxovanadyl ion seems spectroscopically well suited for studies of the effect that divalent earth alkaline metals have on polyelectrolyte conformation, but this is outside the scope of the present work.

3.3.2   Quantification of changes in CW and FT EPR spectra

Figures 3.6 and 3.7 show that addition of oppositely charged polyelectrolyte PDADMAC strongly influences CW EPR spectra of spin probe FS. Those spectral changes are also observable in EPR spectra in the three organic solvent/water mixtures and can be categorized according to three trends:

i)   with increasing *R*-values, i.e., decreasing polyelectrolyte concentration, peak-to-peak linewidths increase

ii)   with increasing *R*-values, broadening effects in the outer wings of each line become increasingly pronounced and render the lineshape non-Lorentzian (see Section 2.3)

iii)   with *decreasing R*-values, relative amplitudes of the three lines become progressively unlike

It can be seen later (Figure 3.16.a) that effects i) and ii) can also be observed for TAM as spin-carrying probe ion, whereas observation iii) is irrelevant for the single line TAM spectrum.

We now turn to quantitative extraction of information from spectral broadening for probe molecules FS and TAM from the measured data sets. This can be achieved by several approaches and the most general one is explained in the following paragraphs. In the next chapter (Section 4.1) the same sets of data are analyzed according to an underlying polyelectrolyte model to obtain knowledge on the counterion distribution in the cell model of polyelectrolytes.

In the present section, a home-written fitting program was employed that assumes that each broadened EPR line may be a superposition of a several Lorentzian lines with different linewidths, i.e. it assumes that transverse relaxation can be described by a stretched exponential decay.[16] This approach is analogous to studies of relaxation times in disordered systems by, e.g., dielectric spectroscopy.[98] The time-domain signal for a single line with resonance offset ω_k, characteristic transverse relaxation time T_2, and stretch factor x is then given by:

$$V(t) = \sum_{k=1}^{n} \exp\left[-\frac{t}{T_{2,k}}\right]^{x} \exp\left[i\omega_k t\right], \tag{3.2}$$

where $n = 1$ for TAM and $n = 3$ for FS spin probes with $k = 1$ corresponding to the low-field line and $k = 3$ corresponding to the high-field line. The CW spectrum is obtained by FT of the sum signal $V(t)$, and subsequent pseudomodulation[67] with the same modulation amplitude as used in the experiments. This simulated CW EPR spectrum is fit to the experimental spectrum, which provides a quantification of the non-Lorentzian lines with a minimum number of fit parameters and without making any assumptions on the *physical process* leading to relaxation. CW EPR spectra of only FS or TAM without PDADMAC can all be fit with stretch factors relatively close to unity (i.e. they are close to pure Lorentzian lines). As neither of them has intramolecular hydrogen atoms only intermolecular unresolved [1]H-hyperfine coupling contributions lead to slight deviations of the stretch factor.[99] Therefore, this stretch factor is a measure of the width of a *distribution of relaxation times*: the lower *x*, the broader the distribution.

The program provides good fits of the data for all compositions of the system in low-viscosity solvents but is restricted to $R<0.1$ in the glycerol/water mixture and in pure water. Above this value we do not consider the simulated data reliable any more, as the deviation of the simulated spectra from the experimental data becomes significant.

All values reported for T_2 in this work are average values of the Williams-Watts distribution of T_2:[100]

$$\langle T_2 \rangle = \frac{1}{x} \cdot T_2 \cdot \Gamma\left(\frac{1}{x}\right),$$

(3.3)

where the brackets denote the average value and $\Gamma(1/x)$ is the gamma function.[101]

The only supposition that has to be made is on the *origin* of the observed broadening. It is assumed to stem from increased electron spin-spin interactions. In the limit of fast translation and rotation of the spin carrying counterions (FS and TAM), dipolar broadening can be excluded, as it is averaged to zero (see Sections 2.2 and 2.3), but in solutions of high viscosity (especially glycerol/water as solvent) residual magnetic dipolar interaction cannot be excluded.[50,55] In the low-viscosity solvents, solely increased *Heisenberg spin exchange interaction* - due to frequent collisions of spin probe molecules in the vicinity of the oppositely-charged polyelectrolyte – is considered as the source of the spectral changes. A characteristic EPR linewidth $<\Delta B>$ of the non-Lorentzian lines can be computed by $\langle \Delta B_k \rangle = [0.412\ (\text{G/MHz}) \cdot \langle T_{2,k} \rangle^{-1}]$.[39] This averaged linewidth is a quantitative measure of the electron spin-electron spin interaction: $<\Delta B> \propto \langle T_2 \rangle^{-1} \propto T_{2,\ intrinsic}^{-1} + T_{e-e}^{-1}$, which is in turn related to local concentration of the spin-carrying counterions. Here, $T_{2,\ intrinsic}^{-1}$ denotes the intrinsic relaxation rate at infinite dilution and T_{e-e}^{-1} denotes the concentration-dependent rate due to intermolecular electron spin interaction. The intrinsic rate differs for the three lines (k=1, 2, 3) for nitroxides, and these differences are related to the rotational correlation time (see below).

As broadening due to both possible mechanisms, magnetic dipolar and spin exchange interaction, is related to local concentrations these semi-quantitative conclusions do not depend on the detailed broadening mechanism. To characterize rotational dynamics for FS by a single parameter, a characteristic value $\langle \tau_c \rangle$ for the rotational correlation time was computed from the so-called "B-parameter": $B = (<\Delta B(k=3)> - <\Delta B(k=1)>)/2$ as introduced in Section 2.3[60,61] and implemented by Robinson et al.[59] Note that the $\langle \tau_c \rangle$ is not the strictly defined average of the distribution of rotational correlation times, which cannot be extracted by this simple data analysis procedure. This data analysis provides quantitative average values that are good characteristics of the distributions of T_2 and τ_c.[102] A more detailed look at the rotational diffusion tensor of FS counterions has already been taken in the previous section. The isotropic ^{14}N hyperfine coupling constants a_{iso}, which were shown to be related to the polarity of the environment of the electron spin, were calculated as average values of the two spacings between the three lines in simulations FS spectra. (a_{iso}=½*[$a_1 + a_2$]) according to the fitting program by Robinson et al.,[59] which could not fully account for the spectral broadenings but gave more reliable values of a_{iso} than simple reading-off from the spectra.

Results of data analysis according to equations 3.2 and 3.3 for FS are presented in Figures 3.12 ($<T_2>$), 3.13 (stretch factors x) and 3.14 (rotational correlation times $<\tau_c>$), whereas for TAM they are summarized in Figure 3.16. In addition, all isotropic hyperfine coupling constants a_{iso} for FS are presented in Figure 3.15. After a short introduction to all important parameters in this section, a more detailed interpretation of the data is given in the following sections, 3.3.3 – 3.3.5.

FS/PDADMAC spectra: relaxation times, stretch factors, rotational correlation times, and ^{14}N hyperfine couplings

In Figure 3.12.a-d the general trends of the averaged relaxation times in the four solvents are displayed. Decrease of relaxation times (i.e. line broadening in the spectra) is most pronounced for the pure aqueous solution spectra, but is also significant for the low-viscosity solvent mixtures ethanol/water and NMPA/water. The behavior for the solutions in pure water and in glycerol/water is qualitatively different from the behavior for low-viscosity solvent mixtures. Furthermore, for the ethanol/water and NMPA/water mixtures not only the trends coincide, but also the absolute values are similar.

In Figure 3.13 stretch factors x for FS/PDADMAC in all four solvents are summarized. Stretch factors x according to equation 3.2 are a measure of the width of the distribution of relaxation times. With increasing R-value stretch factors deviate more and more strongly from their values in the
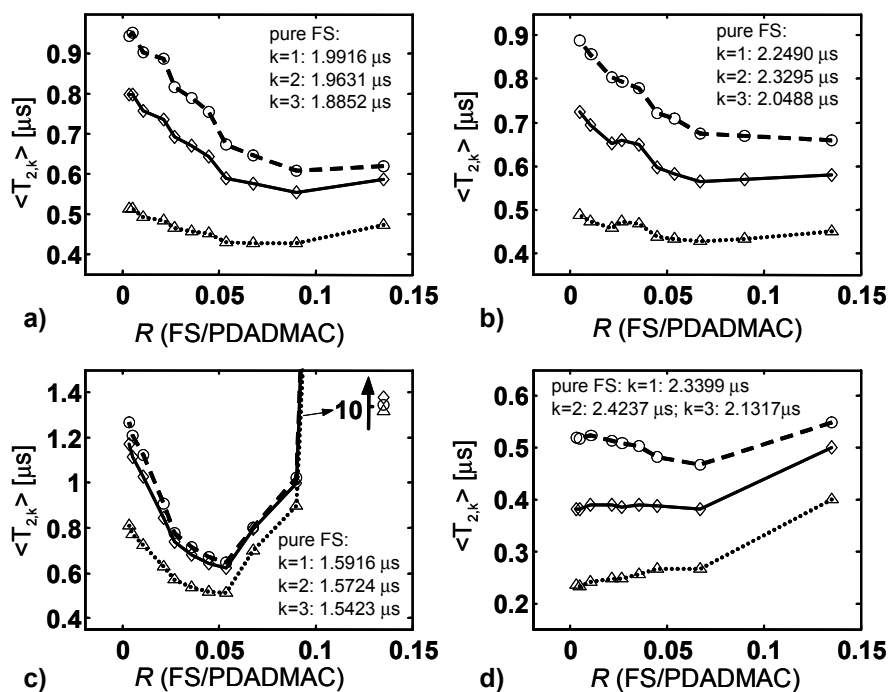
Figure 3.12. Plots of analysis of CW EPR spectra (X-band, ~9.79 GHz) of FS in all solvents used according to eqs. 3.2 and 3.3. The averaged relaxation times $<T_{2,k}>$ of each of the three hyperfine lines are plotted as a function of FS/PDADMAC ratio R.
a) in ethanol/water; **b)** in NMPA/water; **c)** in water; **d)** in glycerol/water;
Diamonds/solid lines: low-field manifolds (k=1); circles/dashed lines: center-field manifolds (k=2); triangles/dash-dot lines: high-field manifolds (k=3).
In plot c) the values for R=0.126 are shown out of scale in the upper right corner.

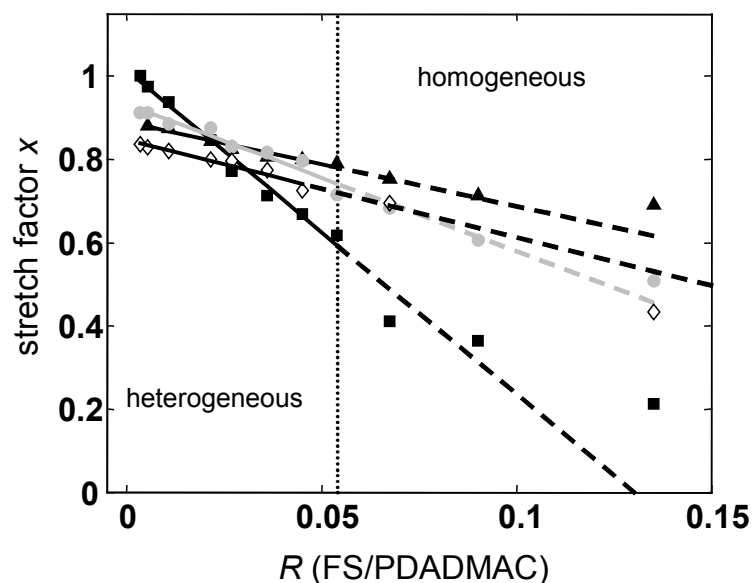**Figure 3.13.** Stretch factors x (see eqs. (3.2), (3.3)) for spin probe FS as function of FS/PDADMAC ratio R in four different solvents (X-band, ~9.79 GHz). Parameter uncertainties are within marker size. Straight lines are linear fits including data points up to R=0.06 (marked by vertical dotted line; extrapolation of the fit: dashed lines).
Filled squares: in water, x(only FS)=1.077; linear fit: x=1.015 - 7.790*R; **filled gray circles:** in ethanol/water, x(only FS)=1.066; linear fit: x=0.933 - 3.533*R; **filled triangles:** in NMPA/water, x(only FS)=1.113; linear fit: x=0.889 - 2.019*R; **open diamonds:** in glycerol/water, x(only FS)=1.15; linear fit: x=0.847 - 2.343*R;

absence of polyelectrolytes (x~1), thus the distribution of relaxation times becomes more heterogeneous (x≠1) with higher R. The trend for x is similar in all systems: it decreases linearly with increasing R. Again, the series in water differs from the series in the three organic solvent/water mixtures: the slope of the decline in x-values is much steeper and x attains values as low as 0.2. The NMPA/water and glycerol/water mixtures are almost identical in the slope of the decrease and are just shifted by an absolute value of 0.05. One should notice that both, relaxation times and stretch factors roughly approach their respective values for FS in the absence of polyelectrolyte with decreasing R, which means with *increasing* polyelectrolyte concentration.

Figure 3.14 shows the rotational correlation times $\langle \tau_c \rangle$ calculated from averaged linewidths as explained before in this section. These characteristic times comprise *averaged* dynamic information on the ensemble of spin probes, also neglecting the actual attachment geometry, which was under investigation in the last section. In all solvents, $\langle \tau_c \rangle$ decreases with increasing R (Figure 3.14.a), an effect that can be attributed to the lower polyelectrolyte concentration with higher R-values and that is most prominent in glycerol/water. This is a result of increased *microviscosity* and thus also of dynamic electrostatic attachment: divalent FS spin probes on average are very close to oppositely charged, long PDADMAC chains, which is indirectly reflected in the calculated rotational correlation times. The fact that even very low concentrations of PDADMAC lead to distinctly longer $\langle \tau_c \rangle$ is a strong indication for the electrostatic origin of this observation. In Figure 3.14.b the same series of rotational correlation times is plotted in a slightly different manner: they are normalized by the polyelectrolyte content
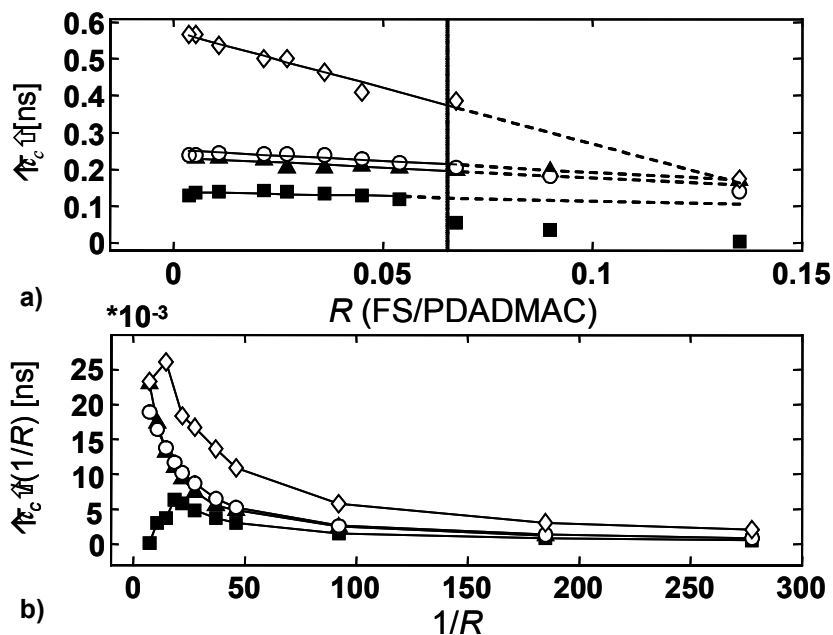
Figure 3.14. Rotational correlation times of FS spin probe calculated from the linewidth differences of high-field and low-field line manifolds (see text) as function of R (a) and $1/R$ (b) in four solvents.
a) Filled squares: in water ($<\tau_c>$(only FS) = 0.004 ns); filled triangles: in NMPA/water ($<\tau_c>$ (only FS): 0.011 ns); open circles: in ethanol/water ($<\tau_c>$ (only FS): 0.006 ns); open diamonds: in glycerol/water ($<\tau_c>$ (only FS) = 0.030 ns). Solid lines are linear fits including data points up to R=0.067 (marked by vertical dotted line; extrapolation of linear fits: dashed lines). Linear fits: in water: $<\tau_c>$=0.153 ns – 0.273 ns*R; in NMPA/water: $<\tau_c>$=0.255 ns – 0.607 ns*R ; in ethanol/water: $<\tau_c>$=0.277 ns – 0.660 ns*R; in glycerol/water: $<\tau_c>$=0.631 ns – 3.353 ns*R.
b) $<\tau_c>$ normalized by polyelectrolyte contents (i.e. divided by $1/R$) plotted as function of $1/R$. Solid lines are guides to the eye. Note that this is analogous to plotting the normalized specific viscosity η_{sp}/c of a polyelectrolyte as function of its concentration c.

(divided by $1/R$, i.e. multiplied by R) and shown as a function of $1/R$. This approach is chosen in analogy to plots of the concentration-normalized specific viscosity η_{sp}/c as function of c,[1] which shows the peculiarity to decrease with increasing concentration. Ordinary polymer behavior (increase of η_{sp}/c with increasing c) is attained only after addition of considerable amounts of inert salt (e.g. NaCl).[1,3]

It is noteworthy that the *counterion*-specific rotational correlation time exhibits the same trend as is usually expected for the *polyelectrolyte*-specific viscosity. As described before one can rationalize this normalized rotational correlation time as a measure of the *local* microviscosity around the spin probes. This parameter exhibits the same trends as the *macroscopic* polyelectrolyte viscosity, which establishes a remarkable correlation of a local counterion and a bulk polyelectrolyte quantity.

For FS in the three solvent mixtures, $\langle\tau_c\rangle/(1/R)$ decreases steeply until it approaches a plateau value for high polyelectrolyte concentrations, whereas in pure water the first three data points increase with increasing $1/R$ before the same trend as for solvent mixtures is attained.

Figure 3.15 displays the isotropic hyperfine couplings taken from the series of FS measurements. In all solvents a significant decrease of a_{iso} is observable upon addition of PDADMAC and for the series in the three low viscosity solvents the hyperfine coupling approaches the value for
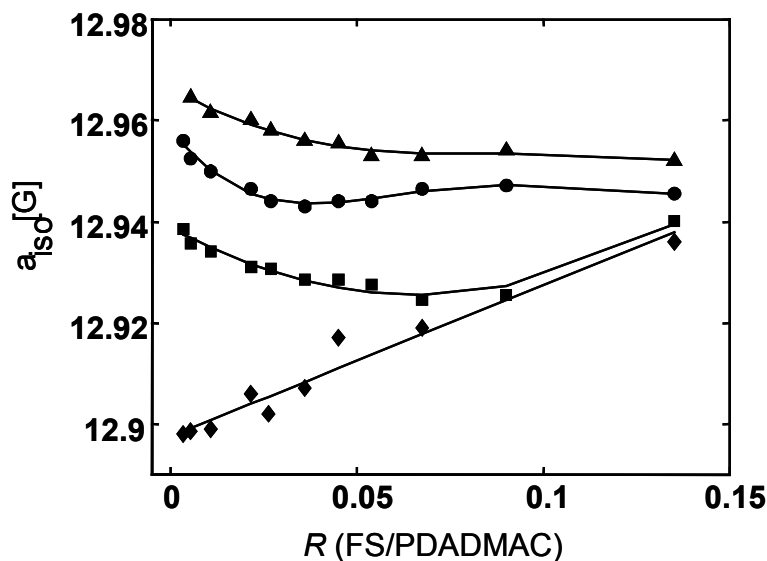
Figure 3.15. Isotropic ^{14}N hyperfine coupling extracted from X-band CW EPR spectra of FS with varying concentration of PDADMAC as a function of R in four solvents.
Filled squares: in water (a_{iso}(only FS)=12.980 G); **filled triangles:** in NMPA/water (a_{iso}(only FS)=12.995 G); **filled circles:** in ethanol/water (a_{iso}(only FS)=12.964 G); **filled diamonds:** in glycerol/water (a_{iso}(only FS)=12.982 G), linear fit (solid line): 12.898 G + 0.298 G*R, all other solid lines are guides to the eye;

pure FS solutions upon increase of polyelectrolyte content (decrease of R) as seen before for stretch factors. Up to R~0.05 the hyperfine coupling constants decrease with a similar incline in those three solvent systems and with the exception of the highest R-value in pure water reach a plateau value for R>0.05. Note that the strongest deviation is only ~0.01 G and is therefore not subject to a quantitative discussion. Only for solutions in glycerol/water, a_{iso} increases linearly with R and advances towards the reference value with no added PDADMAC. The sensitivity of the hyperfine coupling towards solvent proticity and polarity of the solvent is also reflected in the differences of the absolute values of a_{iso}. A very interesting detail seems to be that values of a_{iso} are similar for the highest R-value in all solvents. The different trends between solutions in glycerol/water and the other solvents will be discussed in 3.3.5, when the dynamics of counterions and polymer chains will be under scrutiny.

TAM/PDADMAC spectra: relaxation times and stretch factors

Finally, in Figure 3.16 (a-c) FT EPR spectra and parameters of spectral analysis according to eqs. 3.2 and 3.3, $<T_2>$ and x are presented. Only three representative spectra of TAM/PDADMAC are shown, as the effects on the spectra upon addition of polyelectrolyte are qualitatively similar to those of the FS/PDADMAC system.

It is apparent that the plots of the averaged relaxation times and stretch factors of this spin probe in both investigated solvents bear a strong resemblance. As mentioned before, the major difference to the FS probe ion is that TAM spectra are insensitive to changes in rotational dynamics, while FS spectra are strongly influenced by such changes. This dissimilarity concerning rotational dynamics becomes obvious in Figure 3.16.a/b, as the trends for the extracted averaged relaxation times are similar in both solvents, whereas they follow different trends in the case of FS (see Figure 3.12).
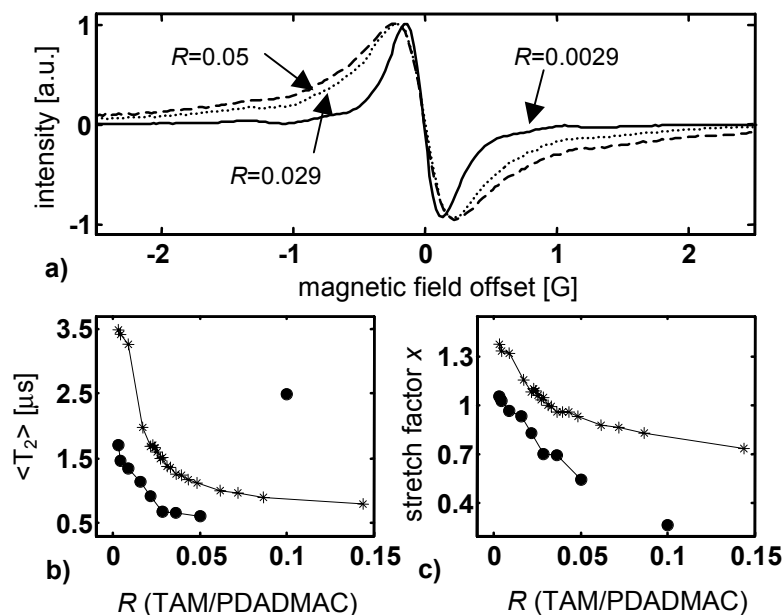
Figure 3.16. Representative FT EPR spectra in glycerol/water, averaged relaxation times $<T_2>$, and stretch factors x (see eqs. 3.2, 3.3) for spin probe TAM as function of TAM/PDADMAC ratio R in two different solvents (EPR frequency: 9.79 GHz). Parameter uncertainties are within marker size. **a)** Three EPR spectra of TAM in glycerol/water at different R-values; solid line: $R=0.0029$; dotted line: $R=0.029$; dashed line: $R=0.050$; spectra are normalized to equal amplitude. **b)** Averaged relaxation times $<T_2>$; filled circles: in glycerol/water ($<T_2>$(only TAM)=3.49μs); asterisks: in water ($<T_2>$(only TAM)=4.65μs). **c)** Stretch factors x as characterization of relaxation time distribution (see eq. 3.2); filled circles: in glycerol/water (x(only TAM)=1.31); asterisks: in water (x(only TAM)=1.48). Lines are meant as guide to the eye.

Having introduced all data that can be derived from CW and FT EPR spectra by the simple analysis procedure according to eqs. 3.2 and 3.3, the remainder of Section 3.3 is now concerned with the interpretation of these data in physical terms. This is done with particular interest to separate - when it is possible - the effects numbered i) to iii) in the beginning of this section and their physical origins.

The interpretation is started by analyzing the broadening that was identified as stemming from spin-exchange interaction (3.3.3 and 3.3.4) before in Section 3.3.5 implications on polyelectrolyte chain dynamics are illustrated.

3.3.3   Agglomeration of spin probes close to single polyelectrolyte chains and buildup of a concentration gradient

FS/PDADMAC: attachment of spin probes to single chains in different solvents

In the basic theory of polyelectrolyte/counterion interactions introduced by Manning (Section 1.2.2) the polymer is approximated as a linear extended chain and the distribution of the point-like counterions is considered as a function of their distance r from the chain. Even without differentiation of so-called site-bound or territorially bound counterions, the fit parameters for FS and TAM spin probes in solutions of PDADMAC comprise information on the distribution of the counterion-tracer probes, which can be compared to predictions of this simple theory and more sophisticated models. At the heart of the interpretation of data is the most general model of a linear (in approximation infinitely

long), fully extended polyion chain that is surrounded by its counterions in a volume around it, as it is indicated in Figure 1.3. Section 4.2 will give strong indications from pulse Double Electron-Electron Resonance (DEER) experiments in frozen solution that even the use of the cylindrical cell model would be justified for CW EPR at room temperature, but for now only the simpler Manning model is used as basis for data interpretation.

Figure 3.17. ESE-detected, field-swept EPR spectra of FS/PDADMAC (X-band, ~9.3 GHz) in glycerol/water at four different R-values. Black solid line: only FS; blue dash-dotted line: $R=0.0036$; red dashed line: $R=0.0455$; magenta dotted line: $R=0.1250$; All spectra are normalized to equal integral.

The fact that broadening in the spectra is most evident in the low polyelectrolyte concentration (higher R) samples is the key to understanding the behavior of $<T_{2,k}>$ and x of FS in ethanol/water, NMPA/water, and glycerol/water. Figures 3.12.a, b, and c, and Figure 3.13 show the room-temperature spectra of FS/PDADMAC but the strong broadening effect is also observed in frozen solution of glycerol/water. In Figure 3.17, four representative electron spin echo (ESE)-detected, field-swept EPR spectra of samples with different R-values are shown (see Section 2.6.1). Note again that it is assumed that by shock-freezing one obtains samples that represent the systems at their glass-transition temperatures, which are viewed as snapshots of the systems in fluid solution. This removes the complication by the dynamics of counterion attachment and allows one to detect the distribution of the ensemble of spin probe counterions. The spectra have a clear tendency to become broader with increasing R, just like the room-temperature CW EPR spectra. There are two mechanisms that lead to such broadening of powder-like spectra in frozen solution, spin exchange interaction *through solvent* and dipolar interaction *through space*. The former is dominant for inter-spin distances shorter than ~1 nm, while the latter clearly dominates for distances longer than 1.5 nm.[52] In the distance range between 1 and 1.5 nm, both types of interactions can contribute to broadening of spectra.

Without quantitative separation of the origins of the broadening effects, two points are nonetheless affirmed by the spectral development seen in Figure 3.17. First, the broadening seems to come into play and significantly change the spectra as compared to pure FS only for $R>0.01$ (not shown), while, second, then the broadening seems to increase gradually with increasing R. Both of these observations are consistent with the trends for relaxation times in liquid solution (Figure 3.12) and manifest the increase of local concentration of FS with increasing R.
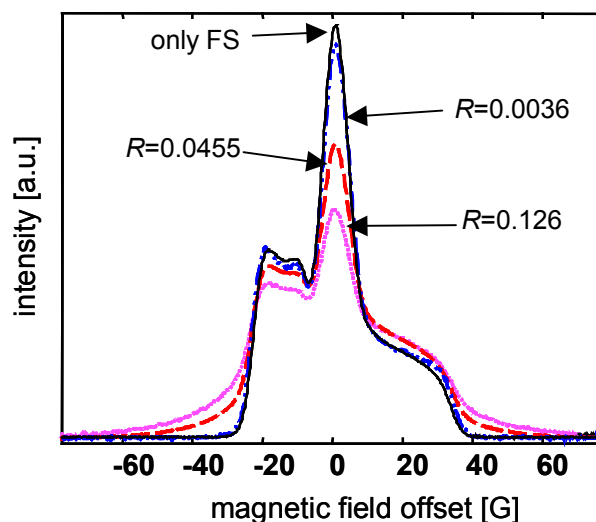
Model: DEA to linear extended chains

Assuming that condensed probe ions are homogeneously distributed along the extended polyelectrolyte chains and that no conformational transition takes place on changing R, one can develop a simple semi-quantitative model that depicts how DEA of multivalent, spin-carrying ions to linear extended polyelectrolyte chains affects the spin-exchange induced line broadening (lowering of $<T_{2,k}>$) and the rotational diffusion of FS spin probes. This model is very general and based on the Manning picture. Figure 3.18 schematically depicts rotational correlation times and spin-exchange induced line broadening (i.e. the contribution of spin
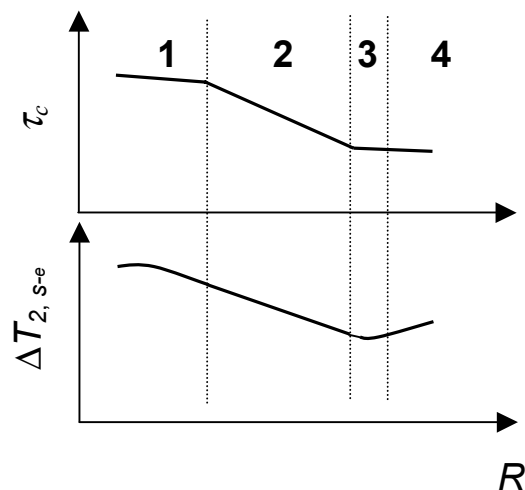

Figure 3.18. Sketch of the rotational correlation times (upper part) and spin-exchange contribution to the relaxation time (lower part) dependence on R for the model of DEA to linear extended polyelectrolyte chains. The lowering of relaxation times is proportional to the local concentration.
The four regimes marked 1-4 are explained in the text.

exchange to the decrease of the relaxation time $\Delta T_{2,s-e}$) for the expected four regimes. Note that in this scenario as in our experiments, the probe concentration is fixed and increase of R is achieved by decrease of polyelectrolyte concentration. At very low R the polymer concentration is so high that the *overlap regime* (regime 1 in Figure 3.18) for polymer chains is reached. Probes are dilute with respect to monomers and are exchanged between physically overlapping polyelectrolyte chains. The probe molecules are confined to overlap regions, i.e. to domains of higher microviscosity. This leads to a strong slowdown of rotational dynamics. Local concentration of probe ions only weakly influences relaxation times in this regime, as the distribution of probes along the polymer chains is such that average distances between individual probe ions are very large and thus spin exchange broadening is less significant than broadening due to decreased mobility.

For higher values of R, a soft transition takes place from the *overlap regime* to a regime in which polymer chains are dilute and probe ions are condensed to single chains. With increasing R the local concentration of probe ions per macroion is raised linearly and spin-exchange broadening starts to dominate the lineshapes. Relaxation times of spin probes thus enter a *linear decrease regime* (regime 2 in Figure 3.18). In this regime, the rotational correlation time is expected to decrease slowly, as with increasing R the microviscosity of the domains of condensed probes is lowered.

At even larger R, a *saturation regime* (regime 3 in Figure 3.18) is attained when the maximum value of probe molecules that can be attached to each single, extended chain is reached. In this regime, spin-exchange interaction has the strongest effect on the relaxation time, which arrives at the minimum value. This is the case once the product of the fraction of probe ions that is condensed (f_{cp},

assumed to be constant) and the ratio of multivalent probe ions to polyelectrolyte charges is close to unity: $f_{cp}*R{\approx}1$. At these values for R, rotational dynamics only decrease slowly.

Finally, further increase of R leads into a local concentration *decrease regime* (regime 4 in Figure 3.18), in which there are more probe ions than can be condensed to the polymer charges. Because of the dynamic character of the condensation process, probe ions reside in the detached state for increasingly longer periods of time with a further increase of R. Rotational dynamics now reach a plateau minimum value. For $R{\rightarrow}{\infty}$, all parameters (concentration, linewidths and rotational dynamics) are again congruent with those of only probe molecules in the solvent.

In the two low-viscosity solvent systems, with increasing R stretch factors deviate ever stronger (linearly) from unity and the averaged relaxation times of all three hyperfine line manifolds decrease up to $R{\sim}0.05$, when they attain plateau values that are even almost identical. This behavior is fully consistent with the introduced model of DEA to polyelectrolyte chains in largely extended conformations. To be more precise, relaxation times and rotational correlation times indicate that the measured series of FS/PDADMAC in the low-viscosity solvent mixtures are in the *linear decrease regime* of Figure 3.18. Note that the strongest contribution to the R-dependent rotational mobility, as it was suggested in the simple scenario of Figure 3.18 and also observed (Figure 3.14.a), is an electrostatic effect. Furthermore, the dependence of stretch factors on R is strong evidence for this interpretation. With increasing R, stretch factors decrease linearly, starting from values that are close to those of the free probes in the solvents. This means, that the width of the linewidth distribution (see equation 3.2) increases with increasing R, in accordance with the expectation that there are higher contributions to the overall spectral linewidth by detached probes on the one hand and higher local concentrations on the other hand, the heterogeneity in relaxation time distribution increases.

The situation looks slightly different for the system in glycerol/water, in which the low-field line relaxation time is almost unaltered, whereas the center-field relaxation times decrease and the high-field relaxation times increase. Despite the obvious differences, FS/PDADMAC spectra in all three solvents have a certain feature in common, namely that the differences between the average relaxation times of the high-field line (triangles in Figure 3.12) and the low-field line (diamonds in Figure 3.12) become smaller with larger R-values. This corresponds to on average faster rotational motion of the counterion probe with decreasing polyelectrolyte content of the solution, which is displayed in Figure 3.14.a and is discussed in Section 3.3.5.

Trends similar to those in the two other organic solvent/water mixtures are observed in glycerol/water only for the stretch factor x and the averaged relaxation time $<T_{2,2}>$ of the center-field line (circles in Figure 3.12.c), which is the line least affected by changes in the rotational correlation time.[16] The decrease in relaxation time in the range $0 < R \leq 0.067$ for this line still reflects increased spin-exchange coupling and local concentration of spin probes, the same behavior of regime 2 in Figure 3.18 that was found for NMPA/water and ethanol/water as solvents. The plateau observed at very low R values with the decrease starting only after the third data point can be attributed to the fact

that at our lowest R values polyelectrolyte concentration is so high that we are in the *overlap regime* (regime 1 in Figure 3.18), which could not be observed in the low-viscosity solvents systems. In Figure 3.17, the ESE-detected EPR spectrum for R=0.0036 corresponds to this regime. In frozen solution, with all dynamic effects influencing the spectra removed, the EPR spectrum looks very much like that of pure FS – no broadening from increased local concentration is observed, which indicates roughly homogeneous dilution of FS in the polyelectrolyte solution. Furthermore, the linear decrease regime is evident when looking at the trend for ESE-detected spectra with increasing R - the broadening becomes gradually stronger.

The trend for the stretch factor x (open diamonds circles in Figure 3.13) also indicates similar behavior in glycerol/water as in NMPA/water and ethanol/water. Center-field relaxation times $<T_{2,2}>$ and stretch factors x thus indicate that PDADMAC chain conformation in glycerol/water is unaltered during increase of R and is similar to that in NMPA/water and ethanol/water.

Exchange broadening is expected to depend on viscosity, as the frequency of molecular collisions depends on the diffusion coefficient. For free diffusion and assuming that the Stoke-Einstein relation holds, the exchange frequency and thus also the linewidth is proportional to the inverse viscosity, so that $<T_{2,2}>$ should be proportional to the viscosity.[50] However, what we observe is a shorter $<T_{2,2}>$ (i.e. larger linewidth) in the glycerol/water mixture (higher viscosity) than in the NMPA/water and ethanol/water mixtures (lower viscosity) as well as a slightly larger deviation of the stretch factor x from unity (up to $R{\sim}0.067$). In particular the latter finding indicates that slower diffusion in the more viscous solvent causes build-up of a larger concentration gradient, so that local counterion concentration in the immediate vicinity of the polyelectrolyte chain would also be larger.[55] The collision frequency is proportional to local concentration, and the concentration increase may thus compensate or even overcompensate the decrease due to slowing down of translational diffusion. Note however, that part of the stronger broadening of the center line is due to slower rotational diffusion.[16]

The *saturation regime* of relaxation times in the explained model marks the "*saturation*" of DEA and not only proves the electrostatic origin of the observed spectral changes but also that there is an agglomeration of FS ions along a concentration gradient, which has been discussed in the section on the equilibrium between freely moving, territorially bound and site-bound counterions (3.3.1). To check if the departure of x from unity can be explained by a simple increase of bulk concentration of FS, whole concentration series of FS for $0.25mM < c(FS) \le 128mM$ in water and glycerol/water were recorded and analyzed following eqs. 3.2 and 3.3. The summary of these measurements can be viewed in Appendix A4: analysis of the data shows that even for 128 mM FS solutions the stretch factor is close to 1. The observed data trends in the three organic solvent/water mixtures can hence be fully reconciled with assuming extended linear polyelectrolyte chains with anisotropy of local spin probe concentration (perpendicular to the chain axis). With increasing ratio of FS to PDADMAC it becomes ever more obvious that large fractions of the divalent FS counterions sojourn in a small volume close to the polyelectrolyte chains, but they agglomerate along a *concentration gradient* from the

polyelectrolyte chains towards the free solution. This agglomeration is driven by the electrostatic attraction of the small divalent counterions and the charges on the polymer backbone.

Nominally, the ethanol/water and glycerol/water on the one hand and NMPA/water on the other hand should have very dissimilar dielectric properties (see Table 3.1). According to basic polyelectrolyte theory (Section 1.2), the distinct relative dielectric permittivities of these mixtures (ε_r~140 for NMPA/water and ε_r~50 for ethanol/water and ε_r~57 for glycerol/water) should lead to different Coulomb interactions between polyelectrolytes and counterions (probe ion) and by changing the solvent quality also to differences in backbone conformations. The remarkable piece of information in these data is that none of this expected behavior is observed, but rather identical DEA and polyelectrolyte-probe ion interaction seem to dominate. This leads to the conclusion that the assumption to model the solvent as just a dielectric continuum is in qualitative disagreement with our results. The proposed explanation for this finding is given in the next section, 3.3.4, when these findings are compared to the results of the purely aqueous system.

TAM/PDADMAC: from transient networks to single chains

Although direct comparison between data with TAM and FS as spin probe is not possible due to the entirely different molecular geometry, the results for the TAM probe (Figure 3.16.b, c) confirm the conclusions on exchange broadening for the FS probe. The trends for averaged relaxation times and stretch factors are similar in both investigated solvents, water and glycerol/water, which is a consequence of the lack of direct information on rotational dynamics. The thirteen-fold increase in viscosity (from water to glycerol/water) does not *qualitatively* change the effects on local concentration and spin-exchange upon variation of R. At R~0.03, a slightly lower value than for FS, $<T_2>$ also approaches a plateau value in both solvents (water and glycerol/water), but at lower values (i.e. broader lines) for the solutions in glycerol/water. Be reminded that in principle with increase in viscosity the *translational* diffusion rate of a molecule decreases and thus molecular collision frequency and spin-exchange coupling also decrease. This is not what is observed in this case: already in solution of pure TAM in water and glycerol/water, the stretch factor of lineshape analysis is 1.48 (water) and 1.31 (glycerol/water), respectively. These large differences to unity for the pure solutions are most likely due to residual anisotropic hyperfine interaction to ^{1}H nuclei on the 12 remote ethyl-alcohol side chains as suggested by Yong et al. (Ref. 91). These authors found that incomplete motional averaging of the tumbling motion for this large molecule has strong impact on the spin-spin relaxation time. This explains why $<T_2>$ is lower and the width of the relaxation time distribution is broader (lower x) in glycerol/water mixtures as compared to pure water, as in this solvent the residual hyperfine coupling is larger than in water. The sharp transition of $<T_2>$ from a steep decrease to a plateau when increasing R above values of 0.03 may correspond to a change from a strong *overlap regime* (similar to regime 1 in Figure 3.18) that is dominated by TAM molecules building transient physical crosslinks between PDADMAC chains (R<0.03) to a regime in which TAM molecules interact with single polyelectrolyte chains (regime 2 in Figure 3.18). Unlike in the case of FS in

ethanol/water and NMPA/water, such transient networks could explain exactly the difference in the sharpness of the transition of relaxation time behavior between FS and TAM spin probes. The reduced effective volume in a network causes more frequent collisions between TAM molecules than in the case of FS ions that at these R-values already interact with single PDADMAC chains. TAM counterions are much larger than FS ions, so that once the single chain regime has been reached ($R \approx 0.03$) the maximum local concentration of TAM counterions that can be accommodated by the chain (i.e. the saturation regime 3 in
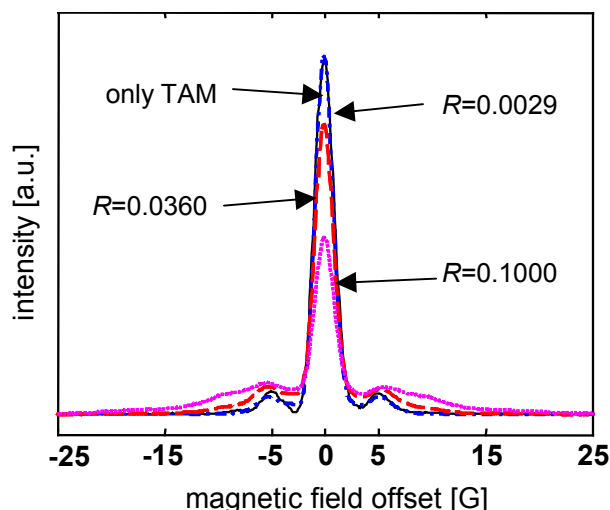

Figure 3.19. ESE-detected, field-swept EPR spectra of TAM/PDADMAC (X-band, ~9.7GHz) in glycerol/water at four different R-values. Black solid line: only FS; blue dash-dotted line: R=0.0028; red dashed line: R=0.036; magenta dotted line: R=0.100; All spectra are normalized to equal integral.

Figure 3.18) has already been attained. In the respective case of FS ions this saturated condensation is reached at $R \approx 0.05$. One should consider the different size of TAM counterions as compared to FS ions. TAM ions are rather large and geometrically anisotropic so that spin exchange coupling might not be correlated with spin probe collisions as simply as for the small FS ions. The only possibility for direct exchange interaction through collisions of the molecular orbitals bearing the unpaired electron is along the TAM C_{3v} symmetry axis. In the saturation regime, these collisions might have reached highest efficiency, hence the decoupling of changes in $<T_2>$ from changes in R. A further decrease of the polyelectrolyte concentration might in this regime only affect the TAM-TAM interaction weakly and then finally lead to the appearance of a fraction of TAM counterions that interacts more weakly with the partially neutralized (by TAM ions) PDADMAC structures and thus gives rise to a spectral component with a smaller linewidth as seen at R=0.1 in glycerol/water. This interpretation is also backed by the trends of stretch factors x in both solvents, both of which still decrease for R>0.03 but not as steeply as in the R-range 0-0.03.

Representative spectra of TAM + PDADMAC taken in frozen solution (T=80K) are displayed in Figure 3.19. It is clearly observable that there is more pronounced broadening at the wings of the single line spectra with increased R, but the effect is by far not as strong as seen from FS spectra in Figure 3.17. Note that the two doublets of peaks at ~5 G and ~10 G that are symmetrically placed around the main TAM line are assigned to so-called [1]H *spin-flip transitions*,[39] which are forbidden electron spin, ^{1}H nuclear spin double-quantum transitions that are excited by the microwave irradiation during the EPR measurement. They stem from ^{1}H nuclear spins, whose hyperfine couplings to the TAM electron spin are in the range of the nuclear Zeeman frequency (and twice that frequency) at the respective B-field (for X-band this is ~14.7 MHz=5.25 G). These additional peaks are already present

in the pure solvent and complicate the interpretation of the observed broadening. Nonetheless, the trend of the broadening in the spectra of Figure 3.19 is clear. At low *R*-values (0.0029) TAM spectra are very similar to those of TAM in absence of PDADMAC. The broadening then increases with increasing *R*, which can be interpreted as a consequence of increased dipolar coupling between TAM electron spins due to increasing local TAM concentration. The spectral lineshape at *R*=0.1 is most strongly broadened, which at first sight might oppose the results from room temperature measurements. Note that the mechanisms of spin probe interaction are different in fluid and frozen solution. As described in the case of FS counterions, in frozen solution only dipolar and through-solvent interaction contribute to broadening of spectra, whereas the main origin of broadening in liquid solution is collisional spin exchange. In this respect, frozen solution ESE-detected spectra are only sensitive to the inter-TAM distances in the samples. The average distances between TAM ions should still decrease even if individual TAM ions build physical crosslinks along single PDADMAC chains, as the overall volume in which TAM ions reside becomes ever smaller with decreasing polyelectrolyte content. So the trend of broadening of ESE-detected spectra in frozen solution can be fully reconciled with the interpretation of liquid solution data from Figure 3.16.

In order to check whether it is reasonable to assume TAM to be a physical crosslinking agent, force-field computer simulations were performed. Figure 3.20 shows a geometry-optimized structure (force-field simulation MMFF94, as implemented in SPARTAN) of one TAM trianion and an excerpt of a PDADMAC chain (16 monomeric units). This simulation, despite the idealized conditions (small chain, vacuum), nonetheless shows that the TAM molecule can have an immense impact on the local structure of the chain that it is attached to. Similar simulations for FS did not show any effect on the local PDADMAC geometry upon binding of FS. It seems safe to conclude that attachment of TAM can lead to a transient deformation of a chain, as the simulation suggests most probably a bending deformation. In addition, the crosslinking ability seems likely, as all three charges simultaneously
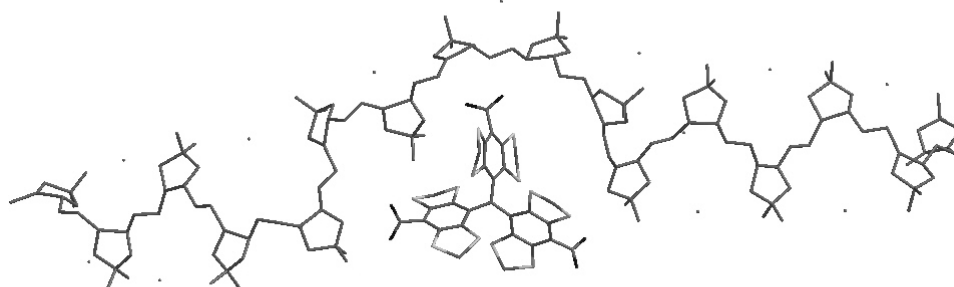

Figure 3.20. Geometry-optimized structure (force-field simulation, MMFF94) of the core of one TAM trianion and a short PDADMAC chain (16 monomeric units, including counterions). Upon electrostatic attachment of TAM the local chain structure is deformed and a "binding pocket" is formed. Note that the 12 sidegroups of the TAM radical are not shown for clarity.

interact with the chain and at high polyelectrolyte concentration (low R, c > c**) it is not possible to distinguish if adjacent charged units belong to the same or to different polyelectrolyte chains. The large organic TAM molecule may also interact with the polyelectrolyte chain by hydrophobic (i.e., of non-electrostatic nature) interactions, which may increase affinity to reside close to the polyion.[1,103,104]

In a recent publication, I have suggested that in the single chain regime TAM trianions do not only lead to local deformations of the chain,[22] but can also lead to locally collapsed chain domains or connect remote parts of individual chains, hence leading to *intra*-polyelectrolyte crosslinked structures. This possibility will be discussed further in Section 4.3, when additional high-field/high-frequency pulse EPR experiments are presented that quantitatively probe local distribution of TAM spin probes in frozen solution.

3.3.4 Effect of dynamic electrostatic attachment on polyelectrolyte chain conformation

In the last section it has been shown that in ethanol/water, NMPA/water and in glycerol/water as solvents, the broadening of the relaxation time distribution and the increase in local FS concentration can be consistently explained in a model of DEA to a linear extended polyelectrolyte chain (Figure 3.18). This is not the case for FS/PDADMAC in water, which can be seen from Figures 3.12.c and 3.13. The initial drop of relaxation times upon increase of R to 0.05 is much steeper than in ethanol/water or NMPA/water (those solvents with viscosities comparable to that of water) - in water they are almost halved, whereas in organic solvent/water they drop only by ~25%. The decrease of the stretch factors x is also more pronounced in pure water as solvent (from the linear fits at least twice as large as in ethanol/water) but the values for R>0.05 clearly deviate from the linear fit, so that for those fits only points up to R=0.06 have been taken into account. As the stretch factors are a measure of the distribution of relaxation times, it becomes obvious that this distribution in water this is different from that in the other solvents. Note that nominally the relative permittivity of water (ε_r=80) is in between the values for ethanol/water (ε_r=50) and NMPA/water (ε_r=140). For R>0.05, where the *saturation regime* (plateau of $<T_{2,k}>$) is reached in the organic solvent/water mixtures, in water the relaxation times again increase immensely and at R=0.126 attain values of ~10 μs. Interpretation of this unexpectedly large value seems more difficult than of the data corresponding to lower R-values. It can be deduced from the CW EPR spectrum and the respective fit (eq.
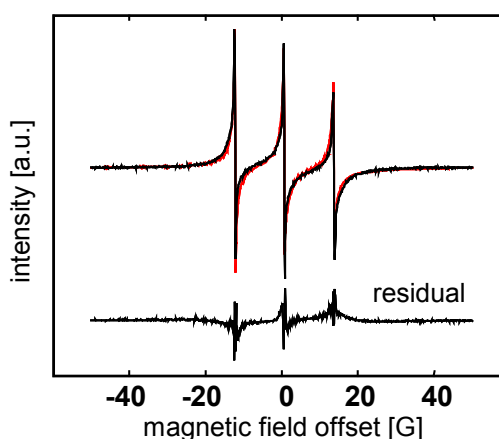

Figure 3.21. CW EPR (X-band, ~9.4 GHz) spectrum of FS in water with R=0.126 and spectral fit as described by equation (3.2).
Black solid line: EPR spectrum
Red line: Fit
The residual after subtraction of the fit from the spectrum is also shown.

3.2), which are shown in Figure 3.21, that the simulation of the spectrum is rather poor, but it is obvious that there is a simultaneous appearance of very sharp lines in the spectra and broadening of the flanks, which has increased to such an extent that it already distorts the lineshape and the baseline.

In comparison to FS data in the solvent mixtures, the development of the relaxation times suggests a far stronger spin-exchange interaction between FS spin probes and the plot of the stretch factor shows that the distribution of relaxation times grows more heterogeneous (i.e. x decreases) with increasing R (filled squares in Figure 3.13). The latter point is of special importance because the EPR spectra for those high R-values (see Figure 3.21) suggest that there are essentially free (unbound) FS ions - as seen in the narrow peaks – and strongly interacting FS probes, which is the explanation for the very broad flanks. Such a two-state scenario corresponds to a bimodal relaxation time distribution and would thus also explain why in this case only rather poor fits are obtained with stretched exponential broadening, which corresponds to a broad monomodal distribution.

Model: Polyelectrolyte conformational change upon increase of R

As a starting point for the interpretation of the data for purely aqueous solutions, one can picture a model that takes into account a polyelectrolyte conformational transition when the FS/PDADMAC ratio R is increased. Assuming that in the *overlap regime* (regime 1 in Figure 3.18) the small number of multivalent probe ions per chain is not sufficient to modify the extended chain conformations, the difference starts to come into play in the *linear decrease regime* 2. In this scenario, condensed counterions increasingly alter those parts of the chain to which they are condensed. By screening the electrostatic repulsion of chain backbone charges, condensed probe ions induce collapses of certain domains, so that with increasing R there are higher contributions from collapsed domains of single chains to the overall distribution of conformations. Such a collapse transition was first proposed by Khokhlov[105] and later discussed by several authors.[106-110] Schiessel and Pincus pointed out that, depending on the microscopic properties of the chains and counterions, a first-order type or second-order type collapse transition may occur.[107]

Increasing R thus also leads to a *decrease regime* like regime 2 in Figure 3.18, but with a much steeper increase of local concentration of probes as the chains are compacted. Probe counterions that interact with a globular domain of a macroion are confined to the smaller volume occupied by the collapsed chain and are thus more likely to collide with another probe counterion. This manifests itself in enhanced spin exchange broadening of CW EPR spectra. Consequently, at a certain point the simple Manning theory for extended chains breaks down and it becomes difficult to tell at which values for R the minimum corresponding to regime 3 in Figure 3.18 will be attained.

Despite this difficulty it is reasonable to assume that for the (partly) collapsed chains binding of multivalent counterions is less favored than for fully extended chains. This assumption is based on two effects. Firstly, if a chain is compacted, the loss of conformational entropy upon counterion binding is significantly higher. Secondly, in a collapsed domain of a polyelectrolyte chain there will be a close approach of multivalent probe ions at values for R, for which in the extended case average

distances are much higher. Therefore, intermolecular interactions of like-charged probe ions cannot be neglected any more. Thus the maximum local concentration of multivalent counterions will be reached at lower ratios R. Ejection of a significant fraction of counterions from a collapsed polyelectrolyte chain is also suggested by the theoretical treatment of Kramarenko et al.[106] It is quite hard to predict rotational dynamics in this scenario, because of the dynamic quality of the electrostatic attachment of counterions and also a change in the distribution of condensed and free probe ions as compared to the more simple scenario of Figure 3.18.

The data of FS/PDADMAC in water can be explained consistently with this model that includes a transition of PDADMAC chains from more or less extended conformations to states with higher contributions of globular conformations. In other words the observed behavior indicates that a *counterion-mediated chain collapse* takes place. This transition, which apparently has the character of a second-order transition, is completed at $R{\approx}0.06$, when the "most densely packed" collapsed state is reached. In analogy to regime 4 in Figure 3.18, linewidths decrease again with further increasing R-values. The very broad distribution of linewidths at these ratios (stretch factor as low as 0.2, see Figure 3.13) leads to the conclusion that with increasing R an increasing fraction of divalent probe ions resides in solution, where they experience collisions less frequently. In accordance with a scenario that includes a conformational transition of the polyelectrolyte, the mean relaxation time therefore increases after the collapse. This also indicates ejection of part of the counterions from the collapsed chain in agreement with predictions by Kramarenko et al.[106] and contradicting recent predictions by Solis and de la Cruz.[110] The estimate for $<\tau_c>$ may be not so reliable in this regime, as it is obtained by using the linewidth difference parameter B, which is ill-defined here due to the increasingly broad range of actual linewidths that contribute. Therefore, we refrain from giving an interpretation of the deduced effective $<\tau_c>$-values for $R{\geq}0.06$.

The fact that on the one hand spectral parameters of FS probes for ethanol/water, NMPA/water and glycerol/water as solvents behave very similarly, but on the other hand those parameters differ strongly from the pure water solvent values, is unexpected in the framework of basic polyelectrolyte theory. As outlined in the introduction, ethanol/water ($\varepsilon_r{\approx}50$ at 293 K) and glycerol/water ($\varepsilon_r{\approx}57$ at 293 K) are supposed to be better solvents than water for the hydrocarbon backbone of the PDADMAC polyelectrolyte, whereas NMPA/water with its much higher permittivity ($\varepsilon_r{\approx}140$ at 293 K) is viewed as a poor solvent. So, in ethanol/water and glycerol/water the PDADMAC chains should be less inclined to counterion-mediated collapse whereas in NMPA/water the collapsed state should be even more favorable than in water. Obviously, the basic theory, in which solvents are only considered as a dielectric continuum, fails to explain the observations made in this work. Apparently, the actual molecular structure of solvent molecules has to be taken into account. Despite the pronounced difference in permittivity, the chemical structures of NMPA and ethanol molecules are similar and even the trialcohol glycerol bears a strong resemblance to the other two solvent molecules. All molecules consist of a polar part and a small non-polar, alkyl part (propyl- and ethyl-groups for
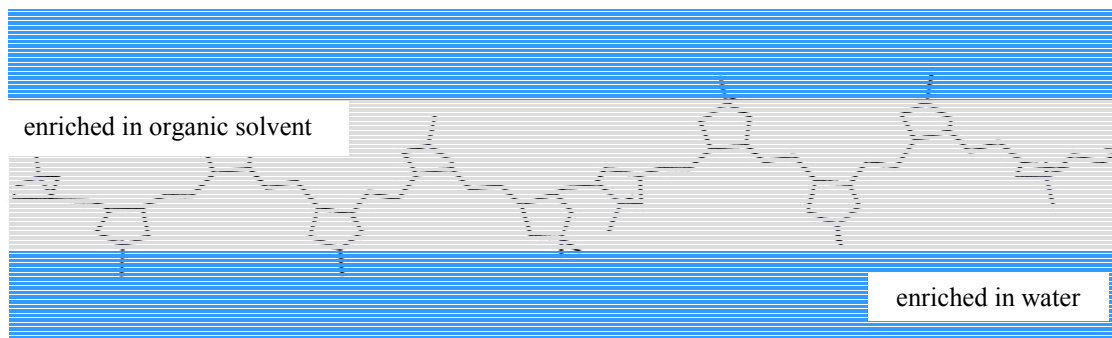
Figure 3.22. Sketch of the proposed preferential solvation of PDADMAC chains by organic solvents ethanol, NMPA, glycerol in solvent mixtures. The gray area around the chain backbone marks the area that on average is enriched in organic solvent. The areas that are enriched in water are marked in light blue.

NMPA and ethanol, respectively, and a propyl backbone for glycerol). These alkyl groups may solvate hydrophobic groups of the polymer chains and may thus "screen" hydrophobic interactions as it is sketched in Figure 3.22. This screening of the hydrophobic monomer-monomer interaction diminishes a driving force for a counterion-mediated chain collapse. The polar groups of the solvents may at the same time interact with the quaternary ammonium groups and the water molecules may be preferably located in the vicinity of the charges. Such preferential solvation was also suggested for phenol in ethanol/water mixtures on the basis of NMR data by Bagno et al.[111] Recently, a study of ethanol/water mixtures using neutron diffraction led to strong indications that such mixtures indeed show molecular segregation and ordering on a local level, which would also agree with the given interpretation.[112] The main conclusion that can be drawn is that permittivity (dielectric constant) of the solvent(s) is not the only significant and, possibly, not even the most important characteristic of the solvent mixtures.

Recently, systematic studies of FS ions in different solvents were have been started in our laboratory.[113] In these studies it has been found that there is a dependence of the effective charge of the FS ions on properties of the solvent mixture. Those results suggest that in water, on average, i.e., in a Debye-Hückel-like picture, there seem to be less potassium counterions close to the FS dianion than in solvent mixtures of ethanol, NMPA, or glycerol with water, so that one could argue that the FS ions interact with PDADMAC in water as dianions, while interaction with PDADMAC in the solvent mixtures might be regarded as that of ions with effectively less than two charges. In this picture, the proposed counterion-mediated chain collapse in water could be attributed to the higher charge density on the FS counterions rather than to preferential PDADMAC solvation. Taking into account rotational dynamics of the spin probe can help assessing the probability of this alternative explanation for the difference of relaxation times and stretch factors of FS/PDADMAC in water as compared to the solvent mixtures. In Section 3.3.1 it has been thoroughly explained that the dynamic electrostatic attachment in water proceeds through the same kind of attachment along the unique axis parallel to one nitrogen-sulfur bond in the FS molecule (see Figure 3.10). Hence, different site-attachment of FS to individual charges on PDADMAC chains cannot be held responsible for the observed deviations.
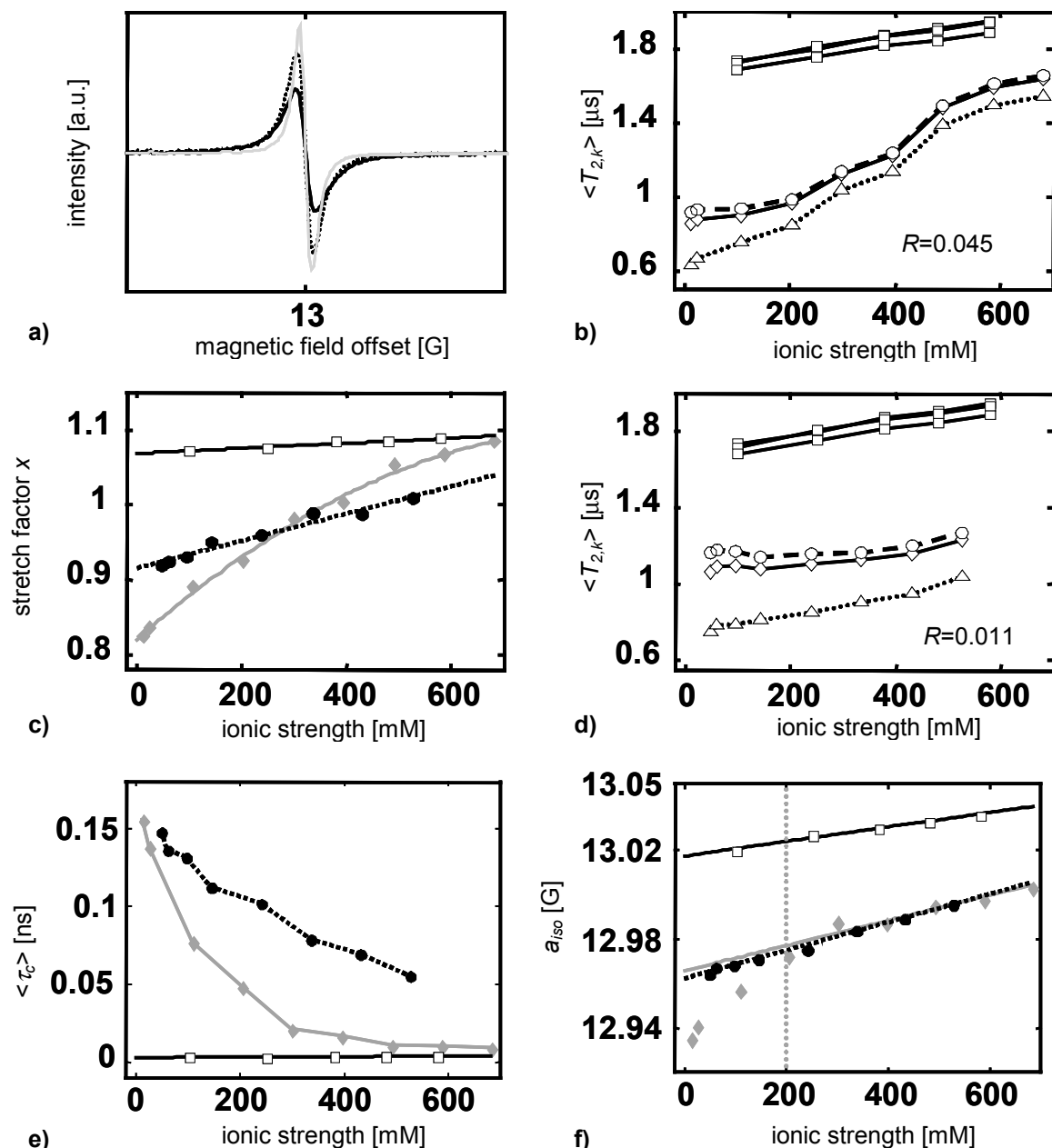
Figure 3.23. Dependence of CW EPR spectra (X-band, ~9.7GHz) and spectral parameters of FS/PDADMAC at three *R*-values in water on concentration of added inert salt NaCl.

a) High-field line of FS of the spectrum at *R*=0.045 without NaCl added (solid black line), at ionic strength of 220 mM (black dotted line) and at ionic strength of 690 mM (gray solid line);

b) averaged relaxation time (see eq. 3.3) of FS/PDADMAC at *R*=0.045; diamonds/solid line: low-field manifolds (*k*=1); circles/dashed line: center-field manifolds (*k*=2); triangles/dotted line: high-field manifolds (*k*=3); also shown are the values for pure FS (open squares/solid lines);

c) stretch factors *x* (see eq. 3.2) of FS/PDADMAC at *R*=0.045 (diamonds/gray solid line), at *R*=0.011 (filled circles/dotted line) and for pure FS (open squares/solid lines);

d) averaged relaxation time (see eq. 3.3) of FS/PDADMAC at *R*=0.011; diamonds/solid line: low-field manifolds (*k*=1); circles/dashed line: center-field manifolds (*k*=2); triangles/dotted line: high-field manifolds (*k*=3); also shown are the values for pure FS (open squares/solid lines);

e) averaged rotational correlation times of FS/PDADMAC at *R*=0.045 (diamonds/gray solid line), at *R*=0.011 (filled circles/dotted line) and for pure FS (open squares/solid lines);

f) isotropic hyperfine couplings of FS/PDADMAC at *R*=0.045 (diamonds/gray solid line), at *R*=0.011 (filled circles/dotted line) and for pure FS (open squares/solid lines); the dotted black line is a linear fit to the data of the *R*=0.011 sample, while the solid gray line is a fit to the *R*=0.045 data points at *I* > 200mM (marked by vertical dotted gray line);

Lines are meant as guides to the eye.

The only effect that cannot be excluded is a different "territorial binding" of the FS ions, i.e., that the charge neutralization by FS ions close to PDADMAC chains is more effective in water than in the solvent mixtures.

Within the framework of this work it cannot be unambiguously proven that the proposed preferential solvation of PDADMAC as depicted in Figure 3.22 actually takes place but together with the next section, 3.3.5, which is concerned with indirect observation of polyelectrolyte chain dynamics, the experimental findings strongly indicate this. In order to further substantiate the proposed counterion-mediated chain collapse, experiments were performed, in which inert salt NaCl was added to selected samples of FS/PDADMAC in water and in glycerol/water. Figure 3.23 combines experimental results of FS/PDADMAC at R=0.011 and R=0.045 and also for pure FS in water with variable amounts of NaCl added. In Section 1.1.2 the effect of increased ionic strength I on Coulomb interaction in the general case of electrolytes and the special case of polyelectrolytes has been introduced shortly (see eq. 1.9). The samples for the systematic investigation of the effect of increased ionic strength have been chosen from the linear decrease regime in Figure 3.12.c. (R=0.011) and from the minimum regime in averaged relaxation time (R=0.045). Figures 3.23 a-f clearly support the interpretation that at R=0.045 the chain adopts a different local structure than at R=0.011. Only after the addition of ~300 mM NaCl (ionic strength 320 mM) trends for the measured parameters of the 0.045-ratio-sample resemble those of the 0.011-ratio-sample. From the marked decrease of linewidths and rotational correlation times as well as the increase of a_{iso}, one may conclude that at very high ionic strengths (500 mM and higher) the electrostatic interactions are screened to such an extent that electrostatic attachment of divalent spin probes is effectively suppressed. For the series at R=0.011, trends of parameters like a_{iso}, $<T_{2,k}>$ and stretch factors x, are almost parallel to those of pure FS without PDADMAC added, they just differ in their absolute values. The strongly different, nonlinear dependence of the parameters on the ionic strength for the R=0.045 system indicates that in this system the probes are in an environment significantly different from that for the R=0.011 system, at least for I<300 mM.

This is clear evidence that the conformational ensembles at low I are different and that the difference is due to electrostatic effects. The earlier conclusion that the counterions are bound to polyelectrolyte chain that have larger contributions of collapsed conformations at R≈0.05 is thus further supported. Moreover, this allows estimating
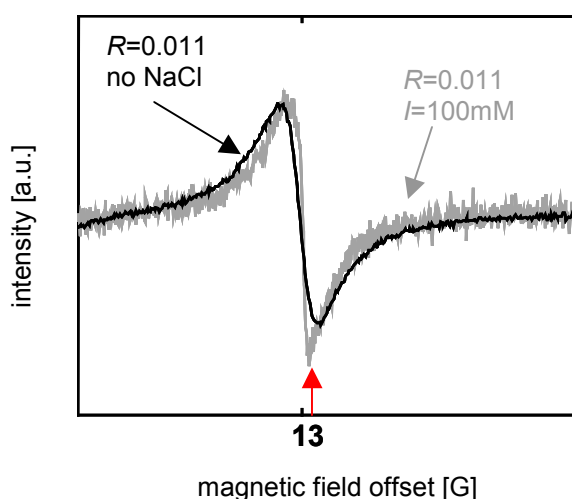

Figure 3.24. Detail plot of the high-field line manifold from CW EPR spectra of FS/PDADMAC (R=0.011) in glycerol/water. Black solid line: without addition of NaCl; gray solid line: at ionic strength I=100mM; analysis of the latter line according to eq. 3.2/3.3 was not successful; the red arrow marks a narrow feature that is superimposed on the broad line;

that the PDADMAC conformational transition induced by FS counterions in water takes place in the range $0.01 < R < 0.04$.

The same systematic series of measurements to probe dependence on ionic strength was performed for three samples ($R=0.011$, $R=0.045$ and pure FS) in glycerol/water. Figure 3.24 shows the high-field line manifolds of two samples ($R=0.011$) without salt added and with an ionic strength of $I=100$mM. The main difficulty for analysis of these spectra becomes obvious in this plot, as the rotational dynamics are slowed down to such a degree that the dynamic electrostatic attachment seems to be modified in glycerol/water as compared to the low-viscosity solvent water.

Because of the slowed down FS/PDADMAC dynamics, addition of intermediate concentrations of salt to those samples seems to screen electrostatic interactions such that one simultaneously detects a fast (detached) rotating FS species in addition to that fraction that partakes in *DEA*. Note that this is a consequence of slowdown in *translational* diffusion – the addition of salt reduces the effective electrostatic attachment sites but because in glycerol/water there is a huge difference in microviscosity between attached and detached states, they are separately observable in the CW EPR spectra. This makes it impossible to reasonably extract spectral parameters according to equations 3.2 and 3.3 and thus to get information on PDADMAC chain conformation but leads to the next point in the discussion, namely the effect of chain dynamics on the CW EPR spectra.

3.3.5   Indirect observation of polyelectrolyte chain dynamics

It is now the aim to separate dynamics of counterion attachment from overall dynamics of the polyelectrolyte chains. So far, dynamic electrostatic attachment was treated as the attachment of a highly mobile counterion to a fully rigid charge on the polymer backbone. In this section not only the differences of counterion attachment in low-viscosity solvents as compared to the high-viscosity system glycerol/water is worked out, but also the disparity between *DEA* of TAM counterions, which are not directly sensitive to rotational reorientation, and FS ions is accentuated.

As the EPR transition frequency of the TAM spin probe at X-band frequencies (~9.7 GHz) does not significantly depend on orientation, the strong line broadening on addition of polyelectrolyte can only be due to a change in the environment of the probe, but not due to changes in rotational dynamics (translational dynamics may change collision frequency and thus broadening). The observed strong changes with maximum broadening at low polyelectrolyte concentration are easily rationalized by enrichment of this counterion probe close to the polyelectrolyte chain, resulting in more frequent collisions and thus in Heisenberg spin exchange broadening. Any alternative explanations such as for instance effects of different local oxygen concentration could hardly explain changes of the observed magnitude. The continuous decrease of stretch factors x and thus deviation from Lorentzian lineshape then proves a heterogeneous distribution of the TAM probes, i.e., a concentration gradient.

The same effect is apparent in the spectra of the FS spin probe, but in this case the spectrum is in addition sensitive to rotational diffusion. The presence of polyelectrolyte causes a moderate

slowdown of this motion, with apparent rotational correlation times increasing with increasing polyelectrolyte concentration and never exceeding 1 ns (see Figure 3.14).

These findings exclude the simplest model of counterion condensation in which one fraction of the counterions forms long-lived (lifetime $\geq$ 1 ns), *static contact ion pairs* with ionic groups of the polyelectrolyte while the remainder freely diffuses in solution. In such a case, the condensed counterions would contribute a spectral component analogous to spin labels attached to a polymer chain (restricted sidegroup motion, no isotropic averaging on the EPR timescale), while the freely diffusing probes would contribute a narrow component with the same $<\tau_c>$as observed in the absence of polyelectrolyte. It has been explained in Sections 3.2 and 3.3.1, when the concept of *DEA* was introduced, that such bimodal spectra are not observed. In contrast, almost isotropic averaging (i.e. fast rotation about all three molecular axes) for the vast majority of the spin-carrying counterions on a sub-nanosecond timescale is evidenced. The details of CW EPR spectra shown in Figure 3.24, though, show that by screening electrostatic interaction in glycerol/water, one can observe a fast-rotating component of fully detached counterions in addition to that fraction that is dynamically attached to PDADMAC chains. It is justified to view this as a bimodal spectrum, and comparison of Figures 3.24 and 3.23.a clarifies that this is a consequence of the slowdown in translational diffusion – in pure water no such appearance of a distinct fast species is detected.

In the absence of charge screening by NaCl there is no indication for bimodal spectra in glycerol/water despite higher solvent viscosity and thus both slower polyelectrolyte chain dynamics and slower translational diffusion of the counterions.

Note that contact ion pairs consisting of two ions with different charge as introduced in the sections on DEA have been extensively discussed before in the context of solutions of low molecular weight electrolytes (see, e.g., Ref. 114) and that for ion pairs formed after covalent bond breaking the dynamics of dissociation and reencounter have been studied by picosecond absorption spectroscopy.[115] Results of the latter study show that the lifetime of ion pairs consisting of a diphenylmethyl cation and a chloride anion in acetonitrile is on the order of 150 ps. A model of dynamic electrostatic attachment in which at any given time there exists a fraction of contact ion pairs with such a short (sub-nanosecond) lifetime could be reconciled both with Manning theory and the results presented in this work.

The CW EPR spectra discussed here depend on local concentration and rotational dynamics of the spin-carrying counterions. A qualitative or semi-quantitative discussion of their dependence on R should thus consider the radial counterion distribution in the vicinity of the chains and the three dynamic processes indicated in Figure 3.25:

a) attachment/detachment of counterion probes due to translational diffusion,

b) rotational diffusion of freely diffusing spin probes, and

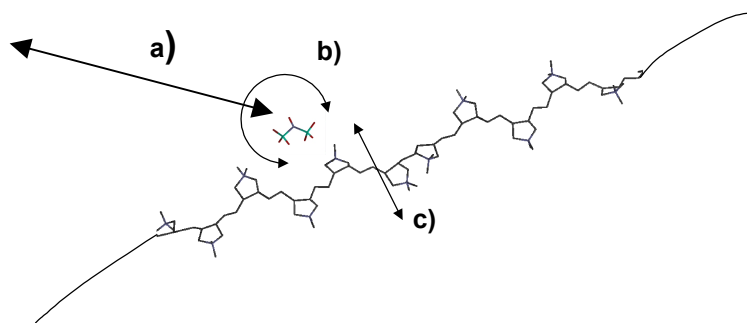c) reorientation of attached counterion probes due to polyelectrolyte chain dynamics.

Figure 3.25. Sketch of the domain of an FS spin probe electrostatically attached to a PDADMAC chain. This is meant as a snapshot of the state when the spin probe is very close to the chain. Three dynamic processes are important: **a)** attachment – detachment dynamics; **b)** rotational dynamics of FS spin probe; **c)** motion of PDADMAC polyelectrolyte chains. A fully stretched polymer conformation is not implied.

While quantification of the counterion distribution has been undertaken in a model-free approach in Section 3.3.3 and will be reassessed within a model from recent polyelectrolyte theory later (Section 4.1), the second point b) has already been in focus in Section 3.2 and 3.3.1. In this section, it is tried to identify which of the processes dominate spectral lineshapes in which regimes of solvent viscosity and polyelectrolyte concentration.

In 3.3.3 it has been explained why the trend for the low-field ($<T_{2,1}>$) and high-field ($<T_{2,3}>$) averaged relaxation times in glycerol/water clearly differs from the one in low-viscosity solvents. Since in glycerol/water mixtures these linewidths are dominated by slow rotational diffusion, experiments in this solvent mixture are better suited for characterizing dynamic attachment than experiments in low-viscosity solvents.

The larger sensitivity of the glycerol/water mixture to dynamics rather than concentration gradients is manifest in the plot of $\langle \tau_c \rangle$ (Figure 3.14). In the *R*-range from 0 to 0.067 good fits are obtained for a linear dependence of $\langle \tau_c \rangle$ on *R* for all solvent systems but the slope of the decay for glycerol/water is fivefold the one for ethanol/water, sixfold the one for NMPA/water and even twelve times the one for water. The results for the rotational diffusion rates and the respective anisotropy of the diffusion tensors in the different solvents summarized in Table 3.2 at least qualitatively show similar trends as the estimated rotational correlation times $\langle \tau_c \rangle$ - most effective slowdown in glycerol/water, least effective hindrance of rotational diffusion in pure water and intermediate behavior for ethanol/water and NMPA/water. This is also a good check for the applicability of the applied estimation of $\langle \tau_c \rangle$, since it delivers similar trends as fitting with a physical model of anisotropic rotation and moreover is inherently model free.

It is apparent from Table 3.2 and Figure 3.14 that the slowdown of rotational diffusion in glycerol/water mixtures with respect to the other solvents is much more dramatic at small *R*-values (high polyelectrolyte content) than in the absence of the polyelectrolyte (slowdown by only a factor of 2.3) or in the presence of only a small concentration of polyelectrolyte. Therefore, this slowdown

cannot be attributed to the viscosity effect on rotational diffusion of the paramagnetic counterion that is described by the Stokes-Einstein relation or a modified version of this theory.[116,117] Indeed, a stronger dependence of $\langle \tau_c \rangle$, $d_{\parallel}$, and in particular $d_{\perp}$ on solvent viscosity is expected for dynamically attached counterions than for freely diffusing counterions for two reasons. First, slower translational diffusion may increase the lifetime of the attached state. Second, influence of the viscosity is much more dramatic for the polyelectrolyte molecule with its large radius of gyration than for a small probe. Residual motion in the attached state is thus dramatically reduced and this effect is detected in slowdown of rotational reorientation of those attached FS ions.

Hence, increased solvent viscosity seems to influence the points marked a) and c) in the text and in Figure 3.25. The slowing down of rotation of attached FS ions could even be a direct consequence of the increased lifetime of the attached states: the FS reorientation is influenced for longer intervals by the chain reorientation, which of course is dramatically slower in the high viscosity mixture than in lower-viscosity solvents. Also, local chain fluctuations are slowed down in high viscosity solutions, which in return could increase the lifetime of the attachment by decreasing the amplitude of polyelectrolyte motion - the attachment lifetime of course depends on the *relative* diffusion of chain and counterion.

One can deduce that the opposite effect is dominant in samples of FS/PDADMAC in water (at least before the proposed conformational transition). Rotation perpendicular to the unique attachment axis ($d_{\perp}$ from Table 3.2) is roughly one order of magnitude faster than in the other solvents and the $\langle \tau_c \rangle$-values of aqueous samples are the fastest in the whole R-range and show least dependence on PDADMAC content. These findings point towards shorter lifetimes of the attached states ($d_{\parallel}$ should be much less affected by attachment) and may also be an indication that local chain fluctuations might be faster and relevant on the timescale of DEA in purely aqueous solution. The last point could also be reconciled with the proposed difference of PDADMAC backbone solvation in water and the organic solvent/water mixtures, since preferential solvation of the chain backbone and hence what has been called *screening of hydrophobic interactions* in 3.3.4 could also reduce local chain motion by formation of a solvent cage around the polymer segment. Thus, in water these local chain movements could explain that rotation perpendicular to the unique axis is much faster in water than in the other low-viscosity solvents.

The plots of the isotropic ^{14}N hyperfine couplings a_{iso} (Figure 3.15) contain additional, time- and space-averaged information on the local environment of the spin probe. In Section 2.3 it has been rationalized that the coupling of the unpaired electron to the NO nitrogen is influenced by factors such as proticity and polarity of the local surroundings. In this respect the plots from Figure 3.15 are quite remarkable, as trends for a_{iso} are almost identical in the three low-viscosity systems but fundamentally different in glycerol/water. In the latter solvent, a_{iso} increases linearly with increasing R and approaches its value in the absence of polyelectrolyte at high R-values (low polyelectrolyte content). In contrast, in the low-viscosity solvents a_{iso} approaches the respective pure solvent value at low R-

values, i.e., high polyelectrolyte content, but the deviations are so small (maximum of ~0.01G) that quantitative interpretation seems futile.

Qualitatively, the difference between glycerol/water and the other solvents could be attributed to different timescales of DEA and lifetimes of the attached state, respectively. The timescale of isotropization of the hyperfine coupling is correlated to the typical time of rotational and translational diffusion of the spin probes. In this respect, it is fully consistent with the explained longer lifetime of attached states and slower PDADMAC chain reorientation that a_{iso} in glycerol/water shows this linear dependence on R: the closer and more abundant polyelectrolyte residues are to the FS ions (i.e., the lower R), the more hydrophobic the surroundings and the stronger the deviation of a_{iso}. In the low-viscosity solvents especially the translational diffusion of counterions, which mainly dominates the attachment-detachment process a), seems to be so fast that during the isotropization (which can effectively be viewed as an integration over couplings in a certain time interval) much stronger contributions from FS ions in the detached state are detected.

4 Interpretation Based on Models from Polyelectrolyte Theory

In this chapter, departing from the qualitative, essentially model-free analysis of Chapter 3, specific physical models are used to interpret data gained from diverse EPR experiments.

The first section, 4.1, contains an analysis of the series of CW EPR spectra of PDADMAC/FS in the different liquid solvent system. This analysis is based on a recent theoretical model of *radial counterion distribution*[35] in polyelectrolyte solutions and delivers quantitative information on the radial distribution of the spin carrying counterions.

In Section 4.2, data from DEER experiments (see 2.6.3 and 3.2.1) on FS spin probes in frozen solution of PDADMAC are presented and analyzed in terms of a simple two-state model of counterion distribution. In contrast to the radial distribution investigated in 4.1, these data allow insight into the counterion distribution *along* the polyion chains.

In the final section, 4.3, the focus is shifted from the small FS spin probe counterions to larger TAM ions in glassy, frozen PDADMAC solution. A series of high-field/high-frequency (W-band, ~94 GHz) ESE-detected EPR spectra and their broadening due to dipolar interaction between spin probes is examined. Average distances and the relative fractions of strongly dipolar coupled organic TAM ions are extracted and a model of cooperative counterion binding is discussed that can explain the obtained parameters.

4.1 Radial distribution of spin probes around polyelectrolyte chains

Only four parameters were the basis for the qualitative and quantitative interpretation of the complete series of CW EPR spectra of FS/PDADMAC and TAM/PDADMAC in solution in the last Chapter:

i)   the *isotropic hyperfine coupling splitting* of FS counterions that has been extracted from fits of the CW EPR spectra,

ii)   *averaged relaxation times* (eq. 3.3) that were identified as a measure of the counterion-counterion interaction,

iii)   *stretch factors* (eq. 3.2), which delivered a quantification of the distribution of relaxation times and the buildup of a local concentration gradient of spin probes, and finally

iv)   *rotational correlation times*, which together with the more sophisticated analysis of rotational diffusion (Sections 3.2/3.3.1) allowed analysis of the counterion and polyelectrolyte chain dynamics.

As mentioned before, analysis according to these four quantities is inherently model-free, i.e., it does not make use of a specific model of polyion-counterion structure or dynamics. In this section, an alternative approach to fitting of the CW EPR spectra in solution is presented that has been derived from a theoretical model describing the polyelectrolyte chains and the surrounding volume of territorial binding as *cylindrical cells*. This alternative analysis aims at characterizing the distribution of spin probe counterions in a physical picture by replacing the interpretation based on parameters ii) and iii).

4.1.1   The charged cylindrical cell model

In a recent publication (Ref. 35) Deshkovski, Obukhov, and Rubinstein have developed an exact solution to the nonlinear Poisson-Boltzmann equation for systems of dilute, rodlike polyelectrolyte and counterions in the cylindrical region around them (see Figure 4.1). In contrast to earlier approaches, these cylindrical structures may bear a net charge, which is a major improvement as compared to former developments of the cylindrical cell model (Section 1.2.3). It is outside the scope of this work to reproduce the full derivation of the model within Poisson-Boltzmann theory. For the purpose of this thesis, it suffices to point out that the theoretical derivation identifies three qualitatively different regimes of counterion distribution, which shall be explained in brief in this section.

The subsequent section then presents the implementation of CW EPR spectral analysis according to the model. Figure 4.1 schematically summarizes all assumptions underlying the model by Deshkovski et al. The solution of elongated, rigid polyelectrolyte chains is supposed to be dilute (no interaction between individual chains, length L<radius of the spheres indicated by dashed lines) and for counterions it is in general energetically favorable to be located within the cylindrical volume around the chains. In the case of multivalent counterions, there is an additional entropic gain to be located in the cylindrical regions and to expel (at least some) monovalent ions to the spherical shell volume. The cylinders in general need not be electroneutral, which is the main advance in comparison to the previously established cylindrical cell-type models of polyelectrolyte-counterion interaction (Section 1.2.3). For this special model, Deshkovski et al. were able to solve the nonlinear Poisson-Boltzmann (PB) equation within a mean-field approximation in an algebraic.

A summary of the full derivation of this solution can be found in the very concise original publication by these authors (Ref. 35).
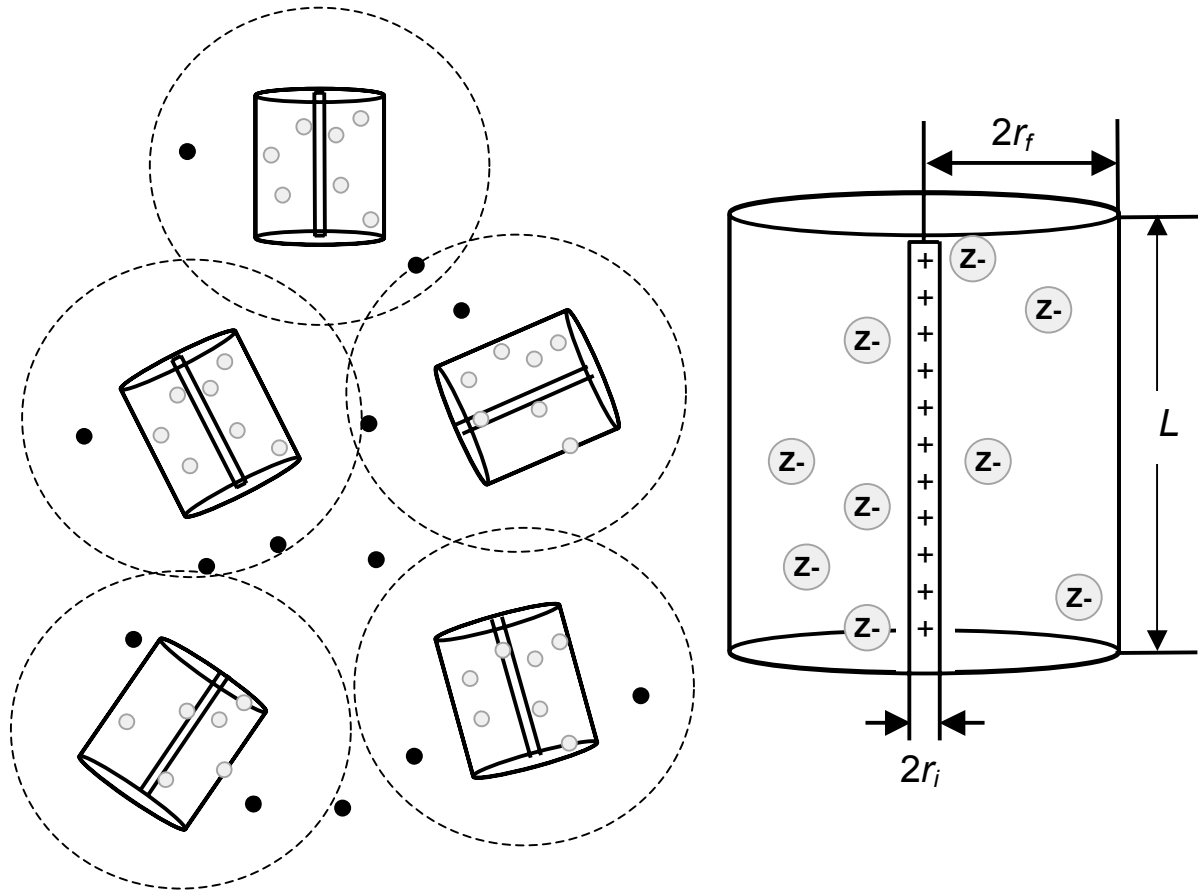
Figure 4.1. Sketch of the cylindrical cell volume description of dilute solutions of rigid polyelectrolytes (adapted from Figure 1 of Ref. 35). L is the chain length, r_i marks the initial and r_f the final radial coordinate of the cylindrical volume; Those counterions of charge $z-$ that are within the cylindrical volume are shown in gray, those that are outside of this volume are drawn in black; The dashed circles around each cylinder indicate the spherical volume, in which the counterions are effectively unbound (no electrostatic interaction with the polyions); Note that cylinders need not be overall electroneutral;

Counterion distribution

The solution obtained by Deshkovski et al. is strictly valid only for monovalent counterions and they find that the natural boundary conditions for the general PB equation in their model are determined by two parameters. The normalized bare linear charge density along the polyion, γ_0, on the one hand and the normalized net linear charge density of the cylinders, γ_R, on the other hand govern the counterion distribution in the system. The authors identify three distinct regimes (they denote them as *phases*, but the word regimes is probably more adequate) of charged chain-counterion distributions that are defined by γ_0 and γ_R, which all have in common that at intermediate radial distances r from the chains ($r_i < r < r_f$) the counterion concentration c(r) shows a power-law dependence on the radial distance:

$$c(r) \propto r^{-2\gamma}. \tag{4.1}$$

The scaling exponents γ and hence the shape of the counterion distribution are different in each of these phases. The resulting three regimes of counterion binding are characterized in the following paragraphs.

Phase I: $\gamma = \gamma_0$, $\gamma_0 < 1$, "weakly charged polyions"

In this regime, the chain is only weakly charged and counterion condensation as described by Manning has not yet commenced. By estimating the number of counterions N at a typical lengthscale r:

$$N = 2\pi \int_r^{2r} c(r') r' dr' \propto r^{2(1-\gamma_0)} \,,$$ (4.2)

which increases with r, one can illustrate that most of the counterions in the cylindrical volume are far away from the charged central chain of the cylinders.

Phase II: $\gamma = 1$, "saturated condensation"

In the second regime, the chain is strongly charged and Manning condensation is fully active. Counterion concentration does not depend on charge densities γ_0 or γ_R and obeys a simple $c \propto r^{-2}$ dependence. Estimation of the number of counterions N at a typical lengthscale r:

$$N = 2\pi \int_r^{2r} c(r') r' dr' \propto r^0 \,,$$ (4.3)

now gives a value independent of r. This regime is called saturated condensation, as moderate changes in the charge densities γ_0 or γ_R do not significantly alter the counterion distribution in the cylinders. In the (γ_R-γ_0) phase diagram of the calculated system (see Ref.35) this is the phase most likely attained by the system for intermediate to high linear charge densities on the chain γ_0 and low to intermediate charge densities on the cylinders γ_R.

Phase III: $\gamma = \gamma_R$, $\gamma_R > 1$, "unsaturated condensation"

This regime is rather similar to phase II, Manning condensation is active but the concentration profile is much steeper (i.e., counterion concentration drops off even quicker than in phase II), which is obvious from the $c \propto r^{-2\gamma_R}$ dependence ($\gamma_R > 1$). The number of counterions N at a typical lengthscale r is given by:

$$N = 2\pi \int_r^{2r} c(r') r' dr' \propto r^{-2(\gamma_R - 1)} \,.$$ (4.4)

Most of the counterions are very close to the chain and the remainder of the cylindrical volume is only sparsely occupied by the counterions.

The challenge for EPR spectroscopy is now to provide information on the r-dependence of the counterion concentration by analysis of the broadenings in the CW EPR spectra of FS in solutions of PDADMAC

4.1.2 Spin probe radial distributions from analysis of CW EPR spectra

In this section, the CW EPR spectra of the spin-carrying counterions in solutions of PDADMAC polyelectrolyte are re-examined within the introduced model of charged cylindrical cells. It was described in Section 3.3 that the CW EPR spectra of these spin probes contain information on the local concentration, which constitutes the link between EPR experiments and the theoretical treatment of counterion distribution.

The materials used in this study clearly do not fulfill some of the assumptions that were made in the derivation of this theoretical description of counterion binding. There are several points that seem problematic when applying such an idealized theory to experimentally accessible systems. First, the tracer counterions that are detected by the experiments are divalent (FS) or trivalent (TAM) ions with spatially separated charges and not monovalent and point-like. Second, PDADMAC chains are intrinsically flexible. Although, they are likely to attain some additional rigidity (longer persistence length) due to electrostatic repulsion of the backbone charges (OSF theory), which is also strongly supported by the results from section 3.3.4 at least for solvent mixtures, those chains are certainly not fully rigid-rodlike as assumed in the model (see Figure 4.1). Third, the PDADMAC polyelectrolyte material has a high polydispersity, so that there are a lot of different chain lengths simultaneously in solution, i.e., L varies. Finally, it is doubtful that throughout the whole R-range the PDADMAC solutions can be depicted as highly dilute.

Despite all these aspects, one can justify the use of the above-developed model for analysis of the studied systems. Our spin-probe counterions never represent more than ~12% of all the counterions of the system. Of course, it is expected that they (as di- and trivalent ions) expel a certain fraction of the original chloride counterions from the "condensed" states, but nevertheless they are certainly embedded within the large overall excess of monovalent counterions. In addition, at least FS ions are also still rather small, i.e., the model of point-like counterions is not unreasonable for FS.

The facts that PDADMAC is not a rigid-rod polyelectrolyte and that the used samples are highly polydisperse may not play as decisive a role in the characterization of EPR data as in the original theory. In Section 3.3 it was shown that at least in the organic solvent-water mixtures the observed trends of relaxation times and stretch factors (eqs. 3.2 and 3.3) can be fully reconciled with counterion condensation to linear, extended polyelectrolyte chain segments. This shows that on the EPR-sensitive length- and timescales for these systems one can assume locally elongated chains. If this is true, though, the respective simulation and fitting of FS/PDADMAC in pure water should yield significantly different results, as otherwise either the proposed conformational transition of PDADMAC in water could not be reconciled with this theoretical approach, or the model would poorly describe phenomena that are clearly manifested in the model-free description.

The high polydispersity of the samples can be neglected if one assumes that all chains are in similar conformations. The high molecular weight of the PDADMAC polyelectrolyte ensures that, in spite of the broad distribution of chain lengths, even the shortest chains are significantly longer than the EPR-sensitive lengthscale. For the magnetic parameters of the spin probe counterions it is insignificant whether they are attached to a chain consisting of 100 or 1000 repeat units.

Unlike uncharged polymers, aqueous solutions of polyelectrolyte materials in general are in the semi-dilute regime already at very low concentrations, which is a consequence of the long-range electrostatic interaction (see Section 1.2.1). Independent of the degree of polymerization, for PDADMAC this overlap concentration was reported to be c**=2.08*10^{-2} mol/l (in monomeric units) by

Wandrey et al. (Ref. 83). It was also remarked in Section 3.3 that indication for an "overlap regime" is found by analyzing spectral parameters of FS and TAM spectra at very low R-values. Thus, it also seems likely that at high polyelectrolyte content, the counterions are in the attraction sphere of several chains simultaneously. This presents a problem for the suitability of the charged cylindrical cell model, which can, however, be mitigated if r_f, the value determining the cylinder volume (Figure 4.1), is chosen short enough. Such a choice is possible, as electroneutrality of the cylinders is not required. Additionally, one has the advantage that at high polyelectrolyte concentrations the spin-exchange interaction between spin-probe counterions is weak (this is observable already in the primary data and has been quantitatively characterized in 3.3.2) and is likely to have only minor influence on the spectra.

Reassessment of CW EPR spectra: Counterions in the phase of saturated condensation in the charged cylindrical cell model

In Section 3.3.2 the model-free characterization of CW EPR spectra was introduced. Fits of the CW EPR spectra were obtained from the time-domain signal of eq. 3.2 after FT and pseudomodulation of the spectrum.[67] In that equation, the broadening was included in the stretch factor that effectively lead to a distribution of Lorentzian linewidths. In this section, the three lines of the CW EPR spectra are each fit to a single Lorentzian line, i.e. the time-domain signal is fit to a single exponential decay. The broadening will now be introduced into the spectra by convolution with a physically motivated broadening function that will be derived in the following paragraphs.

First, one has to clarify which of the three regimes of counterion binding from the charged cylindrical cell model might be appropriate for modeling the investigated system.

Simply from the chemical structure of PDADMAC and the qualitative analysis of CW and pulse EPR data of Section 3.3 phase I can be excluded. In this regime, the polyion would be only weakly charged and the system would be below the threshold of Manning condensation of counterions – both of these features clearly contradict the previous findings.

Phase II and phase III are both regimes in which Manning condensation dominates polyion-counterion interactions. The main difference between these two phases lies in the distribution of counterions within the assumed cylindrical volume around one polyelectrolyte. It is important to note that for the PDADMAC systems in the dilute regime, the cylindrical cells should be (nearly) fully neutralized, i.e., γ_R should be low, but also γ_0 should be high (PDADMAC chains have a high charge density). This leads to the conclusion that if the charged cylindrical cell model is applicable to the investigated PDADMAC solutions, phase II is most likely the appropriate regime for the description. Only a small fraction of all counterions belongs to the class of multivalent spin probes, but even from the simple arguments of Manning theory, they should be preferred in the "condensed" (to the polyion chain) state. Hence, on the one hand the overall system is most probably in the regime of "saturated condensation" but on the other hand the observed counterions belong to a preferably bound class of counterions. In the last section it was shown that the spin-carrying counterions partake in dynamic

electrostatic attachment (DEA) on a sub-nanosecond timescale. Although the original PDADMAC counterions, Cl⁻-ions, are constitutionally different from FS-ions, it seems very unlikely that their mode of attachment is qualitatively different from DEA. In addition, from the model-free approach of Section 3.3 the buildup of a concentration gradient and thus heterogeneity on the nanoscale for the spin probe counterions could be deduced. Because of the fast attachment-detachment equilibrium of all counterions, the nanoheterogeneity of FS (or TAM) concentration, and the large excess of monovalent counterions it seems impossible to characterize the counterions separately on the length scales of the cylindrical cells.

Consequently, the broadening function that is used for fitting of the experimental CW EPR spectra must be derived from equation 4.1 with the scaling exponent $\gamma=1$.

The surface A of a cylinder as shown in Figure 4.1 has a radial dependence of $A \propto r$. Together with the assumed $c \propto r^{-2}$ dependence from the charged cylindrical cell model this amounts to a scaling of the number of counterions at given distance r from the chain with r^{-1}. The computational implementation (neglecting constant terms) of this established relation into a broadening function is shown in equation 4.5 and will be explained in the following:

$$V(t) = \int_{r_i}^{r_f} r^{-1} \exp\left[-\frac{r^{-2}}{r_i^{-2}} c_0 t\right] \cdot \sum_{k=1}^{n} \exp\left[-\frac{t}{T_{2,k}}\right] \exp\left[i\omega_k t\right], \qquad (4.5)$$

where $V(t)$ is the simulated EPR time-domain signal, $n = 1$ for TAM and $n = 3$ for FS spin probes with $k = 1$ corresponding to the low-field line and $k = 3$ corresponding to the high-field line.

In equation 4.5, the time-domain signal for a single line with resonance offset ω_k, and characteristic transverse relaxation time T_2 in the absence of exchange broadening, is now given by the second factor on the right hand side, a single exponential decay function. Exchange broadening is introduced by integration over the pre-exponential factor r^{-1} (as explained before) multiplied by the exponential function that converts the r^{-2}-dependence of the local concentration into a Lorentzian line broadening in the limits from r_i to r_f (see Figure 4.1). This is the first factor on the right hand side of eq. 4.5. The crucial parameters that determine the magnitude of the broadening are the boundary values for the integration, r_i and r_f, and the initial concentration c_0 of counterions at the radius of the chain surface, r_i. The integration is performed numerically in a home-written program (in MATLAB 6.1, The Mathworks, Inc) by use of an adaptive recursive Simpson algorithm (as implemented in this release of MATLAB). This numerical integration is the time-determining step of the simulation and on average a complete fit of one spectrum requires a processing time of at least two hours on a recent PC. The parameters of equation 4.5 that were allowed to vary during the fitting procedure were $T_{2,k}$, which accounted for the different peak-to-peak linewidths stemming from alterations in dynamics, and c_0, the initial concentration at the interface of the polymer chain backbone to the cylindrical cell volume. The critical parameters r_i and r_f were carefully chosen and not varied with change in R. The inner radius was set to $r_i=0.4$ nm, a value chosen from the 3-pulse ESEEM ratio analysis of Section 3.3.1, in which

a minimum distance for contact ion-pairs of FS and PDADMAC of $r_{e\text{-}N}$~0.43 nm was found for all samples investigated.

The value for r_f was more difficult to approximate. A rough approach was followed by assuming chains consisting of 1500 repeat units (M_W/M=240 000g*mol^{-1}/161.5 g*mol^{-1} ≈1500) and distributing them homogeneously according to their nominal concentration into a cubic lattice. These chains then statistically occupy an average cubic volume V with a side length of r_c=$V^{1/3}$. For the sample most concentrated in polyelectrolyte (139 mM, R=0.0036) r_c is 25 nm, whereas for the most dilute sample (3.9 mM, R=0.126) r_c has a value of 90 nm. Both of these values (and several in between) were tested as upper integration limits r_f in the fitting program and resulted in rather good simulations of the tested spectra (R=0.022). Only for values much lower than 25 nm the broadening term in equation 4.5 could not reproduce spectral broadening. For the final data analysis the lower limit of r_f=25 nm was used, as this value should be a valid minimum upper integration limit throughout the whole R-range. Such a simple way of estimating r_f may well be sufficient, considering the lengthscale of sensitivity for CW EPR and the level of approximation that is contained anyway in the theoretical model. As previously described for equation 3.2, the CW spectrum is then obtained by

Figure 4.2. CW EPR spectra (solid black lines, EPR frequency ~9.7 GHz, 293K) and simulations (overlaid red lines) based on the charged cylindrical cell model corresponding to equation 4.5 of FS + PDADMAC at R=0.036 in the four different solvents; Also shown are the residual signals after subtraction of the simulated from the experimental spectrum (solid black lines, shifted to –1.1 for clarity);
a) in ethanol/water; **b)** in NMPA/water; **c)** in water; **d)** in glycerol/water;

FT of the sum signal $V(t)$, and subsequent pseudomodulation[67] with the same modulation amplitude as used in the experiments. This simulated CW EPR spectrum is then fit to the experimental spectrum by varying $T_{2,k}$, c_0 and ω_k. Note that c_0 is the only parameter related to the radial distribution.

Figure 4.2 shows CW EPR spectra of FS + PDADMAC in all four investigated solvents for R=0.036 (solid black lines). Also shown in red are the fits according to equation 4.5 that are based on the Deshkovski-type model for the radial distribution function of counterions. Such fits were performed for all spectra of FS/PDADMAC and TAM/PDADMAC and one could obtain values for the initial counterion concentration c_0 that are comparable to each other within each measured series of samples (e.g. FS/PDADMAC in ethanol/water). It was found that this type of inclusion of broadening into the spectral simulations (equation 4.5) delivers fits of similar quality (quantified by the rms-deviation) as the simple stretched exponential fitting from equations 3.1/3.2, with the exception of the high-R spectra in water as a solvent. For this solvent, fits for R>0.06 could not reproduce the broadening in the outer flanks. This is shown in Figure 4.3, which depicts CW EPR spectra and their simulations according to equation 4.5 of FS + PDADMAC at R=0.067 in ethanol/water and water.

The simulation of the spectrum in ethanol/water is virtually perfect, while the simulation of the purely aqueous solution spectrum clearly cannot reproduce the broadening in the flanks. This result is remarkable already in itself. In Figure 4.2, only for FS/PDADMAC in glycerol/water a significant residual between spectrum and fit is found. Note - as indicated in Section 3.3 - that this less than perfect fit can be attributed to residual dipolar coupling between the FS electron spins that has been shown to be non-negligible in solutions of high viscosity and close average contact between the spin probe molecules, both of which is the case for the samples in glycerol/water. The same is also true for samples of TAM + PDADMAC for R>0.05 in glycerol/water (not shown). The Deshkovski-type exchange broadening thus is not able to fully account for the line broadening. The residual for the FS/PDADMAC samples in glycerol/water becomes progressively larger with increasing R, but never becomes as large as the fit residuals of the corresponding spectra of the water-series.
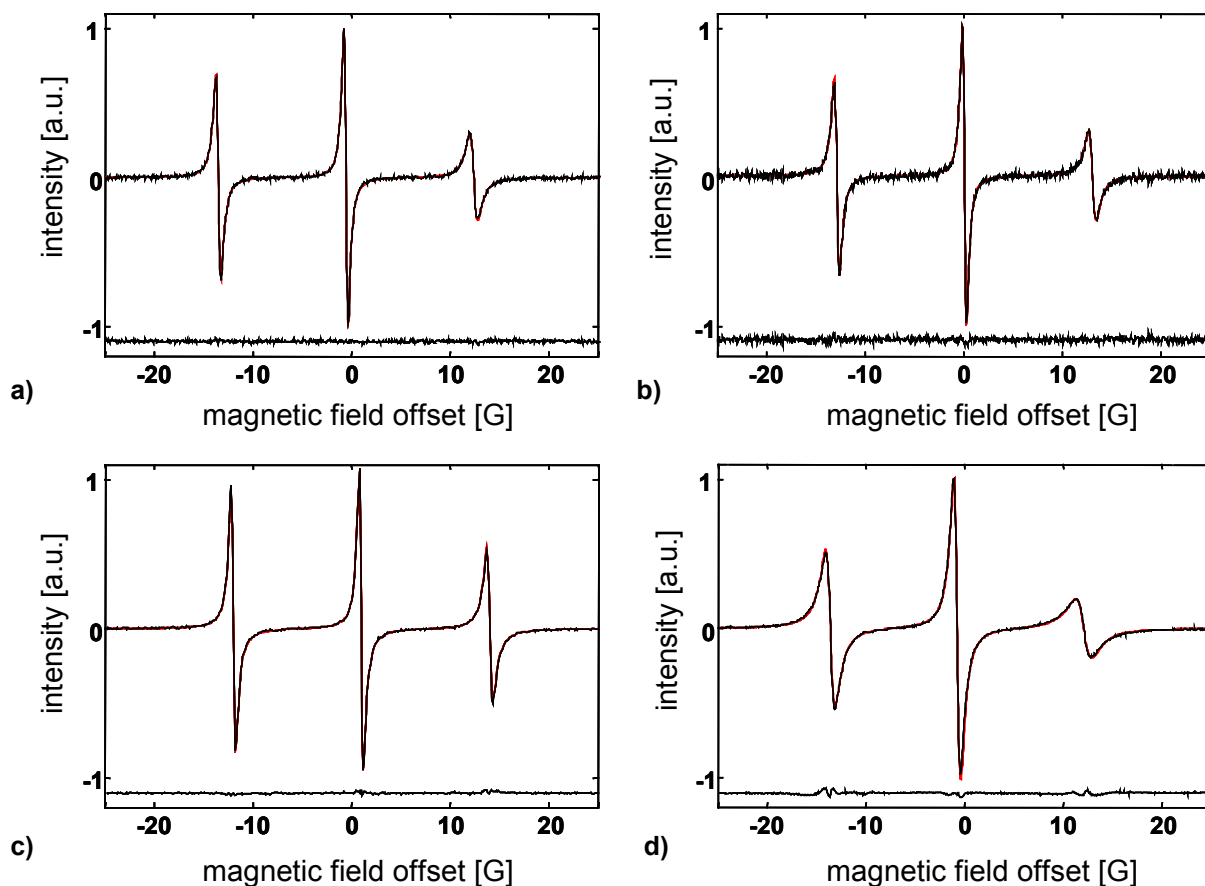

Figure 4.3. CW EPR spectra (solid black lines, EPR frequency ~9.7 GHz, 293K) and simulations (overlaid red lines) based on the charged cylindrical cell model corresponding to equation 4.5 of FS + PDADMAC at R=0.067 in **a)** ethanol/water; **b)** in water; Also shown are the residual signals after subtraction of the simulated from the experimental spectrum (solid black lines, shifted to −1.1 for clarity);
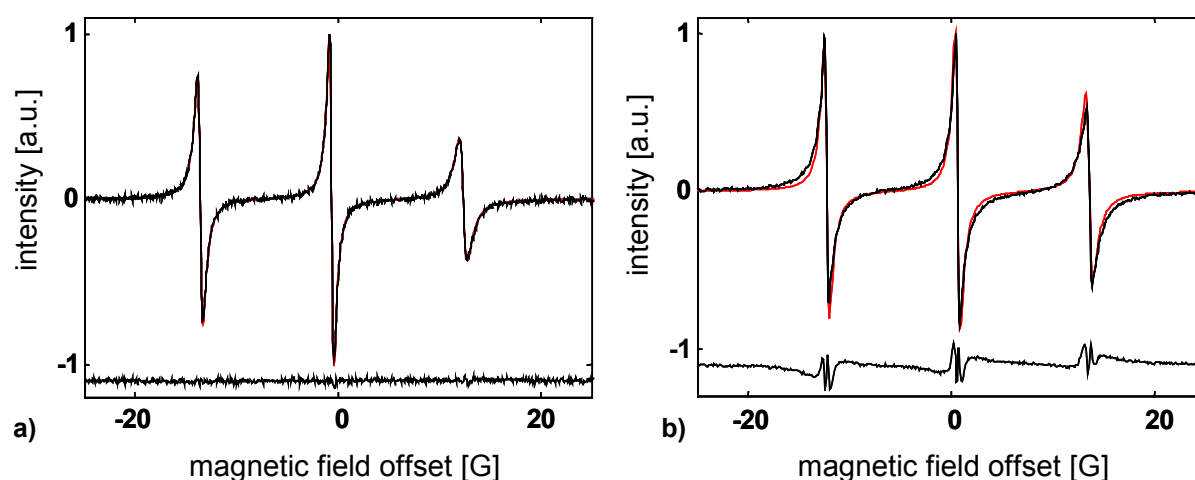
Figure 4.4. CW EPR spectra (solid black lines, EPR frequency ~9.7 GHz, 293K) and simulations (overlaid red lines) based on the charged cylindrical cell model corresponding to equation 4.5 of FS + PDADMAC at *R*=0126 in **a)** glycerol/water; **b)** in water; Also shown are the residual signals after subtraction of the simulated from the experimental spectrum (solid black lines, shifted to −1.1 for clarity);
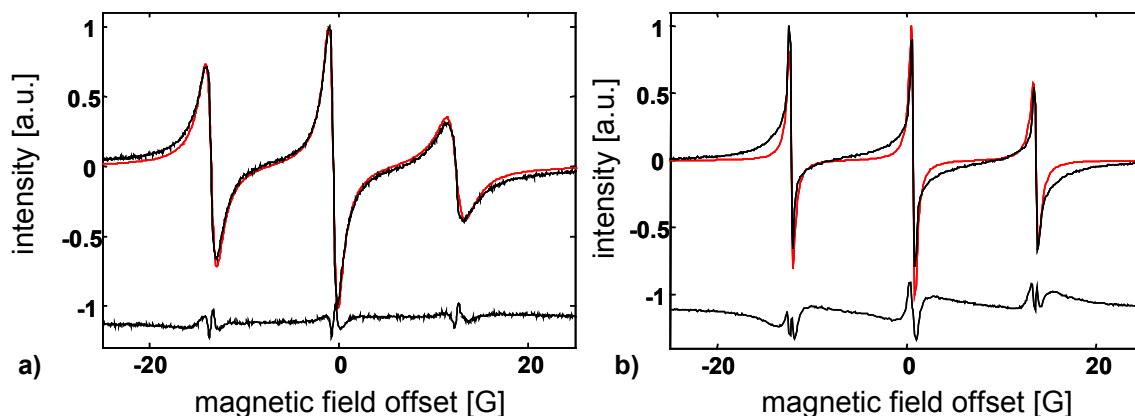
For comparison, Figure 4.4 presents spectra and respective simulations for the FS/PDADMAC samples at *R*=0.126 in glycerol/water (a) and water (b). In addition to the larger residual signal of the aqueous sample spectrum, the qualitative simulation of the combination of peak-to-peak linewidth with broad outer flanks seems to fail in this signal, while for the glycerol/water sample only the broadening is not accounted for completely. The appearance of narrow as well as very broad features in the spectrum of this sample has been discussed in Section 3.3.4, in which the effect of counterion condensation on polyelectrolyte chain conformation has been considered. Compared to the stretched exponential fit of the *R*=0.126-spectrum in water (Figure 3.21), the respective fit with the Deshkovski-type broadening function is of even worse quality. As a consequence, one might deduce that for the spectra of FS + PDADMAC in water at *R*>0.07, the assumptions made within the charged cylindrical cell model are not valid any more and the whole approach breaks down.

If the proposed model of ever-closer distances between spin probe counterions upon attachment to linear extended chains (based on the analysis of section 3.3) and the assumptions in the charged cylindrical cell model were correct, one would expect a linear dependence of c_0 on *R* in the complete *R*-range. Note that this initial concentration c_0 is the parameter that quantifies what was called the *agglomeration* of spin probes close to polyion chains in Section 3.3.3.

Figure 4.5 summarizes the values for c_0 for the series of TAM/PDADMAC (a) and FS/PDADMAC (b) in the respective solvent systems. In the plots of TAM as spin carrying counterion one observes a negligible c_0 for 0 < *R* < 0.03, which in water (blue squares) is followed by a sharp transition in the regime 0.03 < *R* < 0.05 to a plateau maximum value. This transition is not as prominent and sharp in glycerol/water but this may be due to distortions caused by the above-mentioned failure of the fitting routine to reproduce the spectra because of residual dipolar coupling between electron spin on the TAM ions.
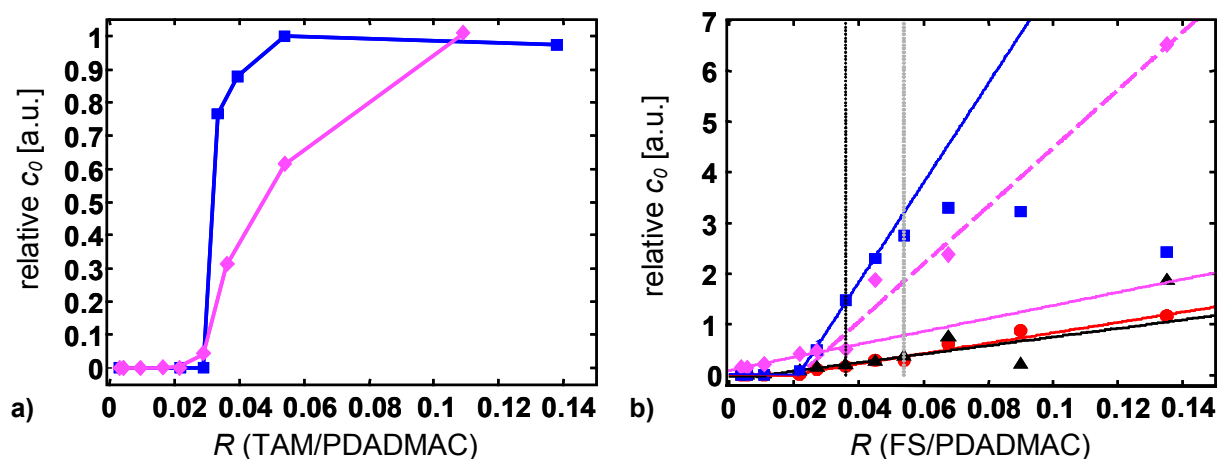
Figure 4.5. Trends of parameter c_0 extracted from spectral fitting of spin probe/PDADMAC CW EPR spectra according to equation 4.5 as explained in the text.
a) for TAM/PDADMAC; **filled blue squares**: in water; **filled magenta diamonds**: in glycerol/water; the plots have been rescaled for comparison and respective solid lines are meant as guide to the eye; **b)** for FS/PDADMAC; **filled blue squares**: in water; **filled black triangles**: in NMPA/water; **filled red circles**: in ethanol/water; **filled magenta diamonds**: in glycerol/water;
Fits: the solid black, red and magenta lines are linear regression fits to the respective data points of the series in NMPA/water (black; $c_0=8.42*R-0.09$), ethanol/water (red; $c_0=10.24*R-0.2$), and glycerol/water (magenta; $c_0=12.79*R+0.1$) up to $R=0.036$ (marked by vertical black dotted line) and extrapolations up to $R=0.15$; the dashed magenta line is a linear fit to the data of the glycerol/water series for $0.036 < R < 0.13$ and its extrapolation to zero ($c_0=57.04*R-1.2$); the solid blue line is a linear fit of the data in water for $0.022 < R < 0.054$ (marked by gray dotted line; $c_0=97.76*R-2.1$);

The behavior of the obtained values of c_0 in systems of FS/PDADMAC is qualitatively different from that of TAM/PDADMAC. In the three low-viscosity solvents, up to values of $R=0.022$ the value of c_0 is negligible, while for glycerol/water as solvent (magenta diamonds) there is a steady increase in c_0 up to $R=0.036$ but at low values ($c_0=12.79*R+0.1$). For the systems in NMPA/water (black triangles) and ethanol/water (red circles) the extracted values of c_0 then gradually rise for the whole R-range, $0.02 < R < 0.126$ and can be approximated as linearly increasing (solid lines), with rather similar slopes (in NMPA/water: $c_0=8.42*R-0.09$; in ethanol/water: $c_0=10.24*R-0.2$). The series in water/glycerol departs from the moderately sloped initial increase at $R=0.036$ (marked by vertical dotted line in Figure 4.5.b) and shows a much steeper linear increase in the remainder of the R-range ($c_0=57.04*R-1.2$, magenta dashed line).

The trend for c_0 of FS/PDADMAC in water is the only one deviating from the monotonous increase that the values for the other series follow. For $0.022 < R < 0.054$ (marked by gray dotted line), a linear increase, which is tenfold steeper than for NMPA/water and ethanol/water ($c_0=97.76*R-2.1$), approximates the trend of the data points quite well. For even larger R-values, it has just been shown that the simulations are not reliable any more (see Figure 4.3.b and 4.4.b) so that the observed decrease of c_0 is caused by the imperfect fitting.

Combination of the findings from Figure 4.3/4.4 and the quantification of broadening in the charged cylindrical cell model allows one to reassess the conclusions from Section 3.3, which is done in the following.

TAM + PDADMAC

The sharp increase in c_0 that is observed in water and qualitatively similar also in glycerol/water at $R \approx 0.03$ reaffirms the model that has been developed for dynamic electrostatic attachment of TAM to PDADMAC in Section 3.3. In Figure 3.16.b there are abrupt drops of the averaged relaxation times $<T_2>$ evident at $R \approx 0.03$ in both solvents. Thus, from two different methods of quantification of DEA, one obtains qualitatively and quantitatively similar results that are in agreement with the proposed structure model of a transition from a polyelectrolyte chain network (probably crosslinked by TAM) for $R < 0.03$ to a system in which TAM counterions interact with single PDADMAC chains. Other models such as gradual disentanglement of the polymer network to more and more single chains would result in a steadier increase of the initial TAM concentration, not to the observed sharp transitions and plateau maxima (c_0) or minima ($<T_2>$), respectively.

The assumed crosslinking effect of the large trianion TAM on PDADMAC can be viewed as reasonable in the light of studies of interaction of relatively large organic dye molecules with polyelectrolyte.[1] In these investigations it was found that binding of large organic molecules might indeed be stronger than binding of small inorganic ions because of additional hydrophobic interaction between counterions and polymer backbone.

FS + PDADMAC in organic solvent/water mixtures

This in turn might also explain why most strikingly no sharp transition is detected in the systems containing PDADMAC and FS as spin probe counterions in the organic solvent/water mixtures. The data for the three solvent mixtures in Figure 4.5 are qualitatively consistent with the model of DEA to linear chains that has been used to analyze the data shown in Figure 3.12. Up to $R \approx 0.02$, the concentration at the polyelectrolyte backbone in NMPA/water and ethanol/water seems to be too low to lead to broadening that does not stem from slowdown of rotational dynamics. The latter point, the slowing of rotational diffusion due to high polyelectrolyte content is actually the reason for the observed decrease in $<T_2>$ in the respective plots of Figure 3.12. Since this relaxation time is ensemble-averaged (see equation 3.3), the slowly reorienting FS ions contribute to $<T_2>$ and lead to the decrease, whereas in the fitting-procedure with equation 4.5, changes in rotational dynamics are accounted for by altered peak-to-peak linewidths, which are just the fit parameters $T_{2,k}$ in equation 4.5. The latter fitting procedure thus provides a better separation of exchange broadening from dynamical lineshape effects.

For $R > 0.02$ the steady increase in c_0 nicely corresponds to progressively larger counterion concentrations along the polyelectrolyte chains, which of course is what one would expect for DEA to linear extended chains. This behavior corresponds to regime 2 in Figure 3.18, while the initial behavior for $0 < R < 0.02$ is representative of regime 1 ("overlap regime") in that figure. Since there is no sharp transition as in the case for TAM as counterion, the conversion from strongly overlapping chains to effectively single chains seems continuous - the FS counterions do apparently not have a

significant network-inducing ability. The fact that in glycerol/water as solvent the continuous increase is observed also for very low *R*-values might be indicative of a larger radial concentration gradient already at high dilution in the concentrated polymer solution. At first, this seems in contradiction to the proposed broadening mechanism of Heisenberg spin exchange due to intermolecular FS collisions. In glycerol/ water as solvent the rotational (see 3.3.1) and translational (see 3.3.5) diffusion is known to slow down due to increased viscosity, which should in turn reduce the frequency of FS-FS collision and hence also exchange coupling.[50] The reason for the contrary effect to occur in these FS/PDADMAC samples has been explained in Section 3.3.5 and may be due to the increased average time that the FS ions are territorially-bound to the polyelectrolytes. The ions might be confined to the effective attachment (e.g. cylindrical) volume for longer times and this effect might overcompensate the slowdown of intermolecular collision frequency that solely stems from solvent viscosity. This qualitative argument is consistent with the charged cylindrical cell model.

Figure 4.6 depicts the relative counterion concentration profile as calculated from $c(r)=c_0*r^{-2}$ for samples at *R*=0.036 (marked by black dotted line in Figure 4.5.b) in all four solvents (see also their CW EPR spectra and simulations in Figure 4.2). In full agreement with the conclusions from Section 3.3 (similar polyelectrolyte conformation and DEA), the concentration profiles of FS in solutions of PDADMAC in NMPA/water and ethanol/water are almost identical, which is indeed even true in the whole *R*-range as can be seen from their similar trends of c_0 in Figure 4.5. The profiles for FS in water and glycerol/water start from higher initial concentrations. For glycerol/water as solvent, it has been
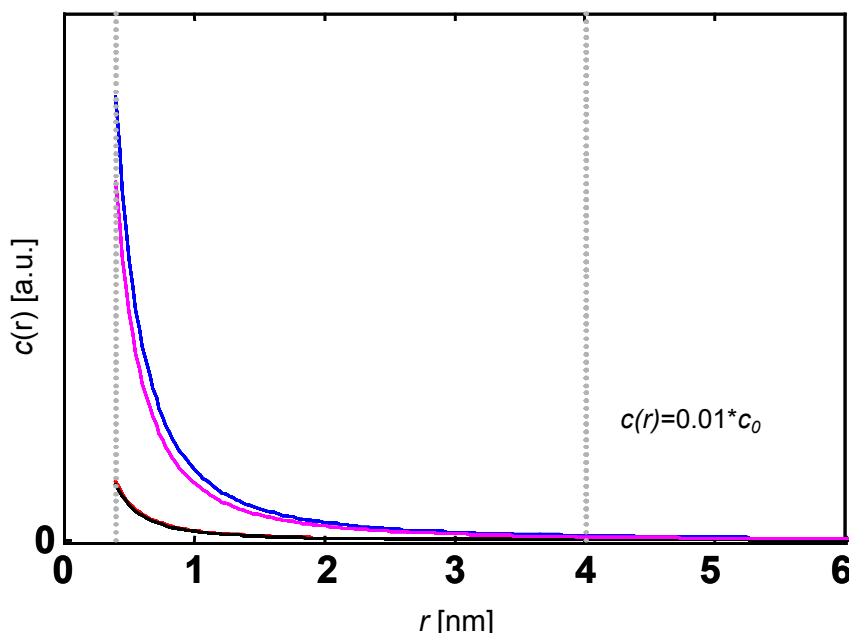
Figure 4.6. Radial concentration profiles of counterions distributed around extended chains; the relative profiles were calculated based on the charged cylindrical cell model from $c(r)=c_0*r^{-2}$ using the c_0-values of FS/PDADMAC (*R*=0.036) in the four solvent systems (marked by black dotted line in Figure 4.5, see also respective CW EPR spectra and simulations in Figure 4.2); **blue line**: in water; **black line**: in NMPA/water; **red line**: in ethanol/water; **magenta line**: in glycerol/water; the gray dotted line marks the distance at which the concentration has dropped to one percent of the initial c_0;

laid out in the last paragraph that this quantifies the higher radial concentration gradient as compared to solutions in the two low-viscosity organic solvent/water mixtures.

Furthermore, by choosing the initial integration radius r_i in equation 4.5 to be 0.4 nm, the radial distribution of counterions levels off very quickly and has reached 1% of its initial value c_0 after 4 nm (marked in Figure 4.6). Within the assumed model, this shows that the chosen integration limits capture a vast majority of counterions according to the r^{-2}-dependent radial distribution function.

FS + PDADMAC in water

The simultaneous appearance of contributions from unbound FS ions (sharp, narrow contributions to the spectrum) and from strongly interacting FS ions (very broad outer flanks) is apparent in Figure 4.4.b. The breakdown of the charged cylindrical cell fitting model for $R>0.06$ (Figure 4.3) for spectra of solutions in water very nicely coincides with the increase of the averaged relaxation times from Figure 3.12.c. From the pure fact that the broadening of the spectra cannot be reproduced by the broadening function in equation 4.5, one has an additional indication for the conformational transition of the PDADMAC chains that was proposed in Section 3.3.4 for the FS/PDADMAC system in water at $R \approx 0.05$. The fitting of experimental spectra with this specific model is subjected to more restrictions than the stretched exponential fitting. This may be the reason for the failure of the fitting routine at intermediate R-values.

In addition, the steep increase in c_0 for $0.022 < R < 0.054$ denotes a steep concentration gradient, i.e. a very high initial concentration at the polymer backbone, which is visualized by the radial concentration profile shown in Figure 4.6.

In conclusion, the Deshkovski-type approach that is based on the nonlinear Poisson-Boltzmann equation works for most of the systems under investigation. Only solutions beyond a ratio of $R>0.06$ for FS/PDADMAC in water exhibit spectra that cannot be reproduced by this model, which is attributed to a severe change of polyelectrolyte conformation. As is shown in the subsequent section, the r^{-2}-dependence of the local concentration in the charged cylindrical cell model is not a unique solution for reproducing the spectral broadening, but nonetheless this approach leads to a meaningful quantification of alterations in CW EPR spectra of spin probe counterions.

4.1.3   Spin probe radial distributions from a generalized scaling approach

In the last section it was explained why the phase of "saturated condensation" was chosen as underlying broadening function. In order to satisfactorily simulate FS/PDADMAC spectra at high R-values, which are not fitted by the "saturated condensation" model, one can now turn to a generalization of the broadening function term in equation 4.5. This is based on the general solution found by Deshkovski et al. in equation 4.1, but without explicit derivation of the scaling factor γ and may take into account other counterion concentration dependences than the simple r^{-2}-dependence of phase II in the cylindrical cell model.

Equation 4.6 is a fitting function similar to equation 4.5, but with a generalized scaling approach to broadening:

$$V(t) = \int_{r_i}^{r_f} r^{-m} \exp\left[-\frac{r^{-n}}{r_i^{-n}} c_0 t\right] \cdot \sum_{k=1}^{n} \exp\left[-\frac{t}{T_{2,k}}\right] \exp\left[i\omega_k t\right], \tag{4.6}$$

in which all parameters have been explained for equation 4.5 and m and n are the two scaling factors. The special case $m=1$ and $n=2$ corresponds to equation 4.5. One may now introduce a fractal dimension d and thus relate the general approach to a physical picture:

$$m = n + 1 - d. \tag{4.7}$$

The cylindrical distribution of counterions in this approach has a dimensionality of $d=2$, and for a spherical distribution one would expect $d=3$ and therefore (setting $n=2$) $m=0$. Note that by changing the scaling factor one effectively scans through the phase diagram described in Section 4.1.1.

In particular, it was attempted to fit those CW EPR spectra by using eq. 4.6 that could not be simulated within the cylindrical cell model (eq. 4.5). To achieve this, first a fixed value of $n=2$ was used and m was selectively varied to values lower than 2 (phase I in Section 4.1.1) or larger than 2 (phase III in Section 4.1.1).

As a test, simulations of spectra that were nicely reproduced by use of equation 4.5 were performed. The fit according to equation 4.6 (Figure 4.7.a $m=1.5$, $n=2$) of the spectrum of FS + PDADMAC in water for $R=0.036$, which had been simulated perfectly within phase II of the charged cylindrical cell model (Figure 4.2.c), is still of good quality but nevertheless the residual signal is slightly larger. The respective simulation of the spectrum with $m=2.5$ (Figure 4.7.b) yields a simulation of equal quality as that performed with the scaling exponent $m=2$.

As a further generalization, even the scaling factors m and n in equation 4.6 (i.e., the fractal dimension d in equation 4.7) were allowed to vary during fitting of those spectra, which could not be fit within the "saturated condensation" model. This resulted in only slight improvement for the
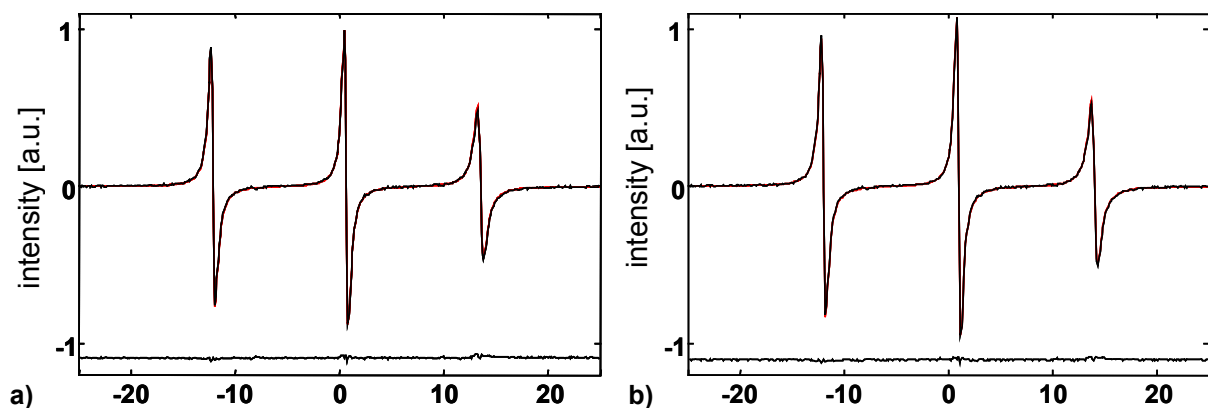
Figure 4.7. CW EPR spectra (solid black lines, EPR frequency ~9.7 GHz, 293K) and simulations (overlaid red lines) based on the generalized scaling approach corresponding to equation 4.6 of FS + PDADMAC at $R=0.067$ in water **a)** with $m=0.5$ and $n=2$ in eq. 4.6; **b)** with $m=1.5$ and $n=2$ in eq. 4.6; Also shown are the residual signals after subtraction of the simulated from the experimental spectrum (solid black lines, shifted to -1.1 for clarity);

simulation of the spectra that could not be satisfactorily fit with the Deshkovski-type model, though. This finding is quite remarkable, given that lifting the constraints on the scaling factors opens up a large number of degrees of freedom in the fitting function. It seems that the fundamental difference in the spectra of $R<0.06$ and spectra of $R>0.06$, namely the simultaneous appearance of the narrow features that were attributed to "unbound" FS ions at high R and the extremely broadened parts, cannot be reproduced within this scaling approach.

It must be concluded that the fit-function that has been derived in the regime of "saturated condensation" reproduces the broadening that is observable in most CW EPR spectra in the measured series remarkably well. The same is true for spectral fitting with functions of scaling exponents $m>2$, but to a lesser extent also for $m<2$. From the fact that the broadening function within this model belongs to a family of functions that represent phase II and phase III of Section 4.1.1, it can be deduced that the system is in one of these regimes. Unlike the model-free fitting from Section 3.3, quantification of this broadening hence delivers direct information from EPR-spectroscopic data that can be analyzed in the framework of polyelectrolyte theory. This of course is no proof that the model and in particular the "saturated condensation" regime actually describes the system of spin probes and polyelectrolyte but in solvent mixtures, in particular NMPA/water and ethanol/water, it can be consistently interpreted in these terms and the supposed conformational change in water may explain the deviations from the behavior in solvent mixtures.

4.2   Counterion distribution along a 1-dimensional chain and reduced number of effective charges

In Sections 3.3 and 4.1, complete series of CW EPR spectra were analyzed in a model-free approach and by using a radial distribution function stemming from an analytical solution of the nonlinear Poisson-Boltzmann equation, respectively. Both of these approaches lead to qualitatively similar results on polyelectrolyte-counterion interaction and polyelectrolyte conformation. They are, however, devoid of any information on the axial distribution of counterions.

At this point this topic is approached by presenting and interpreting results from 4-pulse double electron-electron resonance (DEER) spectroscopy (see Section 2.6.3) on samples of FS/PDADMAC in the frozen glassy solutions in glycerol/water. Details on the experimental setup are summarized in Appendix A2.

It has been explained (Section 2.6.3) that in this double resonance technique one utilizes the dipolar coupling between electron spins at two different positions in the conventional ESE-detected spectrum to determine the distance between them. As presented in Section 3.3.3 (Figure 3.17) the ever-closer approach of FS spin probes upon increase of R leads to progressively stronger dipolar coupling between the spin probes, which should be detectable in the 4-pulse DEER experiment.

4.2.1   Counterion distribution along a 1-dimensional chain

In Figure 4.8.b/d the black solid lines are the DEER time traces of the FS/PDADMAC system in glycerol/water at R=0.0036 (4.8.b) and R=0.022 (4.8.d). While DEER of the low R-sample shows an exponential decay, the time-domain trace of the sample at the intermediate R-value has a clearly non-exponential component, which is most prominent at low dipolar evolution times where it corresponds to the steep initial signal drop. Figure 4.8.a/c shows the ESE-detected spectra of FS/PDADMAC at the respective R-values, in which the spectral positions of the pump-frequency (global spectral maximum) and the observer frequency (local low-field maximum) are marked by arrows.

In the complete series of DEER time-domain data (see, e.g., Fig. 4.8) a general trend is evident: the modulation due to the non-exponential component signal grows more prominent with increasing R. Several approaches were taken to extract information of the pair-correlation function of FS spin probes with the different analysis methods that have been introduced in Chapter 2 and that have already been applied, e.g., to the system of FS/RuCP from Section 3.2. All these methods such as direct integral transformation or fitting of the signals with one or more distinct distances have failed, they could not reproduce the observed time traces.

The simplest and most general fitting function that yielded best fits of the experimental time-domain data was an approach assuming two distinct components of FS spin probes. In these simulations one varied a concentration c_{hom} corresponding to a fraction of spin probes homogeneously distributed in three dimensions and a linear density c_{lin} corresponding to an equal distribution in one dimension in the pair correlation function $G(r)$:

$$G(r) = c_{\mathrm{hom}} N_A + c_{lin} / r^2 \tag{4.8}$$

where N_A is Avogadro's constant, c_{hom} is in units of mmol/L (mol/m^3), and c_{lin} in units of m^{-1}. The time traces were computed from the pair correlation function using the shell factorization model described in Chapter 2.[77] This approach to data analysis is analogous to an approach used earlier by Milov and Tsvetkov in work on chain conformation of spin-labeled poly(vinylpyridine).[118] The utilization of the bimodal pair-correlation function for the simulation of the experimental data is based on the conclusion from Sections 3.3 and 4.1 that the PDADMAC chains in presence of FS in organic solvent/water mixtures attain locally extended conformations. The "linear" component of FS ions in this picture is a result of statistical distribution of FS ions close to such a linear extended polyelectrolyte chain. The component that is homogeneously distributed in three dimensions could in principle be assigned to detached counterions, but may also arise from FS ions that are diluted in overlapping PDADMAC chains or from chains in non-linear conformation. The extracted resulting values for c_{hom} and c_{lin} from this analysis for the whole series are depicted in Figure 4.9. The homogeneously distributed component decreases with increasing R and is effectively zero for values larger than 0.05, whereas the component that is presumably distributed along one dimension follows an opposite trend and increases with R, reaching a plateau value of c_{lin} ~0.8 nm^{-1} for $R > 0.05$.
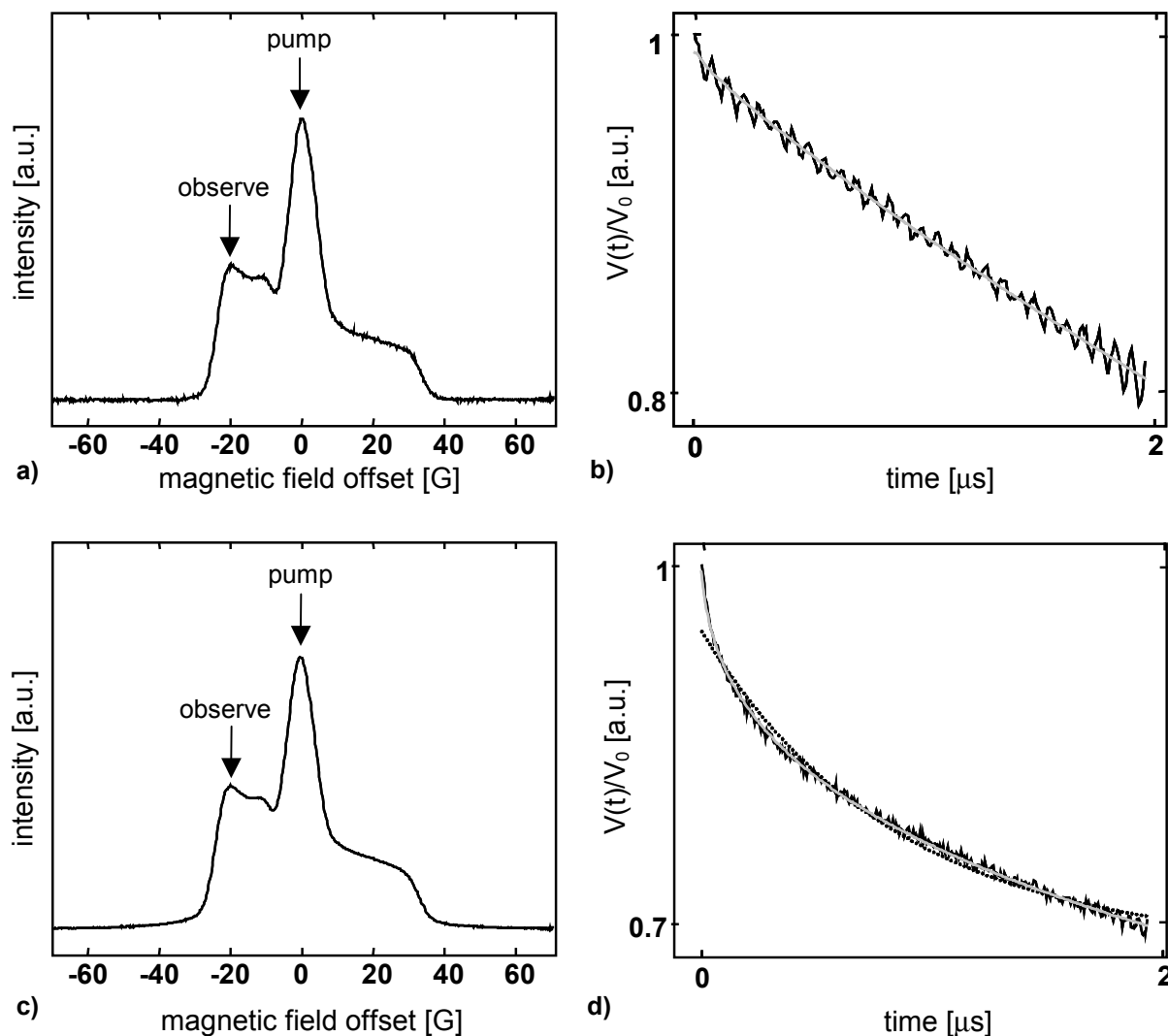
Figure 4.8. Representative ESE-detected spectra (a, c) and DEER time-domain data (b, d) of FS + PDADMAC in frozen glassy solution of glycerol/water (EPR frequency ~9.3 GHz); **a)** ESE-detected spectrum of sample at R=0.0036; **b)** solid black line: DEER time trace of the sample at R=0.0036; the gray solid line is the best fit corresponding to the pair correlation function described by equation 4.8 as explained in the text with a homogeneous component of ~0.8 mM and a negligible linear spin density; the fast oscillating signal is residual modulation due to ^{1}H excitation; **c)** ESE-detected spectrum of sample at R=0.022; the arrows labeled "pump" and "observe" mark the positions of the excitation (pump) and detection (observe) for the 4-pulse DEER experiment; **d)** solid black line: DEER time trace of the sample at R=0.022; the gray solid line is the best fit corresponding to the pair correlation function described by equation 4.8 as explained in the text with a homogeneous component of ~0.4 mM and a linear spin density of ~0.3 nm^{-1}; the dotted black line shows the best fit with single exponential decay;

Considering the conclusions from the CW EPR data, these two divergent trends of the data from Figure 4.9 can best be interpreted as the transition from a network of overlapping polyelectrolyte chains at high PDADMAC concentrations to a regime of isolated and extended polyelectrolyte chains at low polymer concentration. In the former case, FS spin probes are distributed in the polymer network, which corresponds to only part of the volume of the whole solution, which explains that the c_{hom} values are larger than the bulk concentration. With decreasing concentration, the single chain character increases and c_{lin} becomes larger. Note that the local concentration gradient (spatial distribution) of FS that leads to the distribution of linewidths in CW EPR spectra (stretched
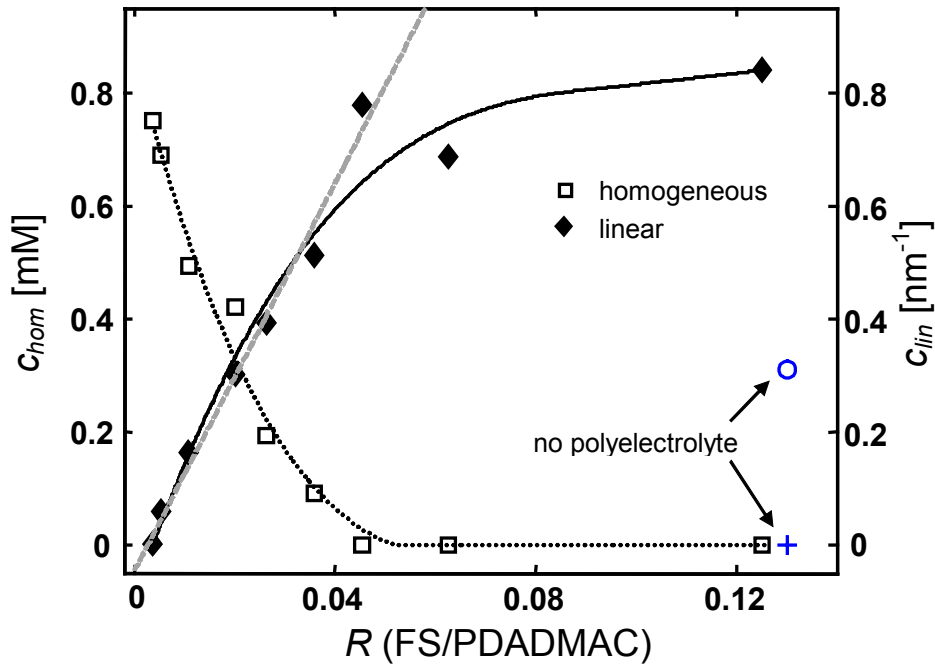
Figure 4.9. Extracted contributions of three-dimensional (homogeneous) and one-dimensional (linear) distributions of FS from fitting the parameters c_{hom} and c_{lin} of equation 4.8 to 4-pulse DEER time traces (EPR frequency 9.3 GHz) of FS + PDADMAC in the whole R-range investigated in glycerol/water. Open squares: homogeneous concentration c_{hom}; filled diamonds: linear concentration c_{lin}; blue open circle: c_{hom} of FS in glycerol/water without PDADMAC; blue cross: c_{lin} of FS in glycerol/water without PDADMAC; The gray dashed line is a linear fit (c_{lin}=(17.16*R - 0.045) nm^{-1}) to the values of the linear concentration up to R=0.0455, while solid and dotted black lines are meant as guides to the eye.

exponential (eqs. 3.1/3.2) or cylindrical-cell-type (eq. 4.5) time-domain broadening functions) corresponds to the *radial* direction with respect to the assumed elongated PDADMAC chains, whereas the linear density deduced from the DEER experiment corresponds to the axial direction along the PDADMAC chains.

From the ESEEM experiments of section 3.3.1, the conclusion was drawn that only 20% of FS spin probes are site-bound forming contact ion-pairs with the PDADMAC charges. Thus, one may conclude that the distance of most of the territorially bound FS from the PDADMAC chains cannot be much larger than roughly a nanometer, otherwise the experimental data at high R-values would not be perfectly fit by a linear distribution. In the last section it was found that within the cylindrical-cell model the counterion concentration decreases rapidly ($\propto r^{-2}$), reaches 16% of the initial concentration at the polyelectrolyte backbone within 1 nm and has fallen to 1% of the initial concentration after 4 nm (see Figure 4.6). These findings are in quantitative agreement, which may be seen as a further indication that the model by Deshkovski et al. provides a rather good approximation of the system of FS/PDADMAC in glycerol/water.

These findings are also consistent with the requirement of short diffusion lengths imposed by observation of fast exchange between site-bound and territorially bound counterions.

As described, the interpretation of the attained plateau-value of zero for c_{hom} in Figure 4.9 is rather straightforward. Due to more and more pronounced single-chain character of the ensemble of

PDADMAC chains, for $R>0.05$ a vast majority of the neighboring spin-carrying counterions must then be located on the same chain, rather than in the bulk or on neighboring chains. This conclusion applies to a sphere with a radius of approximately 5 nm, which is the active volume around the observer ion for a DEER experiment with a maximum dipolar evolution time of 2 μs.[52,75,77]

The assessment of the plateau value of 0.8 nm^{-1} for c_{lin} is more problematic, though. Note that the DEER experiment has a lower detection limit for electron spins of roughly 1.5 nm, which is a consequence of technical constraints in excitation bandwidth (see Section 2.6.3 and Refs. 39, 52). This plateau value corresponds to an average distance between divalent spin-carrying counterions of approximately 1.25 nm and this seems to be the highest loading of the chain with these counterions that can be detected by the four-pulse DEER measurements. Figure 4.9 also shows a linear fit to the values of c_{lin} up to $R=0.0455$ (dashed gray line: $c_{lin} = 17.16 * R – 0.045$). Using this fit, one would expect an exact linear distance between the detected spin probes of 1.5 nm ($c_{lin}=0.667$) for $R=0.042$ which corresponds rather nicely to the beginning of the plateau for c_{lin}. Note that it has been shown that the exchange coupling between the electron spins on the FS counterions, which was the main effect on the CW EPR spectra at ambient temperature, can be neglected in the analysis of the DEER signal.[52]

From the fact that the ESE-detected spectra of FS/PDADMAC still become continuously broader for $0.04 < R < 0.126$ (see Figure 3.17), it is a sound conclusion that the described appearance of the plateau value of the linear spin density is an artificial effect stemming from the detection limit of the 4-pulse DEER method. The increase in broadening, regardless of its origin, is indicative of stronger interaction between the FS electron spins and thus of ever-closer distances between them. Once the FS ions have attained average distances of ~1.25 nm, a further increase in the dipolar coupling cannot contribute to the modulation of the DEER time-domain signal any more and hence the data lack information from spin closer than this. Note that the value of ~1.25 nm is only the uppermost limit of approximation for the average FS distance, which might only be detected because of the large width of the distribution around the corresponding linear charge density.[119] Within the picture of attachment of FS ions to linear PDADMAC chains it is therefore also reasonable to assume that the linear fit (dashed gray line in Figure 4.9) describes the real development of c_{lin} within these systems, at least for R-values smaller than 0.13.

4.2.2   Modification of the linear extended chain model

Based on the interpretation of c_{lin}, a very important additional conclusion can be drawn from the characterization of DEER data as presented so far. The appearance of increasingly stronger contributions of spin probes distributed along one dimension with increasing R is in qualtitative agreement with the findings upon use of the Deshkovski-type radial distribution function for simulation of CW EPR spectra in Section 4.1. It is also qualitatively consistent with the linear extended chain conformation of PDADMAC in organic solvent/water mixtures that has been deduced

in Section 3.3. It is not, though, in *quantitative* agreement with the findings from Section 3.3. If one compares the lengthscales found from the DEER data to those of the used ratios of concentration, there is a significant disagreement. DEER analysis finds an average spacing of FS ions of ~1.5 nm along a linear chain for $R \approx 0.05$. In Section 3.1 the upper limit for the charge spacing in PDADMAC from force-field calculations for the optimization of geometry was found to be b=0.85 nm, the lower limit could be approximated by b=0.5 nm. In the simplest case of fully extended, fully rigid PDADMAC chains and assuming that *all* FS ions are site-attached or at least very close to a cationic attachment site, a ratio of 0.05 would correspond to *one* FS ion per *twenty* PDADMAC ammonium groups, which would in conclusion mean that the average distance between FS ions were 10 nm (b=0.5nm) to 19 nm (b=0.85nm), which is approximately one order of magnitude larger than the value found. The linear fit in Figure 4.9 would have to be (assuming full condensation of FS ions) between $c_{lin} = 1.17 * R$ and $c_{lin} = 2 * R$ in order to be reconciled with all the findings of 3.3 and 4.1 that could be explained within the model of attachment to linear extended polyelectrolyte chains.

It seems that the effective number of charges along the chains that are experienced by the FS counterions is reduced by a factor of roughly ten as compared to the simplistic linear extended chain/cylindrical cell model. Despite the fact that the DEER data are in quantitative disagreement (concerning inter-FS distances) with this oversimplified model, for R>0.05 the DEER data of spin-carrying counterions can be reproduced assuming that counterions are distributed linearly. This leads to the conclusion that the FS ions are nonetheless distributed along a linear object, which has a minimum persistence length of approximately 5 nm. As explained before, this is the lengthscale to which the DEER method is sensitive under the conditions of the experiments.

These two conclusion, the reduced number of effective charges and the linear persistence length of ~5 nm seem to be mutually exclusive. It is now the task to reconcile both, the qualitative and semi-quantitative agreement with the linear extended chain model of Sections 3.3 and 4.1 and the qualitative agreement of DEER data from this section with this model, on the one hand and the ten times reduced number of effective charges on the PDADMAC chains on the other hand. Pooling all insights into the system of FS/PDADMAC that were gained in sections 3.3 – 4.2, one may develop alternative models that consistently depict the system. However, one may already conclude that schemes such as Figure 3.22 showing highly stretched polymer conformations are (useful) oversimplifications. Note that the DEER experiment probes the PDADMAC/FS systems in glycerol/water at the glass transition temperature (approximate T_g=180K) and not at ambient temperatures. It is hence very likely, that the conformational ensemble present in the DEER experiment is different from that investigated in CW EPR at ambient temperature. One can think of several possible conformations that might now be prevalent in the frozen solution, but only one of these is introduced and critically assessed in the following paragraphs.

Section 1.2 gave a concise overview of other models describing polyelectrolyte conformations in solution. Quite a lot of chain conformations could be imagined for which one would not have to

assume partially collapsed polymer chains, but which could explain dramatically reduced effective charge numbers or higher linear charge densities. Although some natural and synthetic polyelectrolytes are known or assumed to adopt rather regular structures in solution, description of polyelectrolyte structure is usually much more complex than description of uncharged polymers.

One could think of a blob-like model (as shortly mentioned in Section 1.2.4) for the polyelectrolyte chains in which – as an estimation from the DEER experimental results – roughly ten PDADMAC repeat units form one larger aggregate, with an effective charge lower than ten because of the inclusion of counterions and an axial extension shorter than the contour length of a decamer. Within such blobs, the chain conformation might follow, e.g., Gaussian statistics, while on the lengthscale of sensitivity with respect to the DEER experiment (~5 nm) these blobs might form linear chains. The obtained CW EPR spectra and DEER time traces could be consistently explained if FS ions interact with the outer surface of these blobs.

From numerical simulations of single polyelectrolyte chains other structures such as cigar-shaped are proposed.[120] It is also possible to explain the reduced charge number but FS distribution along a 1-dimenional chain assuming such structures.

Consequently, it is only possible to speculate about the PDADMAC chain structure in the short (<1nm) or long (>10 nm) regime. From the EPR findings of series of FS and also TAM counterions with PDADMAC one can only safely conclude that on the intermediate lengthscale for those counterions in solution (with the exception of FS/PDADMAC in water), the polyelectrolyte structure appears as linear. Except for the fraction of site-bound counterions, the spin probe ions might indeed mainly interact with conformationally-averaged polyelectrolyte chains. Within this picture, territorially bound FS counterions could be thought to only experience electrostatic interaction with a rather "coarse" electrostatic potential contour along some linear conformation of polyelectrolyte. The main conclusions from Sections 3.3.4 and 4.1 might still be reconciled with the modified extended chain model, though. The proposed explanation that in organic solvent/water mixtures the polyelectrolyte conformation is linear because of screening of the hydrophobic interactions by organic solvents, while in pure water one might observe a conformational transition to more collapsed states only has to be adapted in the light of the DEER results. The transition might take place from more elongated to more and more globular structures, as indeed the changes in entropy of the system from e.g. a chain of blobs to increasingly larger globular domains are not very large and might explain the detected solvent dependence of the EPR data.

All in all, this discussion demonstrates the limitations of the approach that was taken within this work to probe polyelectrolytes solely through their electrostatic interaction with paramagnetic tracers of counterions. For more detailed information on the polyion chain structure in solution through EPR spectroscopy, it will certainly be necessary to undertake complementary investigations of polyelectrolyte materials with covalently attached spin labels, which is pointed out in the outlook given in Chapter 5.

4.3   Distribution of network-forming counterions

This final section of this chapter is concerned with the more detailed description of the polyelectrolyte solutions that contain the trianion TAM-radical as tracer for the counterions. The results gained on this system by methods of CW and FT EPR spectroscopy at X-band frequencies (~9.7GHz) were already presented and discussed in Sections 3.3 and 4.1.

Unlike the divalent FS ion that is a rather small inorganic molecule, the TAM trianion (see Scheme 3.3) represents a class of rigid, triangular-shaped organic molecules with their structure deviating strongly from that of usual polyelectrolyte counterions such as chloride ions. It has been mentioned in the preceding sections that such large organic molecules might not only interact with the oppositely charged polyion by electrostatic but also by hydrophobic interactions. TAM in particular is comprised of three aromatic structural units and of twelve short hydroxyethyl moieties, which all might seek interaction with large organic macromolecules.

The well-defined, rigid structure of this molecule and especially the triangular arrangement of the charges raise the expectation that it might be used as a structural guiding block for supramolecular assemblies. Comparison of the results obtained with FS and TAM as spin probes (Sections 3.3 and 4.1) indicates that TAM molecules actually function as a physical crosslinker in solutions of relatively high polymer content building transient networks. Below a certain polyelectrolyte concentration ($R >$ 0.02, c(PDADMAC)<25 mM) there is indication that a rather abrupt transition takes place to a regime, in which TAM ions interact with single chains of PDADMAC.

In this section, pulse EPR experiments at high-field/high-frequency (W-band, ~94 GHz) are presented that probe the local TAM counterion concentration and thus deliver information similar to that obtained for FS ions with the DEER experiment. The DEER experiment itself is not applicable in this case, as the EPR spectrum of TAM is too narrow to apply microwave pulses at two distinct frequencies with non-overlapping excitation bands. The only other pulse EPR distance measurement technique that could be used in the case of narrow EPR spectra is the so-called SIFTER experiment.[121] This experiment has not been used as it bears the great disadvantage that data analysis is much more intricate and interpretation not as straightforward as for the rather simple approach presented in this section.

4.3.1   TAM spin probe distributions characterized from broadening of high-field ESE-detected spectra

A full series of samples containing the narrow-line TAM spin probe and PDADMAC polyelectrolyte in frozen solution (T=80K) of glycerol/water was investigated at W-band (~94 GHz) EPR frequency. The ESE-detected, field-swept TAM spectra at X-band (~9.7 GHz) shown in Figure 3.19, are apparently symmetric due to the negligible electron-Zeeman and hyperfine anisotropies. In high-field/high-frequency measurements, the spectra are not symmetric any more, which can be seen from

Figure 4.10. Griffin and coworkers (Ref. 122) have reported the spectral asymmetry in ESE-detected spectra recorded at 139.5 GHz and qualitatively identified g-anisotropy as its origin.

Figure 4.10 proves that at ten times higher resonance frequency the dipolar broadening in high-*R*-samples is still apparent and qualitatively very similar to that visible in the X-band spectra - a broadening stretching far into the flanks of the spectra. Despite the now apparent asymmetry, spectral fitting of the W-band EPR spectra is simpler than fitting of the X-band spectra. The two peaks that are symmetrically placed at ~5 G from the maximum of the spectra at X-band frequency and that have been qualitatively assigned to spin-flip transitions in samples containing TAM spin probe do not overlap with the TAM spectrum at W-band frequencies (the spectral position of those spin flip transitions is linearly dependent on the microwave frequency, i.e., if they were excited they would show up at $\pm$ 50 G). Hence, this set of powder spectra was chosen to obtain new information on the local concentration and distribution of TAM counterions in frozen solution of PDADMAC in glycerol/water.

This can be done by a fairly simple, semi-quantitative approach by using the spectrum of the *R*=0.0028 sample (blue line in Figure 4.10) as a reference spectrum that is convolved with varying dipolar spectra (Pake patterns), assuming a Gaussian distribution of the distance between unpaired electrons. The Pake patterns account for the broadening of dipolar origin and are a function of i) the assumed distance between unpaired electrons on TAM ions r_{dip} and ii) the width of the Gaussian distribution Δr_{dip} around this distance. They were taken from a reference base of Pake patterns for intermolecular distances between 0.5 and 5 nm. Fitting was achieved with a home-written program in MATLAB (v.6.1, The Mathworks, Inc.) by FT of the reference spectrum from the frequency/field-domain to the time-domain, subsequent convolution with the time-domain signal of the respective
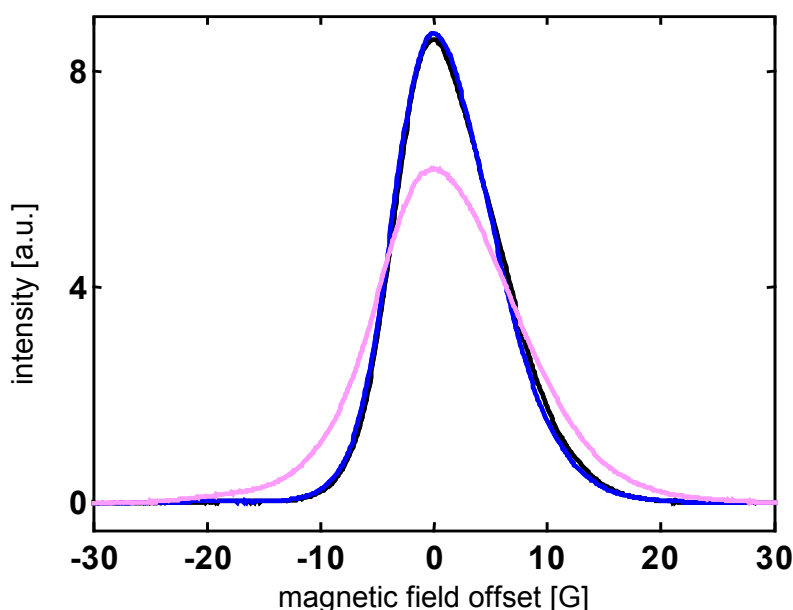

Figure 4.10. Representative ESE-detected, field-swept EPR spectra (W-band, ~94 GHz) of 0.4 mM TAM + PDADMAC in frozen glycerol/water solution (*T*=80 K) at three *R*-values. **Black line:** TAM without polyelectrolyte; **Blue line:** at *R*=0.0028; **Magenta line:** at *R*=0.1; Note the asymmetry of the spectra;

Pake pattern and finally Fourier transformation of the newly created dipolar broadened signal to the frequency/field-domain.

This accounts for the dipolar broadening of the spectra but since the counterions are heterogeneously distributed within the samples (site-bound, territorially bound or even free with different local concentrations), the fraction of electron spins that is dipolar coupled to a close neighboring spin (corresponding to the first peak in the distance distribution) is lower than unity. Therefore, the dipolar-broadened signal V_{dip} is then convolved with the original reference spectrum V_{ref} according to equation 4.9:

$$V_{sim}(\upsilon) = (1-f) \cdot V_{ref}(\upsilon) + f \cdot V_{dip}(\upsilon), \tag{4.9}$$

where f denotes the fraction of the broadened spectral contribution to the simulation.

During the minimization of the rms-deviation, the Gaussian distribution peak and width (parameters i) and ii) from above) and the factor f from equation 4.9 were allowed to vary. Note that in this approach only the first peak of the distance distribution stemming from the first neighbor electron spins contributes to the dipolar broadening. From the r^{-3}-dependence of the dipolar coupling (equation 2.19 in Section 2.2) one can calculate that dipolar broadening to all other electron spins located farther away becomes so small that it is hidden in the intrinsic linewidth of the spectrum (~2.2 G for r=2 nm).

Using the spectrum at R=0.0028 instead of the spectrum for the pure TAM spin probe can be justified by a thorough inspection of those two spectra in Figure 4.10. Both spectra show the same width, i.e. TAM ions in the sample with PDADMAC seem fully isolated and dipolar broadening of the
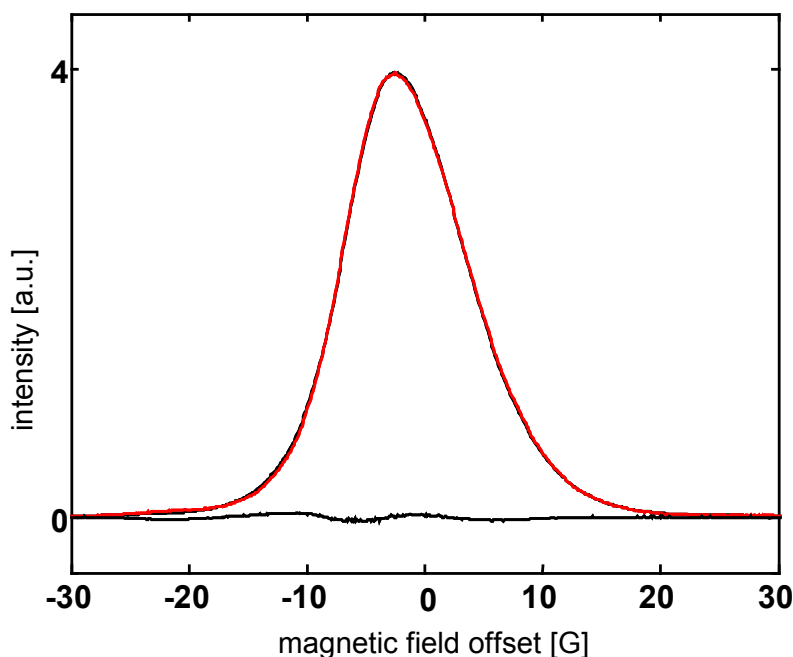
Figure 4.11. ESE-detected, field-swept EPR spectrum (W-band, ~94 GHz) of TAM + PDADMAC in frozen glycerol/water solution (T=80 K) at R=0.05 and simulation by the convolution approach explained in the text. **Black line:** experimental spectrum; **Red line:** simulation with f=0.42 (eq. 4.9) and a dipolar coupling assuming a Gaussian distance r_{dip}=1.5 nm and a width of Δr_{dip}=0.3 nm as origin of the broadening; also shown is the residual after subtraction of the simulated from the experimental spectrum;

spectrum at R=0.0028 can be excluded. As these ESE-detected spectra are also sensitive to changes in spin probe local surroundings (see differences in Figure 4.10) such as polarity, it is likely that the selected spectrum at high polyelectrolyte content accounts much better for the immediate spin probe environment in the respective samples than the spectrum without any polyelectrolyte. This has also been checked qualitatively: use of the pure TAM spectrum as reference delivered simulations of the dipolar broadened spectra that were not nearly as good as those using the R=0.0028 spectrum as reference. A detailed spectral simulation of the TAM trianion in high-field/high-frequency EPR spectra is of general interest for the understanding of triarylmethyl radicals. It is, however, outside the scope of this thesis and will be published later.

Figure 4.11 shows the spectrum at R=0.05, the fit that was achieved by the above-explained procedure yielding f=0.42 and the residual signal after subtraction of the simulated from the experimental spectrum. Fits throughout the whole R-range were of similar quality as that shown in Figure 4.11 and the only variable parameters were f, the average Gaussian distance r_{dip} and Δr_{dip}. Summaries of the extracted distances and the fraction of dipolar-broadened spins are given in Figure 4.12. The width of the assumed Gaussian distribution of distances in all simulation varied between 0.1 and 0.5 nm, and empirically it was found that changes in Δr_{dip} in this range did not affect the simulated spectra significantly, so that f and r_{dip} are the parameters that can be interpreted reliably.

Figure 4.12.a displays that the fraction of dipolar-coupled electron spins, while Figure 4.12.b puts on view the respective distances r_{dip} that separate the coupled fraction of TAM counterions.

The two plots of Figure 4.12 together are the TAM-analogue to Figure 4.9 for FS/PDADMAC, as they contain similar information. The fraction of the spectral component that belongs to dipolar-coupled spins is analogous to the ever-stronger deviation of the FS-ion distribution from a homogeneous distribution, while the plot of the distance r_{dip} corresponds to the development of the concentration of FS ions c_{lin} that is distributed linearly. Note however that underlying Figure 4.9 is the model that the FS counterions are distributed either along a one-dimensional chain or homogeneous in three dimensions, whereas no such information is attainable from Figure 4.12. The same data treatment was also attempted to gain information on the FS/PDADMAC samples that were not accessible by the DEER experiments alone. Spectral fitting as explained for the TAM series was also implemented for FS/PDADMAC series of the X-band ESE-detected EPR spectra (see Figures 3.17 and 4.8.a/c), but resulted in only poor reproduction of the broadened spectra of $R > 0.03$. Failure of the method in this case may be attributed to the on average closer distances of FS ions, which may lead to broadening also from sources different than dipolar coupling, such as exchange coupling through solvent.[52]

The main difference that can be found between FS ions and TAM ions in solution with PDADMAC seems to be the development of the interspin distances for both systems. For TAM/PDADMAC between $0.01 < R < 0.1$, the distance between one TAM ion and the closest TAM neighbor seems to decrease only slightly, from ~1.6 nm to ~1.4 nm, and even for the highest
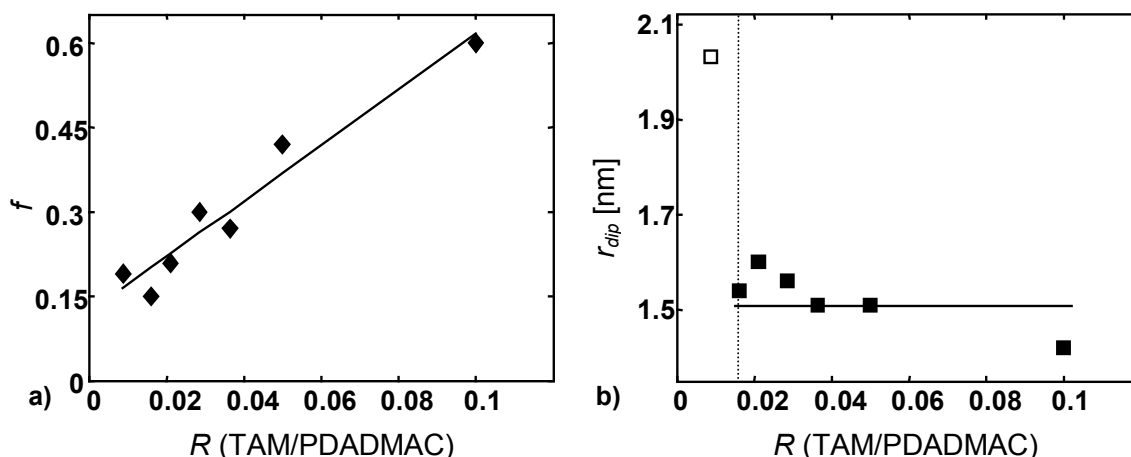
Figure 4.12. Summary of the fit parameters extracted from simulation of ESE-detected, field-swept EPR spectra of TAM + PDADMAC in frozen glycerol/water solution (*T*=80 K) as described in the text. **a)** fraction of dipolar-coupled spin probes (*f*, see eq. 4.9, black diamonds) and linear fit to the data (*f* = 4.94*R + 0.12); **b)** distance of dipolar-coupled spin probes (r_{dip}, black squares), the horizontal black line marks the average distance of ~1.5 nm; the first data point deviates a little stronger from the average distance (open square, marked by vertical dotted line, see text for details);

polyelectrolyte concentration the distance is still as small as ~2.0 nm. In contrast, there is a marked *R*-dependence of the FS-FS linear spin density in Figure 4.9 (with the exception of the artificial plateau for *R* > 0.05 stemming from lack of sensitivity of the DEER experiment for very short distances). One has to be careful, though, when comparing spin probe distances gained from DEER with those from spectral fitting of ESE-detected W-band EPR spectra. Also, it will be difficult to relate these findings from frozen solution spectra to insights acquired from CW/FT EPR spectra in liquid solution. Two conclusions can nonetheless be safely drawn.

4.3.1   "Zip-like" clustering of TAM crosslinks

First, the shortest distance between two electron spins on TAM ions is found as 1.4 nm for a high *R*-value of 0.1. This coincides remarkably well with the minimum distance found between two sp^2-carbon centers of TAM from force-field simulations similar to that shown in Figure 3.19 when two TAM molecules approach each other along one of the C$_2$ molecular axes (see Scheme 3.3 and Figures 4.13/4.14, these are the axes in the direction of central atom-carboxyl group). Since the unpaired electron spin density has been found to be located predominantly (~50%, see Appendix A5) on this central carbon atom from density-functional calculations (Titan v1.0, B3LYP density functional, 6-31* basis set), this is the distance that one would expect for TAM molecules that align in closest contact.

Second, the steady increase as a function of *R* of the fraction of dipolar coupled spins that is reflected in the increase *f* is an effect that can be analyzed in a manner similar to the decrease of the homogeneous concentration and increase of linear spin density of FS ions from DEER (Fig. 4.9).

So, one could interpret the fit parameters for the *R*=0.1-sample as showing that 60% of the TAM counterions are attached to a PDADMAC chain (assuming that for low polyelectrolyte content

all ions that are electrostatically condensed to the polyelectrolyte also experience dipolar broadening) and that they roughly come as close as 1.4 nm to each other.

The significantly larger distance of ~2 nm found for 15% of TAM spin probes at R=0.0087 is only a small increase in the distance if one considers the relatively large size of individual TAM counterions. At this R-value, there are statistically 115 PDADMAC monomeric units per TAM trianion. Even when assuming that each TAM spin probe effectively covered 8 repeat units (as it is suggested from the simulation shown in Figure 3.19), within the simplest possible model of TAM ions attached to linear chains, on average there would be 14 repeat units between these attachment sites and thus also between TAM ions. As in the case of FS/PDADMAC, this picture assuming fully homogeneous distribution of TAM ions is at variance with the experimental/simulated results.

One can explain the two main observations of this data analysis within a rather simple model. Those TAM counterions that are dipolar coupled are always spaced at ~1.5 ($\pm$0.2) nm, and merely the fraction of counterions that attain this spacing varies with polyelectrolyte content. Hence, one could deduce that the TAM ions are distributed over the solution of PDADMAC chains in either of two domains: at closest lateral contact with other TAM spin probes or isolated within PDADMAC. At lower R-values, the majority of spin probes is isolated in a bulk of overlapping polyelectrolyte chains but with increasing R more and more TAM ions populate the closely spaced domain. This is visualized in Figure 4.13, where the system is sketched at three different R-values. The chains that are schematically drawn in this Figure do not necessarily denote different PDADMAC chains, they may very well also be segments of the same macromolecule.
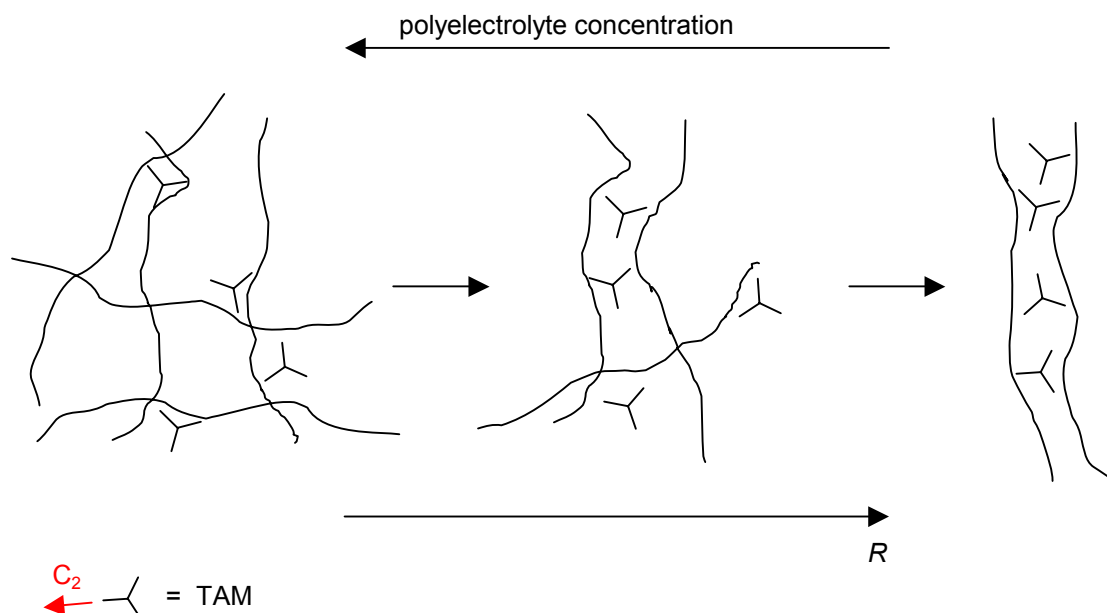
Figure 4.13. Schematic visualization of the plots in Fig. 4.12: with increasing R, TAM spin probes are increasingly attached to spatially close polyelectrolyte domains, which explains the increase in f of Fig. 4.12.a. The sketch can also be viewed from right to left as an increasing dilution of TAM ions, in particular of closely spaced (i.e., strongly coupled) TAM ions, with increasing PDADMAC content. Shown in red: one of the three C_2-symmetry axes;

Be reminded that from the findings of CW/FT EPR measurements in liquid solution (Section 3.3) and from the abrupt transitions of the radial concentrations within the charged cylindrical cell model reported in Section 4.1, it was postulated that TAM acts as a physical cross-linking agent. In this model, for $R < 0.02$ a polyelectrolyte network is formed and for $R > 0.02$ TAM ions seem to interact with single PDADMAC chains. The results presented in this section are from frozen solution so they ideally represent a snapshot of the liquid-state solution at its glass transition temperature. Hence, findings from this section are not necessarily meaningful for the room-temperature, liquid-state solutions of TAM/PDADMAC that have been investigated in the previous sections. Nonetheless, the appearance of a small fraction of closely spaced TAM ions even at low R now might help modifying the transition-like picture drawn before. Even in high dilution there are TAM ions that physically connect certain domains of PDADMAC polyions. These domains probably act as a starting point for other physical crosslinks: once they are formed by connection via TAM, respective PDADMAC molecules act as one single polyion, and there may be significant gain in energy and entropy of the whole system if other TAM ions now act as crosslinker of two adjacent domains.

Like a zip, a whole series of TAM crosslinks could be formed similar to a cooperative binding, once one such junction has been established. In addition, there may also be a geometrical predisposition by the initial link to form new connections. The whole model is schematically depicted in Figure 4.14, which is meant to show the cooperative binding at a given ratio R.

Electrostatic attachment in general increases entropy by the release of counterions as expected for Manning-like condensation of multivalent ions. Additionally, there may be an energetic advantage of forming physical junctions, since voluminous organic TAM ions (with twelve hydroxyethyl side chains) may also interact preferentially with the hydrocarbon backbone of PDADMAC by hydrophobic interaction as seen for organic dyes.[1,103,104] The driving force that could be specific to the
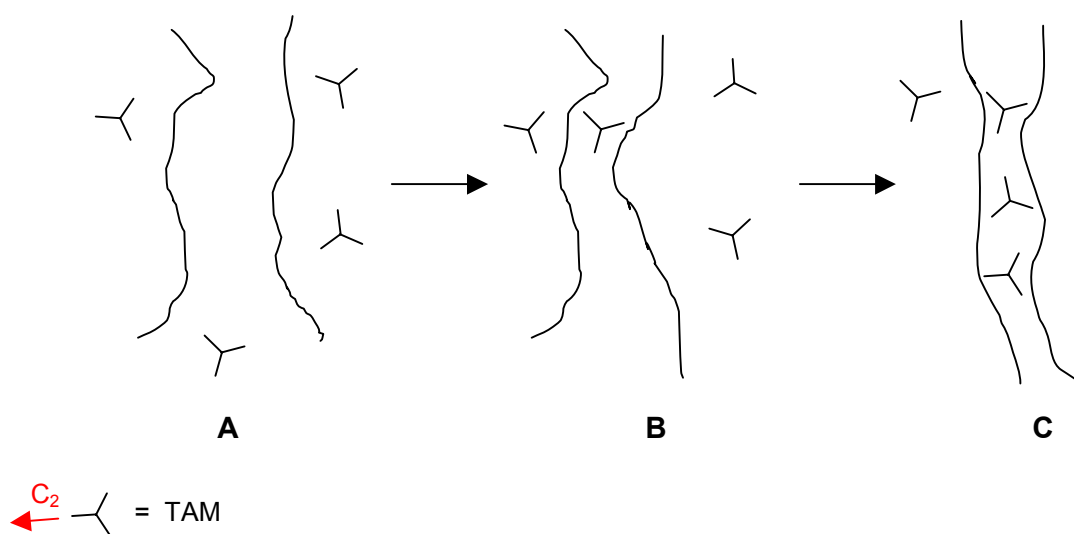
Figure 4.14. Schematic representation of the proposed "zip-like" formation of domains of polyelectrolyte that are cross-linked by TAM tristar-shaped spin probes. **A:** TAM ions interact only with individual chain domains; **B:** One TAM ion is connected to two domains on two different macroions (high polyelectrolyte content) and forms a physical crosslink; **C:** The chain domains adjacent to the crosslink are predisposed to take up TAM ions and increase the connected domain; Shown in red: one of the three C_2-symmetry axes;

zip-like formation of physical networks, may be a combined effect of increases of both, energy and entropy. The combined effects of specific TAM-PDADMAC interaction and release of small counterions may overcompensate possible decreases in entropy originating from the loss in conformational degrees of freedom upon physical crosslinking.

This picture somewhat resembles formation of thermoreversible gels, which has been studied extensively until now.[1,123,124] It is generally acknowledged to be a two-step process of initial creation of small macromolecular aggregates and subsequent further aggregation of these molecular clusters. Despite the heterogeneity of the two-step process, during gel-formation the system remains macroscopically homogeneous.[1] Although the situation is somewhat different in the case of TAM/PDADMAC, one may nonetheless deduce that in analogy to the aggregated and non-aggregated states in thermoreversible gels, in the investigated system there may be isolated and clustered TAM crosslinks at any time even at low ratios of spin probe/polyelectrolyte, respectively. The overall system remains homogeneous on long lengthscales.

Unlike the insights gained from data analysis of CW/FT EPR spectra at ambient temperature, in this W-band EPR convolution approach no information is attainable on whether there is a sharp transition from interpolyelectrolyte networks to single chains at $R \approx 0.02$. The ability of dynamic rearrangement of the system is removed and close approach of TAM ions cannot distinguish between spin probes partaking as crosslinkers and those only attached to single chains (as it is likely to be the case for high R-values), so that the spectral analysis presented in this section is complementary to the room-temperature analysis and can be fully reconciled with the previous findings.

Additional pulse EPR measurements at X-band frequencies

In addition to the convolution of W-band ESE-detected spectra with a dipolar broadening function, also other pulse EPR measurements were carried out to characterize spin probe local concentration. The ESE decay for a radical with an EPR spectrum as narrow as the TAM trianion might be dominated by the effect of *instantaneous diffusion* (ID) of spins, which is a function of the local concentration in spins.[39] Therefore, comparison of the different decay time traces at different R-values might include information on the change in local TAM concentrations. Analysis of the 2-pulse ESE-decays dominated by instantaneous diffusion was less straightforward than lineshape analysis of W-band spectra. Several analysis methods were attempted, such as deconvolution of contributions of other effects from the decay due to ID. This was achieved, e.g., by dividing time traces by a time trace at low flip-angle (32° instead of 180° for the π-pulse), which approximately is not affected by ID.

All these methods led to results that do not contain additional information as compared to the spectral convolution of W-band ESE-detected spectra presented in this section. As the X-band data analysis relies on more approximations and assumptions than W-band data analysis, those results are not presented at this point. The performance of all the different approaches to characterization of samples containing TAM radicals will be discussed in more detail in a separate method-oriented publication.

5   Conclusions and Outlook

In this work methods of EPR spectroscopy were used to investigate polyion-counterion interactions in polyelectrolyte solutions. This subject is usually treated experimentally by light, X-ray, or neutron scattering techniques. The main difference to the numerous scattering studies in this area is that EPR techniques are *local methods* and by employing spin-carrying (i.e., EPR-active) probe ions it is possible to examine polyelectrolytes from the *counterions' point of view*.

Figure 5.1 gives a schematic summary of the most important experimental findings in this thesis. It was possible to gain insight into i) the *dynamics* and *local geometry* of *counterion attachment*, ii) *conformations* and *dynamics* of local segments of the *polyion* in an indirect manner, and iii) the *spatial distribution* of spin probe ions that surround polyions in solution.

Dynamic electrostatic attachment and local attachment geometry

The dianion spin probe Fremy's salt (FS, see Fig. 5.1) was used with cationic polyelectrolytes of two classes – a model rigid-rod-like coordination polyelectrolyte consisting of Ru^{2+}-centers as charge-bearing groups (RuCP, structure shown in Scheme 3.1) and the standard polyelectrolyte PDADMAC (see one repeat unit in Fig. 5.1). By continuous wave (CW) EPR measurements on these systems it could be shown that in the regime of counterion condensation, the counterions are transiently attached to and detached from the polyion with a lifetime of the attached state less than 1ns. This kind of condensation is termed *dynamic electrostatic attachment* (DEA). In addition, from simulations of the respective CW EPR spectra, taking into account the rotational dynamics as a uniaxial Brownian reorientation, the attachment geometry could be examined. For the RuCP model polyelectrolyte it was found that FS ions are electrostatically attached via both negative sulfonate groups (not shown), while they are effectively attached via only *one* sulfonate in the case of PDADMAC (blue inset in Fig. 5.1). While the attachment in the case of RuCP can be seen as the ordinary case – attraction between all charges of a dianion and a dication – the attachment geometry involving PDADMAC as the polyion is surprising.
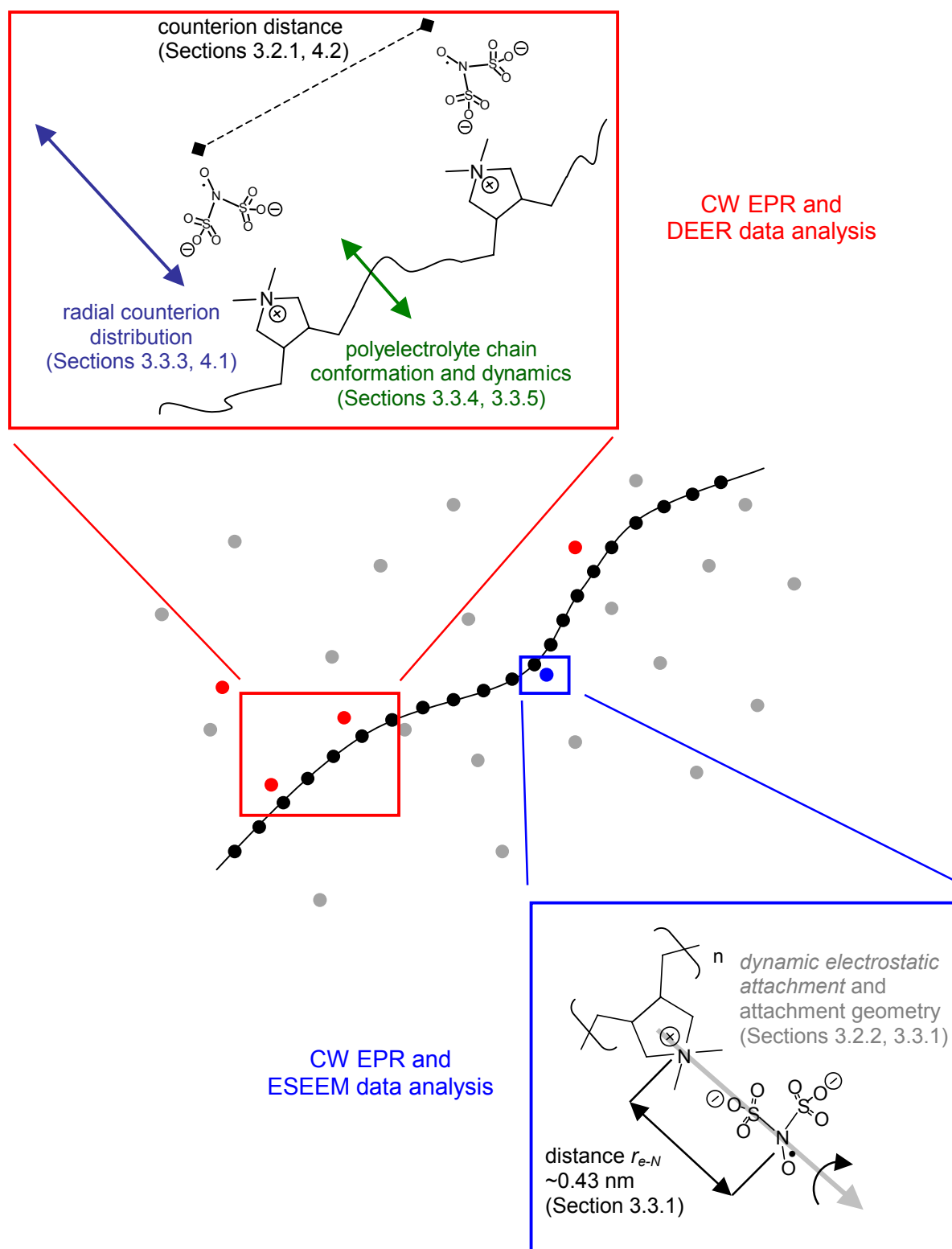
Figure 5.1. Schematic summary of the experimental investigations in this work. The sections containing the respective results are given in brackets. Note that only PDADMAC repeat units are shown, but repeat units of the RuCP model system are also included in the discussion.

From 3-pulse electron spin echo envelope modulation (ESEEM) experiments and ratio analysis of those time-domain data it was possible to obtain an approximate distance of closest approach between the electron on the counterion and the charge-bearing ^{14}N atom on the PDADMAC (blue inset in Fig. 5.1).

This distance was found to be ~0.43 nm, which nicely corresponds to a contact ion pair of FS counterions and the charged group on the polyelectrolyte. Furthermore it can be approximated that at any time only ~20 % of all FS ions are in such a *site-attached* state.

Polyelectrolyte chain conformation and dynamics

For the case of the flexible PDADMAC polyelectrolyte, it was also possible to indirectly obtain information on the polyion conformation and dynamics on the EPR lengthscale of a few nanometers (red inset in Fig. 5.1). This was achieved by variation of the solvent systems from water to three organic solvent/water mixtures, which produced solutions with strongly different macroscopic parameters such as permittivity and viscosity. It was found from model-free analysis of CW EPR measurements that in purely aqueous solution there were substantial differences in the characteristic DEA behavior of spin probe counterions, which can be explained by assuming a different PDADMAC polyion conformation in water at different values of the spin probe/polyion ratio R: a transition from a more elongated to a more globular conformation takes place at R~0.05. In the organic solvent/water mixtures large variations of macroscopic permittivity caused only slight changes in DEA related to effects of solvent viscosity on polyelectrolyte chain dynamics. This qualitative difference between pure water and organic solvent/water mixtures can be understood if the effect of preferential solvation of the polyion chains by organic solvent molecules is considered.

Spatial distribution of counterions

The third group of major findings in this thesis is related to the spatial - radial and lateral - distribution of spin-carrying counterions in solutions containing polyelectrolytes.

The broadenings observable in CW EPR spectra stems from increased spin-exchange interaction, which is a direct measure of the frequency of counterion-counterion collision. Hence, the broadenings contain information on local spin probe concentration, which is analyzed by two approaches in this thesis (red inset in Fig. 5.1). First, the CW EPR spectra are characterized in an approach that is essentially *model-free* and only quantifies broadenings in terms of fits with a stretched exponential decay. The second type of analysis is based on a recent theoretical model (a modified *cylindrical cell* description) of counterion distribution in polyelectrolyte solutions. Using this theoretical model, the CW EPR spectra were simulated and it was possible to obtain values for the counterion concentrations at the site of the polyion. It was further verified that in the organic solvent/water mixtures the counterion concentration decays radially as a function of r^{-2} with the distance r from the polyion. In the case of water as a solvent, this approach breaks down for values of

spin probe/polyion ratio R larger than 0.05, which is in agreement with the proposed different polyelectrolyte conformations when increasing R beyond that value.

In addition to the radial counterion distribution, information on the spin probe distribution *along polyelectrolyte chains* could be gained (red inset in Fig. 5.1). This was achieved with the double electron-electron resonance (DEER) experiment, which is sensitive to distances between spin probes in the range from ~1.5 to 8 nm. In the case of the RuCP model polyelectrolyte, for a significant fraction of the employed FS spin probes a bimodal distance distribution was found that nicely reproduced the spacings of direct and next-neighbor Ru^{2+}-centers along the polyelectrolyte: 2.35 nm and 4.7 nm.

For the system of FS spin probe and PDADMAC polyelectrolyte, no distinct distance distribution could be found from DEER, probably due to the much higher charge density along the chain and the conformational freedom of the polyion chains. The DEER data in this case could be simulated by assuming a two-state distribution of spin probes, one state corresponding to a *homogeneous* (3-dimensional) distribution of spin probes in the polyelectrolyte bulk and the other to a *linear* (1-dimensional) distribution of spin probes that are electrostatically condensed along locally extended PDADMAC chain segments. From this analysis it is suggested that the PDADMAC chains form locally elongated structures of a size of at least ~5 nm, although the exact conformation (e.g., stretched or cigar-shaped) could not be finally determined.

Network-forming spin probes

Finally, the spin probing approach taken in this thesis was extended from small inorganic spin probe counterions FS to large organic, tri-star shaped spin probes of the triarylmethyl class (TAM). These trivalent ions are expected to interact with PDADMAC polyelectrolyte chains not only by electrostatic interaction but also by means of hydrophobic interactions. High-field/high-frequency (W-band, ~94 GHz) ESE-detected spectra of this TAM spin probe in presence of variable amounts of PDADMAC could be fitted by again assuming a two-state distribution of spin probes. The first state is a homogeneous distribution, while the second state assumes closely spaced TAM ions.

From these simulations it was found that at any ratio R of TAM spin probe/PDADMAC, there is a fraction of TAM ions that is in close contact (~1.5 nm), and only this fraction increases with decreasing polyelectrolyte content. This finding indicates that the large organic TAM spin probes can act as network-inducing agents in solutions of PDADMAC polyelectrolyte. The data are consistent with a "zip-like" cooperative binding effect of TAM ions, making this spin probe an interesting building block for supramolecular chemistry.

Outlook: EPR spectroscopy on spin-labeled polyelectrolytes

In this thesis it was shown that EPR spectroscopy of spin-carrying tracers for counterions can give valuable insight into polyelectrolyte systems governed by complex electrostatic interactions. This insight is mainly complementary to the knowledge that can be gained by the widely used scattering methods, since it examines these systems from the counterions' point of view.

It has also become obvious that this approach has its limitiations when direct knowledge about polyelectrolyte chain conformations is needed. This can be overcome by covalently introducing the EPR-active group into the polyion chain, i.e., by investigating spin-labeled polyelectrolytes.

EPR studies of a spin-labeled PDADMAC polyelectrolyte would be complementary to the work presented in this thesis, as one could probe polyelectrolyte systems from the *polyion's point of view*. For this purpose, Dr. Joachim Storsberg and Prof. André Laschewsky from the *Fraunhofer Institute for Applied Polymer Research* in Golm synthesized PDADMAC that contains 2-4 mol% of a TEMPO spin label (see Scheme 5.1). Under the assumption that introduction of spin labels into a few percent of the repeat units does not alter the polyelectrolyte character in a significant manner, this system should provide new insight into polyelectrolyte chain structure and dynamics.
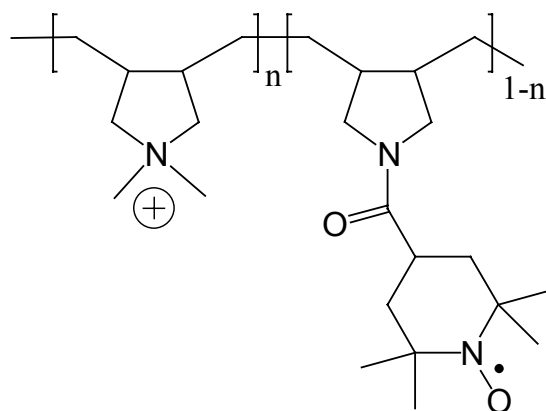
Scheme 5.1. Structure of the TEMPO-labeled PDADMAC polyelectrolyte. Here: n=0.96-0.98 PDADMAC=poly(diallyldimethylammonium chloride); TEMPO: 2,2,6,6-tetramethylpiperidine-1-oxyl;

From CW EPR studies, by variation of solvent, temperature or added salt, one could probe changes in segmental motion of polyelectrolyte, while the DEER experiment might reveal alterations in the local chain conformation upon variation of one of these parameters.

It might even be possible to combine this approach with the approach introduced in this thesis, i.e., to use spin-labeled PDADMAC together with FS spin probes to characterize polyelectrolyte-counterion interactions in even more detail.

It is hoped that this thesis helps in the characterization of the local effects and interactions in complex polyelectrolyte systems. Such a microscopic picture of interactions may be a necessary prerequisite for understanding structure-property relations of these systems.

.   Appendix

A1   Materials – polyelectrolytes, spin probes and solvents

Polyelectrolytes

Cationic polyelectrolyte poly(diallyldimethylammonium chloride), PDADMAC, with an M_W of 240 000 was bought from Polysciences, Inc., and polyelectrolyte poly(sodium 4-styrene sulfonate), PSS, with average M_W of 1,000,000 was purchased from Aldrich Chem. Co.. Both polyelectrolytes were used as received. From gel permeation chromatography (GPC) the average M_W/M_N was measured for PSS($M_W/M_N = 6.7$). For PDADMAC this was not possible, but the polydispersity is certainly far larger than unity ($M_W/M_N \gg 1$).

Spin probes

Fremy's salt (Potassium nitrosodisulfonate), FS, with technical grade of purity was bought from ICN Biomedicals, TAM (triarylmethyl radical "OX063", sodium salt) was a gift from Nycomed Innovations AB, Sweden. CAT1 (4-Trimethylammonium-2,2,6,6-tetramethylpiperidine-1-oxyl iodide) was purchased from Molecular Probes Europe, $MnCl_2$ with a purity of 98 % was bought from Fluka, and $VOSO_4*5H_2O$ with an unknown grade of purity was obtained from Merck, Darmstadt.

Solvents

The solvent systems were deionized Milli-Q-water (permittivity: ε_r=80 at 293 K), 50 vol.% ethanol (Riedel-de Haën)/50 vol.% water (density ρ=0.895, approximate ε_r=50 at 293 K), 70 vol.% N-methylpropionamide (Aldrich Chem. Co.)/30 vol.% water (NMPA/H_2O, ρ=0.951, approximate ε_r=140 at 293 K), 66 wt.% glycerol/34 wt.% water (made from 87 wt.% glycerol/water mixture, Fluka, density $\rho\approx$1.17 g/ml, approximate ε_r=57 at 293 K).

Sample preparation

FS/PDADMAC. Stock solutions of FS (in one of the four respective solvents, 2 mM) and PDADMAC (in the same solvent, 200 mM) were mixed in varying amounts and diluted with the same solvent.

Unless noted otherwise, small amounts of KOH were added to adjust the solution to pH ~9 spin probe.

FS/RuCP. See Section 3.2.1.

TAM/PDADMAC. A stock solution of TAM (in water, 1.6 mM) and PDADMAC (in water or glycerol/water, 200 mM) were mixed in varying amounts and diluted with water or glycerol/water.

VOSO₄/PSS. A stock solution of $VOSO_4$ (in water, 50 mM) and PSS (in water, 200 mM) were mixed in varying amounts and diluted with water. All solutions were adjusted to pH 1-2 with HCl prior to use.

MnCl₂/PSS. A stock solution of $MnCl_2$ (in water, 10 mM) and PSS (in water, 200 mM) were mixed in varying amounts and diluted with water.

A2   EPR Measurements

Experimental Set-up

EPR spectra at 293K and X-band (~9.4 GHz) were measured on a Bruker ELEXSYS 580 spectrometer using an AquaX inlet and a rectangular cavity (4103TM, Q-values typically ~3000). The AquaX consists of a bundle of (14 very narrow quartz capillaries and replaces the usual sample tube in the resonator. Aqueous samples (and organic solvent/water mixtures) are injected and can be measured with much reduced dielectric loss due to absorption of microwave by the water. FT EPR spectra at 293K and X-band were detected on the same spectrometer with the same probehead but with a sample volume of 20 to 40 μl in quartz tubes of 4 mm outer diameter (Wilmad Corp., USA).

All pulse EPR experiments were performed on the same spectrometer using a dielectric resonator (MD4EN) with the exception of 4-pulse DEER measurements presented in Chapter 4. The latter results were obtained with a Bruker Flexline split-ring resonator (ER 4118X-MS3).

All pulse EPR measurements were performed with overcoupling to $Q \approx 100$ and the temperature was set to 80 K by cooling with liquid nitrogen and to 50 K by cooling with liquid helium using an Oxford cryostat and cooling system. Typically, 20 to 40 μl of sample volume were used in quartz tubes of 3 mm outer diameter (Wilmad Corp., USA). The pump pulses were generated by feeding the output of an HP8350B sweep oscillator to one microwave-pulse-forming unit of the spectrometer.

EPR spectra at high-field/high-frequency (W-band, ~94 GHz) were recorded on a Bruker ELEXSYS 680 spectrometer with a Bruker TeraFlex™ probehead. Sample volumes of 1 to 3 μl were filled in home-made round-bottom Suprasil capillaries (inner diameter 0.7 mm, outer diameter 0.87 mm, Wilmad Corp., USA), which were then sealed with fast-drying glue. Measurements at T=80 K were performed by cooling with liquid nitrogen using an Oxford cryostat and cooling system.

A3   CW EPR spectra (293 K) of FS/PDADMAC in glycerol/water

R=0.0036 — 139 mM PDADMAC
R=0.0054 — 92.6 mM PDADMAC
R= 0.0108 — 46.3 mM PDADMAC
R=0.0216 — 23.1 mM PDADMAC
R=0.0270 — 18.5 mM PDADMAC
R=0.0360 — 13.9 mM PDADMAC
R=0.0450 — 11.1 mM PDADMAC
R=0.0676 — 7.4 mM PDADMAC
R=0.0901 — 3.7 mM PDADMAC
R=0.1351 — 1.9 mM PDADMAC
0 mM PDADMAC

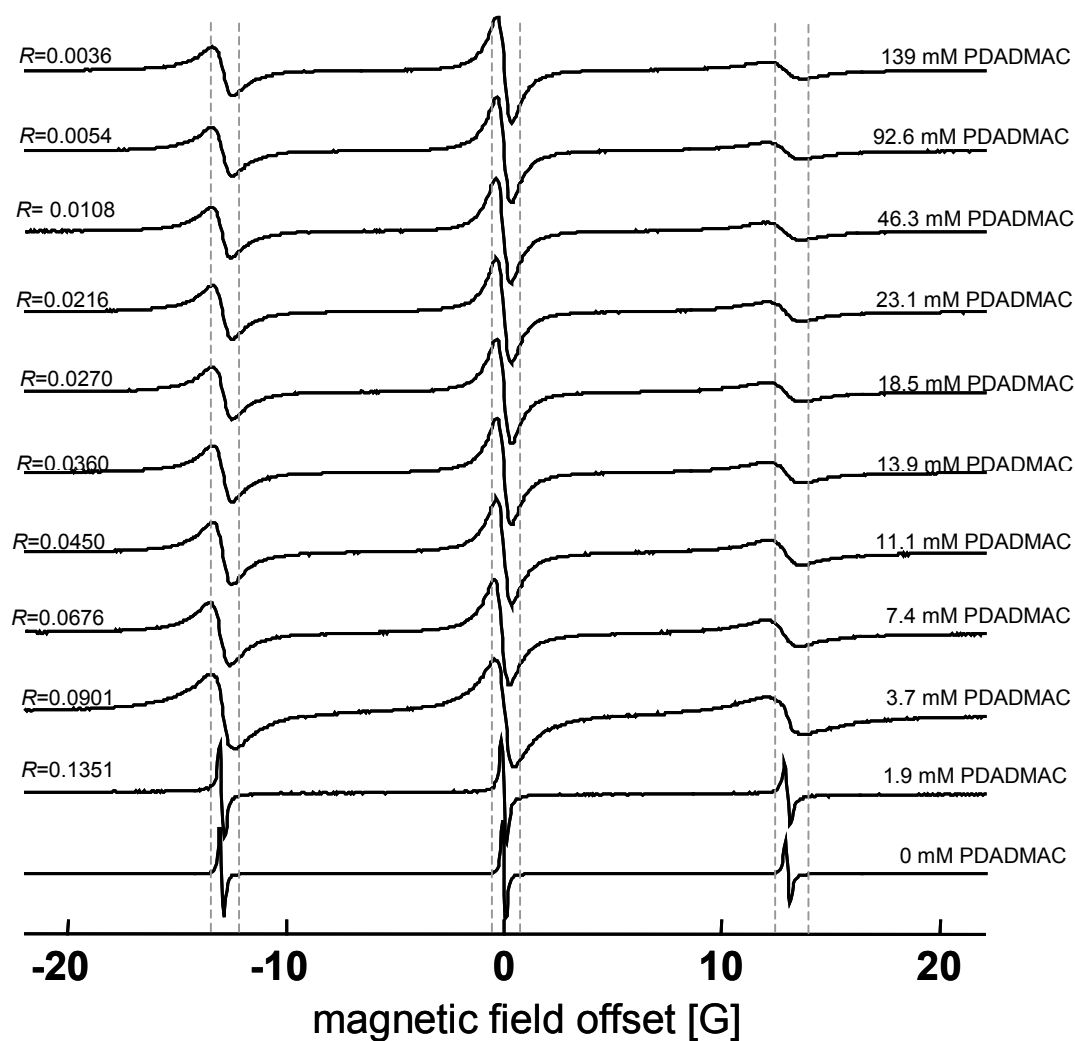magnetic field offset [G]
-20   -10   0   10   20

Figure A.3.1. Complete set of CW EPR spectra at X-band of FS + PDADMAC in glycerol/water. The concentration of PDADMAC (in monomeric charged units) is varied and given on the left hand side above each spectrum. The respective ratios of c(FS)/c(PDADMAC) are given on the left hand side.

The three pairs of gray dashed lines mark the magnetic field position at which the lines in the FS spectrum without PDADMAC have already reached baseline level. It is apparent that most prominently at high *R*-values (low PDADMAC concentration) the three EPR lines have significantly broader flanks. At low *R*-values (high PDADMAC concentration) this broadening is diminished again.

A4 Effect of variation FS concentration on fit parameters from equations 3.2 and 3.3

The fitting of the FT of stretched exponential decay functions to the experimental CW EPR spectra of FS/PDADMAC in various solvents gave stretch factors x that strongly deviated from unity (i.e., the spectral lines deviated more and more strongly from Lorentzian lines). This was attributed to spin-exchange broadening due to increased local concentration together with a heterogeneity of the spin probe distribution (i.e., a concentration gradient), and altered rotational dynamics.

Figure A.4.1 shows the same kind of analysis (see equations 3.2 and 3.2) for two series of CW EPR measurements in which only the FS concentration was varied from 0.2 mM to 128 mM. Figures A.4.1.a) and c) display the averaged relaxation times $<T_{2,k}>$ and the stretch factors x for FS in water, while b) and d) show those fit parameters for the series in glycerol/water.

The main point of the analysis is that even at very high FS concentrations the stretch factors are close to unity, which allows the conclusion that the spectral broadenings observed in solutions with PDADMAC (see Figures 3.12 and 3.13) do not stem from merely increased homogeneous FS concentrations. As explained in the text, the broadenings might include a distribution of different spin-exchange frequencies and thus also a distribution of relaxation times.
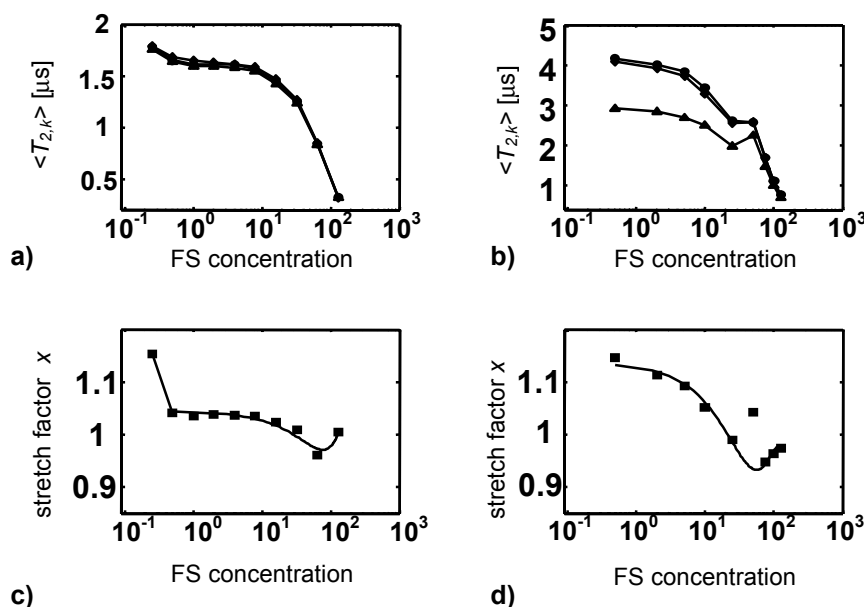
Figure A.4.1 Plots of analysis of CW EPR spectra (X-band, ~9.79 GHz) of FS as a function of the FS concentration in water (a, c) and glycerol/water (b, d) according to eqs. 3.2 and 3.3.
a), b) averaged relaxation times (diamonds: low-field manifolds (k=1); circles: center-field manifolds (k=2); triangles: high-field manifolds (k=3).**c), d)** stretch factors x (see eqs. (3.2), (3.3)).
Lines are meant as a guide to the eye.

A5   DFT simulations of the unpaired electron spin density on a TAM radical
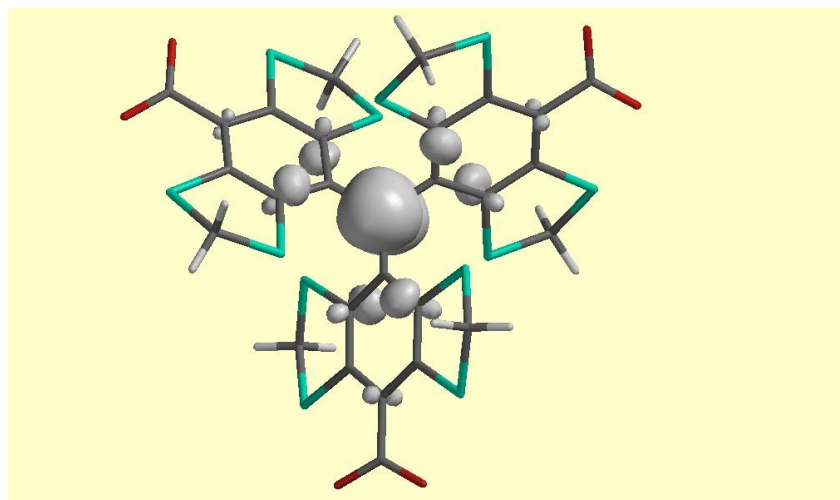

Figure A.5.1. Density functional calculation of a TAM radical spin density distribution (Titan v1.0 B3LYP density functional, 6-31* basis set). ~50% of the spin density is located on the central carbon atom. Color code: gray: C-atoms; white: H; red: O; green: S;

A6   Ratio analysis of 3-p ESEEM

The simplified equations to calculate the extrema of the modulation of the averaged 3-pulse echo ($V_{max,th}(\tau, r_{e-n}, a_{iso})$ and $V_{min,th}(\tau, r_{e-n}, a_{iso})$) are given by:[80]

$$
\begin{aligned}
V_{\substack{max,th\\min,th}}(\tau, r_{e-n}, a_{iso}) = 1 &- \frac{16}{5}\frac{T_\perp^2}{\omega_I^2} + \frac{144}{35}\frac{T_\perp^4}{\omega_I^4} + \frac{2}{3}F'(\tau+T) \\
&\pm \left[\frac{8}{3}F\left(\frac{\tau+T}{2}\right) - \frac{8}{3}F'\left(\frac{\tau+T}{2}\right)\right]
\end{aligned}
\tag{A.6.1}
$$

where the "+"-sign applies for V_{max} and the "-"-sign for V_{min}. In this equation, $T_\perp$ is defined as:

$$
T_\perp = \frac{g_e g_N \beta_e \beta_N}{\hbar r^3},
\tag{A.6.2}
$$

and F and F' are integrals (approximated numerically) that perform the powder average as a function of $T_\perp$ and a_{iso}. The detailed expressions are given in the publication by Ichikawa and coworkers.[80]

References and Notes

[1] H. Dautzenberg, W. Jaeger, J. Kötz, B.Philip, C. Seidel, D. Stscherbina, **Polyelectrolytes – Formation, Characterization and Application**, Carl Hanser Verlag, Munich, (1994)

[2] F. Oosawa, **Polyelectrolytes**, Marcel Dekker Inc., New York (1971)

[3] S. Förster, M. Schmidt, *Adv. Polym. Sci.* **1995**, *120*, 51

[4] G. Decher, *Science* **1997**, *277*, 1232

[5] S. Kumar and R. Nussinov, *ChemBioChem* **2002**, *3*, 604

[6] J. Kötz, S. Kosmella, T. Beitz, *Prog. Polym. Sci.* **2001,** *26*, 1199

[7] S. Ogawa, E. A. Decker, and D. J. McClements, *J. Agric. Food Chem.* **2003**, *51*, 2806

[8] S. H. Lee, *Polymer J.* **2000**, *32*, 716

[9] M. Rubinstein, R. H. Colby, **Polymer Physics**, Oxford University Press (2003)

[10] Y. Kantor and M. Kardar, *Phys. Rev. E* **1995,** *51*, 1299

[11] A. V. Dobrynin, M. Rubinstein, and S. P. Obukhov, *Macromolecules* **1996,** *29*, 2974

[12] H. J. Limbach, C. Holm, and K. Kremer, *Europhys. Lett.* **2002**, *60*, 566

[13] Although there have been publications of experimental verifications of pearl-necklace structures by atomic force microscopy (AFM): S. Minko, A. Kiriy, G. Gorodyska, and M. Stamm, *J. Am. Chem. Soc*. **2002**, *124*, 3218, it is doubtful that these pearl-necklaces are those found in numerical simulations (see Refs. 10-12), since in general there are prominent surface effects in AFM;

[14] T. Radeva (Ed.), **Physical Chemistry of Polyelectrolytes**, Marcel Dekker Inc., New York (2001)

[15] M. Deserno, **Counterion Condensation for Rigid Linear Polyelectrolytes**, Doctoral Dissertation, Mainz (2000)

[16] N. M. Atherton, **Principles of Electron Spin Resonance**, Ellis Horwood, New York (1993)

[17] D. Hinderberger, G. Jeschke, and H. W. Spiess, *Macromolecules* **2002,** *35*, 9698

[18] H. Q. Xue, P. Bhowmik, S. Schlick, *Macromolecules* **1993**, *26*, 3340

[19] G. Tsagaropoulos, J. S. Kim, A. Eisenberg, *Macromolecules* **1996**, *29*, 2222

[20] V. Schädler, A. Franck, U. Wiesner, H. W. Spiess, *Macromolecules* **1997**, *30*, 3832

[21] S. E. Cramer, G. Jeschke, H. W. Spiess, *Macromol. Chem. Phys.* **2002**, *203*, 182

[22] D. Hinderberger, H. W. Spiess, and G. Jeschke, *accepted by Macromol. Symp.* (**2003**)

[23] D. A. McQuarrie, **Statistical Mechanics**, HarperCollins Publishers, New York (1976)

[24] V. Vlachy, *Ann. Rev. Phys. Chem.* **1999**, *50*, 145

[25] P. Debye and E. Hückel, *Phys. Z.* **1923**, *24*, 185

[26] P.J. Flory, **Statistical Mechanics of Chain Molecules**, Wiley, New York (1969)

[27] O. Kratky, G. Porod, *Recuil Trav. Chim. Pays-Bas* **1949**, *68*, 1106

[28] T. Odijk, *J. Polym. Sci., Polym. Phys.* **1977**, *15*, 477

[29] J. Skolnick and M. Fixman, Macromolecules **1977**, *10*, 944

[30] P.-G.De Gennes, **Scaling Concepts in Polymer Physics**, Cornell Univ. Press, Ithaca (1979)

[31] G. Manning, *J. Chem. Phys.* **1969**, *51*, 924

[32] G. Manning, *J. Chem. Phys.* **1969**, *51*, 934

[33] G. Manning, *Acc. Chem. Res.* **1979**, *12*, 443

[34] G. Manning, *J. Chem. Phys.* **1988**, *89*, 3772

[35] A. Deshkovski, S. Obukhov, and M. Rubinstein, *Phys. Rev. Lett.* **2001**, *86*, 2341

[36] M. J. Le Bret, *J. Chem. Phys.* **1982**, *76*, 6248

[37] M. Fixman, *J. Chem. Phys.* **1982**, *76*, 6346

[38] S. Förster, M. Schmidt, and M. Antonietti, *J. Phys. Chem.* **1992**, *96*, 4008

[39] A. Schweiger, G. Jeschke, **Principles of Pulse Electron Paramagnetic Resonance**, Oxford University Press (2001)

[40] W. L. Hubbell, D. S. Cafiso, C. Altenbach, *Nature Struc. Biol.* **2000**, *7*, 735

[41] K. Schmidt-Rohr, H. W. Spiess, **Multidimensional Solid-State NMR and Polymers**, Academic Press, London (1996)

[42] O. Stern, W. Gerlach, *Z. Phys.* **1922**, *8*, 110

[43] G. E. Uhlenbeck, S. Goudsmit, *Naturwiss.* **1925**, *13*, 953

[44] G. E. Uhlenbeck, S. Goudsmit, *Nature.* **1925**, *117*, 264

[45] P. A. M. Dirac, *Proc. Roy. Soc. London* **1928**, *A117*, 610; ibid. **1928**, *A118*, 351

[46] Note that as usual in modern EPR literature, the magnetic induction $\boldsymbol{B}$ is used instead of the magnetic field H; $\boldsymbol{B}=\mu_0 \times H$

[47] A. Abragam, M. H. L. Pryce, *Proc. Roy. Soc. London* **1951**, *A205*, 135

[48] J. Pilbrow, **Transition Ion Electron Paramagnetic Resonance**, Oxford Univ. Press (1990)

[49] C. P. Slichter, **Principles of Magnetic Resonance**, *third edition*, Springer Series in Solid State Science, Vol. 1, Springer-Verlag Berlin (1990)

[50] Yu. N. Molin, K. M. Salikhov, K. I. Zamaraev, **Spin Exchange – Principles and Applications in Chemistry and Biology**, Springer Series in Chemical Physics, Vol. 8, Springer-Verlag, Berlin (1980)

[51]   D. J. Schneider and J. H. Freed in: **Biological Magnetic Resonance, Vol. 8: Spin Labeling – Theory and Applications**, Eds. L. J. Berliner, J. Reuben, Plenum Press, New York (1989), Chapter 1

[52]   G. Jeschke, *Macromol. Rapid Comm.* **2002**, *23*, 227

[53]   A. Bencini, D. Gatteschi, **EPR of Exchange Coupled Systems**, Springer-Verlag Berlin (1990)

[54]   P. W. Anderson in: **Magnetism**, Eds. G. T. Rado, H. Suhl

[55]   K. M. Salikhov, A. G. Semenov, Y. D. Tsvetkov, **Electron Spin Echo and Its Applications**, Nauka, Novosibirsk (1976), Chapter 4 195-235

[56]   L. J. Berliner, S. S. Eaton, G. R. Eaton (Eds.), **Biological Magnetic Resonance, Vol. 19: Distance Measurements in Biological Systems by EPR**, Kluwer Academic Publishers, New York (2000)

[57]   A. H. Beth, B. H. Robinson in: **Biological Magnetic Resonance, Vol. 8: Spin Labeling – Theory and Applications**, Eds. L. J. Berliner, J. Reuben, Plenum Press, New York (1989), Chapter 4

[58]   A. R. Edmonds, **Angular Momentum in Quantum Mechanics**, Princeton University Press, 2nd edition (1960)

[59]   B. H. Robinson, C. Mailer, and A. W. Reese, *J. Mag. Res.* **1999**, *138*, 199; and: *J. Mag. Res.* **1999**, *138*, 210

[60]   S. A. Goldman, G. V. Bruno, C. F. Polnaszek, J. H. Freed, *J. Chem. Phys.* **1972**, *56*, 716

[61]   J. S. Hwang, R. P. Mason, L. P. Hwang, and J. H. Freed, *J. Phys. Chem* **1975**, *79*, 489

[62]   G. te Velde, F. M. Bickelhaupt, E. J. Baerends, C. Fonseca Guerra, S. J. A. van Gisbergen, J. G. Snijders, T. Ziegler, *J. Comput. Chem.* **2001**, *22*, 93

[63]   C. Wegener, A. Savitsky, M. Pfeiffer, K. Möbius, H. J. Steinhoff, *Appl. Magn. Res.* **2001**, *21*, 441

[64]   J. J. Sakurai, **Modern Quantum Mechanics** (Revised Edition), Addison–Wesley Publishing Company, Inc. Reading, MA (1994)

[65]   O. W. Sørensen, G. W. Eich, M. H. Levitt, G. Bodenhausen, R. R. Ernst, *Prog. NMR Spectrosc.* **1983**, *16*, 163

[66]   S. E. Cramer, **Filmbildung industrieller Latices: Anwendung von ESR-Spin-Sonden-Methoden**, Doctoral Dissertation, Mainz (2001)

[67]   J. S. Hyde, M. Pasenkiewicz-Gierula, A. Jesmanowicz, W. E. Antholine, *Appl. Magn. Reson.* **1990**, 1, 483

[68]   E. L. Hahn, *Phys. Rev.* **1950**, *80*, 580

[69]   R. J. Blume, *Phys. Rev.* **1958**, *109*, 1867

[70]   D. M. S. Bagguley (Ed.), **Pulsed Magnetic Resonance: NMR, ESR, and Optics**, Clarendon Publ., Oxford (1992)

[71] M. Lindgren, G. R. Eaton, S. A. Eaton, B.-H. Jonsson, P. Hammarström, M. Svensson, U. Carlsson, *J. Chem. Soc., Perkin Trans. 2* **1997**, 2549

[72] S. S. Eaton, G. R. Eaton in: **Biological Magnetic Resonance, Vol. 19: Distance Measurements in Pulse EPR**, Eds. L. J. Berliner, S. S. Eaton, G. R. Eaton, Plenum Press, New York (2000), Chapter 1

[73] A. D. Milov, K. M. Salikhov, M. D. Shirov, *Fiz. Tverd. Tela (Leningrad)* **1981**, *23*, 957

[74] A. D. Milov, A. B. Ponomarev, Yu. D. Tsvetkov, *Chem. Phys. Lett.* **1984**, *110*, 67

[75] G. Jeschke, *ChemPhysChem* **2002**, *3*, 927

[76] M. Pannier, S. Veit, A. Godt, G. Jeschke, H. W. Spiess, *J. Magn. Res.* **2000**, *142*, 331

[77] G. Jeschke, A. Koch, U. Jonas, A. Godt, *J. Magn. Res.* **2002**, *155*, 72

[78] V. V. Kurshev, A. M. Raitsimring, Yu. D. Tsvetkov, *J. Magn. Res.* **1989**, *81*, 441

[79] P. P. Borbat, H. S. Mchaourab, J. H. Freed, *J. Am. Chem. Soc.* **2002**, *122*, 5304

[80] T. Ichikawa, L. Kevan, M. K. Bowman, S. A. Dikanov, and Yu. D. Tsvetkov, *J. Chem. Phys.* **1979**, *71*, 1167

[81] S. Kelch, M. Rehahn, *Macromolecules* **1999**, *32*, 5818

[82] O. Schmelz, M. Rehahn, *e-polymers* **2002**, no. 47

[83] C. Wandrey, J. Hernandez-Barajas, D. Hunkeler, *Adv. Polym. Sci.* **1999**, *145*, 123

[84] S. T. Dubas, J. B. Schlenoff, *Macromolecules* **1999**, *32*, 8153

[85] B. L. Rivas, I. Moreno-Villoslada, *J. Phys. Chem. B.* **1998**, *102*, 11024

[86] R. M. Petrovich, E. K. Jaffe, *Biochemistry* **1997**, *36*, 13421

[87] T. S. Smith, R. LoBrutto, V. L. Pecoraro, *Coord. Chem. Rev.* **2002**, *228*, 1

[88] C. V. Grant, W. Cope, J. A. Ball, G. G. Maresch, B. J. Gaffney, W. Fink, R. D. Britt, *J. Phys. Chem. B.* **1999**, *103*, 10627

[89] S. K. Misra, *Appl. Magn. Res.* **1996**, *10*, 193

[90] J. H. Ardenkjaer-Larsen, I. Laursen, I. Leunbach, G. Ehnholm, L. G. Wistrand, J. S. Petersson, K. Golman, *J. Mag. Res.* **1998**, *133*, 1

[91] Lu Yong, J. Harbridge, R. W. Quine, G. A. Rinard, S. S. Eaton, G. R. Eaton, C. Mailer, E. Barth, H. J. Halpern, *J. Mag. Res.* **2001**, *152*, 156

[92] N. Kocherginsky, H. M. Swartz, **Nitroxide Spin Labels – Reactions in Biology and Chemistry**, CRC Press, Boca Raton (1995)

[93] M. T. Jones, *J. Chem. Phys.* **1963**, *38*, 2892

[94] M. P. Eastman, G. V. Bruno, J. H. Freed, *J. Chem. Phys.* **1970**, *52*, 2511

[95] B. K. P. Scaife, **Principles of Dielectrics**, Monographs on the Physics and Chemistry of Materials, Vol. 45, Oxford University Press (1989)

[96] A. Polimeno, J. H. Freed, *J. Phys. Chem.* **1995**, 99, 10995

[97] E. Strandberg and P.O. Westlund, *J. Mag. Res. A* **1996**, *122*, 179

[98]   G. W. Scherer, **Relaxation in glass and composites**, Chapter 4, Malabar, Florida, Krieger (1992)

[99]   This has been checked by measuring both spin probes in fully deuterated water, where the deviation from purely Lorentzian lines virtually vanishes

[100] C. P. Lindsey, G. D. Patterson, *J. Chem. Phys.* **1980**, *73*, 3348

[101] I. N. Bronstein, K. A. Semendjaev, G. Musiol, H. Mühlig, **Taschenbuch der Mathematik**, 4. überarbeitete Auflage, Verlag Harri Deutsch, Frankfurt/Main (1999)

[102] In a first publication (Ref. 17) the characteristic relaxation time was transformed to a linewidth as described in the text. Presentation of the data as $<T_2>$ and x as it is done here has the advantage, though, to give the same information and to be more directly related to the fitting procedure;

[103] W. Dawydoff, K.-J. Linow, B. Philipp, *Acta Polym.* **1991**, *42*, 592

[104] W. Dawydoff, K.-J. Linow, B. Philipp, *Acta Polym.* **1991**, *42*, 646

[105] A. R. Khokhlov, *J. Phys. A* **1980**, *13*, 979

[106] E. Y. Kramarenko, A. R. Khokhlov, and K. Yoshikawa, *Macromolecules* **1997**, *30*, 3383.

[107] H. Schiessel and P. Pincus, *Macromolecules* **1998**, *31*, 7935.

[108] H. Schiessel, *Macromolecules* **1999**, *32*, 5673.

[109] C. Y. Shew and A. Yethiraj, *J. Chem. Phys.* **1999**, *110*, 676

[110] F. J. Solis and M. O. de la Cruz, *J. Chem. Phys.* **2000**, *112*, 2030

[111] A. Bagno, M. Campulla, M. Pirana, G. Scorrano, S. Stiz, *Chem. Eur. J.* **1999,** *5*, 1291

[112] S. Dixit, J. Crain, W. C. K. Poon, J. L. Finney, A. K. Soper, *Nature* **2002**, *416*, 829

[113] Feng Shi, Master's Thesis, University of Mainz (2003)

[114] R. Behrends, P. Miecznik, U. Kaatze, *J. Phys. Chem. A* **2002**, *106*, 6039

[115] K. S. Peters and B. Li, *J. Phys. Chem.* **1994**, *98*, 401

[116] R. E. D. McClung and D. Kivelson, *J. Chem. Phys.* **1968**, *49*, 3380

[117] This effect is actually not as strong as Stokes-Einstein theory predicts. Hwang et al. (see Ref. 61) have shown that a nitroxide spin probe rotated more than seven times faster in pure glycerol than expected from bulk viscosity. In our case the slowest rotational correlation times in glycerol/water are only three times as large as in NMPA/water. McClung and Kivelson (see Ref. 116) introduce a relation for the rotational correlation time, which includes an empirical *slip parameter*. This parameter κ ($0 \leq \kappa \leq 1$) accounts for rotational motion faster than expected from bulk viscosity: $\tau_c = \kappa * \tau_c$ (Stokes-Einstein).

[118] A. D. Milov and Yu. D. Tsvetkov, *Appl. Magn. Res.* **1997**, *12*, 495

[119] If the distance distribution is broad enough, all parts of a Gaussian distribution with a mean value of 1.25 nm that extent to $r > 1.5$ nm still contribute to the detected DEER signal.

[120] P. Chodanowski, S. Stoll, *J. Chem. Phys.* **1999**, *111*, 6069

[121] G. Jeschke, M. Pannier, A. Godt, H. W. Spiess, *Chem. Phys. Lett.* **2000**, *331*, 243

[122] C. T. Farrar, D. A. Hall, G. J. Gerfen, M. Rosay, J.-H. Ardenkjaer-Larsen, R. G. Griffin, *J. Mag. Res.* **2000**, *144*, 134

[123] D. A. Rees, *Adv. Carbohydr. Chem.* **1969**, *24*, 267

[124] W. Dawydoff, K.-J. Linow, B. Philipp, *Nahrung* **1984**, *28*, 241

List of Abbreviations and Symbols

α - anisotropy of spin probe rotational diffusion tensor: $d_{\parallel} / d_{\perp}$

a_{iso} – isotropic ^{14}N hyperfine coupling constant

β_e – Bohr magneton

$\boldsymbol{B}$ – magnetic induction, $\boldsymbol{B}=\mu_0 \times \boldsymbol{H}$

CAT 1 - trimethyl ammonium TEMPO, CATionic nitroxide radical

CW – Continuous Wave

$d_{\parallel}$ - rotational diffusion rate parallel to unique axis

$d_{\perp}$ - rotational diffusion rate perpendicular to unique axis

DEA – Dynamic Electrostatic Attachment

DEER – Double Electron-Electron Resonance

DH – Debye-Hückel theory

e – elementary charge, 1.602×10^{-19} As

ELDOR – Electron-Electron Double Resonance

ENDOR – Electron-Nuclear Double Resonance

EPR – Electron Paramagnetic Resonance

ESE – Electron Spin Echo

ESEEM – Electron Spin Echo Envelope Modulation

ESR – Electron Spin Resonance

FS – Fremy's salt

FT – Fourier Transform or Fourier Transformation

FJC – Freely Jointed Chain

FRC – Freely Rotating Chain

ID – Instantaneous Diffusion

l_B – Bjerrum length

lw - linewidth

mw – microwave

NMPA – N-methylpropionamide

OSF – Odijk-Skolnick-Fixman theory

PB – Poisson-Boltzmann

PDADMAC – Poly(diallyldimethylammonium chloride)

PSS – Poly(4-styrene sulfonate)

rf – radiofrequency

rms – root mean square

RuCP – Ruthenium Coordination Polymer

SIFTER – Single Frequency Technique for Electron Refocusing

τ_c – rotational correlation time

T – absolute temperature in Kelvin

TAM – Triarylmethyl trianion

TEMPO - 2,2,6,6-tetramethylpiperidine-1-oxyl

X-band – microwave frequency range of ~9.1 GHz to ~9.8 GHz

W-band – microwave frequency range of ~93 GHz to ~94 GHz

WLC – Worm Like Chain

. Acknowledgments

Due to restrictions for dissertations that are published online, I cannot acknowledge all the people *personally* who supported me throughout the years. So I just say *thank you* to all of them...

Summary

In this thesis methods of EPR spectroscopy were used to investigate polyion-counterion interactions in polyelectrolyte solutions. The fact that EPR techniques are *local methods* is exploited and by employing spin-carrying (i.e., EPR-active) probe ions it is possible to examine polyelectrolytes from the *counterions' point of view*.

It was possible to gain insight into i) the *dynamics* and *local geometry* of *counterion attachment*, ii) *conformations* and *dynamics* of local segments of the *polyion* in an indirect manner, and iii) the *spatial distribution* of spin probe ions that surround polyions in solution.

Analysis of CW EPR spectra of dianion nitroxide spin probe Fremy's salt (FS, potassium nitrosodisulfonate) in solutions of cationic PDADMAC polyelectrolyte revealed that FS ions and PDADMAC form transient ion pairs with a lifetime of less than 1 ns. This effect was termed as *dynamic electrostatic attachment* (DEA). By spectral simulation taking into account the rotational dynamics as a uniaxial Brownian reorientation, also the geometry of the attached state could be characterized. By variation of solvent, the effect of solvent viscosity and permittivity were investigated and indirect information of the polyelectrolyte chain motion was obtained. Furthermore, analysis of CW EPR data also indicates that in mixtures of organic solvent/water PDADMAC chains are preferentially solvated by the organic solvent molecules, while in purely aqueous mixtures the PDADMAC chain segments were found in different conformations depending on the concentration ratio R of FS counterions to PDADMAC repeat units.

Broadenings in CW EPR spectra of FS ions were assigned to spin-exchange interaction and hence contain information on the local concentrations and distributions of the counterions. From analysis of these broadenings in terms of a modified cylindrical cell approach of polyelectrolyte theory, *radial distribution functions* for the FS ions in the different solvents were obtained. This approach breaks down in water above a threshold value of R, which again indicates that PDADMAC chain conformations are altered as a function of R.

Double electron-electron resonance (DEER) measurements of FS ions were carried out to probe the distribution of attached counterions along polyelectrolyte chains. For a significant fraction of FS spin probes in solution with a rigid-rod model polyelectrolyte containing charged Ru^{2+}-centers, a bimodal distance distribution was found that nicely reproduced the spacings of direct and next-neighbor Ru^{2+}-centers along the polyelectrolyte: 2.35 and 4.7 nm. For the system of FS/PDADMAC, DEER data could be simulated by assuming a two-state distribution of spin probes, one state corresponding to a *homogeneous* (3-dimensional) distribution of spin probes in the polyelectrolyte bulk and the other to a *linear* (1-dimensional) distribution of spin probes that are electrostatically condensed along locally extended PDADMAC chain segments. From this analysis it is suggested that the PDADMAC chains form locally elongated structures of a size of at least ~5 nm.

Curriculum Vitae

Dariush Hinderberger, geboren am 10. Mai 1975 in Heidelberg

Schule, Studium und Wissenschaftlicher Werdegang

Seit April 2001	Doktorand in der Arbeitsgruppe von Prof. Dr. H. W. Spiess am Max-Planck-Institut für Polymerforschung in Mainz. Arbeitsgebiet: EPR (Electron Paramagnetic Resonance) Spektroskopie an sog. „weichen Materialien", insbesondere Polyelektrolyten.
Sep. 1999 - August 2000	Forschungsaufenthalt bei Prof. Bruce H. Robinson am Department of Chemistry der University of Washington, Seattle, WA, USA.
	Während dieses Aufenthalts habe ich meine Diplomarbeit angefertigt. In dieser befasste ich mich mit der Charakterisierung von Materialien mit elektro-optischen Eigenschaften, was sowohl synthetische als auch spektroskopische (EPR-Spektroskopie) Arbeit beinhaltete.
	Titel der Arbeit: "Spin Labeling and Electron Paramagnetic Resonance (EPR) Spectroscopic Studies of Electrooptic Model Chromophore"
April 1997 - März 2001	Studium der Chemie an der Technischen Universität Berlin
19. März 2001	Diplom-Hauptprüfung
31. März 1998	Diplom-Vorprüfung
März 1996 - März 1997	Unterbrechung des Studiums zur Ableistung des Zivildienstes beim Deutschen Roten Kreuz, Dienststelle Kandel/Pfalz
Okt. 1994 - Februar 1996	Studium der Chemie an der Ruprecht-Karls-Universität in Heidelberg.
Aug. 1985 - Juni 1994	Besuch des Johann-Wolfgang-Goethe-Gymnasiums in Germersheim am Rhein
	Allgemeine Hochschulreife
Sep. 1981 – Juni 1985	Besuch der Eduard-Orth-Grundschule in Germersheim am Rhein